Università degli Studi di Padova

DIPARTIMENTO DI SCIENZE CHIMICHE
Corso di Dottorato di Ricerca in Scienze Molecolari
Curriculum: Scienze Chimiche
CICLO XXXVI

Tesi di Dottorato

Theoretical and Computational Insights into Non-Linear Response in Action-2D Electronic Spectroscopy

Coordinatore:
Ch.mo Prof. Stefano Corni

Supervisore:
Ch.ma Prof.ssa Barbara Fresch

Dottorando:
Matteo Bruschi

Abstract - English

Two-Dimensional Electronic Spectroscopy (2DES) is a powerful tool for investigating the properties of complex molecular aggregates and nanostructures. By probing the system with a sequence of ultrafast laser pulses, spectral and temporal information are dissected along multiple dimensions, allowing to track energy and charge transfer pathways within multichromophoric systems. Because of the wealth of information contained in the spectra, the origin of certain spectral features can be ambiguous. Therefore, the development of theoretical models and numerical simulations is essential to support their correct interpretation.

Recently, a novel implementation of the technique has been realized, known as Action-2DES (A-2DES), calling for theoretical and numerical efforts to establish the correlation between spectral features and the dynamical processes occurring at the molecular scale. While probing the coherent dynamics induced by the interaction with four collinear laser pulses, the technique relies on the measurement of an incoherent signal proportional to the excited-state population, e.g., fluorescence or photocurrent, allowing the investigation of functional dynamics of systems in *operando* conditions.

In this Thesis, we delve into the theory of A-2DES and its numerical simulation to clarify essential aspects of the incoherent signal detected with this technique. To this end, we employed a combination of perturbative and non-perturbative approaches to describe the light-matter interaction. While the former provides the conceptual basis for the analysis of the response in terms of several dynamical pathways, the latter allows the complete simulation of the entire spectroscopic experiment.

In A-2DES, the signal is detected over a timescale during which the excited-state population may undergo several processes. We investigated the effects of such population dynamics on the spectra by characterizing the spectroscopic response of a model of quantum dot featuring the interplay between exciton and biexciton contributions to the signal.

The involvement of the double-excited manifold in the signal represents a crucial factor shaping the signal in A-2DES. Thus, we analyzed the case in which the double-excited

manifold consists of excited states localized on different weakly interacting chromophores. This setting allows to discuss the origin of cross-peaks and incoherent mixing in the signal, first considering the case of a simple molecular dimer and then in a larger molecular assembly. The analysis shows that mixing effects are intrinsic in the A-2DES, and they must be carefully addressed in the design of the sample and the choice of the detection scheme.

Our investigation further proceeded by focusing on the dependence of the spectral features on varying the excitonic coupling strength, showing how cross-peaks can either reflect the presence of exciton-exciton annihilation or excitonic delocalization between chromophores, depending on the coupling regime.

Finally, we shifted the focus toward a related yet distinct subject, wondering whether emerging quantum computing technologies could contribute to the efficient simulation of 2DES spectra. Accordingly, we designed a quantum algorithm for simulating the non-linear response of multichromophoric systems and provided a proof-of-concept computation considering an excitonic dimer model.

Abstract - Italiano

La spettroscopia elettronica bidimensionale (2DES) è un potente strumento per studiare le proprietà di aggregati molecolari e nanostrutture complesse. Mediante l'interazione con una sequenza di impulsi laser ultraveloci, le informazioni spettrali e temporali del sistema vengono separate lungo diverse dimensioni, consentendo di seguire i percorsi di trasferimento di energia e carica all'interno di sistemi multicromoforici. A causa della quantità di informazioni contenute negli spettri, l'origine di alcune caratteristiche spettrali può risultare ambigua. Pertanto, lo sviluppo di modelli teorici e di simulazioni numeriche è essenziale per supportare la loro corretta interpretazione.

Recentemente è stata realizzata una nuova implementazione della tecnica, nota come *Action*-2DES (A-2DES). Lo sviluppo di modelli teorici e numerici specifici sono necessari per stabilire la correlazione tra le caratteristiche spettrali e i processi dinamici che avvengono su scala molecolare. Mentre la dinamica coerente è indotta dall'interazione con quattro impulsi laser collineari, la tecnica si basa sulla misura di un segnale incoerente proporzionale alla popolazione di stato eccitato, ad esempio fluorescenza o fotocorrente, consentendo di indagare la dinamica funzionale dei sistemi in condizioni operative.

In questa Tesi, abbiamo approfondito la teoria dell'A-2DES e la sua simulazione numerica per chiarire gli aspetti fondamentali del segnale incoerente rivelato con questa tecnica. A tal fine, abbiamo utilizzato la combinazione di un approccio perturbativo e non perturbativo per descrivere l'interazione luce-materia. Mentre il primo fornisce le basi concettuali per l'analisi della risposta in termini di diversi percorsi dinamici, il secondo permette la simulazione completa dell'intero esperimento spettroscopico.

In A-2DES, il segnale è rivelato su una scala temporale durante la quale la popolazione di stato eccitato può andare incontro a diversi processi. Abbiamo analizzato gli effetti di tali dinamiche di popolazione sugli spettri, caratterizzando la risposta spettroscopica in un modello di quantum dot che prevede la presenza di un contributo eccitonico e bieccitonico al segnale.

Il coinvolgimento del manifold di doppia eccitazione è risultato essere un fattore cru-

ciale nell'influenzare il segnale in A-2DES. Dunque, abbiamo analizzato il caso in cui il manifold di doppia eccitazione sia formato da stati eccitati localizzati su diversi cromofori debolmente interagenti. Questa descrizione consente di discutere l'origine dei *cross-peaks* e dell'*incoherent mixing* nel segnale, dapprima considerando il caso di un semplice dimero molecolare e successivamente di un aggregato molecolare. L'analisi evidenzia che gli effetti di *incoherent mixing* sono intrinseci in A-2DES e devono essere valutati con attenzione durante la scelta del campione e dello schema di misura.

La nostra indagine è proseguita concentrandosi sulla dipendenza delle caratteristiche spettrali al variare della forza dell'accoppiamento eccitonico, mostrando come i *cross-peaks* possano riflettere la presenza di annichilazione eccitone-eccitone o di delocalizzazione eccitonica tra cromofori, a seconda del regime di accoppiamento.

Infine, abbiamo spostato l'attenzione su un argomento correlato ma distinto, chiedendoci se le emergenti tecnologie di calcolo quantistico possano contribuire alla simulazione efficiente di spettri 2DES. Di conseguenza, abbiamo progettato un algoritmo quantistico per simulare la risposta non lineare di sistemi multicromofori e ne abbiamo fornito una dimostrazione pratica considerando il modello di un dimero eccitonico.

Contents

1 | Introduction

Light-matter interaction underlies the functioning of many natural and artificial systems.

The most prominent example is represented by the photosynthetic process of plants and bacteria. In the initial step of photosynthesis, known as *light-harvesting*, energy from the sunlight is captured by specific pigments, e.g., (bacterio)chlorophylls and carotenoids, within the antenna complex [1, 2]. Then, the energy, stored as an electronic excitation, migrates from one molecule to the other eventually reaching the reaction center where charge separation takes place. Subsequently, the electrons generated enter into an intricate sequence of charge transfer reactions, ultimately resulting in the production of chemical compounds vital for the sustenance of the cell.

Recently, great efforts have been devoted to designing efficient solar cells for the production of clean and sustainable energy [3]. By exploiting the photovoltaic effect, solar cells convert solar energy into an electric current. Depending on the semiconductor, different types of solar cells have been developed, e.g., silicon-based, organic, quantum dots and perovskite, with the aim of producing more affordable and efficient materials. Solar cells are composed of an active layer, which is a blend of electron-donor and electron-acceptor materials, sandwiched between two electrodes. The light absorbed in the active layer produces an exciton that travels towards the donor-acceptor interface, called heterojunction. Charge separation occurs at the heterojunction, generating free charges that move toward the electrodes, producing an electric current.

1.1. Probing Exciton Dynamics in the Condensed Phase

From the physical chemistry perspective, spectroscopy exploits the light-matter interaction to probe the properties of molecular systems and materials. The simplest kind of spectroscopic experiment is represented by linear techniques, e.g., absorption or emission spectroscopy, which are commonly performed in the frequency domain. In a linear spectrum, the position of the peaks represents the transition frequency of the system, while their amplitude is proportional to the transition dipole moment. Furthermore, the lineshape

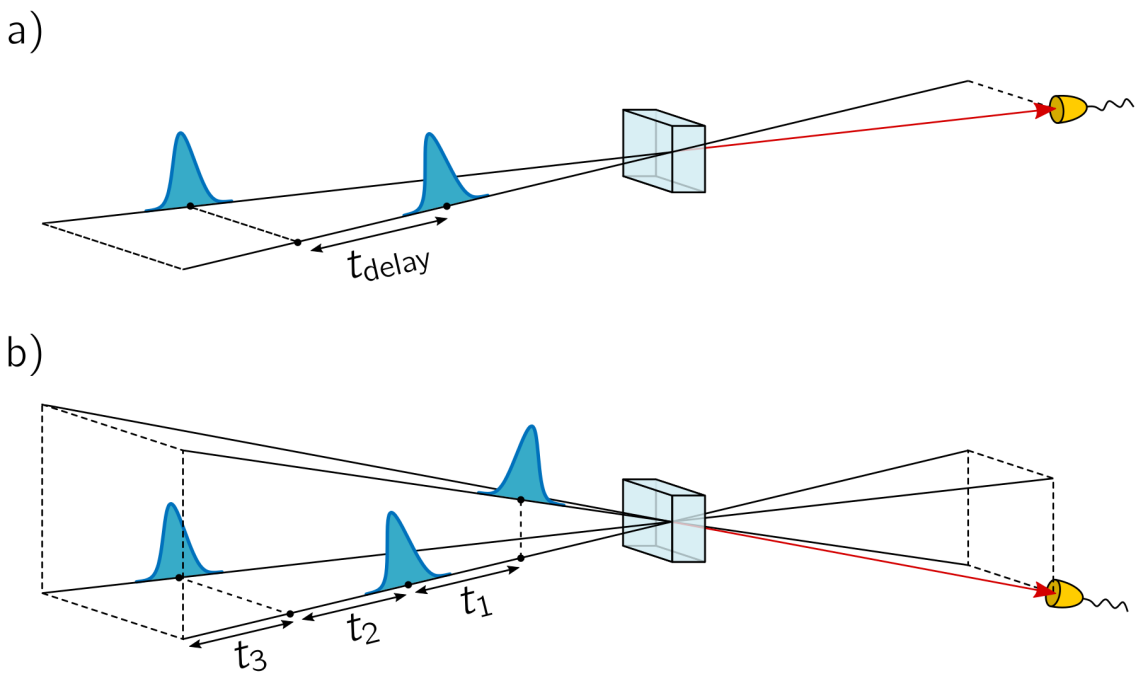

Fig. 1.1: Schematic representation of a) pump-probe spectroscopy and b) Coherent-2D Electronic Spectroscopy (C-2DES) experiments. The signal is represented by a coherent electric field (red arrow) which is collected by the detector.

of the peaks reflects the presence of inhomogeneity within the sample and the interaction with the surroundings, such as solvent molecules, protein scaffold or polymer matrix.

While linear techniques provide valuable information, they offer a rather static picture of the system, in which the temporal dimension is not explicitly involved. In contrast, time-resolved techniques allow to tracking a plethora of molecular processes occurring in the time domain, such as vibrations, charge and energy transfer [4]. However, in order to investigate these processes, ranging from nanoseconds to femtoseconds regime, it is necessary to achieve adequate time resolution. Consequently, the experimental characterization of these phenomena has progressed together with technological advancements. With the advent of lasers, it finally became possible to investigate chemical phenomena occurring on such timescales through the use of ultrafast pulses and the development of a toolbox of non-linear optical spectroscopies.

The most common time-resolved technique is pump-probe spectroscopy (Fig. 1.1a) [5]. In a pump-probe experiment, the sample interacts with two distinct laser pulses, respectively called the "pump" and the "probe", which are both temporally and spatially separated. First, the pump pulse excites the sample to an electronic excited state. After a certain delay time t_{delay}, the probe pulse measures the transient change in the absorption

induced by the previous interaction with the pump. The signal is given as a function of the probe frequency ω_{probe} and the delay time between the pulses t_{delay}.

However, this technique suffers from specific limitations. The first issue is related to the lack of simultaneous time and frequency resolution, due to the time-frequency uncertainty relation. On the one hand, short pulses offer greater temporal resolution but preclude selective excitation. On the other hand, longer pulses allow selective excitation but may obscure the system dynamics. Therefore, it is often necessary to reach a compromise between temporal and spectral resolution. The second problem is related to the fact that the technique is not background-free. Indeed, the signal is acquired simultaneously with the probe pulse by the detector. Therefore, it is necessary to isolate the signal, often resulting in a low signal-to-noise ratio.

1.2. Two-Dimensional Electronic Spectroscopy

Both of these limitations can be circumvented using Two-Dimensional Electronic Spectroscopy (2DES) [6]. 2DES represents the most advanced spectroscopic technique for investigating the non-linear optical response of molecular systems and nanostructures [7–9].

In its conventional implementation, Coherent-2DES (C-2DES) is performed in a fully non-collinear geometry (Fig. 1.1b), where three pulses interact with the sample starting from different vertices of a square. The pulses are temporally separated by delay times t_1, t_2 and t_3. The signal, represented by a coherent electric field, is emitted in a specific spatial direction according to the phase-matching condition, thus allowing background-free detection. By scanning the delay times between the pulses, the signal is measured as a function of t_1, t_2 and t_3. Note that, in this case, the time resolution is not limited by the pulse duration, but is determined by the delay time scan.

By taking the Fourier transform along delay times t_1 and t_3, the signal is typically visualized as a 2D spectrum for each value of the waiting time t_2 (Fig. 1.2). The 2D spectrum can be interpreted as a correlation map between the excitation frequency ω_1 and the emission frequency ω_3, where each spectral feature is identified by coordinates (ω_1, ω_3). In general, it is possible to distinguish between diagonal peaks, where $\omega_1 = \omega_3$, and cross-peaks, where $\omega_1 \neq \omega_3$.

Diagonal peaks provide information about the energy level structure of the system under investigation. The lineshape of these peaks gives insights into the kind of interactions

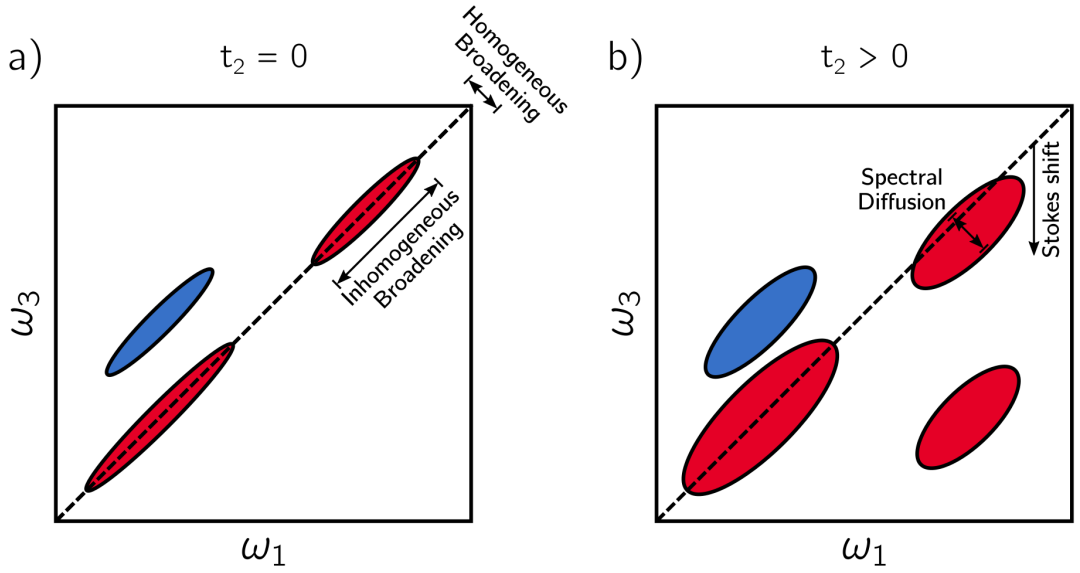

Fig. 1.2: Schematic representation of the 2D spectrum at different waiting times t_2. a) At early waiting times $t_2 = 0$, the peaks show inhomogeneous and homogeneous broadening respectively on the diagonal and anti-diagonal. b) As t_2 increases, the peaks become more rounded due to spectral diffusion. Furthermore, we can notice the drift of peaks towards lower emission frequency due to Stokes shift and the emergence of cross-peaks due to energy transfer between different states.

between the system and the environment. In particular, one of the most significant advantages of 2DES is its ability to differentiate between inhomogeneous and homogeneous broadening, which respectively appear along the diagonal and the anti-diagonal of the spectrum at $t_2 = 0$ (Fig. 1.2a). Inhomogeneous broadening is attributed to the presence of static disorder within the sample, wherein each system exhibits a different transition frequency due to its surroundings. In contrast, homogeneous broadening results from the occurrence of relaxation and dephasing processes for each system.

As t_2 increases, the peaks become progressively rounded due to the phenomenon of spectral diffusion, where environmental fluctuations cause the loss of correlation between the excitation and the emission frequency (Fig. 1.2b). Other properties of the lineshapes can be linked to the details of the system-environment interaction [10]. Furthermore, Stokes shift due to vibrational relaxation and solvent reorganization results in a drift of the peak towards lower emission frequency during the waiting time t_2.

Instead, cross-peaks reveal information about interaction and correlation between different states, allowing to characterize energy migration pathways. As t_2 increases, cross-peaks can appear due to relaxation between different states or energy transfer between molecules (Fig. 1.2b). In contrast, the presence of cross-peaks at $t_2 = 0$ represents a witness of excitonic delocalization, i.e., the eigenstates are given by the superposition of

localized excitations on different chromophores.

With its simultaneous time and frequency resolution, 2DES has revolutionized our understanding of excited-state dynamics, revealing insights that were previously inaccessible through linear spectroscopy. Given the wealth of information contained in the spectrum, the interpretation of spectral features requires the use of theoretical models and numerical simulations [11]. Optical spectroscopy is commonly interpreted in the framework of non-linear response theory [12, 13]. The contributions to the signal can be described in terms of different pathways followed by the system, distinguished in Ground-State Bleaching (GSB), Stimulated Emission (SE) and Excited-State Absorption (ESA). While GSB provides insights into the ground-state dynamics, both SE and ESA contain valuable information about processes occurring in the excited state.

1.3. A Short Tale of Long-Lived Quantum Coherences

C-2DES found immediate application in the investigation of biological systems [14–16]. However, the profound synergy between the interpretation of 2DES experiments and the understanding of exciton dynamics in terms of different theoretical models became clear from the discussion of the early results.

At the turn of the century, two conceptual frameworks were used to discuss energy transfer processes: an incoherent hopping mechanism between chromophores, as described by Förster theory [17], and the environment-mediated transition between delocalized excitations [18], as described by Redfield theory [19]. These theoretical settings find their justification in two different limiting cases: Förster theory assumes localized excitations as a good representation and treats the intermolecular coupling perturbatively. On the other hand, the Redfield master equation is formulated starting from possibly delocalized eigenstates, while the coupling with the environment acts as a perturbation inducing energy transfer. In its secular form, Redfield theory predicts a fast decoherence, in the femtoseconds timescale, for the different electronic states.

However, the observation of long-lived beatings along t_2 in C-2DES of the Fenna-Matthew-Olson (FMO) complex [20] suggested that electronic coherences may help to enhance the efficiency of the photosynthetic process. This finding contributed to the rise of quantum biology [21], triggering a vibrant discussion at the intersection of chemistry, physics, and biology about the possible role of quantum effects at the biological scale [22, 23]. Nevertheless, despite the initial excitement, there was no consensus about whether

such fragile quantum behavior could persist in a warm, wet and disordered environment as the biological one [24]. Subsequently, an impressive mole of theoretical work was devoted to testing different dynamical models in the simulation of spectra [25–27].

Later studies highlighted how those beatings could also be attributed to vibrational coherences, characterized by longer dephasing time [28, 29]. Moreover, the coherent excitation conditions of ultrafast spectroscopy experiments, under which such beatings were measured, drastically differ from those of the incoherent natural illumination typical of light-harvesting [30]. Recently, it was concluded that these beatings should be attributed to vibrational and vibronic coherences rather than electronic ones [31]. Furthermore, biological systems do not attempt to avoid decoherence and dissipation, instead, they harness them to efficiently direct energy transfer to the reaction center.

Although it is now clear that photosynthetic systems do not rely on electronic coherences to enhance the efficiency of the light-harvesting process, the insights gained from this exploration offer promising avenues for the design and investigation of novel artificial systems [22], in particular molecular aggregates [32–34], conjugated polymers [35, 36], quantum dots [37–40], perovskites [41–43] and polaritonic materials [44, 45]. On the other hand, the theoretical efforts to support the interpretation of the results led to improved theories for open quantum system dynamics such as the Hierarchical Equations of Motion (HEOM) [46, 47] and efficient numerical schemes to tackle the non-linear response of complex excitonic systems [48–50].

1.4. Action Detection Poses New Questions

In these two decades of 2DES, the technique has not remained unchanged but instead has undergone several advances. In particular, 2DES has been extended to different spectral regions such as terahertz [51], UV [52] and X-ray. Furthermore, the use of pulses of different colors, as demonstrated in 2D electronic-vibrational spectroscopy [53], has enabled the investigation of correlations between nuclear and electronic degrees of freedom. In the same way, polarization-dependent pulse sequences allowed for the selective reduction of diagonal peaks in the spectrum while enhancing cross-peak contributions [54].

One of the most significant advancements in the field is represented by Action-2D Electronic Spectroscopy (A-2DES) [55, 56]. In A-2DES, the sample interacts with a sequence of four collinear laser pulses (Fig. 1.3). As a result, an incoherent signal is emitted during the detection time t_d, which is proportional to the excited-state population. Depending

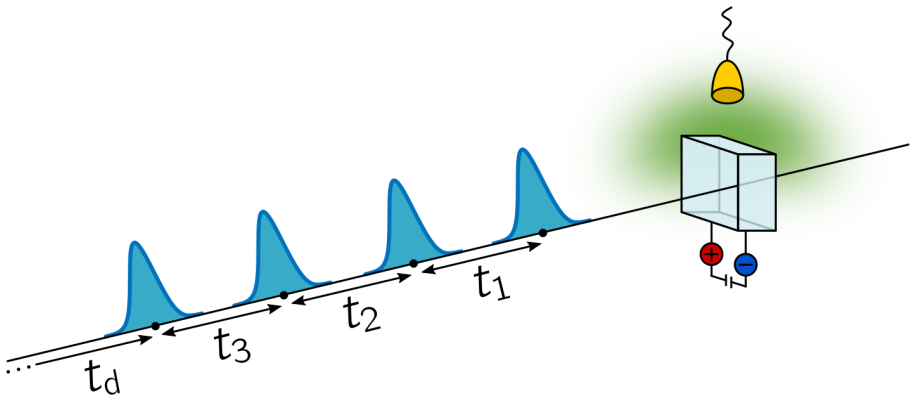

Fig. 1.3: Schematic representation of Action-2D Electronic Spectroscopy (A-2DES) experiment with fluorescence or photocurrent detection.

on the sample, the nature of the incoherent signal can be different, e.g., fluorescence [57], photocurrent [58, 59], photoions [60] and photoelectrons [61]. Since the pulses are collinear, it is not possible to differentiate the signal based on the phase-matching condition. Instead, the different components can be isolated by controlling the phase of the laser pulses, either using phase-cycling [62, 63] or phase-modulation [64] schemes.

The technique has several advantages compared to its coherent counterpart. In particular, the combination with single-molecule [65] and microscopy [66] techniques allows to achieve spatial resolution beyond the diffraction limit. Furthermore, its ability to measure functional signals makes A-2DES suitable for investigating systems in *operando* conditions [67]. In addition, the capability to detect different observables may highlight distinct mechanisms contributing to the signal, as demonstrated for fluorescence and photocurrent detection in quantum dots [59] and perovskite [68] solar cells, allowing for a more comprehensive characterization of the system under investigation. Moreover, the lack of non-resonant solvent contribution, which instead may affect the optical response in C-2DES during the pulse overlap [69], offers a cleaner access to the early waiting-time dynamics [70].

However, while A-2DES and C-2DES share multiple similarities, the spectral features obtained from the two techniques exhibit significant differences, as recently demonstrated in comparative studies [70, 71]. A first difference arises from the additional light-matter interaction in A-2DES, which leads to two kinds of ESA pathways: one resulting in a single excited-state population (ESAI) and the other in a double excited-state population (ESAII) [57, 72]. Having opposite signs, the two pathways can destructively interfere leading to the mutual cancellation of the associated spectral features. The second difference is related

to the process of signal generation. In C-2DES the coherent signal is emitted on a short timescale, in the range of hundreds of femtoseconds, limited by the dephasing of the optical coherence. In contrast, the incoherent signal in A-2DES results from population relaxation, which typically occurs on a much longer timescale in the nanoseconds regime. During this period, the double-excited state population can undergo several non-radiative relaxation channels, e.g., exciton-exciton annihilation, Auger recombination. As a result, the ESAII contribution can be reduced, eventually leading to an ESA-free spectrum [73].

The origin of the spectral features in A-2DES, compared to the more established C-2DES, is a matter of active research. Recent A-2DES experiments on the LH2 complex revealed the presence of prominent cross-peaks at early waiting times [66, 74]. Consequently, several theoretical studies have been conducted to unravel the origin of these cross-peaks. In the analysis of a molecular dimer, Maly and Mančal highlighted that the emergence of cross-peaks at early waiting times represents a witness of exciton-exciton annihilation within the system, while provides limited insights into the presence of excitonic delocalization between chromophores [75]. Extending the analysis to multichromophoric systems, Kunsel et al. demonstrated that cross-peaks in the A-2DES spectra of LH2 complex actually reflect the presence of exciton-exciton annihilation between the B800 and B850 rings, exposing clean GSB signal between them [76]. In contrast, Schröter et al. proposed that cross-peaks may reveal the initial delocalization between chromophores before incoherent Förster mechanism sets in [77]. In an attempt to clarify the interpretation of cross-peaks in A-2DES, Kühn et al. concluded that cross-peaks can provide information on both exciton-exciton annihilation and excitonic delocalization, depending on the degree of interaction [73].

Moreover, it has been found that the phenomenon of incoherent mixing can affect the A-2DES signal. In this case, due to non-linear population dynamics [78], e.g., exciton-exciton annihilation and Auger recombination, or to non-linearity in the detection [79], linear responses can mix and enter in the signal, potentially hiding non-linear information. Recently, efforts have been devoted to distinguishing the incoherent mixing contribution from the non-linear response [80].

1.5. Scope and Outline of the Thesis

The ongoing debate on the origin of certain spectral features appearing in A-2DES calls for the development of novel theoretical and numerical approaches to avoid potential pitfalls in the interpretation of the signal. The scope of this Thesis is to contribute to this

effort. Specifically, we explore different simulation methods and apply them to analyze specific aspects of the action signal (Fig. 1.4).

In Chapter 2, we present the state-of-the-art for the simulation of the optical response. We introduce the two main methods for modeling 2DES spectroscopy, namely the perturbative and the non-perturbative approach to light-matter interaction.

The rest of the Thesis is intended as a collection of papers, some of which have already been published, while others are in preparation. The notation may slightly vary from one chapter to the other for the sake of convenience. However, the notation is always introduced self-consistently within each chapter.

In Chapter 3, we present the numerical simulation of the optical response of a quantum dot system as a case study to unravel the interplay between the exciton and biexciton contributions to the spectrum. We analyze how the relative weights of the exciton and biexciton signals determine the lineshape of the peaks, how they depend on the physical nature of the detected signal, i.e., fluorescence or photocurrent, and the relaxation dynamics during the detection time. Furthermore, we consider how the choice of the detection mode and the use of time-gating may aid the evaluation of relevant parameters, such as the biexciton binding energy and the timescales of the biexciton relaxation.

In Chapter 4, we discuss the relation between the non-linear response and the incoherent mixing contribution by analyzing the action signal in terms of one- and two-particle observables. Considering a weakly interacting molecular dimer, we show how cross-peaks at early waiting times, reflecting exciton-exciton annihilation, can be equivalently interpreted as arising from incoherent mixing. This equivalence, on the one hand, highlights the information content of spectral features related to incoherent mixing and, on the other hand, provides an efficient numerical scheme to simulate the action response of weakly interacting systems.

In Chapter 5, we extend these results to a molecular assembly composed of N chromophores, in the case where the output intensity is not proportional to the number of excitations generated. Accordingly, we identify different sources of non-linearities involving the two-exciton manifold, pointing out that the presence of incoherent mixing does not necessarily require dynamical interactions. We show how, in such situations, the ground-state bleaching contribution can dominate the non-linear signal and partially or completely hide the stimulated emission component, depending on the number of molecules involved.

In Chapter 6, we examine how excitonic coupling modifies the picture of the action

response of weakly interacting units analyzed in the previous Chapters. We discuss the case of a molecular dimer in different coupling regimes to investigate how exciton-exciton annihilation and excitonic delocalization are reflected in the spectral features. We analyze the change in amplitude of the spectral features as a function of the coupling strength and discuss the nature of the cross-peaks in different coupling regimes. Here, we also consider the waiting-time dynamics of the spectral features. However, further work is needed in this direction.

In Chapter 7, we deviate from the main subject of this study and wonder whether coherence at work in a quantum computer offers an effective way to simulate non-linear spectroscopy. We present a quantum algorithm for computing the optical response of molecular systems, by combining quantum dynamical simulation and non-linear response theory. The protocol is tested on a near-term quantum device providing digital quantum simulation of the linear and non-linear response of monomer and dimer molecular systems. The results are encouraging even though further technological developments are needed to reach the quantum advantage in the efficient simulation of the dynamics governed by the molecular Hamiltonian.

Finally, we provide the concluding remarks and trace the directions of future research arising from this work.

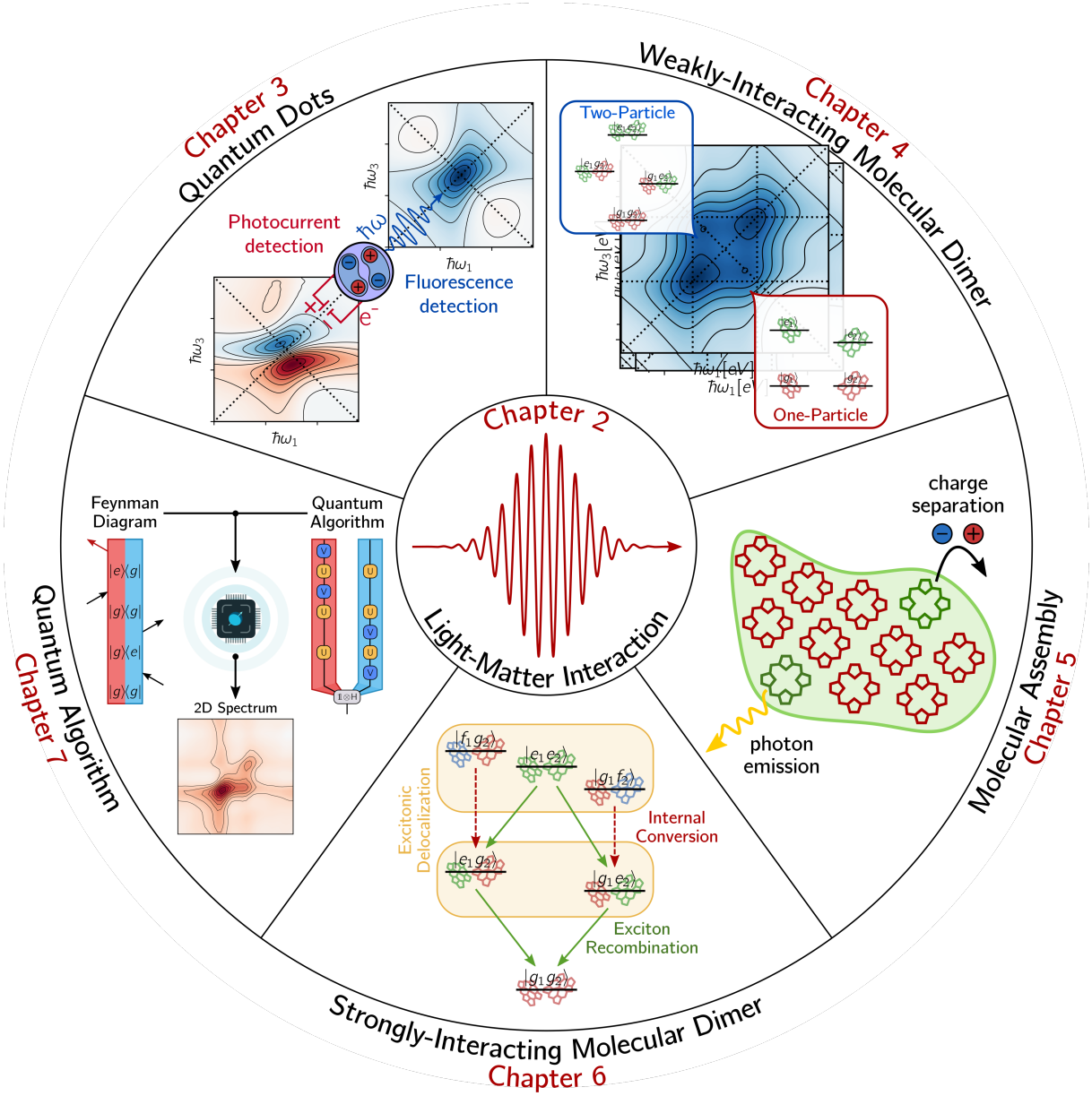

Fig. 1.4: Graphical outline of the Thesis.

References

(1) Scholes, G. D.; Fleming, G. R.; Olaya-Castro, A.; van Grondelle, R. Lessons from Nature about Solar Light Harvesting. *Nat. Chem.* **2011**, *3*, 763–774.

(2) Croce, R.; van Amerongen, H. Natural Strategies for Photosynthetic Light Harvesting. *Nat. Chem. Biol.* **2014**, *10*, 492–501.

(3) Solak, E. K.; Irmak, E. Advances in Organic Photovoltaic Cells: a Comprehensive Review of Materials, Technologies, and Performance. *RSC Adv.* **2023**, *13*, 12244–12269.

(4) Zewail, A. H. Femtochemistry: Atomic-Scale Dynamics of the Chemical Bond using Ultrafast Lasers (Nobel Lecture). *Angew. Chem., Int. Ed.* **2000**, *39*, 2586–2631.

(5) Berera, R.; van Grondelle, R.; Kennis, J. T. M. Ultrafast Transient Absorption Spectroscopy: Principles and Application to Photosynthetic Systems. *Photosynth. Res.* **2009**, *101*, 105–118.

(6) Jonas, D. M. Two-Dimensional Femtosecond Spectroscopy. *Annu. Rev. Phys. Chem.* **2003**, *54*, 425–463.

(7) Gelzinis, A.; Augulis, R.; Butkus, V.; Robert, B.; Valkunas, L. Two-dimensional spectroscopy for non-specialists. *Biochim. Biophys. Acta - Bioenerg.* **2019**, *1860*, 271–285.

(8) Collini, E. 2D Electronic Spectroscopic Techniques for Quantum Technology Applications. *J. Phys. Chem. C* **2021**, *125*, 13096–13108.

(9) Biswas, S.; Kim, J.; Zhang, X.; Scholes, G. D. Coherent Two-Dimensional and Broadband Electronic Spectroscopies. *Chem. Rev.* **2022**, *122*, 4257–4321.

(10) Cho, M. Coherent Two-Dimensional Optical Spectroscopy. *Chem. Rev.* **2008**, *108*, 1331–1418.

(11) Jansen, T. L. C. Computational Spectroscopy of Complex Systems. *J. Chem. Phys.* **2021**, *155*, 170901.

(12) Mukamel, S., *Principles of Nonlinear Optical Spectroscopy*; Oxford University Press: 1995.

(13) Hamm, P.; Zanni, M., *Concepts and Methods of 2D Infrared Spectroscopy*; Cambridge University Press: 2011.

(14) Brixner, T.; Stenger, J.; Vaswani, H. M.; Cho, M.; Blankenship, R. E.; Fleming, G. R. Two-Dimensional Spectroscopy of Electronic Couplings in Photosynthesis. *Nature* **2005**, *434*, 625–628.

(15) Schlau-Cohen, G. S.; Ishizaki, A.; Fleming, G. R. Two-Dimensional Electronic Spectroscopy and Photosynthesis: Fundamentals and Applications to Photosynthetic Light-Harvesting. *Chem. Phys.* **2011**, *386*, 1–22.

(16) Lambrev, P. H.; Akhtar, P.; Tan, H.-S. Insights into the Mechanisms and Dynamics of Energy Transfer in Plant Light-Harvesting Complexes from Two-Dimensional Electronic Spectroscopy. *Biochim. Biophys. Acta - Bioenerg.* **2020**, *1861*, 148050.

(17) Forster, T. Energiewanderung und Fluoreszenz. *Naturwissenschaften* **1946**, *33*, 166–175.

(18) Davydov, A. S. The Theory of Molecular Excitons. *Sov. Phys. Usp.* **1964**, *7*, 145.

(19) Redfield, A. The Theory of Relaxation Processes. *Adv. Magn. Opt. Reson.* **1965**, *1*, 1–32.

(20) Engel, G. S.; Calhoun, T. R.; Read, E. L.; Ahn, T.-K.; Mančal, T.; Cheng, Y.-C.; Blankenship, R. E.; Fleming, G. R. Evidence for Wavelike Energy Transfer through Quantum Coherence in Photosynthetic Systems. *Nature* **2007**, *446*, 782–786.

(21) Ball, P. Physics of Life: The Dawn of Quantum Biology. *Nature* **2011**, *474*, 272–274.

(22) Scholes, G. D.; Fleming, G. R.; Chen, L. X.; Aspuru-Guzik, A.; Buchleitner, A.; Coker, D. F.; Engel, G. S.; van Grondelle, R.; Ishizaki, A.; Jonas, D. M.; Lundeen, J. S.; McCusker, J. K.; Mukamel, S.; Ogilvie, J. P.; Olaya-Castro, A.; Ratner, M. A.; Spano, F. C.; Whaley, K. B.; Zhu, X. Using Coherence to Enhance Function in Chemical and Biophysical Systems. *Nature* **2017**, *543*, 647–656.

(23) Mančal, T. A Decade with Quantum Coherence: How our Past Became Classical and the Future Turned Quantum. *Chem. Phys.* **2020**, *532*, 110663.

(24) Ball, P. Is Photosynthesis Quantum-ish? *Phys. World* **2018**, *31*, 44.

(25) Pisliakov, A. V.; Mančal, T.; Fleming, G. R. Two-Dimensional Optical Three-Pulse Photon Echo Spectroscopy. II. Signatures of Coherent Electronic Motion and Exciton Population Transfer in Dimer Two-Dimensional Spectra. *J. Chem. Phys.* **2006**, *124*, 234505.

(26) Ishizaki, A.; Fleming, G. R. Theoretical Examination of Quantum Coherence in a Photosynthetic System at Physiological Temperature. *Proc. Natl. Acad. Sci. USA* **2009**, *106*, 17255–17260.

(27) Panitchayangkoon, G.; Voronine, D. V.; Abramavicius, D.; Caram, J. R.; Lewis, N. H. C.; Mukamel, S.; Engel, G. S. Direct Evidence of Quantum Transport in Photosynthetic Light-Harvesting Complexes. *Proc. Natl. Acad. Sci. USA* **2011**, *108*, 20908–20912.

(28) Christensson, N.; Kauffmann, H. F.; Pullerits, T.; Mančal, T. Origin of Long-Lived Coherences in Light-Harvesting Complexes. *J. Phys. Chem. B* **2012**, *116*, 7449–7454.

(29) Butkus, V.; Zigmantas, D.; Valkunas, L.; Abramavicius, D. Vibrational vs. Electronic Coherences in 2D Spectrum of Molecular Systems. *Chem. Phys. Lett.* **2012**, *545*, 40–43.

(30) Kassal, I.; Yuen-Zhou, J.; Rahimi-Keshari, S. Does Coherence Enhance Transport in Photosynthesis? *J. Phys. Chem. Lett.* **2013**, *4*, 362–367.

(31) Cao, J.; Cogdell, R. J.; Coker, D. F.; Duan, H.-G.; Hauer, J.; Kleinekathöfer, U.; Jansen, T. L. C.; Mančal, T.; Miller, R. J. D.; Ogilvie, J. P.; Prokhorenko, V. I.; Renger, T.; Tan, H.-S.; Tempelaar, R.; Thorwart, M.; Thyrhaug, E.; Westenhoff, S.; Zigmantas, D. Quantum Biology Revisited. *Sci. Adv.* **2020**, *6*, eaaz4888.

(32) Milota, F.; Prokhorenko, V. I.; Mancal, T.; von Berlepsch, H.; Bixner, O.; Kauffmann, H. F.; Hauer, J. Vibronic and Vibrational Coherences in Two-Dimensional Electronic Spectra of Supramolecular J-Aggregates. *J. Phys. Chem. A* **2013**, *117*, 6007–6014.

(33) Lim, J.; Paleček, D.; Caycedo-Soler, F.; Lincoln, C. N.; Prior, J.; von Berlepsch, H.; Huelga, S. F.; Plenio, M. B.; Zigmantas, D.; Hauer, J. Vibronic Origin of Long-Lived Coherence in an Artificial Molecular Light Harvester. *Nat. Commun.* **2015**, *6*, 7755.

(34) Bolzonello, L.; Fassioli, F.; Collini, E. Correlated Fluctuations and Intraband Dynamics of J-Aggregates Revealed by Combination of 2DES Schemes. *J. Phys. Chem. Lett.* **2016**, *7*, 4996–5001.

(35) De Sio, A.; Troiani, F.; Maiuri, M.; Réhault, J.; Sommer, E.; Lim, J.; Huelga, S. F.; Plenio, M. B.; Rozzi, C. A.; Cerullo, G.; Molinari, E.; Lienau, C. Tracking the Coherent Generation of Polaron Pairs in Conjugated Polymers. *Nat. Commun.* **2016**, *7*, 13742.

(36) Malý, P.; Lüttig, J.; Turkin, A.; Dostál, J.; Lambert, C.; Brixner, T. From Wavelike to Sub-Diffusive Motion: Exciton Dynamics and Interaction in Squaraine Copolymers of Varying Length. *Chem. Sci.* **2020**, *11*, 456–466.

(37) Righetto, M.; Bolzonello, L.; Volpato, A.; Amoruso, G.; Panniello, A.; Fanizza, E.; Striccoli, M.; Collini, E. Deciphering Hot- and Multi-Exciton Dynamics in Core–Shell QDs by 2D Electronic Spectroscopies. *Phys. Chem. Chem. Phys.* **2018**, *20*, 18176–18183.

(38) Seiler, H.; Palato, S.; Kambhampati, P. Investigating Exciton Structure and Dynamics in Colloidal CdSe Quantum Dots with Two-Dimensional Electronic Spectroscopy. *J. Chem. Phys.* **2018**, *149*, 074702.

(39) Seiler, H.; Palato, S.; Sonnichsen, C.; Baker, H.; Kambhampati, P. Seeing Multiexcitons through Sample Inhomogeneity: Band-Edge Biexciton Structure in CdSe Nanocrystals Revealed by Two-Dimensional Electronic Spectroscopy. *Nano Lett.* **2018**, *18*, 2999–3006.

(40) Collini, E.; Gattuso, H.; Kolodny, Y.; Bolzonello, L.; Volpato, A.; Fridman, H. T.; Yochelis, S.; Mor, M.; Dehnel, J.; Lifshitz, E.; Paltiel, Y.; Levine, R. D.; Remacle, F. Room-Temperature Inter-Dot Coherent Dynamics in Multilayer Quantum Dot Materials. *J. Phys. Chem. C* **2020**, *124*, 16222–16231.

(41) Bakulin, A. A.; Selig, O.; Bakker, H. J.; Rezus, Y. L.; Müller, C.; Glaser, T.; Lovrincic, R.; Sun, Z.; Chen, Z.; Walsh, A.; Frost, J. M.; Jansen, T. L. C. Real-Time Observation of Organic Cation Reorientation in Methylammonium Lead Iodide Perovskites. *J. Phys. Chem. Lett.* **2015**, *6*, 3663–3669.

(42) Seiler, H.; Palato, S.; Sonnichsen, C.; Baker, H.; Socie, E.; Strandell, D. P.; Kambhampati, P. Two-Dimensional Electronic Spectroscopy Reveals Liquid-like Lineshape Dynamics in CsPbI3 Perovskite Nanocrystals. *Nat. Commun.* **2019**, *10*, 4962.

(43) Ramesh, S.; Giovanni, D.; Righetto, M.; Ye, S.; Fresch, E.; Wang, Y.; Collini, E.; Mathews, N.; Sum, T. C. Tailoring the Energy Manifold of Quasi-Two-Dimensional Perovskites for Efficient Carrier Extraction. *Adv. Energy Mater.* **2022**, *12*, 2103556.

(44) Finkelstein-Shapiro, D.; Mante, P.-A.; Sarisozen, S.; Wittenbecher, L.; Minda, I.; Balci, S.; Pullerits, T.; Zigmantas, D. Understanding Radiative Transitions and Relaxation Pathways in Plexcitons. *Chem* **2021**, *7*, 1092–1107.

(45) Peruffo, N.; Mancin, F.; Collini, E. Coherent Dynamics in Solutions of Colloidal Plexcitonic Nanohybrids at Room Temperature. *Adv. Opt. Mater.* **2023**, *11*, 2203010.

(46) Ishizaki, A.; Fleming, G. R. Unified Treatment of Quantum Coherent and Incoherent Hopping Dynamics in Electronic Energy Transfer: Reduced Hierarchy Equation Approach. *J. Chem. Phys.* **2009**, *130*, 234111.

(47) Tanimura, Y. Numerically "Exact" Approach to Open Quantum Dynamics: The Hierarchical Equations of Motion (HEOM). *J. Chem. Phys.* **2020**, *153*, 020901.

(48) Mancal, T.; Pisliakov, A. V.; Fleming, G. R. Two-Dimensional Optical Three-Pulse Photon Echo Spectroscopy. I. Nonperturbative Approach to the Calculation of Spectra. *J. Chem. Phys.* **2006**, *124*, 234504.

(49) Brüggemann, B.; Pullerits, T. Nonperturbative Modeling of Fifth-Order Coherent Multidimensional Spectroscopy in Light Harvesting Antennas. *New J. Phys.* **2011**, *13*, 025024.

(50) Gelin, M. F.; Chen, L.; Domcke, W. Equation-of-Motion Methods for the Calculation of Femtosecond Time-Resolved 4-Wave-Mixing and N-Wave-Mixing Signals. *Chem. Rev.* **2022**, *122*, 17339–17396.

(51) Reimann, K.; Woerner, M.; Elsaesser, T. Two-Dimensional Terahertz Spectroscopy of Condensed-Phase Molecular Systems. *J. Chem. Phys.* **2021**, *154*, 120901.

(52) Borrego-Varillas, R.; Nenov, A.; Ganzer, L.; Oriana, A.; Manzoni, C.; Tolomelli, A.; Rivalta, I.; Mukamel, S.; Garavelli, M.; Cerullo, G. Two-Dimensional UV Spectroscopy: a New Insight into the Structure and Dynamics of Biomolecules. *Chem. Sci.* **2019**, *10*, 9907–9921.

(53) Arsenault, E. A.; Bhattacharyya, P.; Yoneda, Y.; Fleming, G. R. Two-Dimensional Electronic–Vibrational Spectroscopy: Exploring the Interplay of Electrons and Nuclei in Excited State Molecular Dynamics. *J. Chem. Phys.* **2021**, *155*, 020901.

(54) Read, E. L.; Engel, G. S.; Calhoun, T. R.; Mančal, T.; Ahn, T. K.; Blankenship, R. E.; Fleming, G. R. Cross-Peak-Specific Two-Dimensional Electronic Spectroscopy. *Proc. Natl. Acad. Sci. USA,* **2007**, *104*, 14203–14208.

(55) Tiwari, V. Multidimensional Electronic Spectroscopy in High-Definition - Combining Spectral, Temporal, and Spatial Resolutions. *J. Chem. Phys.* **2021**, *154*, 230901.

(56) Karki, K. J.; Ciappina, M. F. Advances in Nonlinear Spectroscopy using Phase Modulated Light Fields: Prospective Applications in Perturbative and Non-Perturbative Regimes. *Adv. Phys.: X* **2022**, *7*, 2090856.

(57) Lott, G. A.; Perdomo-Ortiz, A.; Utterback, J. K.; Widom, J. R.; Aspuru-Guzik, A.; Marcus, A. H. Conformation of Self-Assembled Porphyrin Dimers in Liposome Vesicles by Phase-Modulation 2D Fluorescence Spectroscopy. *Proc. Natl. Acad. Sci. USA* **2011**, *108*, 16521–16526.

(58) Nardin, G.; Autry, T. M.; Silverman, K. L.; Cundiff, S. T. Multidimensional Coherent Photocurrent Spectroscopy of a Semiconductor Nanostructure. *Opt. Express* **2013**, *21*, 28617–28627.

(59) Karki, K. J.; Widom, J. R.; Seibt, J.; Moody, I.; Lonergan, M. C.; Pullerits, T.; Marcus, A. H. Coherent Two-Dimensional Photocurrent Spectroscopy in a PbS Quantum Dot Photocell. *Nat. Commun.* **2014**, *5*, 5869.

(60) Roeding, S.; Brixner, T. Coherent Two-Dimensional Electronic Mass Spectrometry. *Nat. Commun.* **2018**, *9*, 2519.

(61) Uhl, D.; Bangert, U.; Bruder, L.; Stienkemeier, F. Coherent Optical 2D Photoelectron Spectroscopy. *Optica* **2021**, *8*, 1316–1324.

(62) Tian, P.; Keusters, D.; Suzaki, Y.; Warren, W. S. Femtosecond Phase-Coherent Two-Dimensional Spectroscopy. *Science* **2003**, *300*, 1553–1555.

(63) Tan, H.-S. Theory and Phase-Cycling Scheme Selection Principles of Collinear Phase Coherent Multi-Dimensional Optical Spectroscopy. *J. Chem. Phys.* **2008**, *129*, 124501.

(64) Tekavec, P. F.; Lott, G. A.; Marcus, A. H. Fluorescence-Detected Two-Dimensional Electronic Coherence Spectroscopy by Acousto-Optic Phase Modulation. *J. Chem. Phys.* **2007**, *127*, 214307.

(65) Fersch, D.; Malý, P.; Rühe, J.; Lisinetskii, V.; Hensen, M.; Würthner, F.; Brixner, T. Single-Molecule Ultrafast Fluorescence-Detected Pump–Probe Microscopy. *J. Phys. Chem. Lett.* **2023**, *14*, 4923–4932.

(66) Tiwari, V.; Matutes, Y. A.; Gardiner, A. T.; Jansen, T. L. C.; Cogdell, R. J.; Ogilvie, J. P. Spatially-Resolved Fluorescence-Detected Two-Dimensional Electronic Spectroscopy Probes Varying Excitonic Structure in Photosynthetic Bacteria. *Nat. Commun.* **2018**, *9*, 4219.

(67) Bakulin, A. A.; Silva, C.; Vella, E. Ultrafast Spectroscopy with Photocurrent Detection: Watching Excitonic Optoelectronic Systems at Work. *J. Phys. Chem. Lett.* **2016**, *7*, 250–258.

(68) Zhou, N.; Ouyang, Z.; Hu, J.; Williams, O. F.; Yan, L.; You, W.; Moran, A. M. Distinguishing Energy- and Charge-Transfer Processes in Layered Perovskite Quantum Wells with Two-Dimensional Action Spectroscopies. *J. Phys. Chem. Lett.* **2020**, *11*, 4570–4577.

(69) Bouda, K.; Fučíková, A.; Pšenčík, J.; Alster, J. Solvent Signals in Two-Dimensional Electronic Spectroscopy. *AIP Adv.* **2022**, *12*, 115306.

(70) Malý, P.; Lüttig, J.; Mueller, S.; Schreck, M. H.; Lambert, C.; Brixner, T. Coherently and Fluorescence-Detected Two-Dimensional Electronic Spectroscopy: Direct Comparison on Squaraine Dimers. *Phys. Chem. Chem. Phys.* **2020**, *22*, 21222–21237.

(71) Malý, P.; Mueller, S.; Lüttig, J.; Lambert, C.; Brixner, T. Signatures of Exciton Dynamics and Interaction in Coherently and Fluorescence-Detected Four- and Six-Wave-Mixing Two-Dimensional Electronic Spectroscopy. *J. Chem. Phys.* **2020**, *153*, 144204.

(72) Perdomo-Ortiz, A.; Widom, J. R.; Lott, G. A.; Aspuru-Guzik, A.; Marcus, A. H. Conformation and Electronic Population Transfer in Membrane-Supported Self-

Assembled Porphyrin Dimers by 2D Fluorescence Spectroscopy. *J. Phys. Chem. B* **2012**, *116*, 10757–10770.

(73) Kühn, O.; Mancal, T.; Pullerits, T. Interpreting Fluorescence Detected Two-Dimensional Electronic Spectroscopy. *J. Phys. Chem. Lett.* **2020**, *11*, 838–842.

(74) Karki, K. J.; Chen, J.; Sakurai, A.; Shi, Q.; Gardiner, A. T.; Kühn, O.; Cogdell, R. J.; Pullerits, T. Before Förster. Initial Excitation in Photosynthetic Light Harvesting. *Chem. Sci.* **2019**, *10*, 7923–7928.

(75) Malý, P.; Mancal, T. Signatures of Exciton Delocalization and Exciton–Exciton Annihilation in Fluorescence-Detected Two-Dimensional Coherent Spectroscopy. *J. Phys. Chem. Lett.* **2018**, *9*, 5654–5659.

(76) Kunsel, T.; Tiwari, V.; Matutes, Y. A.; Gardiner, A. T.; Cogdell, R. J.; Ogilvie, J. P.; Jansen, T. L. C. Simulating Fluorescence-Detected Two-Dimensional Electronic Spectroscopy of Multichromophoric Systems. *J. Phys. Chem. B* **2019**, *123*, 394–406.

(77) Schröter, M.; Pullerits, T.; Kühn, O. Using Fluorescence Detected Two-Dimensional Spectroscopy to Investigate Initial Exciton Delocalization Between Coupled Chromophores. *J. Chem. Phys.* **2018**, *149*, 114107.

(78) Grégoire, P.; Srimath Kandada, A. R.; Vella, E.; Tao, C.; Leonelli, R.; Silva, C. Incoherent Population Mixing Contributions to Phase-Modulation Two-Dimensional Coherent Excitation Spectra. *J. Chem. Phys.* **2017**, *147*, 114201.

(79) Bargigia, I.; Gutiérrez-Meza, E.; Valverde-Chávez, D. A.; Marques, S. R.; Srimath Kandada, A. R.; Silva, C. Identifying Incoherent Mixing Effects in the Coherent Two-Dimensional Photocurrent Excitation Spectra of Semiconductors. *J. Chem. Phys.* **2022**, *157*, 204202.

(80) Kalaee, A. A. S.; Damtie, F.; Karki, K. J. Differentiation of True Nonlinear and Incoherent Mixing of Linear Signals in Action-Detected 2D Spectroscopy. *J. Phys. Chem. A* **2019**, *123*, 4119–4124.

2 | Theory and Simulation of 2D Electronic Spectroscopy

In this Chapter, we provide the theoretical foundations for the interpretation and simulation of Two-Dimensional Electronic Spectroscopy (2DES). In particular, we present the two main approaches for describing light-matter interaction, i.e., the perturbative and the non-perturbative approaches. In the following Chapters, both descriptions are used to tackle specific issues in the interpretation of 2D spectra.

In the perturbative approach, the light-matter interaction is assumed to be weak compared to the energy scale of the system Hamiltonian. According to the non-linear response theory, the state of the system and its optical response can be expanded at the different orders in the light-matter interaction. As a result, the spectroscopic observable are proportional to the system response function which can be conveniently represented in terms of (double-sided) Feynman Diagrams (FDs). On the other hand, the non-perturbative approach relies on extracting the spectroscopic observable from the dynamics of the system driven by the external electromagnetic field. In this way, the total optical response of the system is obtained, from which the response at the different orders of the light-matter interaction has to be extracted.

The kind of observables that are experimentally detected depends on the specific spectroscopic technique. In the following, we will discuss the two different versions of 2DES: the coherent-detected technique (C-2DES) and the action-detected technique (A-2DES). In the former, the measured signal is represented by the coherent electric field emitted by the macroscopic polarization induced in the sample, while in the latter, the incoherent signal, e.g., fluorescence or photocurrent, is proportional to the excited-state population.

2.1. Light-Matter Interaction

We will confine our discussion to the semi-classical description of the light-matter interaction. In this framework, the system is treated according to the laws of quantum

mechanics, whereas light is regarded as a classical electromagnetic field. The total Hamiltonian is given by:

$$\hat{H}(t) = \hat{H}_0 + \hat{H}'(t) \tag{2.1}$$

where $\hat{H}_0$ is the system Hamiltonian and $\hat{H}'(t)$ is the light-matter interaction Hamiltonian. By diagonalizing the system Hamiltonian, $\hat{H}_0 |k\rangle = \epsilon_k |k\rangle$, the eigenstates of the system $|k\rangle$ are obtained, along with the corresponding eigenvalues ϵ_k, representing their energies.

Instead, the light-matter interaction promotes transitions between the different eigenstates. In the dipole approximation, the interaction Hamiltonian can be written as:

$$\hat{H}'(t) = -\hat{\boldsymbol{\mu}} \cdot \boldsymbol{E}(t) \tag{2.2}$$

where $\hat{\boldsymbol{\mu}}$ is the dipole moment operator of the system and $\boldsymbol{E}(t)$ is the external electric field. To avoid cumbersome vectorial notation, we assume that the electric field is linearly polarized $\boldsymbol{E}(t) = E(t)\boldsymbol{e}$, with polarization unit vector $\boldsymbol{e}$. Therefore, the interaction Hamiltonian can be rewritten as $\hat{H}'(t) = -\hat{\mu}E(t)$, where $\hat{\mu} = \hat{\boldsymbol{\mu}} \cdot \boldsymbol{e}$ is the projection of the dipole moment onto the electric-field polarization.

2.2. State Vector and Pure States

An isolated system described by the wavefunction $|\psi(t)\rangle$ is considered to be in a *pure state*. Its temporal evolution is governed by the Schrödinger equation:

$$\frac{d}{dt} |\psi(t)\rangle = -\frac{i}{\hbar} \hat{H}(t) |\psi(t)\rangle \tag{2.3}$$

under the effect of the total Hamiltonian $\hat{H}(t)$ (Eq. 2.1). In general, the solution of this equation takes the form:

$$|\psi(t)\rangle = U(t, t_0) |\psi(t_0)\rangle \tag{2.4}$$

where $|\psi(t_0)\rangle$ is the initial condition and $U(t, t_0)$ is the time-evolution operator. Nevertheless, this solution represents only a formal expression with limited practical utility.

However, in the absence of light-matter interaction, the evolution of the system can be expressed as:

$$|\psi(t)\rangle = U_0(t, t_0) |\psi(t_0)\rangle \tag{2.5}$$

where the time-evolution operator:

$$U_0(t, t_0) = \exp\left\{-\frac{i}{\hbar}\hat{H}_0(t - t_0)\right\}. \tag{2.6}$$

is only determined by the system Hamiltonian $\hat{H}_0$. In the eigenstate basis, the time evolution of the system takes a simple analytical form given by the linear combination:

$$\begin{aligned} |\psi(t)\rangle &= \sum_k c_k(t)\,|k\rangle \\ &= \sum_k c_k(t_0) e^{-\frac{i}{\hbar}\epsilon_k(t-t_0)}\,|k\rangle \end{aligned} \tag{2.7}$$

where $c_k(t) = \langle k|\psi(t)\rangle$ is the complex probability amplitude. Since the state vector contains all the relevant information about the isolated system under investigation, it is possible to calculate the expectation value of an observable $\hat{\mathcal{O}}$ as:

$$\mathcal{O}(t) = \langle\psi(t)|\hat{\mathcal{O}}|\psi(t)\rangle\,. \tag{2.8}$$

2.3. Density Matrix and Mixed States

A system is said to be in a *mixed state* when there is incomplete knowledge of its state. In this case, the system is described in terms of the statistical density matrix:

$$\rho(t) = \sum_n p_n\,|\psi_n(t)\rangle\langle\psi_n(t)| \tag{2.9}$$

where p_n is the probability of occurrence of a given pure state $|\psi_n(t)\rangle$. Similarly to the Schrödinger equation for the wavefunction (Eq. 2.3), the time evolution of the density matrix is ruled by the Liouville-von Neumann equation:

$$\frac{d}{dt}\rho(t) = -\frac{i}{\hbar}\left[\hat{H}(t), \rho(t)\right] \tag{2.10}$$

where $[\cdot, \cdot]$ is the commutator.

In the absence of light-matter interaction, the evolution of the density matrix is given by:

$$\rho(t) = U_0(t, t_0)\rho(t_0)U_0^\dagger(t, t_0) \tag{2.11}$$

with $\rho(t_0)$ as initial condition. In the eigenstates basis, this can be written as:

$$\begin{aligned}\rho(t) &= \sum_{k,l} \rho_{kl}(t)\,|k\rangle\langle l| \\ &= \sum_{k,l} \rho_{kl}(t_0) e^{-\frac{i}{\hbar}(\epsilon_k-\epsilon_l)(t-t_0)}\,|k\rangle\langle l|\end{aligned} \tag{2.12}$$

whose diagonal elements $\rho_{kk}(t) = |c_k(t)|^2$ are referred to as *populations*, which represent the probability of the system to be found in a certain state, while off-diagonal elements $\rho_{kl}(t) = c_k(t)c_l^*(t)$ are called *coherences*, which reflect a coherent superposition between different energy states.

In this case, the density matrix completely characterized the state of the statistical ensemble and the expectation value of an observable $\hat{\mathcal{O}}$ can be evaluated by taking the trace:

$$\mathcal{O}(t) = \mathrm{Tr}\{\hat{\mathcal{O}}\rho(t)\}. \tag{2.13}$$

2.4. Perturbative Approach

Optical spectroscopy is typically rationalized using a perturbative approach [1, 2], where the light-matter interaction is regarded as weak perturbation to the system Hamiltonian. This approach not only provides the theoretical framework for the interpretation of the spectra but also represents a convenient protocol for the simulation of the optical response.

The perturbative approach finds its roots in the response theory [3]. The state of the system is expanded into the different orders of the light-matter interaction, allowing the extraction of the optical response at a specific order. Consequently, the spectroscopic signal can be expressed in terms of a field-dependent part and a system response function, which is defined solely on the basis of the unperturbed properties of the system, as the dipole moment operator and the system Hamiltonian.

2.4.1. Time-Dependent Perturbation Theory

In order to develop a perturbative expansion in the light-matter interaction for the density matrix, we first introduce the interaction picture. In this representation, denoted hereafter by the subscript I, the density matrix and the operators are transformed under the time-

evolution operator corresponding to the unperturbed system Hamiltonian $\hat{H}_0$ (Eq. 2.6):

$$\hat{\mathcal{O}}_I(t) = U_0^\dagger(t,t_0)\hat{\mathcal{O}}(t)U_0(t,t_0) \tag{2.14}$$

$$\rho_I(t) = U_0^\dagger(t,t_0)\rho(t)U_0(t,t_0). \tag{2.15}$$

In the interaction picture, the Liouville-von Neumann equation (Eq. 2.10) takes the form:

$$\frac{d}{dt}\rho_I(t) = -\frac{i}{\hbar}[\hat{H}'_I(t), \rho_I(t)] \tag{2.16}$$

which can be solved iteratively to obtain the following perturbative expansion for the density matrix:

$$\rho_I(t) = \sum_n^\infty \rho_I^{(n)}(t). \tag{2.17}$$

The density matrix at the n-th order in the light-matter interaction is given by:

$$\begin{aligned}\rho_I^{(n)}(t) = \Big(-\frac{i}{\hbar}\Big)^n \int_{t_0}^{t} d\tau_n \int_{t_0}^{\tau_n} d\tau_{n-1} \cdots \int_{t_0}^{\tau_2} d\tau_1 \times \\ [\hat{H}'_I(\tau_n), [\hat{H}'_I(\tau_{n-1}), \ldots [\hat{H}'_I(\tau_1), \rho_I(t_0)] \ldots]]\end{aligned} \tag{2.18}$$

where the initial state of the system, described by the density matrix $\rho_I(t_0)$, is perturbed by a sequence of interactions $\hat{H}'_I(\tau_n)$ acting at time τ_n. By expressing the interaction Hamiltonian in the dipole approximation (Eq. 2.2) and returning to the Schrödinger picture, we obtain:

$$\begin{aligned}\rho^{(n)}(t) = \left(\frac{i}{\hbar}\right)^n \int_{t_0}^{t} d\tau_n \int_{t_0}^{\tau_n} d\tau_{n-1} \cdots \int_{t_0}^{\tau_2} d\tau_1 E(\tau_n)E(\tau_{n-1}) \ldots E(\tau_1) \times \\ U(t,t_0)[\hat{\mu}_I(\tau_n), [\hat{\mu}_I(\tau_{n-1}), \ldots [\hat{\mu}_I(\tau_1), \rho(t_0)] \ldots]]U_0^\dagger(t,t_0).\end{aligned} \tag{2.19}$$

At this point, the treatment is still exact since no approximations have been made. In the following, we assume that $\rho(t_0)$ represents the equilibrium density matrix. Since it does not evolve in time under the system Hamiltonian, we can set the initial time to $t_0 \to -\infty$. Moreover, it is convenient to introduce a new set of variables:

$$\begin{aligned}\tau_1 &= 0 \\ t_1 &= \tau_2 - \tau_1 \\ &\cdots \\ t_{n-1} &= \tau_n - \tau_{n-1} \\ t_n &= t - \tau_n\end{aligned} \tag{2.20}$$

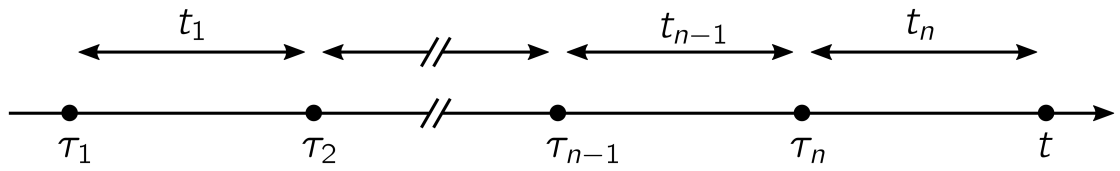

Fig. 2.1: Schematic representation of the time-ordering of the light-matter interactions, where τ_n is the absolute time at which the interaction occurs, while t_n is the delay times between interactions.

which represents the delay times between light-matter interactions, as depicted in Fig. 2.1.

2.4.2. Spectroscopic Observables and Response Functions

Following non-linear response theory, we now proceed to establish the connection between the system response and the spectroscopic observables that are experimentally detected for both the cases of coherent detection and action detection.

In coherent detection, the spectroscopic observable is represented by the macroscopic polarization induced in the sample by the light-matter interaction. The polarization is determined as the expectation value of the dipole moment operator:

$$P(t) = \mathrm{Tr}\{\hat{\mu}\rho(t)\} \tag{2.21}$$

which, acting as a source of the electric field, emits a coherent signal $E_S(t) \propto iP(t)$. By employing the perturbative expansion for the density matrix (Eq. 2.17), the n-th order polarization is obtained:

$$P^{(n)}(t) = \mathrm{Tr}\{\hat{\mu}\rho^{(n)}(t)\}. \tag{2.22}$$

By substituting Eq. 2.19, the n-th order polarization can be expressed as the convolution of a field-dependent part and the system response function:

$$\begin{aligned} P^{(n)}(t) = \int_0^\infty dt_n \int_0^\infty dt_{n-1} \cdots \int_0^\infty dt_1 \; R_C^{(n)}(t_n, t_{n-1}, \ldots, t_1) \times \\ E(t-t_n)E(t-t_n-t_{n-1}) \ldots E(t-t_n-t_{n-1} \cdots - t_1). \end{aligned} \tag{2.23}$$

The n-th order (coherent) response function is now defined as the linear combination of

$(n+1)$-Time Correlation Functions (TCFs) of the dipole moment operator:

$$\mathrm{R}_C^{(n)}(t_n, t_{n-1}, \ldots, t_1) = \left(\tfrac{i}{\hbar}\right)^n \mathrm{Tr}\{\hat{\mu}(t_n + t_{n-1} \cdots + t_1)[\hat{\mu}(t_{n-1} \cdots + t_1), \ldots [\hat{\mu}(0), \rho(-\infty)]]\}. \tag{2.24}$$

Since for an isotropic medium, the even orders of the polarization typically vanish due to symmetry, the lowest-order non-linearity is represented by the third order in the light-matter interaction, corresponding to the linear combination of four-TCF of the dipole moment operator.

Instead, in action detection, the measured incoherent signal, e.g., fluorescence or photocurrent, is proportional to the excited-state population:

$$S(t) = \mathrm{Tr}\{\hat{S}\rho(t)\} \tag{2.25}$$

where the operator $\hat{S} = \sum_k \Phi_k \, |k\rangle\langle k|$ acts as a projector onto the eigenstates of the system weighted by the quantum yield Φ_k [4]. The incoherent signal at the n-th order in the light-matter interaction is given by:

$$S^{(n)}(t) = \mathrm{Tr}\{\hat{S}\rho^{(n)}(t)\} \tag{2.26}$$

which can be expressed as:

$$\begin{aligned} S^{(n)}(t) = \int_0^\infty dt_n \int_0^\infty dt_{n-1} \cdots \int_0^\infty dt_1 \; R_{IC}^{(n)}(t_n, t_{n-1}, \ldots, t_1) \times \\ E(t - t_n) E(t - t_n - t_{n-1}) \ldots E(t - t_n - t_{n-1} \cdots - t_1) \end{aligned} \tag{2.27}$$

where the n-th order (incoherent) response function is given by the linear combination of n-TCF of the dipole moment operator:

$$\mathrm{R}_{IC}^{(n)}(t_n, t_{n-1}, \ldots, t_1) = \left(\tfrac{i}{\hbar}\right)^n \mathrm{Tr}\{\hat{S}[\hat{\mu}(t_n + t_{n-1} \cdots + t_1)[\hat{\mu}(t_{n-1} \cdots + t_1), \ldots [\hat{\mu}(0), \rho(-\infty)]]]\}. \tag{2.28}$$

Since only even orders can generate an excited-state population, the lowest order non-linearity is now represented by the fourth order in the light-matter interaction, corresponding again to the four-TCF of the dipole moment operator.

Notice that the difference between the coherent and incoherent response functions lies in the role of the last dipole moment operator. Indeed, while in the former case, it represents the emission of the coherent signal, in the latter case, it represents an actual light-matter

interaction. This fact underlies the difference between coherent and incoherent detection.

Although there seems to be an apparent discrepancy in the order of the response between coherent and incoherent signals, they fundamentally probe the same kind of optical processes. Indeed, as recently demonstrated, it is possible to establish a connection between the n-th order response function in the coherent signal and the $(n+1)$-th order response function in the incoherent signal, in terms of the same generalized response function [5].

2.4.3. From Response Function to Feynman Diagrams

The response functions (Eqs. 2.24 and 2.28) contain all the relevant information about the system at a given order of the light-matter interaction.

By expanding the commutators, each dipole moment operator can act either on the *bra* or *ket* side of the density matrix. Therefore, the response function gives rise to 2^n terms, which represents the possible pathway followed by the system upon the light-matter interaction. In non-linear optical spectroscopy, the electric field is typically given by a sequence of M pulses:

$$E(t) = \sum_{m}^{M} \left[E_m^+(t) + E_m^-(t) \right] \tag{2.29}$$

where $E_m^+(t)$ and $E_m^-(t)$ are respectively the rotating and counter-rotating components of the electric field, defined as:

$$E_m^{\pm}(t) = \mathcal{E}_m(t-\tau_m) e^{\pm i(\boldsymbol{k}_m \cdot \boldsymbol{r} - \omega_m t + \phi_m)} \tag{2.30}$$

with envelope $\mathcal{E}_m(t)$, central time τ_m, wavevector $\boldsymbol{k}_m$, frequency ω_m and phase ϕ_m. As a result, the evaluation of the spectroscopic observable (Eqs. 2.23 and 2.27) results particularly challenging since $2^n \times (2M)^M$ terms have to be calculated.

However, the number of terms contributing to the signal can be significantly reduced by taking a series of approximations:

- **time-ordering:** when the pulse duration is shorter than the delay time, the pulse overlap can be neglected, allowing to assign each interaction to a specific pulse.
- **Rotating-Wave Approximation (RWA):** when the pulse duration is longer than the optical period and the resonance condition is satisfied, highly oscillating terms can be discarded as they would give a negligible contribution upon integration. There-

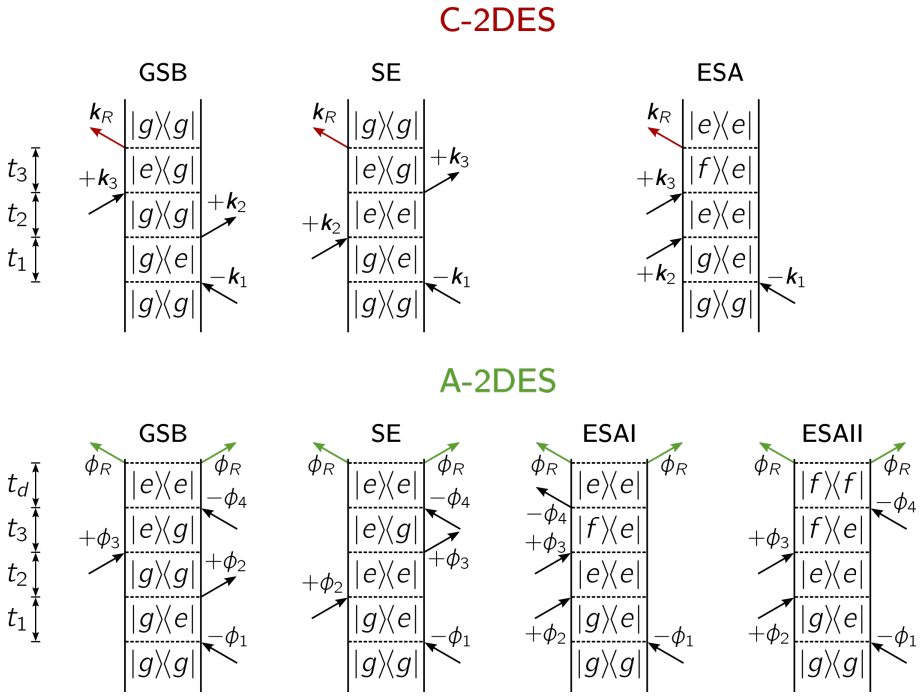

Fig. 2.2: Feynman diagrams for the rephasing signal in C-2DES and A-2DES.

fore, either the rotating $E_m^+(t)$ or counter-rotating $E_m^-(t)$ components of the field contributes to each interaction.

- **phase discrimination:** the terms of the response function are selected based on their wavevector according to the phase-matching condition $\boldsymbol{k}_S = \sum_m \ell_m^S \boldsymbol{k}_m$, or based on their phase using phase-cycling or phase-modulation condition $\phi_S = \sum_m \ell_m^S \phi_m$, where ℓ_m^S are integers.
- **impulsive limit:** when the pulse is short compared to the relevant system timescales but longer than the optical period, the pulse envelope can be approximated by a delta function, $\mathcal{E}(t) = \delta(t)$. In this limit, the convolution results straightforward and the spectroscopic response corresponds to the response function.

2.4.4. Feynman Diagrams

The different terms of the optical response can be conveniently represented using Feynman Diagrams (FDs) which identify the pathways followed by the system upon light-matter interaction. In the following, we report the rules for the interpretation of these diagrams [1, 2]:

- time runs from the bottom to the top.

- the two vertical lines represent the state of the system, corresponding respectively to the *ket* and *bra* side of the density matrix.
- each black arrow represents the interaction with the electric field, contributing with $E_m^+(t)$ when pointing to the right, or with $E_m^-(t)$ when pointing to the left, and leading to excitation when pointing towards the diagram or de-excitation when pointing outwards.
- the red arrow represents the emission of the coherent signal with wavevector $\boldsymbol{k}_S = \sum_m \ell_m^S \boldsymbol{k}_m$, while the green arrow represents the emission of the incoherent signal with phase $\phi_S = \sum_m \ell_m^S \phi_m$, where ℓ_m^S are integers.
- The overall sign of the contribution is given by $(-1)^{n_B}$, where n_B is the number of interactions on the *bra* side of the diagram.

With phase discrimination, it is not only feasible to separate the different contributions at various orders of the light-matter interaction, but also to selectively isolate a subset of pathways that contribute to that order. In particular, the different pathways can be discriminated based on the wavevector of the signal $\boldsymbol{k}_S$ according to the phase-matching condition, or based on their phase ϕ_S using phase-cycling or phase-modulation. At third order in the polarization or fourth order in the populations, pathways can be distinguished into Rephasing (R), Non-Rephasing (NR) and Double-Quantum Coherence (DQC) signals:

$$\begin{aligned} \boldsymbol{k}_R &= -\boldsymbol{k}_1 + \boldsymbol{k}_2 + \boldsymbol{k}_3 \qquad & \phi_R &= -\phi_1 + \phi_2 + \phi_3 - \phi_4 \\ \boldsymbol{k}_{NR} &= +\boldsymbol{k}_1 - \boldsymbol{k}_2 + \boldsymbol{k}_3 \qquad & \phi_{NR} &= +\phi_1 - \phi_2 + \phi_3 - \phi_4 \\ \boldsymbol{k}_{DQC} &= +\boldsymbol{k}_1 + \boldsymbol{k}_2 - \boldsymbol{k}_3 \qquad & \phi_{DQC} &= +\phi_1 + \phi_2 - \phi_3 - \phi_4. \end{aligned} \tag{2.31}$$

In Fig. 2.2, we depict the different Feynman diagrams contributing to the rephasing signal for a three-level system, composed of a ground state $|g\rangle$, a first excited state $|e\rangle$ and second excited state $|f\rangle$. The different contributions can be distinguished into Ground-State Bleaching (GSB), Stimulated Emission (SE) and Excited-State Absorption (ESA) pathways.

In the following, we illustrate the interpretation of the Feynman diagram for the SE pathway, but similar considerations can be made for the other pathways. Initially, the system is in the ground state. After the first interaction, the system is found in an optical coherence between the ground and the excited state which oscillates during the delay time t_1. Then, the interaction with a second pulse generates either a ground or an excited state population which evolves during the delay time t_2. The third interaction brings the

system back in a coherence that oscillates along t_3. In the case of C-2DES, the signal is emitted during t_3, while for A-2DES, an additional interaction generates an excited-state population which produces the incoherent signal emitted during the detection-time t_d.

Between the two sets of Feynman diagrams, we can find both similarities and differences. Firstly, we notice that each Feynman diagram in C-2DES has at least one counterpart in A-2DES. This is because both techniques are probing the same generalized response function [5]. However, while there is a one-to-one correspondence for GSB and SE pathways, in the case of ESA there are two possible alternatives for A-2DES: one ending in the first-excited state and the other in the second-excited state population. Furthermore, the difference in the order of the light-matter interaction leads to an opposite sign of the pathways between the two detection schemes. Specifically, in C-2DES, GSB and SE exhibit positive signs, whereas ESA is negative. Conversely, in A-2DES, GSB, SE, and ESAI are negative, while ESAII is positive. In the following Chapters, we will examine several examples where this different decomposition of the non-linear signal causes important changes in the spectra obtained with the two detection schemes.

2.5. Non-Perturbative Approach

Non-perturbative approaches to the light-matter interaction are based on the extraction of spectroscopic observables from the dynamics of the system driven by an external electric field [6, 7]. Avoiding the calculation of the response function, the state of the system is obtained by numerically integrating an Equation-of-Motion (EoM). As a result, the total spectroscopic observable is obtained from which the different components of the optical response have to be isolated using different methods, i.e., phase-matching [8], phase-cycling [9], or phase-modulation [10].

This approach allows to go beyond the limits imposed by the perturbative treatment. In particular, the method is suitable for treating the case of strong light-matter interaction. Furthermore, by circumventing the approximations commonly employed in the non-linear response theory, it is possible to account for finite-bandwidth and pulse-overlap effects. In the case of A-2DES, it also provides a natural framework for investigating the relaxation dynamics during the detection time leading to the emission of the signal.

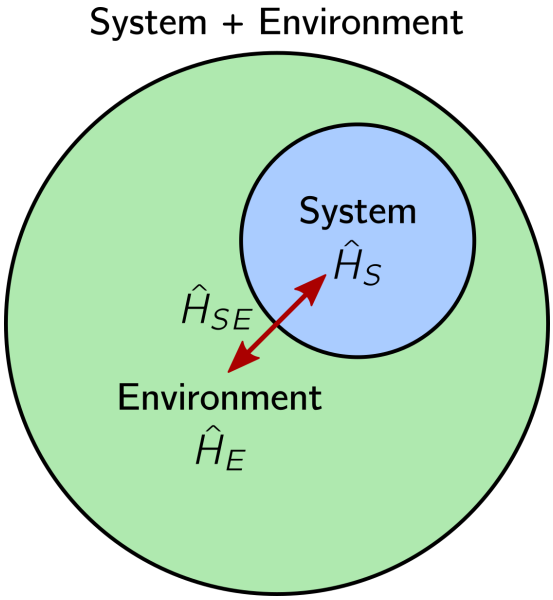

Fig. 2.3: Schematic representation of an open quantum system in interaction with the environment.

2.5.1. Reduced Density Matrix and Quantum Master Equation

Up to this point, we considered the density matrix in its statistical sense, as representing the mixed state of an ensemble of isolated systems. However, realistic systems are not isolated but, instead, are embedded in an environment, e.g., solvent, protein scaffold or polymer matrix, with which they interact. In this context, the system can be described within the theory of open quantum systems (Fig. 2.3) [11]. The interaction with the environment, which is commonly modeled as a thermal bath, induces relaxation and decoherence processes in the system dynamics. The total Hamiltonian is given by:

$$\hat{H}(t) = \hat{H}_S(t) \otimes \mathbb{1}_E + \mathbb{1}_S \otimes \hat{H}_E + \hat{H}_{SE} \tag{2.32}$$

where $\hat{H}_S(t)$ is the system Hamiltonian which includes the light-matter interaction, $\hat{H}_E$ is the environment Hamiltonian, $\hat{H}_{SE}$ is the system-environment interaction Hamiltonian, while $\mathbb{1}_S$ and $\mathbb{1}_E$ are the identity operators over the system and environment degrees of freedom, respectively.

The system-plus-environment state is described by the density matrix $\rho_{SE}(t)$, whose time evolution is described by the Liouville-von Neumann equation (Eq. 2.10):

$$\frac{d}{dt}\rho_{SE}(t) = -\frac{i}{\hbar}\left[\hat{H}(t), \rho_{SE}(t)\right]. \tag{2.33}$$

Since we are typically only interested in the state of the system, we can perform a partial

trace over the environment degrees of freedom:

$$\rho_S(t) = \mathrm{Tr}_E \{\rho_{SE}(t)\} \tag{2.34}$$

resulting in the reduced density matrix $\rho_S(t)$, which describes the state of the system independently of the environment.

The advantage of working with the reduced density matrix lies in the fact that, instead of dealing with the dynamics of the system-plus-environment, it is possible to formulate an effective Equation-of-Motion (EoM) for the dynamics of the system alone. Several numerically exact methods allow for a non-perturbative and non-Markovian treatment of the system-environment coupling, which include Hierarchical Equations of Motion (HEOM) [12], Time Evolving Density operator with Orthogonal Polynomials Algorithm (TEDOPA) [13], and Quasi-Adiabatic Path Integrals (QUAPI) [14] methods. However, despite their generality, these methods are computationally expensive and rapidly become impractical as the number of degrees of freedom increases.

For this reason, one usually resorts to approximate methods based on Quantum Master Equation (QME) [11, 15]. In the Markovian limit, QMEs take the form:

$$\frac{d}{dt}\rho_S(t) = -\frac{i}{\hbar}\left[\hat{H}_S(t), \rho_S(t)\right] + \mathcal{D}\left[\rho_S(t)\right] \tag{2.35}$$

where $\mathcal{D}[\cdot]$ is the dissipator superoperator, which accounts for the relaxation and decoherence processes induced on the system due to the interaction with the environment. Different approaches have been used to derive a QME. Following an axiomatic approach, the Lindblad QME ensures the positivity and trace preservation of the reduced density matrix [11, 16–18]. Alternatively, following a microscopic derivation, the Redfield QME is obtained by using a second-order perturbative expansion in the system-environment coupling [11, 15, 19]. However, it is known that this equation does not guarantee the positivity of the reduced density matrix, potentially leading to unphysical results. To solve this problem, the secular approximation is commonly invoked, which concerns the decoupling of coherence and population dynamics.

2.5.2. Pulse Sequence

In A-2DES, the system interacts with a train of four collinear laser pulses:

$$E(t) = \sum_{i=1}^{4} E_i(t) \tag{2.36}$$

with the i-th pulse described by the convolution of a Gaussian envelope and an oscillating function:

$$E_i(t) = E_i^0 \exp\left\{ -\frac{(t-\mathcal{T}_i)^2}{2\sigma_i^2} \right\} \cos[\omega_i(t-\mathcal{T}_i) + \phi_i] \tag{2.37}$$

where E_i^0 is the electric-field amplitude, σ_i is the pulse duration, ω_i is the carrier-frequency and ϕ_i is the phase of the pulse. The first pulse is centered at time $t_0 = \tau_1$, while the following pulses are separated from the previous one by delay times $t_1 = \tau_2 - \tau_1$, $t_2 = \tau_3 - \tau_2$ and $t_3 = \tau_4 - \tau_3$, respectively. For convenience, we make use of a cumulative delay time: $\mathcal{T}_i = \sum_{j=0}^{i-1} t_j$.

In literature, other schemes based on a different number of pulses in the sequence have been proposed for A-2DES, e.g., two-pulse [20, 21] and three-pulse [22, 23] sequences.

2.5.3. Populations and Incoherent Signal

By solving the Equation-of-Motion, the evolution of the reduced density matrix of the system under the interaction with the pulses is obtained, from which spectroscopic observables can be extracted.

After the interaction with the pulse train, the system emits an incoherent signal along the detection-time t_d, which is proportional to the excited-state population. The time-resolved signal is defined by the operator:

$$\hat{\mathcal{S}} = \sum_k \Gamma_k \hat{\mathcal{P}}_k \tag{2.38}$$

where $\hat{\mathcal{P}}_k = |k\rangle\langle k|$ is the projector onto the k-th state and Γ_k is the rate of the incoherent process contributing to the signal, e.g., the emission of a photon in fluorescence detection or the charge-separation in photocurrent detection. The time-resolved incoherent signal is given by the expectation value:

$$\mathcal{S}(t_d) = \mathrm{Tr}\{\hat{\mathcal{S}}\rho_S(t_d)\}. \tag{2.39}$$

In an experiment, it is often not possible to directly measure the time-resolved signal $\mathcal{S}(t_d)$

as a function of the detection-time t_d. Instead, the experimentally accessible observable is typically represented by the time-integrated signal:

$$\overline{\mathcal{S}} = \int_0^\infty dt'_d \; \mathcal{S}(t'_d). \tag{2.40}$$

By integrating the signal within a finite time window:

$$\overline{\mathcal{S}(t_d)} = \int_0^{t_d} dt'_d \; \mathcal{S}(t'_d) \tag{2.41}$$

time-gating of the signal can be performed, as recently suggested [24–26]. This could help limit processes involving populations during the detection time, such as exciton-exciton annihilation.

2.5.4. Phase Discrimination

Since pulses are collinear in A-2DES, the signal contains all the contributions to the optical response from various orders in the light-matter interaction. To isolate specific components of the signal, the phase of the pulses has to be manipulated from one train to another, either using phase-cycling [27, 28] or phase-modulation [29] schemes. As a consequence, the detected incoherent signal depends on the phase of the pulses. Therefore, the various components of the optical response can be separated by taking linear combinations of the phase-dependent signal, as commonly done by taking the Fourier transform of the signal.

In the following, we explain the details of the phase-cycling and phase-modulation schemes and compare them from the experimental and theoretical points of view.

Phase-Cycling

The phase-cycling method was first introduced into the domain of optical spectroscopy by Tian et al. [27], as an adaptation from NMR spectroscopy [30–32]. A detailed description of the method is presented in ref. [28].

From one train to another, the relative phase between two pulses $\phi_{ij} = \phi_i - \phi_j$ is varied independently from the others by a constant phase interval $\Delta\phi_{ij}$:

$$\Delta\phi_{21} = \frac{2\pi}{L} \qquad \Delta\phi_{31} = \frac{2\pi}{M} \qquad \Delta\phi_{41} = \frac{2\pi}{N} \tag{2.42}$$

where L, M, and N are the numbers of sampled points for the phase of each pulse. Therefore, the relative phases can be expressed as integer multipliers of the phase intervals:

$$\phi_{21} = l \cdot \Delta\phi_{21} \qquad \phi_{31} = m \cdot \Delta\phi_{31} \qquad \phi_{41} = n \cdot \Delta\phi_{41} \tag{2.43}$$

where the indices l, m, and n take values from 0 to $L-1$, $M-1$, and $N-1$, respectively. For a given set of delay times, the experiment is repeated $1 \times L \times M \times N$-fold, by cycling over all the possible phase combinations.

As a result, each component of the optical response is tagged by a total phase given by the linear combination of the phases of each pulse $\phi_S = \alpha\phi_1 + \beta\phi_2 + \gamma\phi_3 + \delta\phi_4$, where the coefficients α, β, γ, and δ represent the number of interactions with each pulse. As the signal emission originates from a population state, these coefficients are not independent and thus the following condition must be fulfilled:

$$\alpha + \beta + \gamma + \delta = 0. \tag{2.44}$$

By expressing the coefficient α as a function of the others, $\alpha = -\beta - \gamma - \delta$, the total phase can be written as $\phi_S = \beta\phi_{21} + \gamma\phi_{31} + \delta\phi_{41}$.

A specific component of the optical response is obtained by taking the Fourier series of the signal with respect to the phases of the pulses:

$$\mathcal{S}(\beta,\gamma,\delta) = \frac{1}{LMN}\sum_{l=0}^{L-1}\sum_{m=0}^{M-1}\sum_{n=0}^{N-1}\mathcal{S}(l,m,n)e^{-i\beta l\Delta\phi_{21}}e^{-i\gamma m\Delta\phi_{31}}e^{-i\delta n\Delta\phi_{41}}. \tag{2.45}$$

In order to isolate rephasing ($\beta = +1$, $\gamma = +1$, $\delta = -1$), non-rephasing ($\beta = -1$, $\gamma = +1$, $\delta = -1$) and double-quantum coherence ($\beta = +1$, $\gamma = -1$, $\delta = -1$) signals, a 27-fold phase-cycling is required, with $L = M = N = 3$ [33]. However, different phase-cycling schemes have been proposed to isolate other components of the optical response [22, 23, 28].

Phase-Modulation

The phase-modulation scheme was initially proposed by Tekavec et al. [29]. In this approach, which represents a sort of continuous phase-cycling, the phase of each pulse ϕ_i is modulated from a train to the following at a specific phase-modulation frequency Ω_i as:

$$\phi_i = 2\pi\Omega_i mT \tag{2.46}$$

where m is the repetition index of the train and T is the inter-train delay time.

Typically, the inter-train delay T is imposed by the experimental setup since is related to the reciprocal of the laser repetition frequency, $\Omega_{rep} = T^{-1}$. Therefore, the phase-modulation frequencies Ω_i are chosen to be integer divisors of the laser repetition rate Ω_{rep}:

$$k_i = \frac{\Omega_i}{\Omega_{rep}}. \tag{2.47}$$

For a given set of delay times, the index m is varied from 0 to the $lcm(k_1, k_2, k_3, k_4)$ - 1. To isolate the various components of the optical response, we take the Fourier transform with respect to the experimental time mT:

$$\mathcal{S}(\Omega_S) = \sum_{mT} \mathcal{S}(mT) e^{-i2\pi\Omega_S mT} \tag{2.48}$$

where $\mathcal{S}(\Omega_S)$ is the component of the signal modulated at the linear combination of phase-modulation frequencies $\Omega_S = \sum_i \ell_i \Omega_i$, where $\ell_i = 0, \pm 1, \pm 2$, etc. represents the number of interactions with each pulse. As in phase-cycling, these coefficients are not independent and, in order to obtain a population at the end of the four pulses, the following relation must be fulfilled:

$$\sum_i \ell_i = 0. \tag{2.49}$$

In this case, rephasing is modulated at $\Omega_R = -\Omega_1 + \Omega_2 + \Omega_3 - \Omega_4$, non-rephasing is modulated at $\Omega_{NR} = +\Omega_1 - \Omega_2 + \Omega_3 - \Omega_4$ and double-quantum coherence is modulated at $\Omega_{DQC} = +\Omega_1 + \Omega_2 - \Omega_3 - \Omega_4$.

Comparison between Phase-Cycling and Phase-Modulation

Both phase-cycling and phase-modulation schemes exploit the control of the phase of the pulses to extract specific components of the optical response of the system. While in phase-cycling, the phase of each pulse is varied independently of the others, in phase-modulation, the phases of the pulses are varied simultaneously.

Despite theoretical studies have confirmed how both methods give identical results when properly executed [34], each of them possesses its own advantages and disadvantages. Phase-cycling is more convenient when only specific components of the optical response are of interest. In this case, it is possible to choose a scheme optimized to selectively isolate such components, thus reducing the number of required phase combinations [28]. This fact is particularly useful in numerical simulations, where the number of repetitions

may affect the computational cost. However, if other components need to be extracted, it is necessary to change phase-cycling scheme.

In contrast, phase-modulation allows to extract simultaneously all the contributions to the optical response. Its continuous nature offers a greater advantage from the experimental standpoint, as it allows faster data acquisition. However, due to the absence of optimized protocols, a higher number of repetitions is generally required compared to phase-cycling, thus resulting less convenient for numerical simulations. Furthermore, it is more common for unwanted contributions to leak into the components of interest.

Ultimately, the choice between the two phase-discrimination schemes depends on the desired level of accuracy and efficiency for extracting the components.

2.6. 2D Spectra

In 2DES, the signal $\mathcal{S}(t_1, t_2, t_3)$ is measured as a function of the delay times t_1, t_2 and t_3. To obtain the 2D spectrum, the signal is Fourier transformed along suitable delay times. Typically, the Fourier transform is taken with respect to t_1 and t_3. In the case of rephasing signal, it is obtained by:

$$\mathcal{S}_R(\omega_1, t_2, \omega_3) = \int_0^{+\infty} dt_1 \int_0^{+\infty} dt_3 \, e^{-i\omega_1 t_1} e^{+i\omega_3 t_3} \, \mathcal{S}_R(t_1, t_2, t_3) \tag{2.50}$$

while the non-rephasing signal is obtained by:

$$\mathcal{S}_{NR}(\omega_1, t_2, \omega_3) = \int_0^{+\infty} dt_1 \int_0^{+\infty} dt_3 \, e^{+i\omega_1 t_1} e^{+i\omega_3 t_3} \, \mathcal{S}_{NR}(t_1, t_2, t_3) \tag{2.51}$$

which allows to visualize the signal as a 2D spectrum as a function of frequency ω_1 and ω_3, for each value of the waiting time t_2. Notice that, since rephasing and non-rephasing have opposite evolving coherences along t_1, the sign of the Fourier transform is different in the two cases.

Since the 2D spectrum is complex, it includes both real and imaginary parts. Typically, the real part is considered in the analysis of the response. However, we point out how the real part contains both absorptive and dispersive components. Since this fact may complicate the interpretation of the spectra, the absorptive signal is obtained by summing the rephasing and non-rephasing signals:

$$\mathcal{S}_{Abs}(\omega_3, T_2, \omega_1) = \mathcal{S}_R(\omega_3, T_2, \omega_1) + \mathcal{S}_{NR}(\omega_3, T_2, \omega_1) \tag{2.52}$$

which removes the phase twist in the rephasing and non-rephasing spectra due to the dispersion component [2].

References

(1) Mukamel, S., *Principles of Nonlinear Optical Spectroscopy*; Oxford series in optical and imaging sciences; Oxford University Press: 1995.

(2) Hamm, P.; Zanni, M., *Concepts and Methods of 2D Infrared Spectroscopy*; Cambridge University Press: 2011.

(3) Kubo, R. Statistical-Mechanical Theory of Irreversible Processes. I. General Theory and Simple Applications to Magnetic and Conduction Problems. *J. Phys. Soc. Jpn.* **1957**, *12*, 570–586.

(4) Perdomo-Ortiz, A.; Widom, J. R.; Lott, G. A.; Aspuru-Guzik, A.; Marcus, A. H. Conformation and Electronic Population Transfer in Membrane-Supported Self-Assembled Porphyrin Dimers by 2D Fluorescence Spectroscopy. *J. Phys. Chem. B* **2012**, *116*, 10757–10770.

(5) Malý, P.; Mueller, S.; Lüttig, J.; Lambert, C.; Brixner, T. Signatures of Exciton Dynamics and Interaction in Coherently and Fluorescence-Detected Four- and Six-Wave-Mixing Two-Dimensional Electronic Spectroscopy. *J. Chem. Phys.* **2020**, *153*, 144204.

(6) Seidner, L.; Stock, G.; Domcke, W. Nonperturbative Approach to Femtosecond Spectroscopy: General Theory and Application to Multidimensional Nonadiabatic Photoisomerization Processes. *J. Chem. Phys.* **1995**, *103*, 3998–4011.

(7) Gelin, M. F.; Chen, L.; Domcke, W. Equation-of-Motion Methods for the Calculation of Femtosecond Time-Resolved 4-Wave-Mixing and N-Wave-Mixing Signals. *Chem. Rev.* **2022**, *122*, 17339–17396.

(8) Brüggemann, B.; Pullerits, T. Nonperturbative Modeling of Fifth-Order Coherent Multidimensional Spectroscopy in Light Harvesting Antennas. *New J. Phys.* **2011**, *13*, 025024.

(9) Mancal, T.; Pisliakov, A. V.; Fleming, G. R. Two-Dimensional Optical Three-Pulse Photon Echo Spectroscopy. I. Nonperturbative Approach to the Calculation of Spectra. *J. Chem. Phys.* **2006**, *124*, 234504.

(10) Damtie, F. A.; Wacker, A.; Pullerits, T.; Karki, K. J. Two-Dimensional Action Spectroscopy of Excitonic Systems: Explicit Simulation using a Phase-Modulation Technique. *Phys. Rev. A* **2017**, *96*, 053830.

(11) Breuer, H.; Petruccione, F., *The Theory of Open Quantum Systems*; Oxford University Press: 2002.

(12) Tanimura, Y. Numerically "Exact" Approach to Open Quantum Dynamics: The Hierarchical Equations of Motion (HEOM). *J. Chem. Phys.* **2020**, *153*, 020901.

(13) Tamascelli, D.; Smirne, A.; Lim, J.; Huelga, S. F.; Plenio, M. B. Efficient Simulation of Finite-Temperature Open Quantum Systems. *Phys. Rev. Lett.* **2019**, *123*, 090402.

(14) Makri, N. Improved Feynman Propagators on a Grid and Non-Adiabatic Corrections within the Path Integral Framework. *Chem. Phys. Lett.* **1992**, *193*, 435–445.

(15) May, V.; Kühn, O., *Charge and Energy Transfer Dynamics in Molecular Systems*; Wiley-VCH: Weinheim, 2011.

(16) Lindblad, G. On the Generators of Quantum Dynamical Semigroups. *Commun. Math. Phys.* **1976**, *48*, 119–130.

(17) Gorini, V.; Kossakowski, A.; Sudarshan, E. C. G. Completely Positive Dynamical Semigroups of N-Level Systems. *J. Math. Phys.* **1976**, *17*, 821–825.

(18) Manzano, D. A Short Introduction to the Lindblad Master Equation. *AIP Adv.* **2020**, *10*, 025106.

(19) Redfield, A. In *Advances in Magnetic Resonance*; Advances in Magnetic and Optical Resonance, Vol. 1; Academic Press: 1965, pp 1–32.

(20) Zhou, N.; Ouyang, Z.; Hu, J.; Williams, O. F.; Yan, L.; You, W.; Moran, A. M. Distinguishing Energy- and Charge-Transfer Processes in Layered Perovskite Quantum Wells with Two-Dimensional Action Spectroscopies. *J. Phys. Chem. Lett.* **2020**, *11*, 4570–4577.

(21) Ouyang, Z.; Zhou, N.; Hu, J.; Williams, O. F.; Yan, L.; You, W.; Moran, A. M. Nonlinear Fluorescence Spectroscopy of Layered Perovskite Quantum Wells. *J. Chem. Phys.* **2020**, *153*, 134202.

(22) Mueller, S.; Draeger, S.; Ma, X.; Hensen, M.; Kenneweg, T.; Pfeiffer, W.; Brixner, T. Fluorescence-Detected Two-Quantum and One-Quantum-Two-Quantum 2D Electronic Spectroscopy. *J. Phys. Chem. Lett.* **2018**, *9*, 1964–1969.

(23) Mueller, S.; Brixner, T. Molecular Coherent Three-Quantum Two-Dimensional Fluorescence Spectroscopy. *J. Phys. Chem. Lett.* **2020**, *11*, 5139–5147.

(24) Malý, P.; Mancal, T. Signatures of Exciton Delocalization and Exciton–Exciton Annihilation in Fluorescence-Detected Two-Dimensional Coherent Spectroscopy. *J. Phys. Chem. Lett.* **2018**, *9*, 5654–5659.

(25) Kunsel, T.; Tiwari, V.; Matutes, Y. A.; Gardiner, A. T.; Cogdell, R. J.; Ogilvie, J. P.; Jansen, T. L. C. Simulating Fluorescence-Detected Two-Dimensional Electronic Spectroscopy of Multichromophoric Systems. *J. Phys. Chem. B* **2019**, *123*, 394–406.

(26) Bruschi, M.; Gallina, F.; Fresch, B. Simulating Action-2D Electronic Spectroscopy of Quantum Dots: Insights on the Exciton and Biexciton Interplay from Detection-Mode and Time-Gating. *Phys. Chem. Chem. Phys.* **2022**, *24*, 27645–27659.

(27) Tian, P.; Keusters, D.; Suzaki, Y.; Warren, W. S. Femtosecond Phase-Coherent Two-Dimensional Spectroscopy. *Science* **2003**, *300*, 1553–1555.

(28) Tan, H.-S. Theory and Phase-Cycling Scheme Selection Principles of Collinear Phase Coherent Multi-Dimensional Optical Spectroscopy. *J. Chem. Phys.* **2008**, *129*, 124501.

(29) Tekavec, P. F.; Lott, G. A.; Marcus, A. H. Fluorescence-Detected Two-Dimensional Electronic Coherence Spectroscopy by Acousto-Optic Phase Modulation. *J. Chem. Phys.* **2007**, *127*, 214307.

(30) Aue, W. P.; Bartholdi, E.; Ernst, R. R. Two-Dimensional Spectroscopy. Application to Nuclear Magnetic Resonance. *J. Chem. Phys.* **1976**, *64*, 2229–2246.

(31) Bain, A. D. Coherence Levels and Coherence Pathways in NMR. A Simple Way to Design Phase Cycling Procedures. *J. Magn. Reson. (1969)* **1984**, *56*, 418–427.

(32) Keusters, D.; Tan, H.-S.; Warren Role of Pulse Phase and Direction in Two-Dimensional Optical Spectroscopy. *J. Phys. Chem. A* **1999**, *103*, 10369–10380.

(33) De, A. K.; Monahan, D.; Dawlaty, J. M.; Fleming, G. R. Two-Dimensional Fluorescence-Detected Coherent Spectroscopy with Absolute Phasing by Confocal Imaging of a Dynamic Grating and 27-step Phase-Cycling. *J. Chem. Phys.* **2014**, *140*, 194201.

(34) Anda, A.; Cole, J. H. Two-Dimensional Spectroscopy Beyond the Perturbative Limit: The Influence of Finite Pulses and Detection Modes. *J. Chem. Phys.* **2021**, *154*, 114113.

3 | Simulating Action-2D Electronic Spectroscopy of Quantum Dots

3.1. Introduction

Two-Dimensional Electronic Spectroscopy (2DES) probes the dynamics of excited states by triggering a multitude of excitation pathways through a sequence of ultrafast laser pulses. The pivotal technique is represented by Coherent-2DES (C-2DES) based on the measurement of a coherent signal, proportional to the macroscopic polarization, resolved along specific phase-matching directions, upon the interaction with three non-collinear laser pulses. Following its success in the study of exciton dynamics in molecular aggregates and nanostructures, modifications of the original setup have been recently developed [1]. Among the others, Action-2DES (A-2DES) has received increasing attention in the last decade [2]. This technique relies on the detection of an incoherent signal, proportional to the fourth-order excited-state populations, generated by the interaction with four collinear laser pulses. The components of the optical response are resolved by manipulating the phases of the laser pulses, using phase-cycling [3] or phase-modulation [4] schemes.

Depending on the nature of the measured signal, A-2DES allows to probe excited-state populations through the use of different detection-modes, i.e., fluorescence [4, 5], photocurrent [6, 7], photoions [8] or photoelectron [9]. These action signals offer a unique perspective to observe the connection between the ultrafast dynamics of the system and measurable properties, such as photoluminescence and photocurrent generation, opening up to the study of devices in *operando* conditions [10]. Moreover, A-2DES can be combined with single-molecule and microscopy techniques to achieve a spatial resolution beyond the diffraction-limit [11–13], thus circumventing the inhomogeneities which intrinsically contributes to spectral broadening, especially in the case of nanostructures [14]. A-2DES experiments have been performed on a variety of systems, such as atomic vapors [4, 15, 16], molecular dimers [5, 17], dyads [18] and aggregates [19], photosynthetic sys-

Adapted from Bruschi, M.; Gallina, F.; Fresch, B. *Phys. Chem. Chem. Phys.* **2022**, *24*, 27645-27659.

tems [12, 20], metal-molecule interfaces [21], organic [22, 23] and perovskite [24] solar cells, PbS [7] and CdSe [25] quantum dots.

Because of the high informative content of these spectra, together with the plethora of dynamical processes influencing the response, theoretical simulations of model systems are crucial to disentangle and decipher spectral features [26]. Previous theoretical works have analyzed the response of A-2DES by pointing out the necessity of carefully reconsidering the origin of the spectral features compared to its coherent analog, in order to avoid potential pitfalls in their interpretation [27–34]. An important example was given by Malý and Mančal in ref. [30] by considering the role of cross-peaks in the optical response of a molecular heterodimer: while cross-peaks at zero waiting-time are a good witness of excitonic delocalization in C-2DES spectrum, the same spectral features in fluorescence-detected A-2DES may be present even in the case of weak-coupling between chromophores, due to exciton-exciton annihilation active during the detection-time. The same annihilation process may cause the absence of spectral features typically due to Excited-State Absorption, i.e., the A-2DES spectrum results ESA-free [34]. Kunsel et al. [32] extended the analysis to multichromophoric systems such as LH2, shedding light on the interpretation of fluorescence-detected A-2DES experiments of these systems [12, 20].

While in molecular systems the presence of multiple excitations is extremely unstable, in nanostructures such as colloidal Quantum Dots (QDs), they may play a crucial role in determining the action response. A pioneering demonstration was provided by Karki et al. who measured both photocurrent and fluorescence signals from samples of PbS QDs [7]. More recently, multiple-quantum 2DES experiments by Mueller et al. have characterized the multiexciton photophysics in alloyed core-shell QDs using fluorescence detection [25].

In this work, we theoretically investigate the details of the non-linear action response of a minimal model of semiconducting QDs. A theoretical analysis of the photocurrent response of an analogous system has been recently presented by Chen et al. pointing out the effects of the sample-electrode coupling in the photocurrent response [35]. Here, we will focus on the interplay between the exciton and the biexciton contributions in shaping the total A-2DES spectra collected through different detection-modes, i.e., fluorescence and photocurrent detection. Such an interplay is a relevant case study for both conceptual and practical reasons. A first consideration refers to the already mentioned issue of understanding the differences between the C-2DES and A-2DES response. At the level of perturbation theory, the interaction with the fourth pulse generates an additional Excited-State Absorption (ESA) pathway which does not enter in the response of a C-

2DES experiment [27]. Therefore, while the biexciton would appear as a simple negative contribution in a C-2DES spectrum [36, 37], its effect in A-2DES should be analyzed. The point is tightly connected to the study of the effects of exciton-exciton annihilation in interacting molecules which have been debated in previous works [30, 31, 34] but with important distinct features. Differently from small organic chromophores, multiexciton states are quite commonly generated in QDs upon photoexcitation, independently of possible interdot coupling. In a QD, biexcitons are relatively stable [38] and can contribute actively to the measured signal [39, 40], especially in photocurrent detection, when fast interfacial charge-separation can effectively compete with exciton-exciton recombination [7, 41, 42]. We will discuss thoroughly how these processes determine the contributions of several optical pathways to the final spectrum. In essence, the biexciton recombination dynamics plays an analogous role to the exciton-exciton annihilation process in molecular aggregates, but it only depends on the internal system dynamics rather than on intermolecular coupling. As the generation of biexcitons naturally depends also on laser intensity, numerical simulation protocols going beyond the perturbative response function are better suited for the study of their spectral features.

Our simulation protocol, described in Sec. 3.2, is based on a non-perturbative approach to the light-matter interaction and it directly implements the phase-modulation scheme in close analogy with the experimental procedure [43]. Besides the advantage of accounting for finite-bandwidth and pulse-overlap effects [44], it allows a flexible description of different relaxation pathways through the modeling of the dissipator of a Quantum Master Equation (QME) in the Lindblad form. This setting will allow us to naturally include the slow incoherent processes involved in the action detection scheme in the simulation of the spectra. In Sec. 3.3.1, we will connect the fully dynamical picture given by the solution of the QME with the analysis of the spectra based on the contribution of different Feynman pathways from non-linear response theory [45, 46]. Building this connection will allow us to point out and discuss the effects of the detection-time dynamics on the 2D spectrum obtained with different action signals. In Sec. 3.3.2, we will do so by isolating the effects of changing the detection-mode and implementing time-gating of the collected signal. Time-gating of the fluorescence emission has been proposed as a useful technique to monitor the dynamics during the exciton-exciton annihilation process [30, 32]. Indeed, the timescale of the signal detection is definitely slower than the ultrafast timescale probed during photoexcitation and time-gating can be used to change the weights of different contributions to the total spectrum according to their dynamics. In Sec. 3.3.3, we show how controlling such weights is also the key to facilitating the reading of meaningful in-

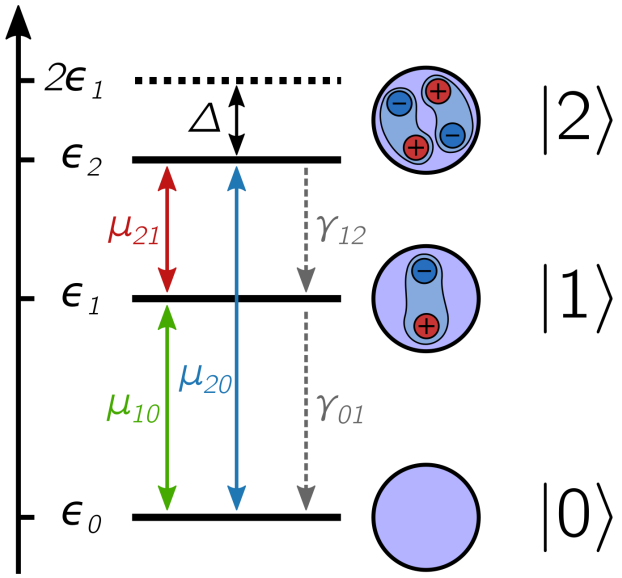

Fig. 3.1: Level structure of the excitonic states of a QD system composed of a ground state $|0\rangle$, an exciton state $|1\rangle$ and a biexciton state $|2\rangle$, each with corresponding energy ϵ_k. The biexciton binding energy is given by the difference between twice the energy of the exciton and the energy of the biexciton, $\Delta = 2\epsilon_1 - \epsilon_2$. Different states are coupled through the transition dipole moment $\mu_{kk'}$ and incoherent relaxation occurs through a cascade mechanism with rates $\gamma_{kk'}$.

formation from the analysis of the spectrum. For example, different optimal gating-time can be devised to estimate the biexciton binding energy, depending on the ratio of the exciton and the biexciton quantum yields. Furthermore, time-gating can be used to track the evolution of the relative amplitudes of spectral features providing information on the relaxation dynamics.

3.2. Theory and Simulations

3.2.1. Model System

The electronic structure of nanocrystals can be described at different levels of theory. Here, we use the simplest picture explaining the absorption bands of small colloidal CdSe QDs in the strong-confinement regime [47].

Upon photoexcitation, an electron (e) is promoted to the conduction-band and the corresponding hole (h) is created in the valence-band. The spherical symmetry of the confining potential leads to a hydrogen-like structure for the envelope function of the charge-carriers, labeled by a principal quantum number and the corresponding angular momentum (e.g., $1S$, $2S$, $1P$, etc.). Due to the spin-orbit coupling, the valence-band

which originates from the p orbitals of Selenium atoms is further split according to the total angular momentum, with the state $1S_{3/2}$ being the lowest in energy. By explicitly considering the significant Coulomb interaction between hole and electron, we switch from the electron-hole basis to the excitonic basis, which is optically probed [48]. In small CdSe QD, the two lowest energy excitons, conventionally named $1S$ and $2S$, roughly correspond to the transitions $1S_{3/2}(h) \rightarrow 1S(e)$ and $2S_{3/2}(h) \rightarrow 1S(e)$ in the hole-electron picture. A more detailed description of the quantum mechanical interactions within the nanocrystal would reveal additional splitting of the bands, the so-called fine-structure of the excitons [38, 49], however the coarse structure of the energy levels will suffice for the scope of this study.

Recently, Collini et al. presented a series of C-2DES spectra of samples of small CdSe QDs both in solution and in solid-state aggregates [50]. We will refer to nanocrystals of the diameter of 2.8 nm and we will assume that the spectral bandwidth of the laser only covers the lowest energy exciton ($1S$) at around 2.34 eV, while the $2S$ manifold, lying more than 0.25 eV higher in energy, is excluded. The biexciton is generated from the band-edge exciton by the subsequent excitation of a second electron-hole pair. Since no other states are involved in the dynamics, this is the ideal setting to focus on the interplay between the exciton and the biexciton contributions to the A-2DES spectra.

The energy structure of the QD nanocrystal is thus treated as a three-level system composed of the ground state $|0\rangle$, the band-edge exciton manifold $|1\rangle$ and the biexciton manifold $|2\rangle$ (Fig. 3.1). The corresponding Hamiltonian reads

$$\hat{H}_0 = \sum_{k=0}^{K=2} \epsilon_k \, |k\rangle\langle k| \tag{3.1}$$

where ϵ_k is the energy of each state. Due to the Coulomb and exchange interactions between the multiple holes and electrons, the biexciton energy is typically offset from twice the exciton energy and their difference defines the biexciton binding energy, $\Delta = 2\epsilon_1 - \epsilon_2$. This parameter quantifies the exciton-exciton correlation enhanced by the confinement effect of the nanostructure and it is typically in the range of some tens of meV in small CdSe QDs. If not otherwise stated, the energies of the various states are $\epsilon_0 = 0.00$ eV, $\epsilon_1 = 2.34$ eV and $\epsilon_2 = 4.66$ eV, corresponding to $\Delta = 20$ meV.

When the nanostructure interacts with the laser pulses, transitions between the different

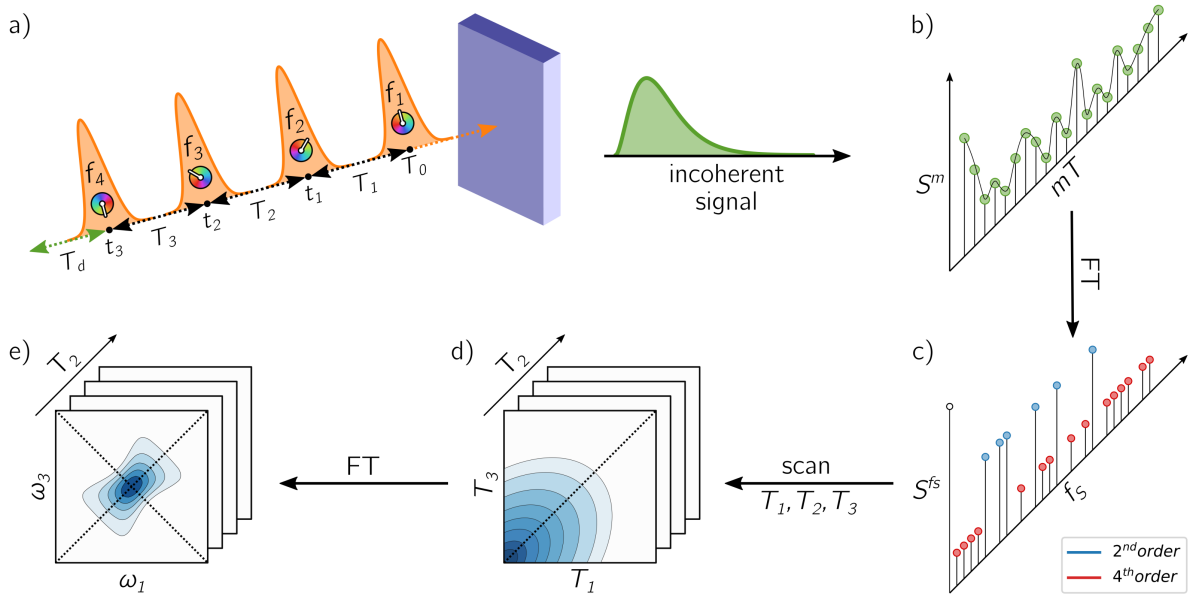

Fig. 3.2: Schematic representation of the working principle of A-2DES: a) the sample, interacting with a sequence of four phase-modulated laser pulses, emits an incoherent signal which is b) collected after each train and stored as a function of the phase-modulation index and the intertrain delay-time mT. By taking the Fourier transform along this axis, c) the Phase-Modulation Spectrum (PMS) is obtained which contains the various contributions to the optical response (i.e., second-order, fourth-order, etc. in the light-matter interaction) as a function of the phase-modulation frequency f_S. By following the evolution of the various components in the PMS as a function of the delay-times, d) a set of temporal data is collected and, by taking the Fourier transform along suitable axes, e) the corresponding 2D spectrum is obtained.

manifolds are induced according to the transition dipole moment operator:

$$\hat{\mu} = \sum_{k \neq k'} \mu_{kk'} \left| k \right\rangle \left\langle k' \right| . \tag{3.2}$$

Since the transition dipole moment connecting two neighboring manifolds usually have similar magnitude [25], the light-matter coupling strength is assumed to be the same for the transition from the ground to the exciton state and from the exciton state to the biexciton manifold, $\mu_{kk'} E_i^0 = 8$ meV, where E_i^0 is the amplitude of the electric field. The direct transition from the ground state to the biexciton state, although in principle allowed, is not within the considered spectral bandwidth of the laser.

3.2.2. Action-2D Electronic Spectroscopy

In the following, we introduce the working principles of A-2DES using a phase-modulation scheme. Fig. 3.2 outlines the main steps to obtain the 2D spectra starting from the

Symbols	Meaning	Values
$\mu_{kk'}E_i^0$	light-matter coupling strength	8 meV
σ_i	pulse duration	5 fs
$\hbar\omega_i$	carrier-energy	2.34 eV
T_0	center of the 1^{st} pulse	50 fs
M	total phase-modulation index	179
f_1	modulation frequency 1^{st} pulse	0 Hz
f_2	modulation frequency 2^{nd} pulse	250 Hz
f_3	modulation frequency 3^{rd} pulse	600 Hz
f_4	modulation frequency 4^{th} pulse	1000 Hz
T	intertrain delay-time	1/3000 s

Tab. 3.1: Parameters used in the simulation of the 2D spectra.

quantum dynamics triggered by the train of laser pulses. All these steps are implemented in the numerical simulation protocol in close analogy to the experimental procedure.

Overall, the sample interacts with $M+1$ trains of four laser pulses, separated by an intertrain delay-time T. In the phase-modulation protocol, the phase of each pulse, which can assume a finite set of values between 0 and 2π, is varied at a given modulation frequency. The m-th train, made of four collinear laser pulses (Fig. 3.2a), is written as:

$$\begin{aligned} E^m(t) &= \sum_{i=1}^{4} E_i^m(t) \\ &= E_1^m(t) + E_2^m(t) + E_3^m(t) + E_4^m(t). \end{aligned} \tag{3.3}$$

Each pulse is described by the convolution of a Gaussian envelope and an oscillating function:

$$E_i^m(t) = E_i^0 \exp\left\{ -\frac{(t-\mathcal{T}_i)^2}{2\sigma_i^2} \right\} \times \cos[\omega_i(t-\mathcal{T}_i) + \phi_i^m] \tag{3.4}$$

where E_i^0 is the electric-field amplitude, σ_i is the pulse duration, ω_i is the carrier-frequency and ϕ_i^m is the phase of the pulse in the m-th train. The first pulse of each train is centered at time T_0, while the following pulses are separated from each other with a well-defined delay-time: $T_1 = t_1 - T_0$, $T_2 = t_2 - t_1$ and $T_3 = t_3 - t_2$. For convenience, in Eq. 3.4 we make use of a cumulative delay-time: $\mathcal{T}_i = \sum_{j=0}^{i-1} T_j$.

According to the non-linear response theory, the interaction with the former three pulses prepares the system into a coherent superposition of excited states, which is then converted into an observable fourth-order population by the interaction with the last pulse [27]. The incoherent signal, emitted during the detection-time T_d, is thus proportional to the excited-state populations. Let us define $\hat{\mathcal{P}}_k = |k\rangle\langle k|$ as the projection operator onto the k-th state and the coefficients $\gamma_k^{(r)}$ as the rate of the relaxation event contributing to the signal, i.e.,

spontaneous emission for fluorescence and charge-separation for photocurrent detection. Typically, the timescale of the emitted signal is several orders of magnitude longer than the femtosecond timescale probed during photoexcitation. After the fourth pulse, the signal is obtained as the expectation value of the operator $\hat{\mathcal{S}} = \sum_k \gamma_k^{(r)} \hat{\mathcal{P}}_k$ taken over the density matrix of the system, which leads to the explicit form of the time-resolved signal:

$$\begin{aligned} S(T_d) &= \mathrm{Tr}\left\{\hat{\mathcal{S}}\rho(T_d)\right\} \\ &= \sum_k \gamma_k^{(r)} P_k(T_d) \end{aligned} \tag{3.5}$$

where $P_k(T_d) = \langle k|\rho(T_d)|k\rangle$ represents the population of the k-th state. Experimentally, the measured signal is typically integrated from the end of the fourth pulse along the detection-time T_d:

$$\begin{aligned} \bar{S}(T_d) &= \int_{\mathcal{T}_4}^{\mathcal{T}_4+T_d} dT_d'\ S(T_d') \\ &= \sum_k \gamma_k^{(r)} \bar{P}_k(T_d) \end{aligned} \tag{3.6}$$

where $\bar{P}_k(T_d) = \int_{\mathcal{T}_4}^{\mathcal{T}_4+T_d} dT_d' P_k(T_d)$ is the time-integrated population of the k-th state. Compared to C-2DES, the detection-time T_d represents an additional dynamical variable in A-2DES. Furthermore, we emphasize that the incoherent signal depends parametrically, through the system density matrix, also on the phase-modulation index m and the set of delay-times as $S^m(T_1, T_2, T_3, T_d)$.

To disentangle the different contributions to the optical response, a phase-modulation scheme is employed [4]. In practice, the phase of each pulse $\phi_i^m = 2\pi m f_i T$ is linearly modulated from a train to the following by varying the phase-modulation index $m \in [0, M]$, where f_i is the phase-modulation frequency of the i-th pulse and T is the intertrain delay-time, namely the time between the first pulse of two consecutive trains. For each set of delay-times and phase relations, the intensity of the signal obtained after excitation is stored as a function of the phase-modulation index and the intertrain delay-time mT (Fig. 3.2b). By taking the Fourier transform along this variable, the Phase-Modulation Spectrum (PMS) is retrieved S^{f_s} (Fig. 3.2c), which contains the various contributions to the optical response of the system. Each peak in the PMS is labeled by a certain modulation frequency f_S given by the linear combinations of the modulation frequency of each pulse f_i: $f_S = \sum_{i=1}^4 \ell_S^i f_i$, where $\ell_S^i = 0, \pm 1, \pm 2,$, etc. The decomposition of the optical response in the PMS reflects the spatial decomposition of the polarization along the phase-matching directions in the non-collinear setup of C-2DES [45]. Each component in the PMS can

be regarded as the signal related to a set of excitation pathways induced by a specific sequence of interactions with the laser pulses. Despite the cost of performing several phase realizations of the experiment, the phase-modulation protocol has the advantage of simultaneously obtaining the second-order response, i.e., linear absorption spectra, the fourth-order response, i.e., Rephasing, Non-Rephasing and Two-Quantum signals, and even higher-order response in the light-matter coupling.

Both in the experiment and numerical simulation, the choice of the modulation frequencies is of key importance to isolate the components of interest. Also notice, that higher-order contributions can always enter at the same modulation frequency as lower-order contributions, therefore the strength of the excitation needs to be taken into account when interpreting the obtained spectra. From the numerical point of view, a suitable choice of modulation frequencies should also aim at minimizing the length of the phase-modulation sequence M in order to reduce the computational cost of running the dynamical evolution for each phase realization. By following these principles, we have selected the modulation frequencies reported in Tab. 3.1, together with the values of other specific parameters used for the simulations. The numerical values are compatible with the experimental setup of refs. [23, 50].

At this point, by following the evolution of the components of the PMS as a function of the delay-times T_1, T_2 and T_3, we obtain the time-dependent signal (Fig. 3.2d) and, by taking the Fourier transform along suitable delay-times, the corresponding spectra are recovered (Fig. 3.2e). In general, the frequency axes chosen to display the 2D spectrum depend on the specific signal considered. In the case of the Rephasing spectrum, the signal extracted from the PMS is Fourier transformed along the delay-times T_1 and T_3 to obtain a 2D spectrum as a function of the frequencies ω_1 and ω_3 for each value of T_2. In Sec. 3.3.1, we will consider two classes of 2D spectra characterized by the order of the coherences that are detected. The more common Rephasing and Non-Rephasing signals are characterized by coherences between states that are separated by a single excitation, i.e., ground-exciton coherence or exciton-biexciton coherence. The second class is represented by Two-Quantum signals [51], i.e., Two-Quantum-One-Quantum (2Q1Q) and One-Quantum-Two-Quantum (1Q2Q), which directly investigate also coherences between states separated by two excitations, i.e., ground-biexciton coherence. Their respective positions in the PMS are: Rephasing at $f_S = -f_1 + f_2 + f_3 - f_4 = 150$ Hz, Non-Rephasing at $f_S = f_1 - f_2 + f_3 - f_4 = 650$ Hz, 2Q1Q at $f_S = 2f_1 - f_2 - f_3 = 850$ Hz and 1Q2Q at $f_S = -f_1 - f_2 + 2f_3 = 950$ Hz.

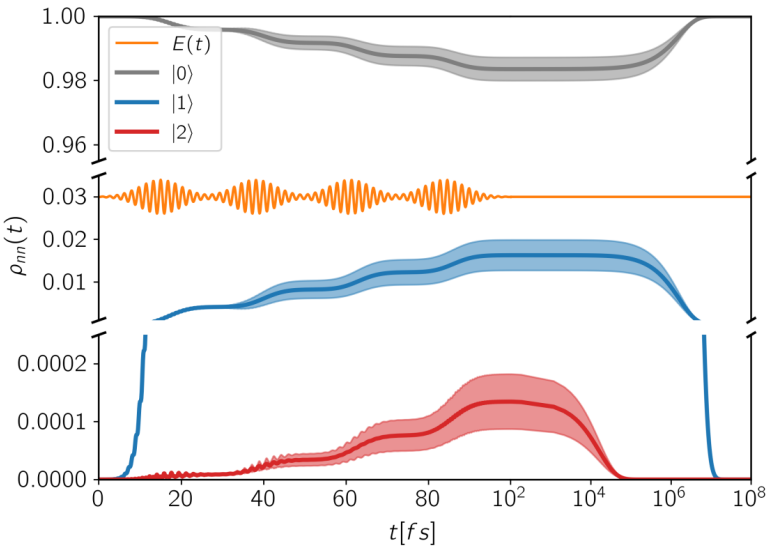

Fig. 3.3: Population dynamics of the excitonic states of a QD system interacting with a train of four laser pulses. The full lines are the average population of each state, while the shaded areas represent their standard deviations with respect to the specific phase realization of the pulses. The employed delay-times are: $T_0 = 15$ fs, $T_1 = 23$ fs, $T_2 = 23$ fs, $T_3 = 23$ fs.

For the simulations, the delay-times have been scanned in steps of 10 fs from 0 to 300 fs, working in the rotating-frame at a frequency of $\omega_{RF} = 3.56$ [rad]/fs (doubled in the case of Two-Quantum signals). In order to smooth the spectra, each signal has been zero-padded in the time-domain. In the following, only the real part of each spectrum is shown and the amplitude is normalized relative to its absolute maximum/minimum. For the Rephasing and Non-Rephasing signals, T_1 and T_3 are scanned while setting $T_2 = 0$ fs. For 2Q1Q and 1Q2Q signals, T_1 and T_2 are scanned while setting $T_3 = 0$ fs. Notice that the Two-Quantum signals correspond to the set of pathways where the system interacts twice with the first pulse (2Q1Q) or with the third pulse (1Q2Q) while there is no interaction with the fourth pulse.

3.2.3. Quantum Dynamics

By avoiding the evaluation of the response function, non-perturbative approaches to the simulation of 2DES spectra rely on the explicit dynamics of the density matrix under the effect of the electric field, at the cost of introducing an effective strategy to extract the pertinent component of the optical response [52, 53].

In this context, the phase-modulation scheme is implemented to resolve the various components of the overall signal [43]. Making use of the theory of open quantum system, the evolution of the density matrix during the experiment is obtained by solving the Quantum

Master Equation in the Lindblad form [54, 55], assuming $\hbar = 1$ in the following:

$$\begin{aligned}\frac{d}{dt}\rho(t) = &- i[\hat{H}_0, \rho(t)] + i[\hat{\mu}E(t), \rho(t)] + \\ &+ \sum_{k,k'} \gamma_{kk'}\left[\hat{L}_{kk'}\rho(t)L^{\dagger}_{kk'} - \frac{1}{2}\{L^{\dagger}_{kk'}\hat{L}_{kk'}, \rho(t)\}\right]\end{aligned} \tag{3.7}$$

where $[\cdot,\cdot]$ represents the commutator and $\{\cdot,\cdot\}$ is the anti-commutator. The density matrix $\rho(t) = \sum_{k,k'} \rho_{kk'}(t)\,|k\rangle\langle k'|$ describes the state of the system, whose diagonal elements represent the populations of each excitonic state while the off-diagonal elements represent the coherences between them. In the QME, the first term accounts for the coherent evolution due to the system Hamiltonian (Eq. 3.1), the second term accounts for the light-matter interaction in the dipole-approximation (Eqs. 3.2 and 3.3) and the last term accounts for the effects of the coupling with the environment, inducing decoherence and relaxation processes in the dynamics. An incoherent transition between states k' and k is described by the Lindblad operator $\hat{L}_{kk'} = |k\rangle\langle k'|$ with an associated characteristic rate $\gamma_{kk'}$. Therefore, we define the relaxation mechanism as a cascade process from the biexciton to the exciton state, with $\hat{L}_{12} = |1\rangle\langle 2|$, and then from the exciton to the ground state, with $\hat{L}_{01} = |0\rangle\langle 1|$ (Fig. 3.1). The rates include all the decay channels, which may or may not contribute to the recorded signal, e.g., the transition from the biexciton to the exciton manifold can happen through radiative emission or fast Auger recombination. In addition, we introduce pure dephasing contributions through the Lindblad operators $\hat{L}_{00} = |0\rangle\langle 0|$, $\hat{L}_{11} = |1\rangle\langle 1|$ and $\hat{L}_{22} = |2\rangle\langle 2|$. Except otherwise stated, the characteristic relaxation times used in this work are $\gamma_{01}^{-1} = 10$ ns and $\gamma_{12}^{-1} = 100$ ps, while the decoherence time is $\gamma_{kk}^{-1} = 100$ fs. These parameters have been chosen in agreement with recent studies on similar systems [25].

In Fig. 3.3, we report the evolution of the diagonal elements of the density matrix induced by a train of pulses applied at regular delay-times. During each pulse, populations are coherently transferred between different states. The shaded area represents the variability of the population with respect to the specific phase realization of the pulses which is highly dependent on the decoherence time. Indeed, when the delay-times T_i exceeds the decoherence time γ_{kk}^{-1}, no modulation of the final populations is observed. While decoherence primarily influences the system dynamics during photoexcitation, the relaxation mechanisms act on a slower timescale and become relevant especially during the detection-time T_d.

Notice that according to Eq. 3.7, in the absence of the external electric field, the

evolution of populations is decoupled from coherences. This means that, after the end of the fourth pulse, the dynamics of populations can be described in terms of a simple kinetic equation:

$$\frac{d}{dt}\vec{P}(t) = -\boldsymbol{K}\vec{P}(t) \tag{3.8}$$

where the probability vector $\vec{P}(t) = \sum_k P_k(t)\,|k\rangle$ contains the occupation probability of each state and the kinetic matrix is defined by the rates of the relaxation processes connecting different diagonal elements of the density matrix, that is:

$$K_{kk'} = -(1-\delta_{kk'})\gamma_{kk'} + \delta_{kk'}\sum_{l\neq k}\gamma_{lk}. \tag{3.9}$$

The kinetic equation can be solved analytically or numerically and the general solution can be written as the linear combination of decay modes:

$$\begin{aligned}\vec{P}(t) &= e^{-\boldsymbol{K}t}\vec{P}(0)\\ &= \boldsymbol{V}e^{-\boldsymbol{\Lambda}t}\boldsymbol{V}^{-1}\vec{P}(0)\end{aligned} \tag{3.10}$$

where $\boldsymbol{\Lambda}$ and $\boldsymbol{V}$ are respectively the eigenvalues and the eigenvectors matrices obtained by solving $\boldsymbol{KV} = \boldsymbol{V\Lambda}$. The solution of the kinetic equation allows us to record the signal over a detection-time T_d spanning several orders of magnitude, as shown in Fig. 3.3.

In the simulations, the Lindblad QME (Eq. 3.7) has been numerically integrated using the (4th order) Runge-Kutta method with a time-step of 0.1 fs from 0 fs until 100 fs after the center of the fourth pulse. Then, the kinetic scheme for the populations is solved by diagonalizing $\boldsymbol{K}$ and evolving using a time-step of 100 fs.

3.3. Results and Discussion

3.3.1. Exciton and Biexciton Contributions to the A-2DES Spectra

By applying the numerical procedure described in the previous section, we simulate the 2D spectra originating from the exciton and the biexciton states on the basis of the fourth-order population generated by the last pulse, ideally before any quantitative relaxation process occurs during T_d. Although the non-perturbative solution of the system dynamics is a powerful method for the calculation of non-linear signals, the perturbative approach remains the key tool for the interpretation of the optical response in terms of different dynamical pathways. Accordingly, we will examine the exciton and biexciton con-

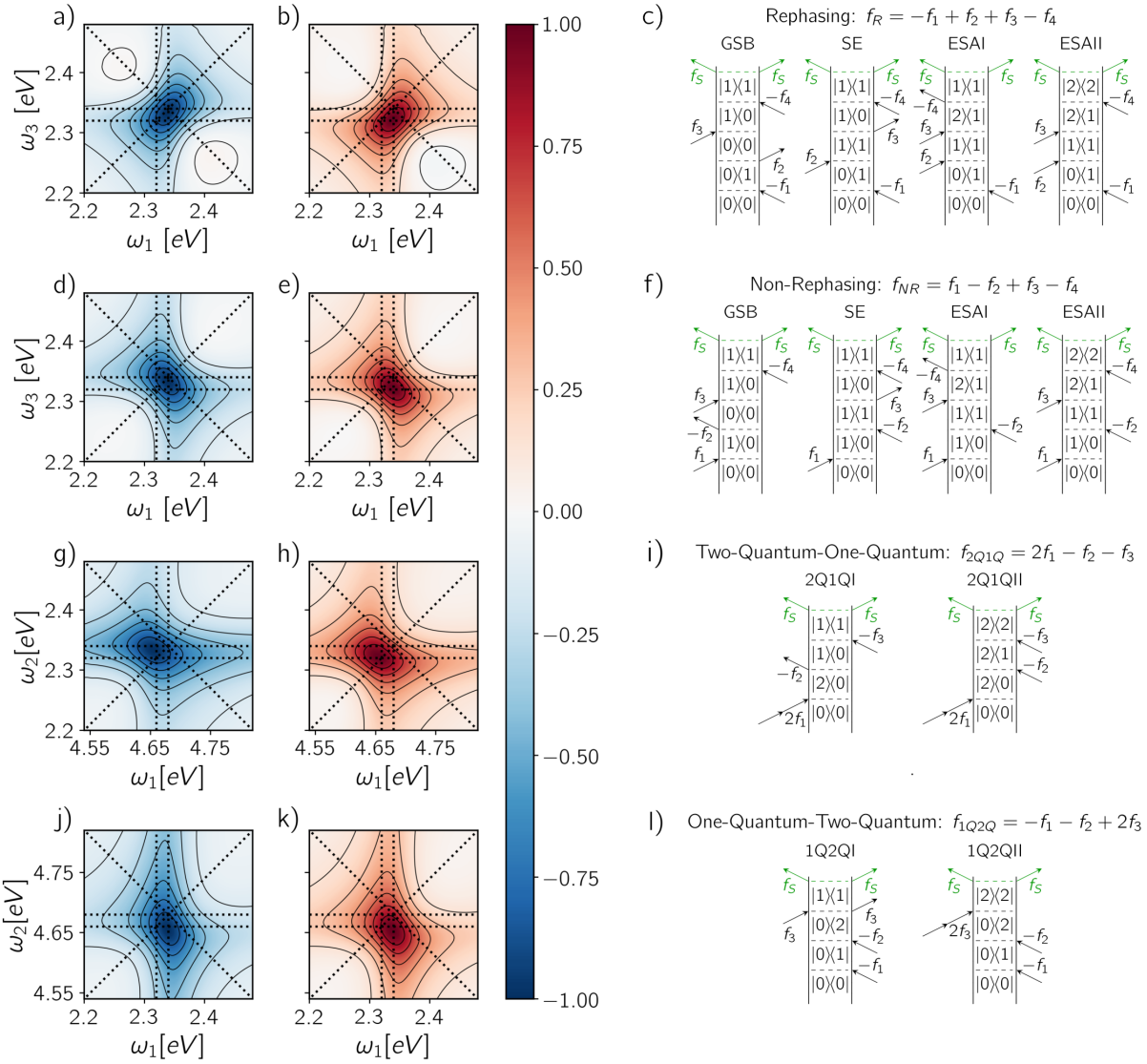

Fig. 3.4: a) Exciton contribution, b) biexciton contribution and the corresponding c) Feynman diagrams for the Rephasing signal. In the same order: d-f) for Non-Rephasing signal, g-i) for 2Q1Q signal and j-l) for 1Q2Q signal. Each spectrum is normalized with respect to its absolute maximum/minimum. The signal has been integrated up to a detection-time $T_d = 1$ ps.

tributions by using perturbative terminology [45, 46] to analyze how they combine in the total spectrum.

We start by discussing the exciton and the biexciton contributions for the Rephasing (Fig. 3.4a,b) and Non-Rephasing (Fig. 3.4d,e) signals along with the corresponding Feynman diagrams (Fig. 3.4c,f). Each Feynman diagram represents a dynamical pathway, specified by the sequence of coherence or population states of the system, induced by the interaction with the laser pulses. In the Rephasing and Non-Rephasing signals, the system interacts once with each pulse, as represented by the four black arrows in the Feynman diagrams. The incoherent signal, depicted as two green arrows, is due to the relaxation of the population generated by the fourth interaction. The sign by which a certain pathway contributes to the spectrum is given by the factor $(-1)^n$, where n is the number of interactions on the *bra* side in the corresponding diagram. Depending on the sequence of interactions involved in a Feynman pathway, its contribution can be distinguished into Ground-State Bleaching (GSB), Stimulated Emission (SE) and Excited-State Absorption (ESA). The interaction with the first pulse prepares the system in a ground-exciton coherence oscillating during the delay-time T_1. Then, the interaction with a second pulse generates a population that can be either in the ground or in the exciton state. The ground state population is associated with the GSB pathway upon the subsequent interaction with the last two pulses, while the exciton population follows the SE pathway, if the system emits upon interaction with the third pulse, or alternatively an ESA pathway, if it absorbs a photon from the third pulse. Whereas both GSB and SE pathways end in the exciton manifold, due to the interaction with the fourth pulse, two types of ESA pathways are possible in A-2DES: the ESAI, leading to a final population in the exciton manifold, and the ESAII, ending in the biexciton manifold.

It should be stressed that it is not possible to isolate the signal corresponding to a specific pathway (GSB, SE or ESA) from the full dynamical evolution of the density matrix since they represent just terms of a perturbative expansion [30]. However, in principle, we can resolve the exciton and the biexciton contributions on the basis of the final population state from which the incoherent signal originates. Therefore, the exciton contribution results from the GSB, SE and ESAI pathways, while the biexciton contribution results from the ESAII pathway. Accordingly, the Rephasing spectrum of the exciton manifold (Fig. 3.4a) shows a prominent negative peak along the diagonal at coordinates $(\omega_{10}, \omega_{10})$, corresponding to the GSB and SE pathways, and a less intense off-diagonal contribution from the ESAI centered at $(\omega_{10}, \omega_{21})$ which introduces an asymmetry in the peak leading to a lineshape elongated below the diagonal. On the other hand, the spectrum associated with

the biexciton contribution (Fig. 3.4b) exhibits a positive off-diagonal peak at coordinates $(\omega_{10}, \omega_{21})$ related to the ESAII pathway.

The opposite sign of the spectral contributions of the exciton and the biexciton is conserved also along other phase-modulation components. For example, within the same set of dynamical simulations, we can investigate less common contributions of the response, such as the Two-Quantum-One-Quantum (2Q1Q) and One-Quantum-Two-Quantum (1Q2Q) signals. The measurement of these components in an action-detected setting has been recently realized by Mueller et al. [51, 56] and applied to the study of QD nanocrystals [25]. In this case, a two-quantum (2Q) coherence, i.e., coherence between states that are two excitations apart, is correlated with a one-quantum (1Q) coherence, i.e., coherence between states that are one excitation apart. In the following, we discuss the exciton and biexciton contributions in the 2Q1Q (Fig. 3.4g,h) and 1Q2Q (Fig. 3.4j,k) spectra along with the corresponding Feynman diagrams (Fig. 3.4i,l). The two signals are both characterized by only two Feynman diagrams, differing in the temporal sequence of the one- and two-quantum coherences. In 2Q1Q, the interaction of the system with the first pulse causes the absorption of two photons, generating a 2Q coherence between the ground and the biexciton states which evolves along T_1. The subsequent interaction converts the state into a 1Q coherence: if the 1Q coherence which is established is a ground-exciton coherence, the signal is eventually emitted from the exciton manifold (2Q1QI), while in the case of an exciton-biexciton coherence, the signal is emitted from the biexciton state (2Q1QII). Similarly, for the 1Q2Q experiment, one pathway leads to the exciton population (1Q2QI), while the other leads to the biexciton population (1Q2QII) after the fourth pulse. The corresponding spectra are obtained by taking the Fourier transform of the delay-times T_1 and T_2, directly correlating the two coherences. In the 2Q1Q spectrum, the exciton and the biexciton contributions are centered respectively at two different spectral positions $(\omega_{20}, \omega_{10})$ and $(\omega_{20}, \omega_{21})$, while in the case of 1Q2Q spectrum, they are found at the same coordinates $(\omega_{10}, \omega_{20})$.

Because the contribution of the biexciton is always of opposite sign than the exciton one, cancellation between different pathways may take place and the resulting spectral lineshape will crucially depend on their relative weights. Let us focus on the Rephasing spectra, where the ESAI and ESAII pathways contribute in the same spectral location with opposite signs. To analyze the total spectrum, the contribution of different manifolds can be weighted by a phenomenological relative yield coefficient Γ, which quantifies the mean number of emitted photons in fluorescence detection, or charge-carriers in photocurrent detection, generated from the biexciton state, relative to the average number generated

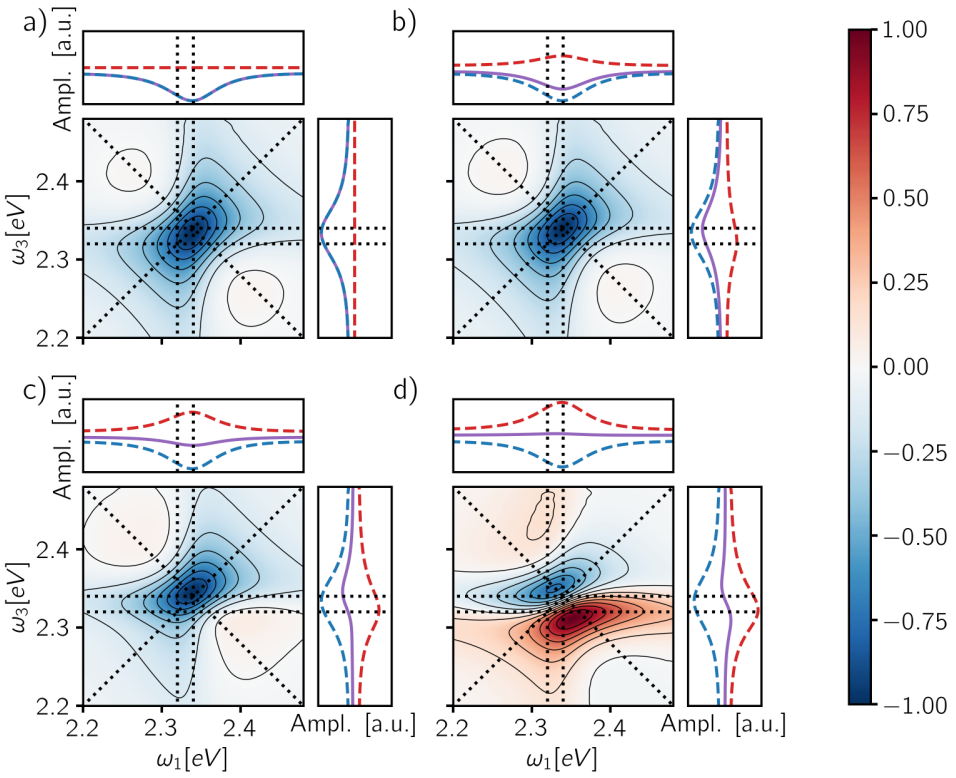

Fig. 3.5: Rephasing spectra calculated as a weighted sum of the exciton and biexciton contributions (Eq. 3.11) after the end of the fourth pulse for a phenomenological yield coefficient a) $\Gamma = 0$, b) $\Gamma = 1$, c) $\Gamma = 2$ and d) $\Gamma = 3$. Each spectrum is normalized to its absolute maximum/minimum. The panels on the top and the right of each spectrum report the total signal (purple solid line), the isolated exciton contribution (blue dashed line) and the isolated biexciton contribution (red dashed line) averaged along ω_3 and ω_1 axes respectively. The signal has been integrated up to a detection-time $T_d = 1$ ps.

from the exciton [7, 27, 30]. The overall spectrum is then expressed in terms of exciton and biexciton contributions as follows

$$\begin{aligned} S &= S_X + \Gamma \cdot S_{BX} \\ &= -GSB - SE - (1-\Gamma)ESA \end{aligned} \tag{3.11}$$

where the decomposition in terms of Feynman pathways, given in the second equality, underlies the common assumption that the two ESA pathways are similar except for their relative sign. In some conditions, the relative yield coefficient Γ can be inferred from the photophysics of the system under consideration: for example, $\Gamma = 2$ if the biexciton contributes with two photons, or charges, and the exciton with one. This is the situation commonly expected when considering independent emitters [30, 34]. In this case, $S = -GSB - SE + ESA$ and the corresponding spectrum is shown in Fig. 3.5c. Interestingly, this is the combination of pathways corresponding to the signal obtained by C-2DES, with the spectrum featuring a diagonal peak (GSB+SE) whose amplitude is partially bleached by the negative contribution of the ESA pathway in the off-diagonal position. Another notable case discussed in the literature of molecular aggregates [30, 32] is the biexciton state having the same yield as the exciton because of complete exciton-exciton annihilation processes. In this case, $\Gamma = 1$ and the A-2DES spectrum is ESA-free, $S = -GSB - SE$. In this case, the spectrum features a symmetrical diagonal peak originating from the GSB and the SE pathways (Fig. 3.5b). In another case, the annihilation process can involve both excitons, so that Γ becomes negligible and the spectrum reduces to the contribution of the exciton with an asymmetric peak elongated below diagonal (Fig. 3.5a). Finally, the biexciton may have a significantly higher yield than the exciton, as reported in photocurrent detection [7]. In this case, Γ is expected to be higher than 2 and the spectrum is characterized by a dispersive lineshape profile (Fig. 3.5d).

3.3.2. Effects of Different Detection-Modes and Time-Gating

The special cases discussed in the previous section require strong assumptions on the relaxation dynamics of the excited manifolds of the system under consideration. While for molecular aggregates probed using fluorescence, it is generally safe to assume a quantitative relaxation from the double-excited state to the single-excited state before signal detection [17, 32], the biexcitons of QDs are characterized by a broader phenomenology which should be taken into account to correctly interpret the interplay between exciton and biexciton contributions in the total spectrum. In this section, we will answer the following questions: how can we determine the relative yield coefficient Γ from the relaxation

rates governing the system dynamics (Eq. 3.7)? Are there "experimental knobs" that can be used to control the relative weights of exciton and biexciton contributions in the final spectrum?

We start by further specifying the total relaxation rates between two manifolds, $\gamma_{kk'}$ in Eq. 3.7, in terms of a radiative (r) and a non-radiative (nr) contributions:

$$\gamma_{kk'} = \gamma_{kk'}^{(r)} + \gamma_{kk'}^{(nr)}, \tag{3.12}$$

where $k \neq k'$. Although this nomenclature explicitly refers to fluorescence detection, where the radiative contribution is associated with spontaneous emission, we will use it with a more general meaning where "radiative" indicates processes that contribute to the detected signal (Eq. 3.5) while "non-radiative" groups all the other relaxation channels, e.g., exciton trapping and Auger recombination. Therefore, we introduce the Generalized Quantum Yield (GQY) which is state-specific and explicitly depends on the chosen detection-mode. This can be expressed in terms of the microscopic rate constants. For the exciton, the GQY is:

$$\Phi_1 = \frac{\gamma_{01}^{(r)}}{\gamma_{01}^{(r)} + \gamma_{01}^{(nr)}} = \frac{\gamma_{01}^{(r)}}{\gamma_{01}} \tag{3.13}$$

while for the biexciton is:

$$\Phi_2 = \frac{\gamma_{12}^{(r)}}{\gamma_{12}^{(r)} + \gamma_{12}^{(nr)}} = \frac{\gamma_{12}^{(r)}}{\gamma_{12}}. \tag{3.14}$$

By definition, the GQY is bounded: if the radiative contribution exceeds the non-radiative one $\gamma_k^{(r)} \gg \gamma_k^{(nr)}$, the GQY is $\Phi_k \to 1$, otherwise for $\gamma_k^{(r)} \ll \gamma_k^{(nr)}$, the GQY is $\Phi_k \to 0$. Then, the signal in Eq. 3.5 can be written in terms of the total relaxation rate, the GQY and the population of each state:

$$\begin{aligned} S(T_d) &= \gamma_{01}^{(r)} P_1(T_d) + \gamma_{12}^{(r)} P_2(T_d) \\ &= \gamma_{01}\Phi_1 P_1(T_d) + \gamma_{12}\Phi_2 P_2(T_d) \end{aligned} \tag{3.15}$$

and the interplay between the exciton and the biexciton contributions is regulated by the ratio between the two terms.

To proceed in our analysis, we assume that the ratio between the total relaxation rates γ_{12}/γ_{01} is a constant that characterizes the system, while the GQY and the populations can be influenced, to some extent, by changing the settings of the spectroscopic experiment. Specifically, the ratio of the GQY Φ_2/Φ_1 strongly depends on the adopted detection-mode, while the ratio of the populations $P_2(T_d)/P_1(T_d)$ depends on the detection-time.

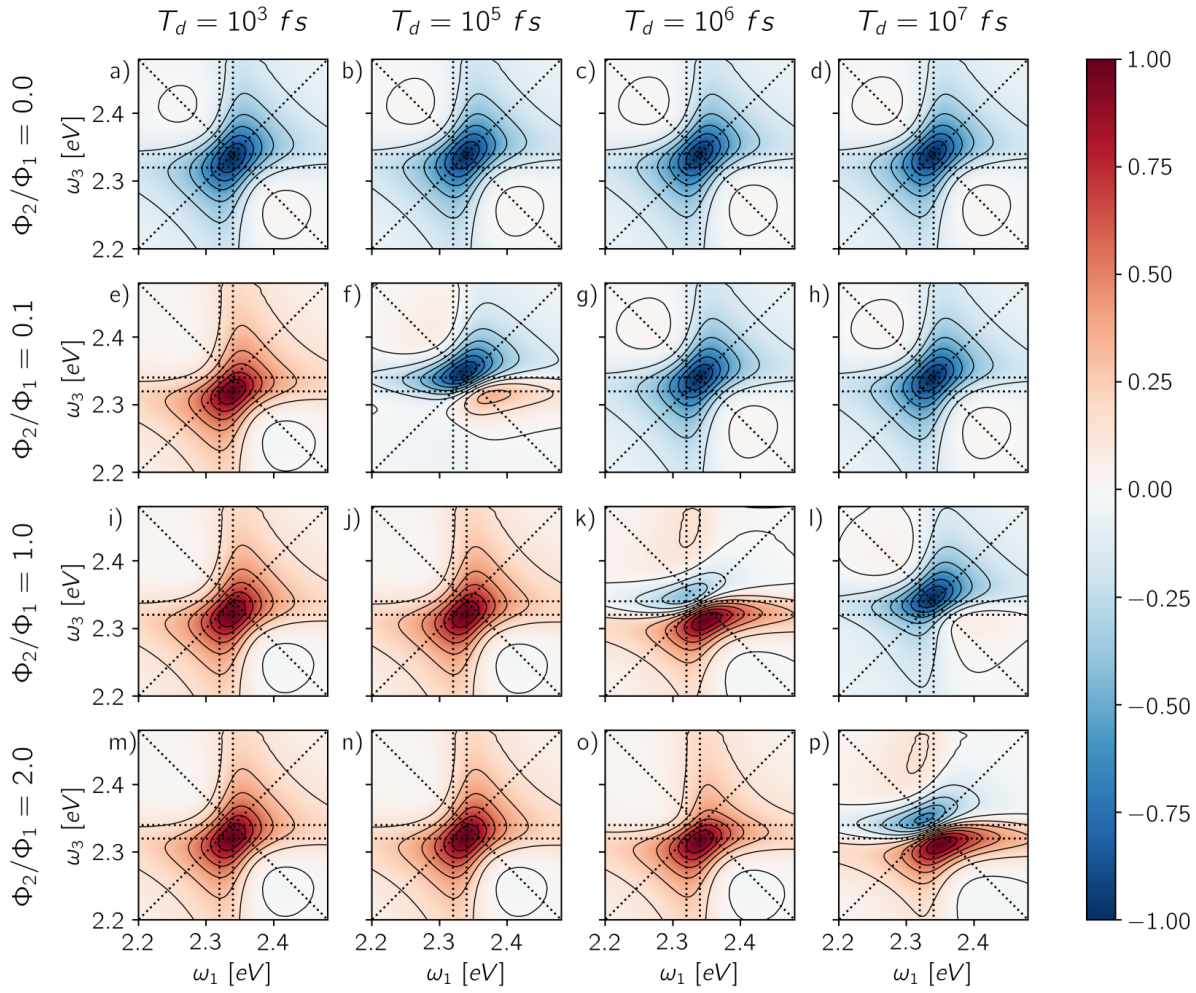

Fig. 3.6: Rephasing spectra for different values of GQY ratio ($\Phi_2/\Phi_1 = 0.0,\ 0.1,\ 1.0,\ 2.0$) on the columns and different detection-times ($T_d = 10^3$ fs, 10^5 fs, 10^6 fs, 10^7 fs) on the rows. Each spectrum is normalized with respect to its absolute maximum/minimum.

Fluorescence detection is typically associated with a low GQY ratio because higher excited states mainly relax non-radiatively to the first excited state from which radiative emission occurs. However, while in molecular systems this ratio is commonly negligible, nanocrystals may exhibit a wider photophysical phenomenology with the GQY of the biexciton varying significantly in every single nanostructure and even approaching unity, when Auger decay channels are suppressed by thick shells [39, 57–59]. When the sample can be detected through photocurrent, the radiative contribution from multiexciton manifolds can be even higher, thus reversing the relative magnitude of the GQY of exciton and biexciton. When higher excitation frequencies are used, the presence of higher Quantum Yields may also depend on the presence of Multiple Exciton Generation (MEG) [7].

The last column of Fig. 3.6 shows the spectra obtained from the integrated signal for

different GQY ratios. When the biexciton does not contribute directly to the detected signal ($\Phi_2/\Phi_1 = 0$), a quantitative relaxation of the biexciton to the exciton manifold takes place before emission. In this case, the signal originating from the ESAII pathway is transferred quantitatively to the exciton manifold during the detection-time and therefore it cancels exactly the ESAI signal. In other words, we realize the case of $\Gamma = 1$ (Fig. 3.5b) resulting in an ESA-free spectrum. In all the other cases, because the radiative decay of the biexciton is faster than the decay from the exciton manifold, we are in situations where $\Gamma > 1$ and the active contribution of the biexciton is observed in the off-diagonal position. Notice that the transfer of the ESAII contribution into the exciton manifold is a relatively slow dynamical process taking place during the detection-time T_d.

The presence of a detection-time T_d is another element of novelty of A-2DES compared to C-2DES and represents an additional experimental parameter influencing the optical response of the system. Time-gating techniques can be used, in principle, to resolve the emission by integrating the signal within a finite temporal window during the detection. This technique has been already experimentally implemented in time-resolved fluorescence, photoluminescence [60] and microscopy [61]. Although the possibility of combining time-gating with fluorescence-detected A-2DES has been recently proposed [30, 32], an experimental implementation is still lacking to our knowledge. While in fluorescence detection, time-gating can be achieved by photon-counting techniques, fast transient photocurrent measurements have also been reported in QDs assemblies [62].

Through the choice of the detection-time, it is possible to parametrically control the ratio between the biexciton and exciton populations $P_2(T_d)/P_1(T_d)$. Therefore, the dynamics of the spectral features as a function of T_d reflects the relaxation dynamics of the excited manifolds. The effect of changing the detection-time is reported in Fig. 3.6, where each row shows the spectra resulting from varying the integration window for each value of the GQY ratio. When the biexciton does not contribute actively to the signal for $\Phi_2 = 0.0$ (Fig. 3.6a-d), the biexciton contribution cannot become explicit and all spectra show a prominent negative diagonal feature mainly due to the GSB and SE pathways. However, for T_d shorter than the biexciton recombination ($T_d < \gamma_{12}^{-1}$), spectra result slightly asymmetric, characterized by a counter-clockwise peak twist and a broadening below the diagonal. Indeed, when the signal is collected before Auger relaxation, the ESA cancellation is not complete and the spectrum reveals the off-diagonal feature at $(\omega_{10}, \omega_{21})$, corresponding to the ESAI pathway. As the detection-time increases ($T_d > \gamma_{12}^{-1}$), the symmetry of the peak is restored because the biexciton converts to exciton and the ESAI pathway is completely canceled by the ESAII, resulting in the ESA-free spectrum.

When the biexciton contributes radiatively to the signal, the lineshape may change drastically as the T_d proceeds. A similar trend is observed for all cases in which $\Phi_2/\Phi_1 \neq 0$. In particular, at early T_d, the main contribution to the spectra is the positive off-diagonal peak originating from the biexciton. Even in the case of a relatively small biexciton QY ($\Phi_2/\Phi_1 = 0.1$), the faster relaxation rate implies that the spectrum is dominated by the biexciton contribution at early detection-time. As the T_d increases, the diagonal contribution from the exciton manifold gains amplitude and because of cancellation effects, the spectrum results in a dispersive lineshape. Due to the partial cancellation of positive and negative contributions, the maximum and the minimum do not fall at the same position as the isolated contributions, shown in Fig. 3.4, but the peaks are respectively red- and blue-shifted along the frequency axes.

In general, the details of the evolution of the overall spectral lineshape as a function of the detection-time depend on the kinetics of the populations relaxation (Eq. 3.10). In this case, we consider an idealized model where the non-radiative relaxation is characterized by a single rate. However, the kinetic scheme can be easily generalized by introducing other processes, notably hot-carrier relaxation and trapping due to surface effects, inducing more complex non-exponential behavior. Notice that a different dynamics during the detection-time implies a different combination of the exciton and biexciton contributions resulting in a different lineshape. Nonetheless, the individual contributions are defined prior to any relaxation dynamics (Sec. 3.3.1) and therefore, as long as the relaxation is slow compared to the timescale of the pulse train, they do not depend on the details of the relaxation processes.

We shall emphasize how the effects of the detection-mode and time-gating are in some sense complementary. Considering different combinations of the two parameters may produce similar results: isolating the exciton contribution (Fig. 3.6a-d,g,h,l), isolating the biexciton contribution (Fig. 3.6e,i,j,m-o) or featuring their simultaneous presence (Fig. 3.6f,k,p). The choice of the detection-mode and the use of time-gating may be used in combination to isolate specific contributions in the 2D spectra. Analogous combinations of the exciton and the biexciton signal determine the Non-Rephasing, 2Q1Q and 1Q2Q spectra, reported in the App. 3.A (Figs. 3.A.9, 3.A.10, 3.A.11).

3.3.3. Signatures of Binding Energy and Relaxation Rates

In the previous section, we discussed how the combination of the exciton and the biexciton contributions gives rise to a variety of spectral lineshapes according to the specific

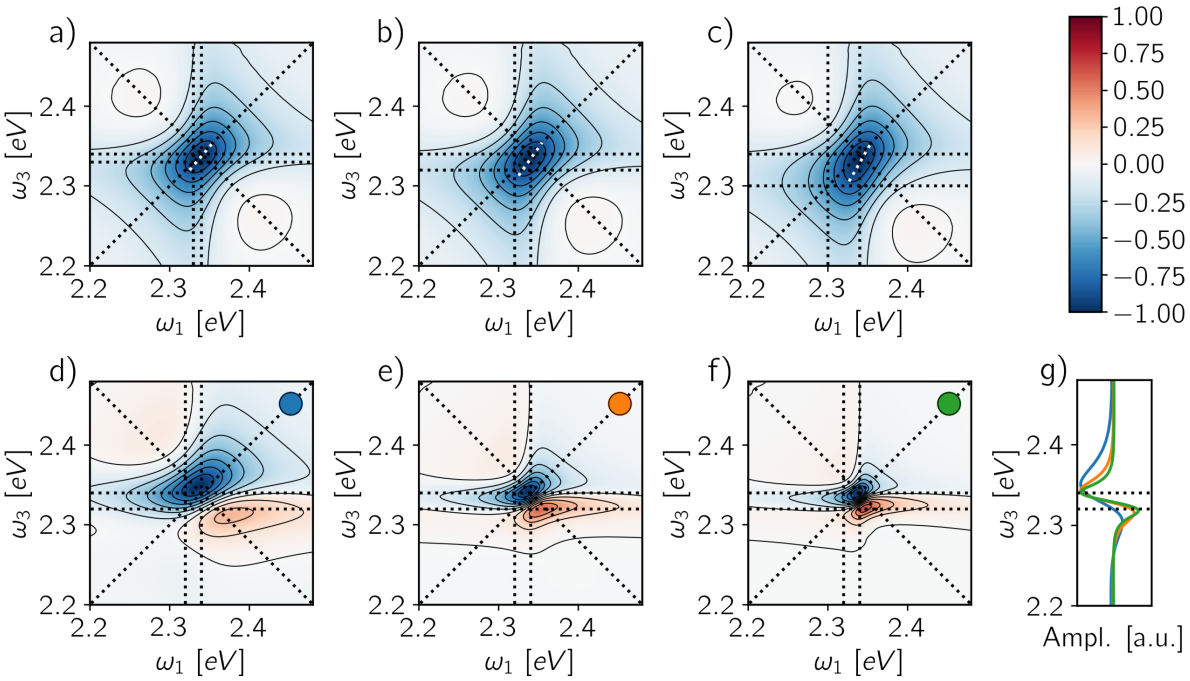

Fig. 3.7: Rephasing spectra for different biexciton binding energies a) $\Delta = 10$ meV, b) $\Delta = 20$ meV and c) $\Delta = 40$ meV for a GQY ratio $\Phi_2/\Phi_1 = 0.0$ and a detection-time of $T_d = 1$ ps. The white dotted line highlights the ellipticity of each peak. Rephasing spectra for different decoherence times d) $\gamma_{kk}^{-1} = 100$ fs, e) $\gamma_{kk}^{-1} = 200$ fs and f) $\gamma_{kk}^{-1} = 300$ fs for a GQY ratio $\Phi_2/\Phi_1 = 0.1$ and a detection-time $T_d = 100$ ps. Each spectrum is normalized with respect to its absolute maximum/minimum. g) Averaged signal along ω_1 axis for the spectra d-f), the corresponding colors are reported in the inset.

system dynamics and experimental settings, such as the detection-mode and time-gating. This diversity implies that the information about the system may be encoded in different spectral features. Now, we will focus on two parameters characterizing our simplified model of exciton and biexciton manifolds in nanocrystals, namely the biexciton binding energy and the biexciton relaxation rate, discussing their connection with spectral signatures.

The biexciton binding energy gives a direct measure of the correlation between two excitons in the QD and is defined by the difference between twice the exciton energy and the biexciton one, $\Delta = 2\epsilon_1 - \epsilon_2$. Experimentally, it can be measured using pump-probe spectroscopy, however, two-dimensional techniques offer the possibility to resolve the signal along two frequency axes and to operate at low excitation power, ideally limiting the number of overlapping processes in the signal [37, 63–67]. In 2DES experiments, the biexciton binding energy is obtained from a fitting procedure of the 2D spectra using a parameterized model. However, its quantification remains challenging and sample inhomogeneities are detrimental.

In this context, the possibility of combining A-2DES with single-molecule techniques to probe individual QD is a promising route to characterize the biexciton manifold. The biexciton binding energy can be expressed in terms of the transition frequencies probed in the A-2DES Rephasing spectra as $\Delta = \omega_{10} - \omega_{21}$. Therefore, the spectral position of the ESA feature is the key to evaluating the binding energy, either by directly considering its spectral coordinates $(\omega_{10}, \omega_{21})$ or by taking the distance of the ESA feature from the main diagonal peak located at $(\omega_{10}, \omega_{10})$ along the ω_3 axis. Notice that in the cases where the biexciton manifold does not contribute directly to the signal ($\Phi_2/\Phi_1 = 0$) and the amplitude is integrated over the detection-time, the spectrum is ESA-free and the information on the binding energy is completely lost. The only possibility to observe the effect of the biexciton is to avoid the cancellation of the ESAI pathway by employing a short time-gating window, as shown in Fig. 3.7a-c, where the spectra are obtained by integrating the signal for 1 ps after the end of the fourth pulse. Even in this case, as long as the binding energy is smaller than the peak broadening, the ESAI contribution appears as a peak-twist of the main diagonal contribution. As the value of Δ increases (Fig. 3.7a-c), the ESAI contribution is centered further apart from the diagonal, resulting in a more pronounced twist.

The situation changes when the biexciton gives a radiative contribution to the signal, as shown in Fig. 3.7d-f, where the spectra for a GQY ratio $\Phi_2/\Phi_1 = 0.1$ and a time-gating window of 100 ps are reported for three different decoherence rates. In this case, the biexciton binding energy can be evaluated directly as the distance along ω_3 between the negative and the positive spectral features. The projection of the lineshape profile along ω_3 (Fig. 3.7g) shows how such an estimation is robust against the peak-shift of the exciton and biexciton contributions due to cancellation effects, even when the broadening is large. Indeed, the peak positions are more susceptible to variations along ω_1 axis than ω_3 for different weights of exciton and biexciton contributions. Moreover, since the phase-modulation protocol provides direct access to other components of the Phase-Modulation Spectrum, the estimation of the biexciton binding energy can be checked by looking at other fourth-order signals, i.e., 1Q2Q and 2Q1Q. In these cases, the binding energy can be written in terms of one- and two-quantum transition frequencies as $\Delta = 2\omega_{10} - \omega_{20}$. Particularly convenient is the case of 1Q2Q spectra, where all the spectral contributions are centered at $(\omega_{10}, \omega_{20})$ (Fig. 3.4j,k). Therefore, in this situation, the main spectral peak allows a good estimation of the biexciton binding energy independently of the application of the time-gating.

Besides varying the contribution of the biexciton, the detection-time can be understood

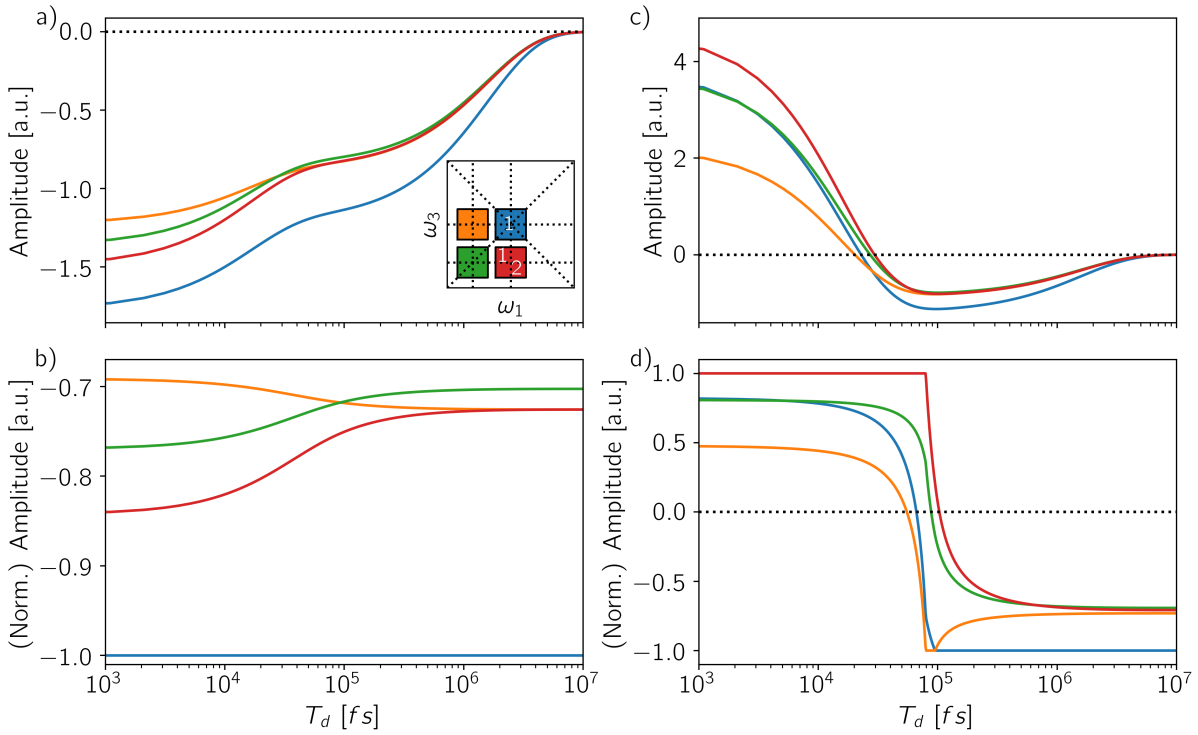

Fig. 3.8: Temporal evolution of the amplitude along the detection-time T_d for four coordinates in the spectrum (inset of a): at coordinates $(\omega_{10}, \omega_{10})$ GSB and SE from the exciton (blue), at coordinates $(\omega_{10}, \omega_{21})$ ESAI from the exciton and ESAII from the biexciton (red), while coordinates at $(\omega_{21}, \omega_{21})$ (green) and $(\omega_{10}, \omega_{21})$ (orange) represent two control positions. a) Time-resolved signal and b) (normalized) time-integrated signal for GQY ratio $\Phi_2/\Phi_1 = 0.0$. c) Time-resolved signal and d) (normalized) time-integrated signal for GQY ratio $\Phi_2/\Phi_1 = 0.1$.

as a further dimension to analyze, by monitoring how the spectral features change as a function of T_d. Indeed, by time-gating the signal, one can in principle follow the incoherent dynamics connecting different manifolds. Let us pinpoint four different spectral positions in the Rephasing spectrum to define a square (inset of Fig. 3.8a): the diagonal peak at $(\omega_{10}, \omega_{10})$ (blue square) featuring the GSB and SE from the exciton, the off-diagonal peak at $(\omega_{10}, \omega_{21})$ (red square) featuring the interplay of the two Excited-State Absorption pathways from the exciton (ESAI) and the biexciton (ESAII), and two control positions, one above the diagonal at $(\omega_{21}, \omega_{10})$ (orange square) and one on the diagonal at $(\omega_{21}, \omega_{21})$ (green square). We report the amplitude of these spectral positions as a function of the detection-time for two different GQY ratios: $\Phi_2/\Phi_1 = 0.0$ (Fig. 3.8a,b) and $\Phi_2/\Phi_1 = 0.1$ (Fig. 3.8c,d). In Fig. 3.8a,c, we follow the instantaneous evolution according to Eq. 3.5 without any integration step, while in Fig. 3.8b,d, the signal is integrated within a temporal window of increasing length (Eq. 3.6) and normalized with respect to the amplitude of the dominant peak. The instantaneous temporal profile of the spectral amplitudes directly reflects the dynamics of the populations showing two different relaxation timescales: the biexciton lifetime at $T_d \approx 10^5$ fs and the exciton relaxation at $T_d \approx 10^7$ fs. In the case of $\Phi_2/\Phi_1 = 0.0$ (Fig. 3.8a), the amplitudes are negative over the entire T_d axis and the spectrum is always dominated by the diagonal peak (blue line). Because of the normalization to the main diagonal peak, the integrated signal (Fig. 3.8b) brings to evidence only the timescale of the biexciton relaxation. The biexciton lifetime controls the dynamics of the cancellation of the ESA pathways which is reflected by the decrease in amplitude of the off-diagonal feature below the diagonal (red line) to match the amplitude of the control position above the diagonal (orange line) at $T_d \approx 10^5$ fs. For $\Phi_2/\Phi_1 = 0.1$ (Fig. 3.8c), the instantaneous amplitudes of the peaks change the sign from positive to negative along T_d. At early detection-time, the spectrum is dominated by the biexciton contribution, related to the positive off-diagonal peak due to ESAII pathway (red line) while, as the detection-time gets longer, the biexciton relaxes and the main contribution in the spectra becomes the negative diagonal peak. Such a change of the dominant spectral contribution is even more evident in the integrated and normalized spectral amplitudes (Fig. 3.8d) where the inversion of the dominant peak offers a direct estimation of the biexciton lifetime. The evolution of the spectral features for other signals, i.e., 2Q1Q and 1Q2Q, as a function of the detection-time are reported in the App. 3.A (Figs. 3.A.12, 3.A.13) and can be analyzed along the same line.

The availability of several contributions to the response representing the same relaxation dynamics in different spectral positions may be a valuable resource to resolve more

complicated multiexciton dynamics in realistic systems.

3.4. Conclusions

Multiexciton states of QDs are at the heart of nanocrystal-based technology and A-2DES is a promising technique to study their properties. In this work, we have simulated and analyzed the role of the biexciton state in the action response, discussing how it depends on the detection-mode and the time-gating of the signal. Despite the simplicity of the model system, i.e., a three-level open quantum system, a variety of spectral lineshapes can be generated as the result of the interplay between the exciton and the biexciton contributions to the total spectrum. When the biexciton provides a non-vanishing contribution to the detected signal, the 2D spectrum at early gating-time is dominated by an off-diagonal positive feature originating from the biexciton, whose position depends on the binding energy. As the gating-time increases, a dispersive lineshape results from the interplay of the exciton and biexciton signals having opposite signs. When the signal is completely integrated along the detection-time, the generated spectra depend on the ratio between the quantum yields of the biexciton and the exciton, ranging from a fully diagonal (ESA-free) to a dispersive lineshape, as determined by the detection-mode.

Amongst the other important applications, excitons in QD materials are candidate substrates for quantum technologies, including quantum computing [68, 69]. In this context, preparation and manipulation of exciton states can be achieved by optical pulses [70–73] and the collinear geometry facilitates rapid data acquisition, making A-2DES a valuable testbed for quantum information processing coupled with photocurrent readout [74]. To assist developments in this direction, numerical simulation protocols going beyond the perturbative response function are needed. In this work, we adopted the non-perturbative simulation protocol developed in ref. [43] augmented with an explicit description of the detection-time dynamics. To focus on the internal recombination process, we have assumed non-interacting units in our simulations. Another crucial issue that needs to be investigated is related to interdot coupling, since charge and exciton migration may compete with the internal dynamics, especially in the solid state [20, 29]. Moreover, strongly coupled dimers of colloidal QDs have been designed and the possibility of excitonic delocalization over the two units has been discussed, based on both theoretical and experimental evidence [50, 75–79].

3.A. Additional Figures

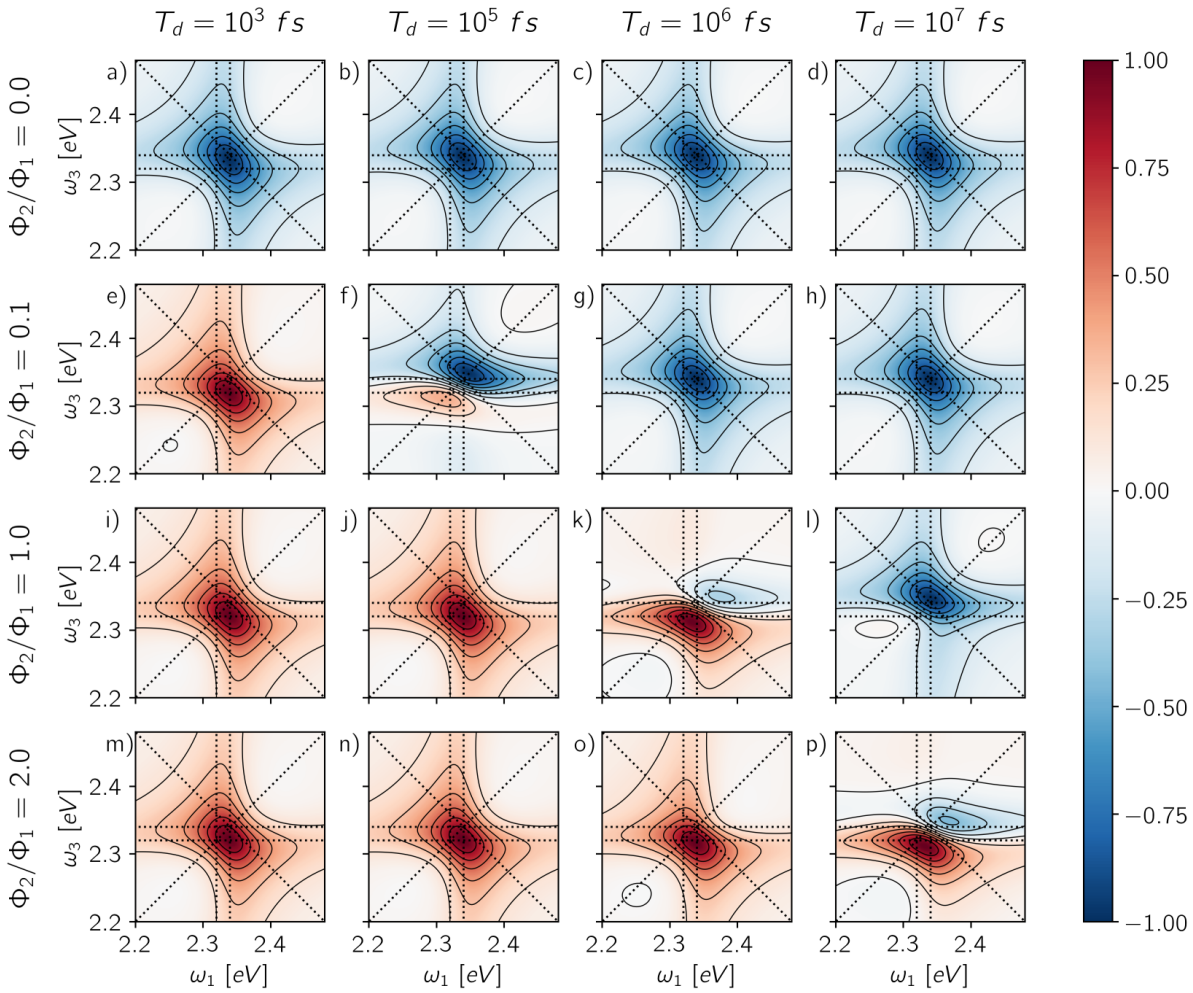

Fig. 3.A.9: Non-Rephasing spectra for different values of GQY ratio ($\Phi_2/\Phi_1 = 0.0,\ 0.1,\ 1.0,\ 2.0$) on the columns and different detection-times ($T_d = 10^3$ fs, 10^5 fs, 10^6 fs, 10^7 fs) on the rows. Each spectrum is normalized with respect to its absolute maximum/minimum.

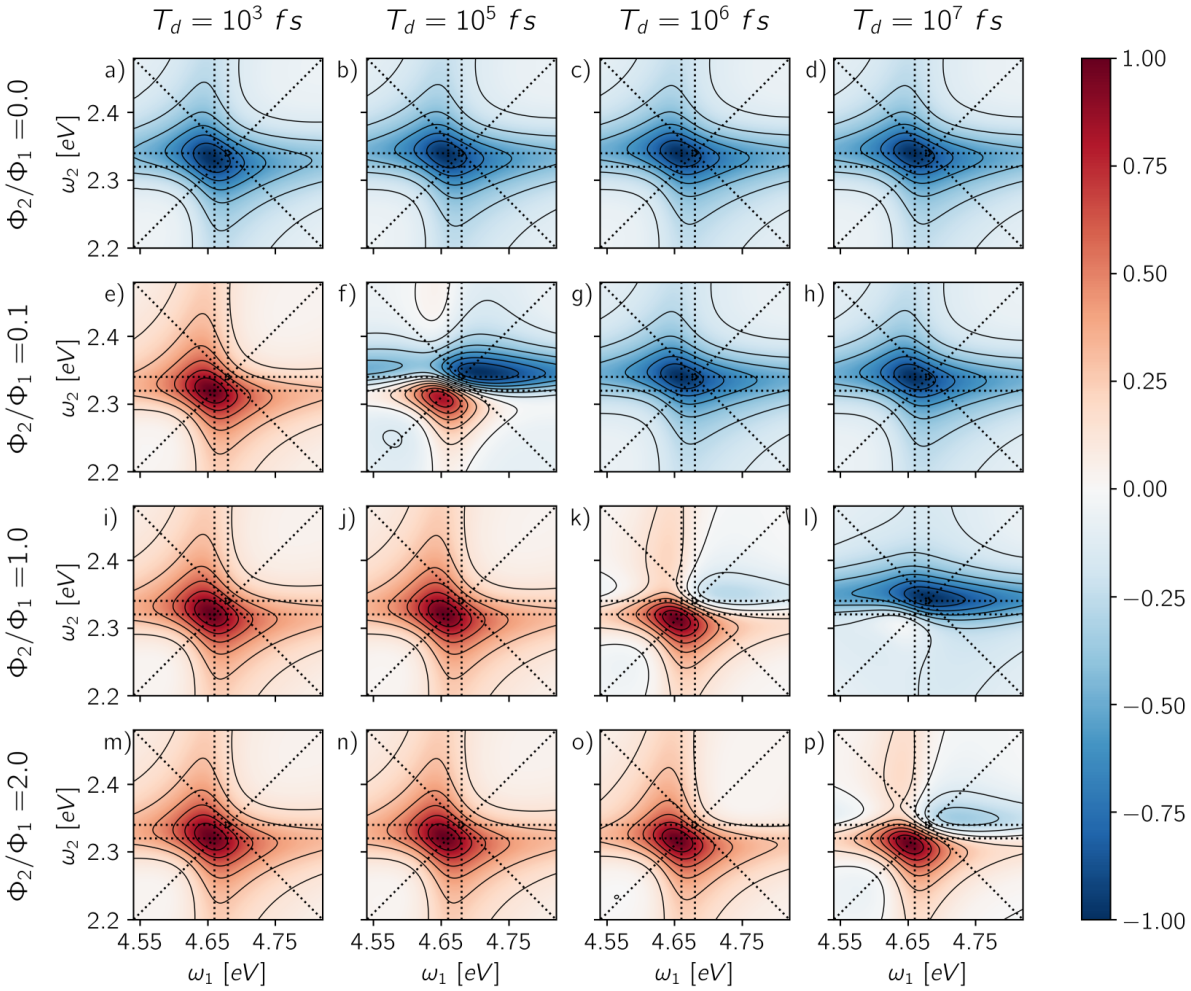

Fig. 3.A.10: 2Q1Q spectra for different values of GQY ratio ($\Phi_2/\Phi_1 = 0.0,\ 0.1,\ 1.0,\ 2.0$) on the columns and different detection-times ($T_d = 10^3$ fs, 10^5 fs, 10^6 fs, 10^7 fs) on the rows. Each spectrum is normalized with respect to its absolute maximum/minimum.

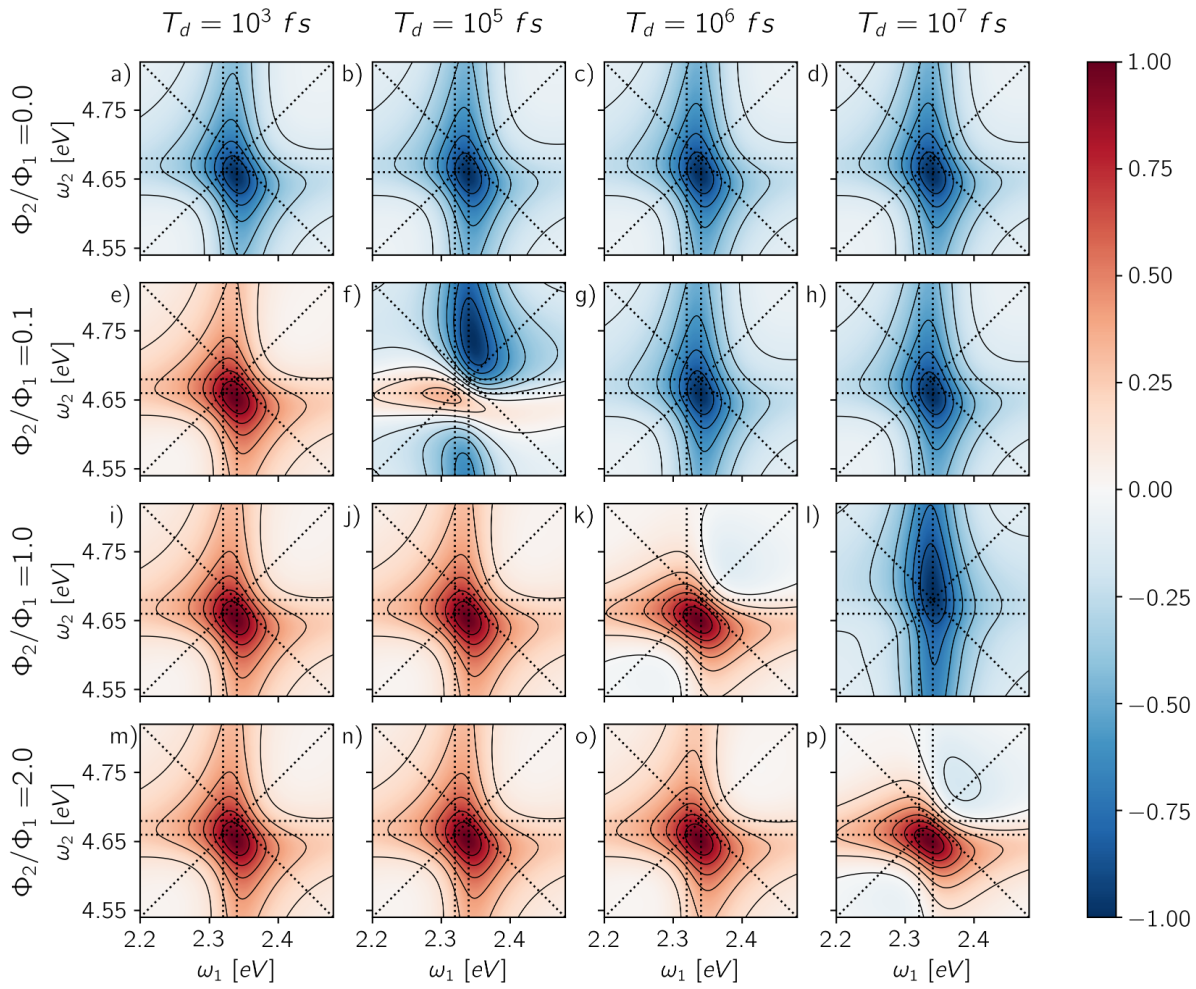

Fig. 3.A.11: 1Q2Q spectra for different values of GQY ratio ($\Phi_2/\Phi_1 = 0.0,\ 0.1,\ 1.0,\ 2.0$) on the columns and different detection-times ($T_d = 10^3$ fs, 10^5 fs, 10^6 fs, 10^7 fs) on the rows. Each spectrum is normalized with respect to its absolute maximum/minimum.

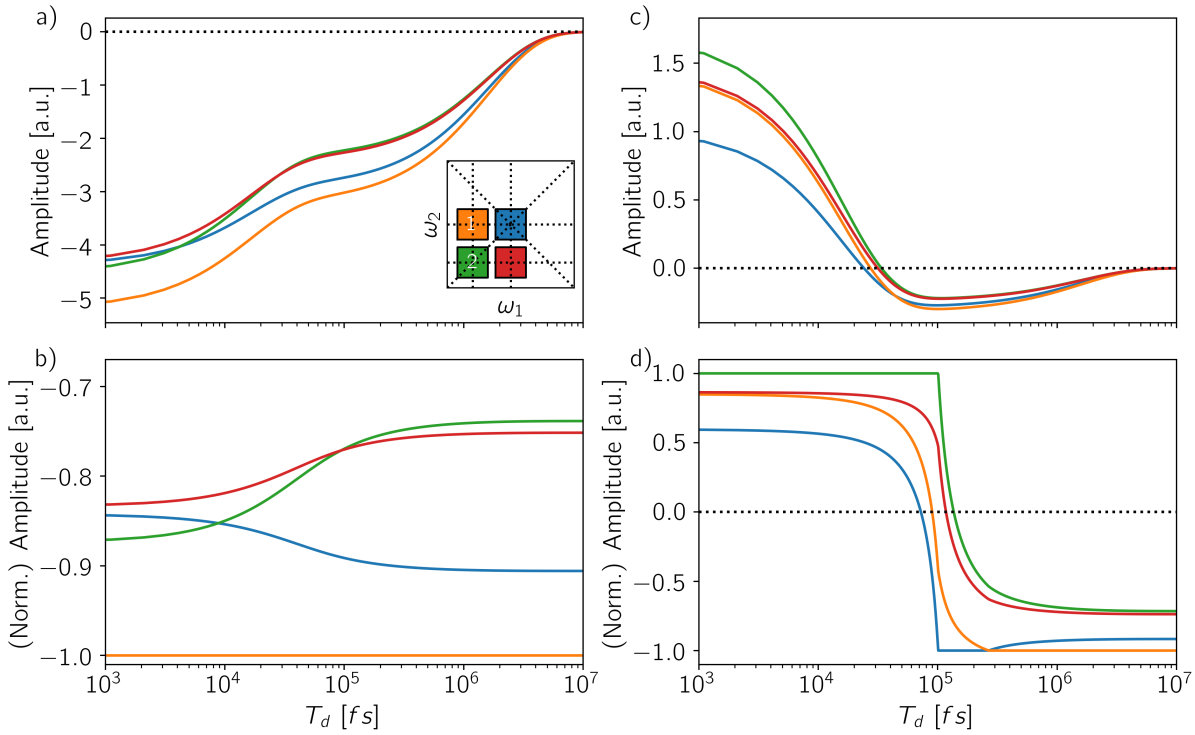

Fig. 3.A.12: Temporal evolution of the amplitude along the detection-time T_d for four coordinates in the 2Q1Q spectrum (inset of a): at coordinates $(\omega_{20}, \omega_{10})$ 2Q1QI pathway from the exciton (orange), at coordinates $(\omega_{20}, \omega_{21})$ 2Q1QII pathway from the biexciton (green), while coordinates at $(\omega_{20}+\Delta, \omega_{21})$ (red) and $(\omega_{20}+\Delta, \omega_{10})$ (blue) represent two control positions. a) Time-resolved signal and b) (normalized) time-integrated signal for GQY ratio $\Phi_2/\Phi_1 = 0.0$. c) Time-resolved signal and d) (normalized) time-integrated signal for GQY ratio $\Phi_2/\Phi_1 = 0.1$. The normalization is taken with respect to the absolute maximum/minimum of each map.

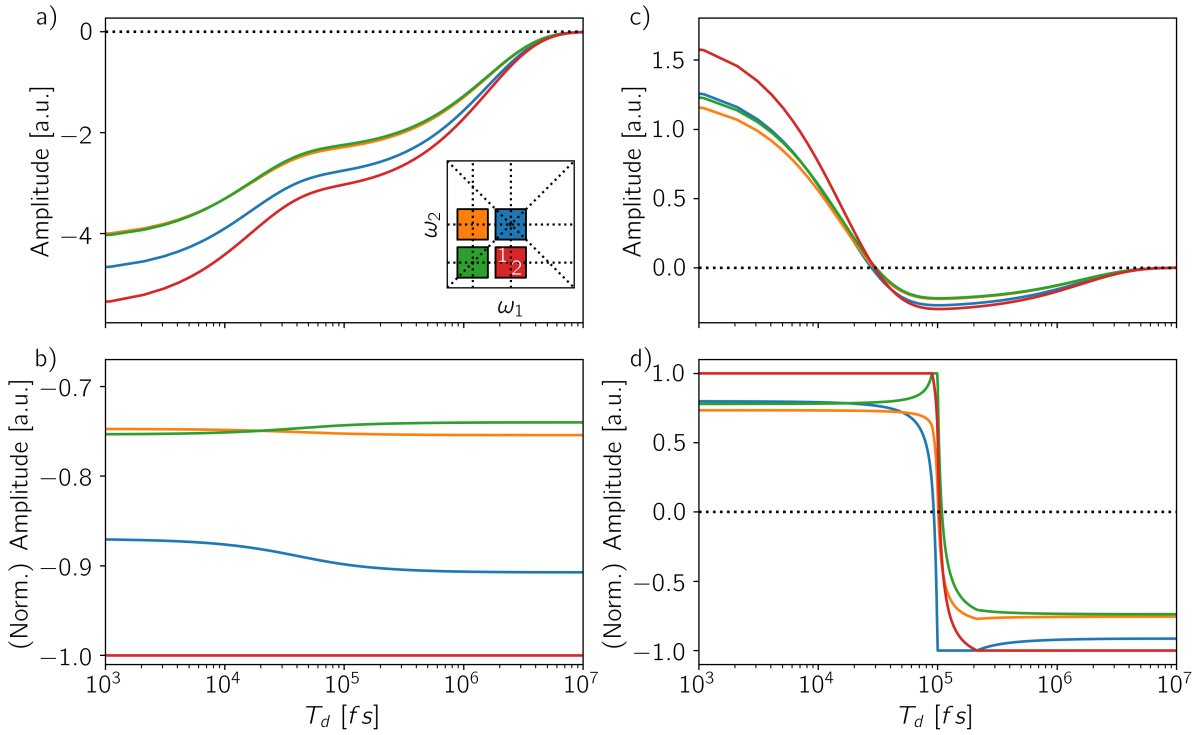

Fig. 3.A.13: Temporal evolution of the amplitude along the detection-time T_d for four coordinates in the 1Q2Q spectrum (inset of a): at coordinates $(\omega_{10}, \omega_{20})$ 1Q2QI from the exciton and 1Q2QII from the biexciton (red), while coordinates at $(\omega_{10} - \Delta, \omega_{20})$ (green), at $(\omega_{10}, \omega_{20} + \Delta)$ (blue) and at $(\omega_{10} - \Delta, \omega_{20} + \Delta)$ (orange) represent three control positions. a) Time-resolved signal and b) (normalized) time-integrated signal for GQY ratio $\Phi_2/\Phi_1 = 0.0$. c) Time-resolved signal and d) (normalized) time-integrated signal for GQY ratio $\Phi_2/\Phi_1 = 0.1$. The normalization is taken with respect to the absolute maximum/minimum of each map.

References

(1) Oliver, T. A. A. Recent Advances in Multidimensional Ultrafast Spectroscopy. *R. Soc. Open Sci.* **2018**, *5*, 171425.

(2) Karki, K. J.; Ciappina, M. F. Advances in Nonlinear Spectroscopy Using Phase Modulated Light Fields: Prospective Applications in Perturbative and Non-Perturbative Regimes. *Adv. Phys.: X* **2022**, *7*, 2090856.

(3) Tian, P.; Keusters, D.; Suzaki, Y.; Warren, W. S. Femtosecond Phase-Coherent Two-Dimensional Spectroscopy. *Science* **2003**, *300*, 1553–1555.

(4) Tekavec, P. F.; Lott, G. A.; Marcus, A. H. Fluorescence-Detected Two-Dimensional Electronic Coherence Spectroscopy by Acousto-Optic Phase Modulation. *J. Chem. Phys.* **2007**, *127*, 214307.

(5) Lott, G. A.; Perdomo-Ortiz, A.; Utterback, J. K.; Widom, J. R.; Aspuru-Guzik, A.; Marcus, A. H. Conformation of Self-Assembled Porphyrin Dimers in Liposome Vesicles by Phase-Modulation 2D Fluorescence Spectroscopy. *Proc. Natl. Acad. Sci. USA* **2011**, *108*, 16521–16526.

(6) Nardin, G.; Autry, T. M.; Silverman, K. L.; Cundiff, S. T. Multidimensional Coherent Photocurrent Spectroscopy of a Semiconductor Nanostructure. *Opt. Express* **2013**, *21*, 28617–28627.

(7) Karki, K. J.; Widom, J. R.; Seibt, J.; Moody, I.; Lonergan, M. C.; Pullerits, T.; Marcus, A. H. Coherent Two-Dimensional Photocurrent Spectroscopy in a PbS Quantum Dot Photocell. *Nat. Commun.* **2014**, *5*, 1–7.

(8) Roeding, S.; Brixner, T. Coherent Two-Dimensional Electronic Mass Spectrometry. *Nat. Commun.* **2018**, *9*, 2519.

(9) Uhl, D.; Bangert, U.; Bruder, L.; Stienkemeier, F. Coherent Optical 2D Photoelectron Spectroscopy. *Optica* **2021**, *8*, 1316–1324.

(10) Bakulin, A. A.; Silva, C.; Vella, E. Ultrafast Spectroscopy with Photocurrent Detection: Watching Excitonic Optoelectronic Systems at Work. *J. Phys. Chem. Lett.* **2016**, *7*, 250–258.

(11) Aeschlimann, M.; Brixner, T.; Fischer, A.; Kramer, C.; Melchior, P.; Pfeiffer, W.; Schneider, C.; Strüber, C.; Tuchscherer, P.; Voronine, D. V. Coherent Two-Dimensional Nanoscopy. *Science* **2011**, *333*, 1723–1726.

(12) Tiwari, V.; Matutes, Y. A.; Gardiner, A. T.; Jansen, T. L. C.; Cogdell, R. J.; Ogilvie, J. P. Spatially-Resolved Fluorescence-Detected Two-Dimensional Electronic Spectroscopy Probes Varying Excitonic Structure in Photosynthetic Bacteria. *Nat. Commun.* **2018**, *9*, 4219.

(13) Tiwari, V. Multidimensional Electronic Spectroscopy in High-Definition - Combining Spectral, Temporal, and Spatial Resolutions. *J. Chem. Phys.* **2021**, *154*, 230901.

(14) Gattuso, H.; Fresch, B.; Levine, R. D.; Remacle, F. Coherent Exciton Dynamics in Ensembles of Size-Dispersed CdSe Quantum Dot Dimers Probed via Ultrafast Spectroscopy: A Quantum Computational Study. *Appl. Sci.* **2020**, *10*.

(15) Bruder, L.; Binz, M.; Stienkemeier, F. Efficient Isolation of Multiphoton Processes and Detection of Collective Resonances in Dilute Samples. *Phys. Rev. A* **2015**, *92*, 053412.

(16) Bruder, L.; Eisfeld, A.; Bangert, U.; Binz, M.; Jakob, M.; Uhl, D.; Schulz-Weiling, M.; Grant, E. R.; Stienkemeier, F. Delocalized Excitons and Interaction Effects in Extremely Dilute Thermal Ensembles. *Phys. Chem. Chem. Phys.* **2019**, *21*, 2276–2282.

(17) Malý, P.; Lüttig, J.; Mueller, S.; Schreck, M. H.; Lambert, C.; Brixner, T. Coherently and Fluorescence-Detected Two-Dimensional Electronic Spectroscopy: Direct Comparison on Squaraine Dimers. *Phys. Chem. Chem. Phys.* **2020**, *22*, 21222–21237.

(18) Tiwari, V.; Matutes, Y. A.; Konar, A.; Yu, Z.; Ptaszek, M.; Bocian, D. F.; Holten, D.; Kirmaier, C.; Ogilvie, J. P. Strongly Coupled Bacteriochlorin Dyad Studied using Phase-Modulated Fluorescence-Detected Two-Dimensional Electronic Spectroscopy. *Opt. Express* **2018**, *26*, 22327–22341.

(19) Gutiérrez-Meza, E.; Malatesta, R.; Li, H.; Bargigia, I.; Kandada, A. R. S.; Valverde-Chávez, D. A.; Kim, S.-M.; Li, H.; Stingelin, N.; Tretiak, S.; Bittner, E. R.; Silva-Acuña, C. Frenkel Biexcitons in Hybrid HJ Photophysical Aggregates. *Sci. Adv.* **2021**, *7*, eabi5197.

(20) Karki, K. J.; Chen, J.; Sakurai, A.; Shi, Q.; Gardiner, A. T.; Kühn, O.; Cogdell, R. J.; Pullerits, T. Before Förster. Initial Excitation in Photosynthetic Light Harvesting. *Chem. Sci.* **2019**, *10*, 7923–7928.

(21) Aeschlimann, M.; Brixner, T.; Cinchetti, M.; Feidt, M.; Haag, N.; Hensen, M.; Huber, B.; Kenneweg, T.; Kollamana, J.; Kramer, C.; Pfeiffer, W.; Ponzoni, S.; Stadtmüller, B.; Thielen, P. Observation of Optical Coherence in a Disordered Metal-Molecule Interface by Coherent Optical Two-Dimensional Photoelectron Spectroscopy. *Phys. Rev. B* **2022**, *105*, 205415.

(22) Bian, Q.; Ma, F.; Chen, S.; Wei, Q.; Su, X.; Buyanova, I. A.; Chen, W. M.; Ponseca, C. S.; Linares, M.; Karki, K. J.; Yartsev, A.; Inganäs, O. Vibronic Coherence Contributes to Photocurrent Generation in Organic Semiconductor Heterojunction Diodes. *Nat. Commun.* **2020**, *11*, 617.

(23) Bolzonello, L.; Bernal-Texca, F.; Gerling, L. G.; Ockova, J.; Collini, E.; Martorell, J.; van Hulst, N. F. Photocurrent-Detected 2D Electronic Spectroscopy Reveals Ultrafast Hole Transfer in Operating PM6/Y6 Organic Solar Cells. *J. Phys. Chem. Lett.* **2021**, *12*, 3983–3988.

(24) Zhou, N.; Ouyang, Z.; Hu, J.; Williams, O. F.; Yan, L.; You, W.; Moran, A. M. Distinguishing Energy- and Charge-Transfer Processes in Layered Perovskite Quantum Wells with Two-Dimensional Action Spectroscopies. *J. Phys. Chem. Lett.* **2020**, *11*, 4570–4577.

(25) Mueller, S.; Lüttig, J.; Brenneis, L.; Oron, D.; Brixner, T. Observing Multiexciton Correlations in Colloidal Semiconductor Quantum Dots via Multiple-Quantum Two-Dimensional Fluorescence Spectroscopy. *ACS Nano* **2021**, *15*, 4647–4657.

(26) Jansen, T. L. C. Computational Spectroscopy of Complex Systems. *J. Chem. Phys.* **2021**, *155*, 170901.

(27) Perdomo-Ortiz, A.; Widom, J. R.; Lott, G. A.; Aspuru-Guzik, A.; Marcus, A. H. Conformation and Electronic Population Transfer in Membrane-Supported Self-Assembled Porphyrin Dimers by 2D Fluorescence Spectroscopy. *J. Phys. Chem. B* **2012**, *116*, 10757–10770.

(28) Mukamel, S. Communication: The Origin of Many-Particle Signals in Nonlinear Optical Spectroscopy of Non-Interacting Particles. *J. Chem. Phys.* **2016**, *145*, 041102.

(29) Grégoire, P.; Srimath Kandada, A. R.; Vella, E.; Tao, C.; Leonelli, R.; Silva, C. Incoherent Population Mixing Contributions to Phase-Modulation Two-Dimensional Coherent Excitation Spectra. *J. Chem. Phys.* **2017**, *147*, 114201.

(30) Malý, P.; Mancal, T. Signatures of Exciton Delocalization and Exciton–Exciton Annihilation in Fluorescence-Detected Two-Dimensional Coherent Spectroscopy. *J. Phys. Chem. Lett.* **2018**, *9*, 5654–5659.

(31) Schröter, M.; Pullerits, T.; Kühn, O. Using Fluorescence Detected Two-Dimensional Spectroscopy to Investigate Initial Exciton Delocalization between Coupled Chromophores. *J. Chem. Phys.* **2018**, *149*, 114107.

(32) Kunsel, T.; Tiwari, V.; Matutes, Y. A.; Gardiner, A. T.; Cogdell, R. J.; Ogilvie, J. P.; Jansen, T. L. C. Simulating Fluorescence-Detected Two-Dimensional Electronic Spectroscopy of Multichromophoric Systems. *J. Phys. Chem. B* **2019**, *123*, 394–406.

(33) Kalaee, A. A. S.; Damtie, F.; Karki, K. J. Differentiation of True Nonlinear and Incoherent Mixing of Linear Signals in Action-Detected 2D Spectroscopy. *J. Phys. Chem. A* **2019**, *123*, 4119–4124.

(34) Kühn, O.; Mancal, T.; Pullerits, T. Interpreting Fluorescence Detected Two-Dimensional Electronic Spectroscopy. *J. Phys. Chem. Lett.* **2020**, *11*, 838–842.

(35) Chen, Q.; Kwok, Y. H.; Zhou, W.; Chen, G.; Mukamel, S. Time-Dependent Simulation of Photocurrent-Detected Two-Dimensional Spectroscopy of Open Systems. *J. Chem. Phys.* **2021**, *155*, 194113.

(36) Wong, C. Y.; Scholes, G. D. Using Two-Dimensional Photon Echo Spectroscopy to Probe the Fine Structure of the Ground State Biexciton of CdSe Nanocrystals. *J. Lumin.* **2011**, *131*, 366–374.

(37) Caram, J. R.; Zheng, H.; Dahlberg, P. D.; Rolczynski, B. S.; Griffin, G. B.; Dolzhnikov, D. S.; Talapin, D. V.; Engel, G. S. Exploring Size and State Dynamics in CdSe Quantum Dots using Two-Dimensional Electronic Spectroscopy. *J. Chem. Phys.* **2014**, *140*, 084701.

(38) Klimov, V. I.; Mikhailovsky, A. A.; McBranch, D. W.; Leatherdale, C. A.; Bawendi, M. G. Quantization of Multiparticle Auger Rates in Semiconductor Quantum Dots. *Science* **2000**, *287*, 1011–1013.

(39) Zhao, J.; Chen, O.; Strasfeld, D. B.; Bawendi, M. G. Biexciton Quantum Yield Heterogeneities in Single CdSe (CdS) Core (Shell) Nanocrystals and Its Correlation to Exciton Blinking. *Nano Lett.* **2012**, *12*, 4477–4483.

(40) Lubin, G.; Tenne, R.; Ulku, A. C.; Antolovic, I. M.; Burri, S.; Karg, S.; Yallapragada, V. J.; Bruschini, C.; Charbon, E.; Oron, D. Heralded Spectroscopy Reveals Exciton–Exciton Correlations in Single Colloidal Quantum Dots. *Nano Lett.* **2021**, *21*, 6756–6763.

(41) Huang, J.; Huang, Z.; Yang, Y.; Zhu, H.; Lian, T. Multiple Exciton Dissociation in CdSe Quantum Dots by Ultrafast Electron Transfer to Adsorbed Methylene Blue. *J. Am. Chem. Soc.* **2010**, *132*, 4858–4864.

(42) Lian, S.; Christensen, J. A.; Kodaimati, M. S.; Rogers, C. R.; Wasielewski, M. R.; Weiss, E. A. Oxidation of a Molecule by the Biexcitonic State of a CdS Quantum Dot. *J. Phys. Chem. C* **2019**, *123*, 5923–5930.

(43) Damtie, F. A.; Wacker, A.; Pullerits, T.; Karki, K. J. Two-Dimensional Action Spectroscopy of Excitonic Systems: Explicit Simulation Using a Phase-Modulation Technique. *Phys. Rev. A* **2017**, *96*, 053830.

(44) Anda, A.; Cole, J. H. Two-Dimensional Spectroscopy Beyond the Perturbative Limit: The Influence of Finite Pulses and Detection Modes. *J. Chem. Phys.* **2021**, *154*, 114113.

(45) Mukamel, S., *Principles of Nonlinear Optical Spectroscopy*; Oxford University Press: Oxford, 1995.

(46) Hamm, P.; Zanni, M., *Concepts and Methods of 2D Infrared Spectroscopy*; Cambridge University Press: 2011.

(47) Klimov, V. I. Spectral and Dynamical Properties of Multiexcitons in Semiconductor Nanocrystals. *Annu. Rev. Phys. Chem.* **2007**, *58*, 635–673.

(48) Palato, S.; Seiler, H.; Baker, H.; Sonnichsen, C.; Brosseau, P.; Kambhampati, P. Investigating the Electronic Structure of Confined Multiexcitons with Nonlinear Spectroscopies. *J. Chem. Phys.* **2020**, *152*, 104710.

(49) Kambhampati, P. Unraveling the Structure and Dynamics of Excitons in Semiconductor Quantum Dots. *Acc. Chem. Res.* **2011**, *44*, 1–13.

(50) Collini, E.; Gattuso, H.; Kolodny, Y.; Bolzonello, L.; Volpato, A.; Fridman, H. T.; Yochelis, S.; Mor, M.; Dehnel, J.; Lifshitz, E.; Paltiel, Y.; Levine, R. D.; Remacle, F. Room-Temperature Inter-Dot Coherent Dynamics in Multilayer Quantum Dot Materials. *J. Phys. Chem. C* **2020**, *124*, 16222–16231.

(51) Mueller, S.; Draeger, S.; Ma, X.; Hensen, M.; Kenneweg, T.; Pfeiffer, W.; Brixner, T. Fluorescence-Detected Two-Quantum and One-Quantum-Two-Quantum 2D Electronic Spectroscopy. *J. Phys. Chem. Lett.* **2018**, *9*, 1964–1969.

(52) Mancal, T.; Pisliakov, A. V.; Fleming, G. R. Two-Dimensional Optical Three-Pulse Photon Echo Spectroscopy. I. Nonperturbative Approach to the Calculation of Spectra. *J. Chem. Phys.* **2006**, *124*, 234504.

(53) Brüggemann, B.; Kjellberg, P.; Pullerits, T. Non-Perturbative Calculation of 2D Spectra in Heterogeneous Systems: Exciton Relaxation in the FMO Complex. *Chem. Phys. Lett.* **2007**, *444*, 192–196.

(54) Lindblad, G. On the Generators of Quantum Dynamical Semigroups. *Commun. Math. Phys.* **1976**, *48*, 119–130.

(55) Gorini, V.; Kossakowski, A.; Sudarshan, E. C. G. Completely Positive Dynamical Semigroups of N-Level Systems. *J. Math. Phys.* **1976**, *17*, 821–825.

(56) Mueller, S.; Brixner, T. Molecular Coherent Three-Quantum Two-Dimensional Fluorescence Spectroscopy. *J. Phys. Chem. Lett.* **2020**, *11*, 5139–5147.

(57) García-Santamaría, F.; Chen, Y.; Vela, J.; Schaller, R. D.; Hollingsworth, J. A.; Klimov, V. I. Suppressed Auger Recombination in "Giant" Nanocrystals Boosts Optical Gain Performance. *Nano Lett.* **2009**, *9*, 3482–3488.

(58) Park, Y.-S.; Malko, A. V.; Vela, J.; Chen, Y.; Ghosh, Y.; García-Santamaría, F.; Hollingsworth, J. A.; Klimov, V. I.; Htoon, H. Near-Unity Quantum Yields of Biexciton Emission from CdSe/CdS Nanocrystals Measured Using Single-Particle Spectroscopy. *Phys. Rev. Lett.* **2011**, *106*, 187401.

(59) Yang, H.; Zhang, L.; Tang, Y.; Xiang, W.; Wang, X.; Xiao, M.; Cui, Y.; Zhang, J. Enhanced Multiexciton Emission Property in Gradient Alloy Core/Shell CdZnSeS/ZnS Quantum Dots: Balance between Surface Passivation and Strain-Induced Lattice Defect. *J. Phys. Chem. C* **2021**, *125*, 10759–10767.

(60) Algar, W. R.; Wegner, D.; Huston, A. L.; Blanco-Canosa, J. B.; Stewart, M. H.; Armstrong, A.; Dawson, P. E.; Hildebrandt, N.; Medintz, I. L. Quantum Dots as Simultaneous Acceptors and Donors in Time-Gated Förster Resonance Energy Transfer Relays: Characterization and Biosensing. *J. Am. Chem. Soc.* **2012**, *134*, 1876–1891.

(61) Zhao, T.; Beckwith, J. S.; Amin, M. J.; Pálmai, M.; Snee, P. T.; Tien, M.; Yang, H. Leveraging Lifetime Information to Perform Real-Time 3D Single-Particle Tracking in Noisy Environments. *J. Chem. Phys.* **2021**, *155*, 164201.

(62) Gao, J.; Kidon, L.; Rabani, E.; Alivisatos, A. P. Ultrahigh Hot Carrier Transient Photocurrent in Nanocrystal Arrays by Auger Recombination. *Nano Lett.* **2019**, *19*, 4804–4810.

(63) Turner, D. B.; Hassan, Y.; Scholes, G. D. Exciton Superposition States in CdSe Nanocrystals Measured Using Broadband Two-Dimensional Electronic Spectroscopy. *Nano Lett.* **2012**, *12*, 880–886.

(64) Gellen, T. A.; Lem, J.; Turner, D. B. Probing Homogeneous Line Broadening in CdSe Nanocrystals Using Multidimensional Electronic Spectroscopy. *Nano Lett.* **2017**, *17*, 2809–2815.

(65) Righetto, M.; Bolzonello, L.; Volpato, A.; Amoruso, G.; Panniello, A.; Fanizza, E.; Striccoli, M.; Collini, E. Deciphering Hot- and Multi-Exciton Dynamics in Core–Shell QDs by 2D Electronic Spectroscopies. *Phys. Chem. Chem. Phys.* **2018**, *20*, 18176–18183.

(66) Seiler, H.; Palato, S.; Kambhampati, P. Investigating Exciton Structure and Dynamics in Colloidal CdSe Quantum Dots with Two-Dimensional Electronic Spectroscopy. *J. Chem. Phys.* **2018**, *149*, 074702.

(67) Seiler, H.; Palato, S.; Sonnichsen, C.; Baker, H.; Kambhampati, P. Seeing Multiexcitons through Sample Inhomogeneity: Band-Edge Biexciton Structure in CdSe Nanocrystals Revealed by Two-Dimensional Electronic Spectroscopy. *Nano Lett.* **2018**, *18*, 2999–3006.

(68) Komarova, K.; Gattuso, H.; Levine, R. D.; Remacle, F. Quantum Device Emulates the Dynamics of Two Coupled Oscillators. *J. Phys. Chem. Lett.* **2020**, *11*, 6990–6995.

(69) Harankahage, D.; Cassidy, J.; Yang, M.; Porotnikov, D.; Williams, M.; Kholmicheva, N.; Zamkov, M. Quantum Computing with Exciton Qubits in Colloidal Semiconductor Nanocrystals. *J. Phys. Chem. C* **2021**, *125*, 22195–22203.

(70) Spiller, T. P.; D'Amico, I.; Lovett, B. W. Entanglement Distribution for a Practical Quantum-Dot-based Quantum Processor architecture. *New J. Phys.* **2007**, *9*, 20.

(71) Fresch, B.; Cipolloni, M.; Yan, T.-M.; Collini, E.; Levine, R. D.; Remacle, F. Parallel and Multivalued Logic by the Two-Dimensional Photon-Echo Response of a Rhodamine–DNA Complex. *J. Phys. Chem. Lett.* **2015**, *6*, 1714–1718.

(72) Smponias, A.; Stefanatos, D.; Paspalakis, E. Efficient Biexciton Preparation in a Quantum Dot—Metal Nanoparticle System Using On-Off Pulses. *Nanomater.* **2021**, *11*, 1859.

(73) Paspalakis, E.; Smponias, A.; Stefanatos, D. Coherent Preparation of the Biexciton State in a Semiconductor Quantum Dot Coupled to a Metallic Nanoparticle. *J. Appl. Phys.* **2021**, *129*, 223104.

(74) Collini, E. 2D Electronic Spectroscopic Techniques for Quantum Technology Applications. *J. Phys. Chem. C* **2021**, *125*, 13096–13108.

(75) Coden, M.; De Checchi, P.; Fresch, B. Spectral Shift, Electronic Coupling and Exciton Delocalization in Nanocrystal Dimers: Insights from All-Atom Electronic Structure Computations. *Nanoscale* **2020**, *12*, 18124–18136.

(76) Cui, J.; Panfil, Y. E.; Koley, S.; Shamalia, D.; Waiskopf, N.; Remennik, S.; Popov, I.; Oded, M.; Banin, U. Colloidal Quantum Dot Molecules Manifesting Quantum Coupling at Room Temperature. *Nat. Commun.* **2019**, *10*, 5401.

(77) Dibenedetto, C. N.; Fanizza, E.; Brescia, R.; Kolodny, Y.; Remennik, S.; Panniello, A.; Depalo, N.; Yochelis, S.; Comparelli, R.; Agostiano, A.; Curri, M. L.; Paltiel, Y.; Striccoli, M. Coupling Effects in QD Dimers at Sub-Nanometer Interparticle Distance. *Nano Res.* **2020**, *13*, 1071–1080.

(78) Dibenedetto, C. N.; Fanizza, E.; De Caro, L.; Brescia, R.; Panniello, A.; Tommasi, R.; Ingrosso, C.; Giannini, C.; Agostiano, A.; Curri, M. L.; Striccoli, M. Coupling in Quantum Dot Molecular Hetero-Assemblies. *Mater. Res. Bull.* **2022**, *146*, 111578.

(79) Koley, S.; Cui, J.; Panfil, Y. E.; Ossia, Y.; Levi, A.; Scharf, E.; Verbitsky, L.; Banin, U. Photon Correlations in Colloidal Quantum Dot Molecules Controlled by the Neck Barrier. *Matter* **2022**.

4 | Unifying Non-Linear Response and Incoherent Mixing in A-2DES

4.1. Introduction

The non-linear optical response triggered by ultrafast laser pulses is the result of a multitude of dynamical processes whose spectral signatures depend specifically on the adopted spectroscopic method. In this context, Two-Dimensional Electronic Spectroscopy (2DES) is the preferred technique to disentangle exciton dynamics of complex systems in both frequency and time domains [1]. The most prominent version, known as Coherent-2DES (C-2DES), relies on the detection of a coherent signal, emitted along a specific phase-matching direction, upon the interaction with three non-collinear laser pulses [2, 3].

Recently, the technique has been developed to combine the potentialities of 2DES with action-detection schemes [4, 5]. In Action-2DES (A-2DES), the interaction with a train of four collinear laser pulses prepares the system into an excited-state population which generates an incoherent signal during a long temporal window called the detection-time. Due to the collinearity of the setup, the signal contains contributions from various orders in the light-matter interaction. To separate these contributions, the phases of the laser pulses are manipulated through either phase-cycling [6, 7] or phase-modulation [8] schemes. Depending on the nature of the incoherent signal, different detection schemes have been implemented based on measuring fluorescence [9–11], photocurrent [12–14], photoions [15] and photoelectrons [16], paving the way for studying systems in *operando* conditions [17, 18]. Furthermore, the combination of A-2DES with microscopy [19] and single-molecule [20, 21] techniques allows to go beyond the diffraction-limit, thus circumventing the effects of inhomogeneous disorder.

Although probing the same ultrafast dynamics, action-detected spectra exhibit significant differences compared to those obtained through coherent-detection. In fact, it was

Adapted from Bruschi, M.; Bolzonello, L.; Gallina, F.; Fresch, B. *J. Phys. Chem. Lett.* **2023**, *14*, 6872–6879.

early recognized that spectral features in A-2DES are determined not only by the coherent dynamics induced by the light-matter interaction but also by the dynamical processes taking place during the detection-time [22]. Contrary to C-2DES [23, 24], the presence of cross peaks at early waiting-times does not represent a univocal signature of excitonic delocalization in A-2DES [10, 25], having been reported even in the case of weakly interacting systems [11, 19]. By analyzing the different contributions to the response function for a molecular dimer, Malý and Mančal demonstrated that cross peaks can emerge from the incomplete cancellation of different pathways as a consequence of exciton-exciton annihilation during the detection-time [26]. Following the same line, several other contributions highlighted the importance of two-exciton manifold dynamics in determining spectral features [27–30].

On the other hand, Grégoire et al. brought to the attention the phenomenon of incoherent mixing as an unwanted contribution in A-2DES spectra [31]. Incoherent mixing occurs from the combination of linear signals due to non-linear population dynamics [31], e.g., exciton-exciton annihilation, bimolecular recombination, and Auger recombination, or due to non-linearities in the detection process [32]. Since incoherent mixing can hide spectral features of the coherent non-linear response, efforts have been devoted to distinguishing these two contributions. In a theoretical analysis of the action signal, Kalaee et al. proposed the existence of a precise phase relationship between the “true” non-linear response and incoherent mixing signals, which can be used to differentiate them [33].

The appearance of cross peaks at early waiting-times and the phenomenon of incoherent mixing have always been considered independently in the literature about A-2DES. The aim of this work is to propose a unifying picture of these two aspects by demonstrating that, beyond sharing a common origin, they actually represent two different views of the same dynamical process when considering a system composed of weakly interacting units.

After a brief presentation of the A-2DES technique, we discuss in detail the case of a pair of chromophores, although the analysis can easily be generalized to more complex interaction networks. To this end, we use one- and two-particle representations [29, 34] as interpretative tools, where the term “particle" refers to a chromophore in our model. By employing Feynman Diagrams (FDs), the optical response of the chromophoric pair is rationalized using both representations, thereby elucidating the pathways followed by the system during coherent excitation. Since the contribution of the pathways to the total spectrum also depends on the processes occurring during the detection-time, we formulate the dynamics in terms of kinetic schemes for one- and two-particle populations.

Interestingly, the resulting signal from one-particle populations evidences the net contribution of incoherent mixing stemming from a set of Feynman diagrams where the two pairs of pulses interact with different chromophores. Therefore, we demonstrate how the presence of cross peaks at early waiting-times in A-2DES of weakly interacting systems can be interpreted either as arising from the imperfect cancellation of Feynman pathways (two-particle perspective) or from incoherent mixing (one-particle perspective), as a result of detection-time dynamics. The contribution of the dynamics-induced non-linearities to the spectrum depends on the specific kinetics of the energy redistribution during the detection-time. This implies, on the one hand, that the phase of the incoherent mixing signal is not *a priori* different from that of the non-linear response and, on the other hand, that the study of incoherent mixing spectral features is informative of dynamical processes in weakly interacting systems. Furthermore, the analysis of the action signal in terms of one-particle observables provides an advantageous computational scheme to simulate the effects of the detection-time dynamics in the A-2DES spectra of weakly interacting systems, by solving a set of dynamical equations scaling linearly with the number of chromophores.

4.2. Results and Discussion

In A-2DES, the system interacts with a train of four collinear laser pulses, separated by delay-times T_1, T_2 and T_3, resulting in the emission of an incoherent signal $\mathcal{S}(T_d)$ during the detection-time T_d (Fig. 4.1a). Typically, signal emission in A-2DES is not time-resolved and the experimentally accessible observable is represented by the time-integrated signal along the detection-time T_d:

$$\overline{\mathcal{S}} = \int_0^\infty dT_d \; \mathcal{S}(T_d). \tag{4.1}$$

By adopting a phase-modulation scheme [8], the phase of the i-th pulse is linearly modulated, from one train to the following, as $\Phi(\Omega_i) = 2\pi\Omega_i mT$, where Ω_i is the modulation frequency, m is the repetition index of the train, and T is the inter-train delay-time. As a consequence, the incoherent signal itself is modulated and it can be decomposed as:

$$\mathcal{S}(mT) = \sum_{\Omega_S} \mathcal{S}(\Omega_S)\, e^{i\Phi(\Omega_S)} \tag{4.2}$$

where $\mathcal{S}(\Omega_S)$ is the component of the signal modulated at the linear combination of frequencies $\Omega_S = \sum_i \ell_i^S \Omega_i$, where $\ell_i^S = 0, \pm 1, \pm 2$, etc. By taking the Fourier transform along mT, the different components of the optical response can be extracted, i.e., rephas-

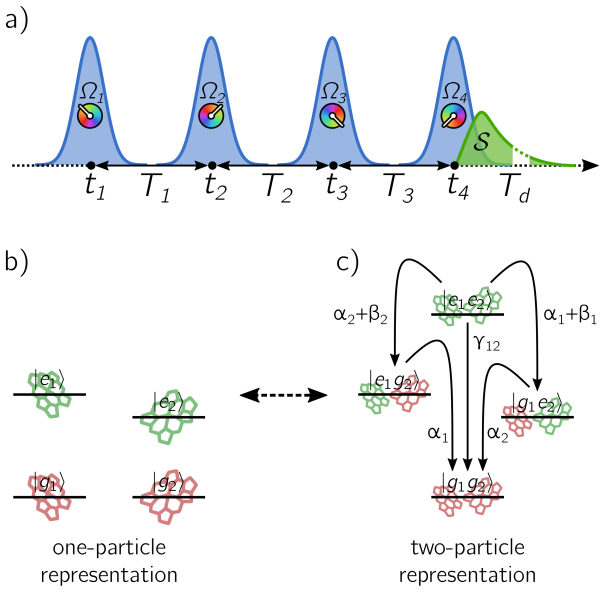

Fig. 4.1: a) Train of four collinear laser pulses, separated by delay-times T_1, T_2 and T_3, whose phases are modulated at frequencies Ω_i, for $i = 1, \ldots, 4$. As a result of the light-matter interaction, the system emits an incoherent signal $\mathcal{S}$ during the detection-time T_d. States of a weakly interacting pair of chromophores in the b) one- and c) two-particle representations, along with the kinetic scheme for populations: α_n is the rate of exciton recombination, while β_n and γ_{12} are the rates of exciton-exciton annihilation of one and two excitons, respectively.

ing ($\Omega_R = -\Omega_1 + \Omega_2 + \Omega_3 - \Omega_4$), non-rephasing ($\Omega_{NR} = +\Omega_1 - \Omega_2 + \Omega_3 - \Omega_4$) and double-quantum coherence ($\Omega_{DQC} = +\Omega_1 + \Omega_2 - \Omega_3 - \Omega_4$) signals. By scanning the different delay-times T_1, T_2 and T_3 and taking the Fourier transform along T_1 and T_3, a 2D spectrum is obtained as a function of $\hbar\omega_1$ and $\hbar\omega_3$ for each value of waiting-time T_2.

This procedure can be numerically implemented in close analogy with the experiment. By employing a non-perturbative treatment of the light-matter interaction, the dynamics of the system is modeled using the Lindblad quantum master equation [30, 35, 36]. Details of the computational procedure and the parameters used for the simulations are reported in the App. 4.A.

Let us consider a pair of chromophores, each treated as a two-level electronic system with a ground- $|g_n\rangle$ and an excited-state $|e_n\rangle$, where the index $n = 1, 2$ denotes the n-th molecule (Fig. 4.1b,c). The chromophoric pair is described by the Hamiltonian:

$$\hat{H} = \hat{H}_1 \otimes \hat{\mathbb{1}}_2 + \hat{\mathbb{1}}_1 \otimes \hat{H}_2 + \hat{V}_{12} \tag{4.3}$$

where $\hat{H}_n = \epsilon_n |e_n\rangle\langle e_n|$ and $\hat{\mathbb{1}}_n = |g_n\rangle\langle g_n| + |e_n\rangle\langle e_n|$ are the Hamiltonian and the identity operator of the n-th chromophore, respectively, while $\hat{V}_{12}$ is the excitonic coupling between

them. The excitation energies ϵ_n of the two chromophores are chosen to match those of the B800 and B850 rings of the LH2 complex, namely $\epsilon_1 = 1.55$ eV and $\epsilon_2 = 1.46$ eV [35]. In the following, the excitonic coupling $\hat{V}_{12}$ is assumed to be small, such that the two chromophores are weakly interacting. The assumption of weak interaction implies that the eigenstates of the chromophoric pair are well approximated by the product of single chromophore states, whereas the dynamical effects of the interaction are captured at the level of perturbation theory in the form of incoherent transfer rates related to Exciton Energy Transfer (EET) and Exciton-Exciton Annihilation (EEA) processes [37–39].

Let us now introduce one- and two-particle representations of the system, as proposed by Mukamel [34] and Kühn et al. [29]. In the one-particle representation (Fig. 4.1b), the state of one chromophore is addressed independently of the other as described by one-particle observables, e.g., one-particle populations $P_{e_1}(t)$ and $P_{e_2}(t)$ representing the probability that one chromophore is excited. Although the one-particle observables are well-defined at every time, the presence of interactions between the two chromophores requires a two-particle representation (Fig. 4.1c) of the system, in which the state of both chromophores is simultaneously considered in terms of two-particle observables, e.g., two-particle populations $P_{e_1g_2}(t)$ and $P_{g_1e_2}(t)$ representing the joint probabilities of one chromophore being excited while the other is in the ground-state, and $P_{e_1e_2}(t)$ representing the probability that both chromophores are excited. Indeed, in EET the excitation is transferred from one chromophore in the first excited-state to the other in the ground-state. Instead, EEA is a two-step process that is possible only when both chromophores are simultaneously excited: first, a higher excited-state is generated on one molecule leaving the other in the ground-state, then, rapid internal conversion to the first excited-state takes place, resulting in the net loss of one exciton. Alternatively, EEA process may result in the annihilation of both excitons. As detailed in App. 4.B, by definition, the two representations are related by $P_{e_1}(t) = P_{e_1g_2}(t) + P_{e_1e_2}(t)$ and $P_{e_2}(t) = P_{g_1e_2}(t) + P_{e_1e_2}(t)$.

The time-resolved incoherent signal is proportional to the two-particle populations weighted by the emission rate of the states:

$$\mathcal{S}(T_d) = \Gamma_1 P_{e_1g_2}(T_d) + \Gamma_2 P_{g_1e_2}(T_d) + \Gamma_{12} P_{e_1e_2}(T_d). \tag{4.4}$$

In general, the different nature of the multi-exciton state can be captured by assuming $\Gamma_{12} \neq \Gamma_1 + \Gamma_2$ [13]. However, when the constrain $\Gamma_{12} = \Gamma_1 + \Gamma_2$ applies, the signal can be

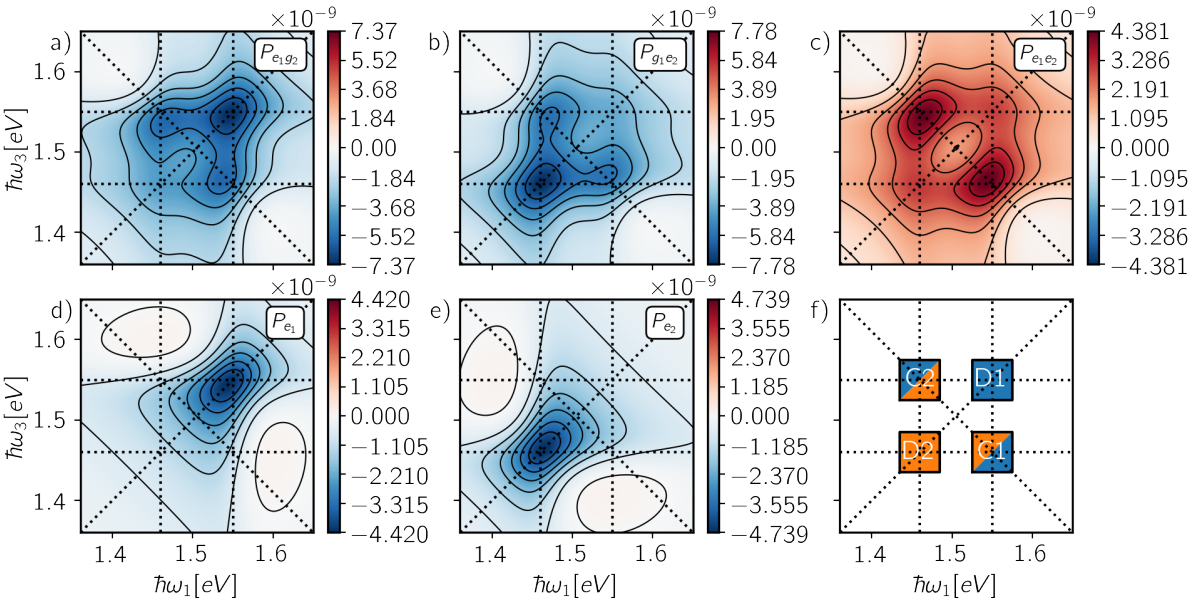

Fig. 4.2: Rephasing spectra from two-particle populations a) $P_{e_1g_2}$, b) $P_{g_1e_2}$, c) $P_{e_1e_2}$ and one-particle populations d) P_{e_1}, e) P_{e_2}, at detection-time $T_d = 0$ fs. In f) are reported the spectral positions of diagonal peaks (D1 and D2) and cross peaks (C1 and C2).

expressed equivalently in terms of one-particle populations:

$$\mathcal{S}(T_d) = \Gamma_1 P_{e_1}(T_d) + \Gamma_2 P_{e_2}(T_d). \tag{4.5}$$

Due to phase-modulation, excited-state populations result modulated, leading to the decomposition of the incoherent signal in Eq. 4.2.

Because of the weak interaction between the chromophores, we now assume a net separation in the timescales of the system dynamics. The first timescale is ruled by the interaction with the laser pulses, which probes the coherent dynamics of the system in the range of hundreds of femtoseconds, for short waiting-times T_2. On such a timescale, the occurrence of EET and EEA can be neglected. In contrast, the detection-time T_d defines a slower timescale, in the nanosecond regime, dictated by the relaxation dynamics at the origin of the incoherent signal. In this case, both EEA and EET processes must be considered.

Although several components of the optical response are readily available from the non-perturbative simulation, in the following, we specifically focus on the rephasing signal $\mathcal{S}(\Omega_R)$ at waiting-time $T_2 = 0$ fs.

Before discussing the role of the dynamical evolution during the detection-time, we

first consider the contributions to the spectrum resulting from populations at $T_d = 0$ fs, immediately after the end of the fourth pulse. This is equivalent to assuming signal emission as the only relaxation pathway active during the detection-time. In Fig. 4.2, we report the contributions to the signals in Eqs. 4.4 and 4.5 from two- (Fig. 4.2a-c) and one-particle populations (Fig. 4.2d,e), respectively. As exemplified in Fig. 4.2f, spectral features for the considered system may appear either as diagonal peaks (D1 and D2) or as cross peaks (C1 and C2).

The spectra from two-particle populations $P_{e_1 g_2}$ and $P_{g_1 e_2}$ exhibit a diagonal peak and two cross peaks of negative sign, whereas $P_{e_1 e_2}$ displays two positive cross peaks. In this context, the cross peaks from two-particle populations represent statistical correlations between the chromophores induced by light-matter interaction, rather than an actual coupling between them [29, 34]. Indeed, when partitioning the signal in terms of one-particle populations P_{e_1} and P_{e_2}, the cross peaks from the two-particle populations cancel out completely and each spectrum exhibits a negative diagonal peak corresponding to the response of an independent molecule, as expected for a pair of weakly interacting chromophores at short waiting-times T_2.

The cancellation of cross peaks that is observed when switching from the two- to one-particle representation relies on the specific phase relation between different excitation pathways. These pathways can be visualized in terms of Feynman diagrams corresponding to Ground-State Bleaching (GSB), Stimulated Emission (SE), and Excited-State Absorption (ESA) contributions [40]. Due to the presence of a fourth pulse, two kinds of ESA pathways are possible in A-2DES: generating either a one-exciton population (ESAI) or a two-exciton population (ESAII) [22]. Each FD contributes to the signal with a sign $(-1)^{n_B}$, where n_B is the number of interactions on the *bra* side. A selection of FDs contributing to the optical response of the system is shown in Fig. 4.3, while the complete set is given in the App. 4.C along with the corresponding response functions. Notice that also FDs can be represented in terms of one- (1P-FD) and two-particle (2P-FD) observables [29, 41], as reported respectively on the right and left of each panel in Fig. 4.3.

The 2P-FDs can be differentiated depending on their final two-particle population. Populations $P_{e_1 g_2}$ and $P_{g_1 e_2}$ originate from GSB (Fig. 4.3a,b) and SE (Fig. 4.3c,d), which appears as both diagonal peaks and cross peaks, and from ESAI (Fig. 4.3e), only contributing to cross peaks. All these pathways are associated with spectral features of negative sign (Fig. 4.2a,b). On the contrary, $P_{e_1 e_2}$ is formed through ESAII pathways (Fig. 4.3f), contributing with positive cross peaks (Fig. 4.2c).

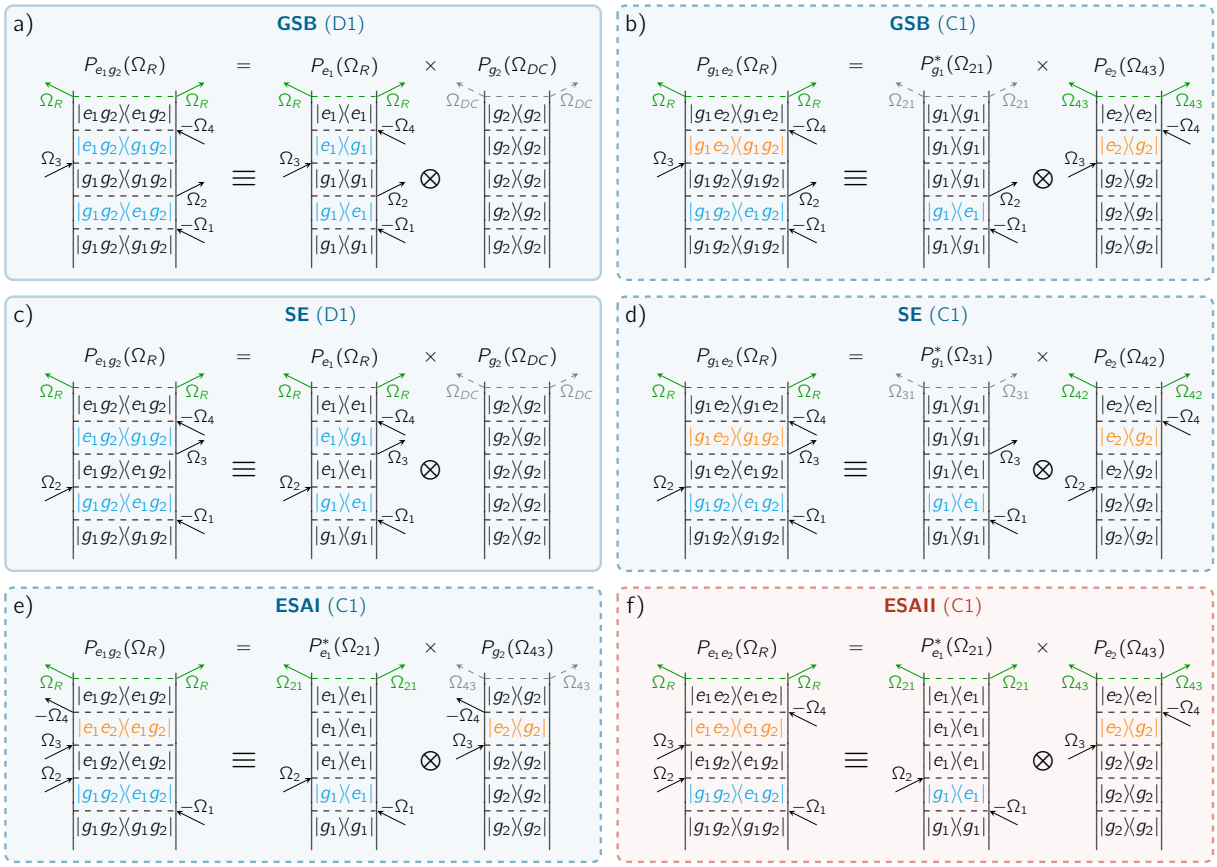

Fig. 4.3: Feynman Diagrams (FDs) for the rephasing signal corresponding to a-b) Ground-State Bleaching (GSB), c-d) Stimulated Emission (SE), e) Excited-State Absorption I (ESAI) and f) Excited-State Absorption II (ESAII) pathways, along with their corresponding spectral position as specified in Fig. 4.2f. In each panel, the two- (2P-FD) and one-particle (1P-FD) representations of FD are depicted respectively on the left and right. At the top of each FD is reported the population, modulated at frequency Ω_S, at the origin of the incoherent signal. FDs can be further distinguished in a,c) self-population pathways (solid contour), where the same chromophore interacts with all four pulses, and b,d-f) cross-population pathways (dashed contour), where each chromophore interacts with a different pair of pulses. Each FD can contribute with either a positive (red panel) or negative (blue panel) sign to the signal.

By decomposing each 2P-FD into the product of two 1P-FDs, it is possible to track the pathway followed by each chromophore individually. From this perspective, the pathways can be distinguished into two categories: self-population pathways (Fig. 4.3a,c), which involve the interaction of one chromophore with all four laser pulses, and cross-population pathways (Fig. 4.3b,d-f), in which each chromophore interacts with a different pair of pulses. This classification is introduced in analogy to that of self- and cross-polarization pathways in C-2DES, proposed by Yang and Fleming [41]. For the considered system, self-population pathways correspond to diagonal peaks (D1 and D2), while cross-population pathways contribute as cross peaks (C1 and C2). It follows that, at $T_d = 0$ fs, negative cross-population pathways of GSB, SE, and ESAI exactly cancel the positive cross-population contributions of ESAII. Therefore, only diagonal peaks associated with GSB and SE self-population pathways appear in the total spectrum. Indeed, these are the only pathways available for a single chromophore to generate a population modulated at the rephasing frequency Ω_R in Eq. 4.5.

However, the sum of the different spectral contributions at $T_d = 0$ fs is not what is experimentally observed, since the situation may change when taking into account the dynamics during the detection-time T_d. Starting from the end of the fourth pulse, we introduce a simple kinetic model that accounts for the relaxation processes active during signal emission. In the following, we focus the discussion on the EEA process, while considerations about the inclusion of the EET are drawn in the App. 4.F. As depicted in Fig. 4.1c, we consider exciton recombination at rate α_n and exciton-exciton annihilation at rates β_n and γ_{12}, corresponding respectively to the loss of one and two excitons in the process. For simplicity, the rates of these processes are assumed to be time-independent, resulting in the following kinetic scheme for the two-particle populations:

$$\begin{cases} \dfrac{d}{dt}P_{e_1g_2}(t) &= -\alpha_1 P_{e_1g_2}(t) + (\alpha_2+\beta_2)P_{e_1e_2}(t) \\ \dfrac{d}{dt}P_{g_1e_2}(t) &= -\alpha_2 P_{g_1e_2}(t) + (\alpha_1+\beta_1)P_{e_1e_2}(t) \\ \dfrac{d}{dt}P_{e_1e_2}(t) &= -(\alpha_1+\beta_1+\alpha_2+\beta_2+\gamma_{12})P_{e_1e_2}(t). \end{cases} \tag{4.6}$$

As outlined in the App. 4.D.1, by solving the kinetic scheme, the time-integrated signal can be expressed in terms of two-particle populations at $T_d = 0$ fs as:

$$\begin{aligned} \overline{\mathcal{S}} &= \Gamma_1\overline{P_{e_1g_2}} + \Gamma_2\overline{P_{g_1e_2}} + \Gamma_{12}\overline{P_{e_1e_2}} \\ &= \Phi_1 P_{e_1g_2}(0) + \Phi_2 P_{g_1e_2}(0) + \left(\Phi_1\cdot\Pi_{e_1e_2\to e_1g_2} + \Phi_2\cdot\Pi_{e_1e_2\to g_1e_2} + \Phi_{12}\right)P_{e_1e_2}(0) \end{aligned} \tag{4.7}$$

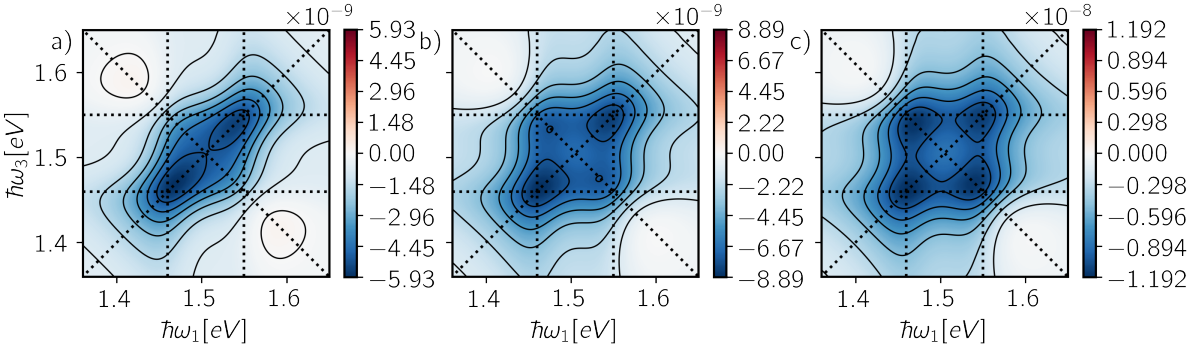

Fig. 4.4: Time-integrated rephasing spectra obtained for a) $\alpha_n^{-1} = 1$ ns, $\beta_n^{-1} = 1$ μs, $\gamma_{12}^{-1} = 1$ μs, b) $\alpha_n^{-1} = 1$ ns, $\beta_n^{-1} = 1$ ps, $\gamma_{12}^{-1} = 1$ μs and c) $\alpha_n^{-1} = 1$ ns, $\beta_n^{-1} = 1$ μs, $\gamma_{12}^{-1} = 1$ ps. The emission rates of the states are set to $\Gamma_n = 1$ ns^{-1} and $\Gamma_{12} = \Gamma_1 + \Gamma_2$.

where $\Phi_1 = \frac{\Gamma_1}{\alpha_1}$ and $\Phi_2 = \frac{\Gamma_2}{\alpha_2}$ are the quantum yields of the one-exciton states, $\Phi_{12} = \frac{\Gamma_{12}}{\alpha_1+\beta_1+\alpha_2+\beta_2+\gamma_{12}}$ is the quantum yield of the two-exciton state, while $\Pi_{e_1e_2\to e_1g_2} = \frac{\alpha_2+\beta_2}{\alpha_1+\beta_1+\alpha_2+\beta_2+\gamma_{12}}$ and $\Pi_{e_1e_2\to g_1e_2} = \frac{\alpha_1+\beta_1}{\alpha_1+\beta_1+\alpha_2+\beta_2+\gamma_{12}}$ are the probabilities that the two-exciton state converts to one or the other one-exciton state during the detection-time. In Eq. 4.7, the first and second terms are responsible for the negative contributions to the spectra (Fig. 4.2a,b), while the third term is responsible for the positive contributions (Fig. 4.2c). Notice that, according to their spectrum at $T_d = 0$ fs (Fig. 4.2a-c), all these terms give rise to cross peaks associated with cross-population pathways (Fig. 4.3b,d-f).

In Fig. 4.4 are shown the time-integrated spectra for various rates α_n, β_n and γ_{12}, leading to different cross peak amplitudes. When exciton recombination is faster than EEA ($\alpha_n \gg \beta_n, \gamma_{12}$), cross peaks do not appear and the spectrum only reflects the contribution of individual chromophores (Fig. 4.4a). Instead, cross peaks start to arise when EEA competes with exciton recombination, as exemplified by the limiting cases of the net loss of one exciton ($\beta_n \gg \alpha_n, \gamma_{12}$) and two excitons ($\gamma_{12} \gg \alpha_n, \beta_n$) in Fig. 4.4b,c, respectively. The cross peak amplitude is determined by the balance between positive and negative contributions from the two-particle populations in Eq. 4.7. An analysis of the peak amplitudes as a function of the different relaxation rates is reported in the App. 4.F. Therefore, in the two-particle representation, the appearance of cross peaks at early waiting-times arises from the imperfect cancellation of different pathways, as previously discussed in terms of the reduced contribution of ESAII due to EEA [26, 28, 29].

We now demonstrate how, for weakly interacting systems, such cross peaks can be interpreted as incoherent mixing contributions. To this end, we derive a kinetic scheme for one-particle populations (Fig. 4.1b) by combining the relevant kinetic equations for

two-particle populations (Eq. 4.6) to obtain:

$$\begin{cases} \dfrac{d}{dt}P_{e_1}(t) &= -\alpha_1 P_{e_1}(t) - (\beta_1 + \gamma_{12})P_{e_1e_2}(t) \\ \dfrac{d}{dt}P_{e_2}(t) &= -\alpha_2 P_{e_2}(t) - (\beta_2 + \gamma_{12})P_{e_1e_2}(t) \end{cases} \tag{4.8}$$

where the two-exciton population $P_{e_1e_2}(t)$ explicitly appears. Because at $T_d = 0$ fs, the total spectrum corresponds to the sum of independent molecular responses, we employ the solution for $P_{e_1e_2}(t)$ of Eq. 4.6 with the initial condition $P_{e_1e_2}(0) = P_{e_1}(0) \times P_{e_2}(0)$. As detailed in the App. 4.D.2, under this assumption, the time-integrated signal can be written in terms of the one-particle populations at $T_d = 0$ fs as follows:

$$\begin{aligned} \overline{\mathcal{S}} &= \Gamma_1\overline{P_{e_1}} + \Gamma_2\overline{P_{e_2}} \\ &= \Phi_1 P_{e_1}(0) + \Phi_2 P_{e_2}(0) - \left(\Phi_1 \cdot \Pi^{EEA}_{e_1\to g_1} + \Phi_2 \cdot \Pi^{EEA}_{e_2\to g_2}\right) P_{e_1}(0) \times P_{e_2}(0) \end{aligned} \tag{4.9}$$

where $\Pi^{EEA}_{e_1\to g_1} = \frac{\beta_1+\gamma_{12}}{\alpha_1+\beta_1+\alpha_2+\beta_2+\gamma_{12}}$ and $\Pi^{EEA}_{e_2\to g_2} = \frac{\beta_2+\gamma_{12}}{\alpha_1+\beta_1+\alpha_2+\beta_2+\gamma_{12}}$ are the probabilities to relax from the excited- to the ground-state of each molecule through EEA during the detection-time. In this alternative decomposition of the signal, the first and second terms correspond to diagonal contributions associated with the response of individual chromophores (Fig. 4.2d,e), while cross peaks are generated by the third term featuring the product of one-particle populations. Notice the correspondence between the terms in the one-particle representation of the signal (Eq. 4.9) and the two classes of FDs (Fig. 4.3). The first and second terms correspond to the one-particle signals $\mathcal{S}(\Omega_R)$, modulated at $\Omega_R = -\Omega_1 + \Omega_2 + \Omega_3 - \Omega_4$, which originates from self-population pathways (Fig. 4.3a,c). In the absence of EEA ($\beta_n, \gamma_{12} = 0$), these are the only contributions appearing in the spectra, consistent with the condition of independent chromophores (Fig. 4.4a). Instead, the third term is responsible for the contribution of incoherent mixing and corresponds to all cross-population pathways (Fig. 4.3b,d-f). Only when EEA is active ($\beta_n, \gamma_{12} \neq 0$), this term leads to the appearance of negative cross peaks in the total spectrum (Fig. 4.4b,c). Indeed, cross-population pathways arise from the product of two 1P-FDs, in which each pair of pulses interacts with different chromophores (Fig. 4.3b,d-f). These one-particle signals $\mathcal{S}(\Omega_{ij})$, originating from two light-matter interactions, corresponds to linear signals modulated at frequency $\Omega_{ij} = \Omega_i - \Omega_j$. As a result, the product of two linear signals can also be modulated at the same frequency as the rephasing, i.e., $\mathcal{S}^*(\Omega_{21}) \times \mathcal{S}(\Omega_{43})$ is modulated at $\Omega_{21} - \Omega_{43} = \Omega_R$. Therefore, in this picture, the emergence of cross peaks is due to the incoherent mixing of linear signals during the detection-time [31, 32]. In this respect, the term “incoherent mixing" may be deceptive. Indeed, the mixing signal inherits

and preserves the phase combination of the fourth-order interaction sequence, and for this reason, it is extracted together with the non-linear response.

To summarize, we have demonstrated that in the weak interaction limit, cross peaks at early waiting-times and the phenomenon of incoherent mixing correspond to alternative pictures, i.e., two- and one-particle representations, of the same underlying physical dynamics.

The analysis presented above highlights several points deserving explicit discussion. First, we notice that cross-population pathways are generated by all the processes, i.e., GSB, SE, and ESA-type pathways, and therefore they can contribute to the spectrum with both positive and negative signs. This clarifies that the incoherent mixing contribution should not be identified exclusively with ESAII pathways. Indeed, when annihilation is efficient and the spectrum is "ESA-free" [29], the GSB contribution can still be determined in part by incoherent mixing. As a consequence, no precise phase relationship is expected between the "true" non-linear signal and incoherent mixing contributions, contrary to what has been theoretically proposed in ref. [33]. In fact, while in the specific model analyzed above incoherent mixing contributes with negative spectral features, it can also contribute with positive sign when the system has a second excited state with a high emission rate. This extension of the model is explicitly considered in the App. 4.G.

Toward an unambiguous definition of incoherent mixing, it is worth to emphasize that one- and two-particle representations are equivalent only for weakly interacting chromophores. In this context, the interpretation of cross peaks as the non-linear signal of the composite system or as the incoherent mixing of the response of its subparts is a matter of representation dictated by the choice of what system is of interest. Whereas in the one-particle representation, the focus is on the single chromophore and cross peaks arise from the spurious interaction with another system, the two-particle representation supports the dimeric nature of the system, even when the interaction is weak, and cross peaks are part of the non-linear response of the system as a whole. In the literature about A-2DES, the former view has been traditionally adopted to interpret the response of extended solid-state systems [31, 42], while the latter has been privileged for analyzing the response of small molecular aggregates [26–28].

Beyond the weak-coupling regime, energy splitting and dipole redistribution related to excitonic delocalization on the two chromophores must be considered. In this case, Feynman diagrams contributing to cross peak positions (Fig. 4.3b,d-f) no longer represent the product of one-particle signals. As a result, they do not generate incoherent mixing but

rather become expression of the non-linear response of the molecular dimer [26–28].

Therefore, while incoherent mixing of one-particle signals can be always recast as the net contribution of fourth-order pathways in the two-particle picture, the factorization of non-linear pathways into the product of one-particle signals does not hold in general. This leads to the central issue of how to identify cross peaks representing incoherent mixing. We remark the two conditions necessary to derive the one-particle representation of the signal (Eq. 4.9), namely weak coupling between chromophores and the timescale separation between the dynamics during the delay-times and the slower mixing process during the detection-time. The latter condition points out that time-gating strategies [26, 28, 30] can be used to reduce the contribution of incoherent mixing to the spectrum. Indeed, as reported in the App. 4.D, the time-gated signal shows how the term related to incoherent mixing grows as the integration window increases.

Recognizing the presence of incoherent mixing is especially important because the associated spectral features may hide relevant spectral dynamics. Since in the weak coupling regime, the environments of the two chromophores can be considered as independent, cross-population pathways do not have rephasing capability [41]. As a result, incoherent mixing contributions are not diagonally elongated and their lineshape is not expected to undergo significant changes along the waiting-time T_2 [31]. On the one hand, this may have the detrimental effect of hiding spectral diffusion of nearby non-linear features. On the other hand, a careful analysis of the cross peak lineshape can clarify whether they are related to incoherent mixing or excitonic delocalization. Nevertheless, the presence of incoherent mixing can be informative of the interaction network at play in the system. Indeed, it has been shown that dynamics-induced non-linearities can be exploited to study the long-range transport mechanism in photovoltaic devices using a pump-probe setting [42–44].

A further point deserving attention is the generality of the incoherent mixing mechanism. Indeed, just as the mixing of linear signals can enter in the fourth-order response, higher-order contributions may appear in the linear signal, e.g., $\mathcal{S}(\Omega_R) \times \mathcal{S}^*(\Omega_{43})$ is modulated at $\Omega_R + \Omega_{43} = \Omega_{21}$, as recently observed in ref. [32], or the mixing between fourth-order and linear signals may contribute to sixth-order response [45]. Hence, incoherent mixing of contributions from different orders is intrinsic to A-2DES and should always be considered in spectral assignments and simulations.

In this regard, we point out that the one-particle representation of the signal provides a numerically efficient way to simulate the effect of incoherent mixing in the action response

of extended systems. In fact, the number of one-particle populations scales linearly, $2N$, with the number of chromophores N, compared to the exponential scaling of the entire combinatorial space, 2^N. Therefore, it is possible to simulate the response of individual subunits and then combine them using a kinetic scheme for one-particle populations. Notice that a similar kinetic scheme has been derived assuming the independence of the excited-state population of each chromophore at every time, $P_{e_1e_2}(t) = P_{e_1}(t) \times P_{e_2}(t)$, obtaining proper non-linear population dynamics [46]. In the continuum limit, the product between populations can be replaced by a quadratic term of the form $P(\mathbf{r}, t)^2$, as originally used to define the concept of incoherent mixing [31]. In light of these considerations, the analysis can be generalized to supramolecular complexes, e.g., LH2 complex, composed of weakly coupled domains, e.g., B800 and B850 rings, interacting only during the detection-time. In this case, both the non-linear response of each domain and the incoherent mixing between different domains can contribute to the signal, eventually overlapping in the spectrum.

4.3. Conclusions

In conclusion, through the use of one- and two-particle representations, we have clarified the nature and the role of incoherent mixing in A-2DES spectra of weakly interacting systems. Overlooking the experimental feasibility of distinguishing between these observables, one- and two-particle representations have been employed as interpretative tools to identify dynamical pathways stemming from different orders in the light-matter interaction. Although giving equivalent results in the limit of weakly interacting systems, the two representations provide different perspectives for interpreting the emergence of spectral features. Notably, the one-particle representation makes evident the distinct nature of self-population and cross-population pathways, thus elucidating the contribution of incoherent mixing in action-detected spectra.

4.A. Simulation Details

In this appendix, we report the parameters used in the non-perturbative simulations: pulse duration $\sigma_i = 5$ fs, carrier-frequency $\hbar\omega_i = 1.50$ eV, light-matter coupling strength $\mu_n E_i^0 = 3$ meV, phase-modulation frequencies $\Omega_1 = 0$ Hz, $\Omega_2 = 250$ Hz, $\Omega_3 = 600$ Hz, $\Omega_4 = 1000$ Hz, phase-modulation repetitions $M = 60$ and inter-train delay-time $T = 1/3000$ s. The delay-times T_1 and T_3 are scanned from 0 to 300 fs in steps of 10 fs, while the waiting-time is kept fixed at $T_2 = 0$ fs. The signal is acquired in the rotating frame at angular frequency $\omega_{RF} = 2.28$ [rad]/fs. In order to smooth the spectra, the signal is zero-padded in the time domain.

The environments of the two chromophores are assumed to be independent. During the coherent excitation induced by the laser pulses, decoherence processes are introduced using the Lindblad operators:

$$\begin{aligned} \hat{L}_1 &= |g_1\rangle\langle g_1| \otimes \mathbb{1}_2 \qquad \hat{L}_3 = \mathbb{1}_1 \otimes |g_2\rangle\langle g_2| \\ \hat{L}_2 &= |e_1\rangle\langle e_1| \otimes \mathbb{1}_2 \qquad \hat{L}_4 = \mathbb{1}_1 \otimes |e_2\rangle\langle e_2| \end{aligned} \tag{4.A.10}$$

with rates set all equal $\gamma_k/h = 1/100$ fs^{-1}.

4.B. Population Observables

In this appendix, we formally introduce one- and two-particle populations along with the relation between them. Population observables can be extracted from the system density matrix $\rho(t)$ after the end of the fourth pulse, obtained from the non-perturbative simulation.

Two-particle populations are obtained by taking the expectation values:

$$\begin{aligned} P_{g_1g_2}(t) &= \mathrm{Tr}\{|g_1g_2\rangle\langle g_1g_2|\,\rho(t)\} \\ P_{e_1g_2}(t) &= \mathrm{Tr}\{|e_1g_2\rangle\langle e_1g_2|\,\rho(t)\} \\ P_{g_1e_2}(t) &= \mathrm{Tr}\{|g_1e_2\rangle\langle g_1e_2|\,\rho(t)\} \\ P_{e_1e_2}(t) &= \mathrm{Tr}\{|e_1e_2\rangle\langle e_1e_2|\,\rho(t)\} \end{aligned} \tag{4.B.11}$$

which represent the probabilities that the dimer is found in a certain two-particle state.

Instead, one-particle populations can be obtained by taking the expectation values:

$$\begin{aligned} P_{g_1}(t) &= \mathrm{Tr}\{|g_1\rangle\langle g_1| \otimes \mathbb{1}_2\, \rho(t)\} \\ P_{e_1}(t) &= \mathrm{Tr}\{|e_1\rangle\langle e_1| \otimes \mathbb{1}_2\, \rho(t)\} \\ P_{g_2}(t) &= \mathrm{Tr}\{\mathbb{1}_1 \otimes |g_2\rangle\langle g_2|\ \rho(t)\} \\ P_{e_2}(t) &= \mathrm{Tr}\{\mathbb{1}_1 \otimes |e_2\rangle\langle e_2|\ \rho(t)\}. \end{aligned} \tag{4.B.12}$$

which represent the probabilities that a monomer is found in a certain state independently of the other.

From Eq. 4.B.12, it follows that one-particle populations are related to two-particle populations by the sum:

$$\begin{aligned} P_{g_1}(t) &= P_{g_1 g_2}(t) + P_{g_1 e_2}(t) \\ P_{g_2}(t) &= P_{g_1 g_2}(t) + P_{e_1 g_2}(t) \\ P_{e_1}(t) &= P_{e_1 g_2}(t) + P_{e_1 e_2}(t) \\ P_{e_2}(t) &= P_{g_1 e_2}(t) + P_{e_1 e_2}(t) \end{aligned} \tag{4.B.13}$$

which is equivalent to take the partial trace over the states of the other molecule. Notice that it is always possible to obtain one-particle populations from two-particle populations.

In contrast, two-particle populations cannot be expressed in terms of one-particle populations in general. However, if we make the assumption that, at the time $t = t_0$, the populations of the two chromophores are uncorrelated, then two-particle populations can be factorized as:

$$\begin{aligned} P_{g_1 g_2}(t_0) &= P_{g_1}(t_0) \times P_{g_2}(t_0) \\ P_{e_1 g_2}(t_0) &= P_{e_1}(t_0) \times P_{g_2}(t_0) \\ P_{g_1 e_2}(t_0) &= P_{g_1}(t_0) \times P_{e_2}(t_0) \\ P_{e_1 e_2}(t_0) &= P_{e_1}(t_0) \times P_{e_1}(t_0). \end{aligned} \tag{4.B.14}$$

In the main text, we consider this specific situation after the interaction with the pulse train, at detection-time $T_d = 0$ fs. Since the two chromophores do not interact during the coherent dynamics induced by the laser pulses, the factorization of two-particle populations in terms of one-particle populations holds. Analogously, also the density matrix of the chromophoric pair can be factorized into the density matrices of the individual chromophores as $\rho(0) = \rho_1(0) \otimes \rho_2(0)$.

4.C. Response Theory and Feynman Diagrams

In this appendix, we provide the expressions for the response functions and report the complete set of Feynman Diagrams for the rephasing signal of A-2DES in the case of weakly interacting chromophoric pair. In formulating the response functions, we make several assumptions: the impulse limit, the time-ordering of the pulses, and the Rotating-Wave Approximation (RWA). Additionally, for simplicity, we assume unitary evolution between the pulses under the system Hamiltonian.

For the linear signals modulated at frequency $\Omega_{ij} = \Omega_i - \Omega_j$, the second-order response functions are:

$$\mathcal{J}_1^{(n)}(t_{ij}) = +\left(\frac{i}{\hbar}\right)^2 |\mu_n|^2 e^{-i\omega_n t_{ij}} e^{+i\Phi(\Omega_{ij})} \tag{4.C.15}$$

$$\mathcal{J}_2^{(n)}(t_{ij}) = -\left(\frac{i}{\hbar}\right)^2 |\mu_n|^2 e^{-i\omega_n t_{ij}} e^{+i\Phi(\Omega_{ij})} \tag{4.C.16}$$

where the superscript index (n) represents the interaction with the n-th chromophore, with $n = 1, 2$. In the expression, μ_n is the transition dipole moment, $\omega_n = \epsilon_n/\hbar$ is the transition frequency, $\Phi(\Omega_{ij})$ is the phase associated to the pathway as a result of phase-modulation, and $t_{ij} = t_i - t_j$ is the delay-time between two pulses centered respectively at t_i and t_j.

For the rephasing signal modulated at frequency $\Omega_R = -\Omega_1 + \Omega_2 + \Omega_3 - \Omega_4$, the fourth-order response functions are, for Ground-State Bleaching (GSB):

$$\mathcal{R}_{GSB}^{(n,n)}(t_{21}, t_{43}) = -\left(\frac{i}{\hbar}\right)^4 |\mu_n|^4 e^{+i\omega_n t_{21}} e^{-i\omega_n t_{43}} e^{+i\Phi(\Omega_R)} \tag{4.C.17}$$

$$\mathcal{R}_{GSB}^{(n,m)}(t_{21}, t_{43}) = -\left(\frac{i}{\hbar}\right)^4 |\mu_n|^2 |\mu_m|^2 e^{+i\omega_n t_{21}} e^{-i\omega_m t_{43}} e^{+i\Phi(\Omega_R)} = \left(\mathcal{J}_2^{(n)}(t_{21})\right)^* \times \mathcal{J}_1^{(m)}(t_{43}) \tag{4.C.18}$$

for Stimulated Emission (SE):

$$\mathcal{R}_{SE}^{(n,n)}(t_{21}, t_{43}) = -\left(\frac{i}{\hbar}\right)^4 |\mu_n|^4 e^{+i\omega_n t_{21}} e^{-i\omega_n t_{43}} e^{+i\Phi(\Omega_R)} \tag{4.C.19}$$

$$\mathcal{R}_{SE}^{(n,m)}(t_{31}, t_{42}) = -\left(\frac{i}{\hbar}\right)^4 |\mu_n|^2 |\mu_m|^2 e^{+i\omega_n t_{31}} e^{-i\omega_m t_{42}} e^{+i\Phi(\Omega_R)} = \left(\mathcal{J}_2^{(n)}(t_{31})\right)^* \times \mathcal{J}_1^{(m)}(t_{42}) \tag{4.C.20}$$

for Excited-State Absorption I (ESAI):

$$\mathcal{R}_{ESAI}^{(n,m)}(t_{21}, t_{43}) = -\left(\frac{i}{\hbar}\right)^4 |\mu_n|^2 |\mu_m|^2 e^{+i\omega_n t_{21}} e^{-i\omega_m t_{43}} e^{+i\Phi(\Omega_R)} = \left(\mathcal{J}_1^{(n)}(t_{21})\right)^* \times \mathcal{J}_2^{(m)}(t_{43}) \tag{4.C.21}$$

$$\mathcal{R}_{ESAI}^{(n,m)}(t_{31}, t_{42}) = -\left(\frac{i}{\hbar}\right)^4 |\mu_n|^2 |\mu_m|^2 e^{+i\omega_n t_{31}} e^{-i\omega_m t_{42}} e^{+i\Phi(\Omega_R)} = \left(\mathcal{J}_1^{(n)}(t_{31})\right)^* \times \mathcal{J}_2^{(m)}(t_{42}) \tag{4.C.22}$$

and for Excited-State Absorption II (ESAII):

$$\mathcal{R}^{(n,m)}_{ESAII}(t_{21},t_{43}) = +\left(\frac{i}{\hbar}\right)^4 |\mu_n|^2|\mu_m|^2 e^{+i\omega_n t_{21}} e^{-i\omega_m t_{43}} e^{+i\Phi(\Omega_R)} = \left(\mathcal{J}_2^{(n)}(t_{21})\right)^* \times \mathcal{J}_2^{(m)}(t_{43}) \qquad (4.C.23)$$

$$\mathcal{R}^{(n,m)}_{ESAII}(t_{31},t_{42}) = +\left(\frac{i}{\hbar}\right)^4 |\mu_n|^2|\mu_m|^2 e^{+i\omega_n t_{31}} e^{-i\omega_m t_{42}} e^{+i\Phi(\Omega_R)} = \left(\mathcal{J}_2^{(n)}(t_{31})\right)^* \times \mathcal{J}_2^{(m)}(t_{42}). \qquad (4.C.24)$$

Fourth-order response functions can be differentiated into self-population pathways [labeled with (n,n)], if the interaction with the pulses only involves the n-th chromophore, and cross-population pathways [labeled with (n,m)], if the interaction involves both chromophores n and m. Notice that, in the case of cross-population pathways, the fourth-order response function can be decomposed into the product of second-order response functions of each chromophore, emphasizing how they originate from the product of linear signals.

Notice that some cross-population pathways associated to SE (Eq. 4.C.20), ESAI (Eq. 4.C.22) and ESAII (Eq. 4.C.24) contributions exhibit a coherence during the waiting-time $T_2 = t_{32} = t_3 - t_2$. For the considered weakly-interacting system, these coherences are inter-site rather than inter-exciton in nature [47]. In the case of independent environments of the two chromophores, these coherences are expected to quickly dephase along T_2, but they may still contribute to the signal to some extent, especially at short waiting-time.

In Figs. 4.C.5-4.C.7, we also report the complete set of Feynman diagrams for the rephasing signal modulated at $\Omega_R = -\Omega_1 + \Omega_2 + \Omega_3 - \Omega_4$ in the one-particle (1P-FD) and two-particle (2P-FD) representations. The various FDs can be distinguished depending on the two-particle population from which the signal is emitted, i.e., $P_{e_1 g_2}$ (Fig. 4.C.5), $P_{g_1 e_2}$ (Fig. 4.C.6), and $P_{e_1 e_2}$ (Fig. 4.C.7). In each panel, 2P-FDs are reported on the left, while the equivalent decomposition in terms of 1P-FDs is reported on the right.

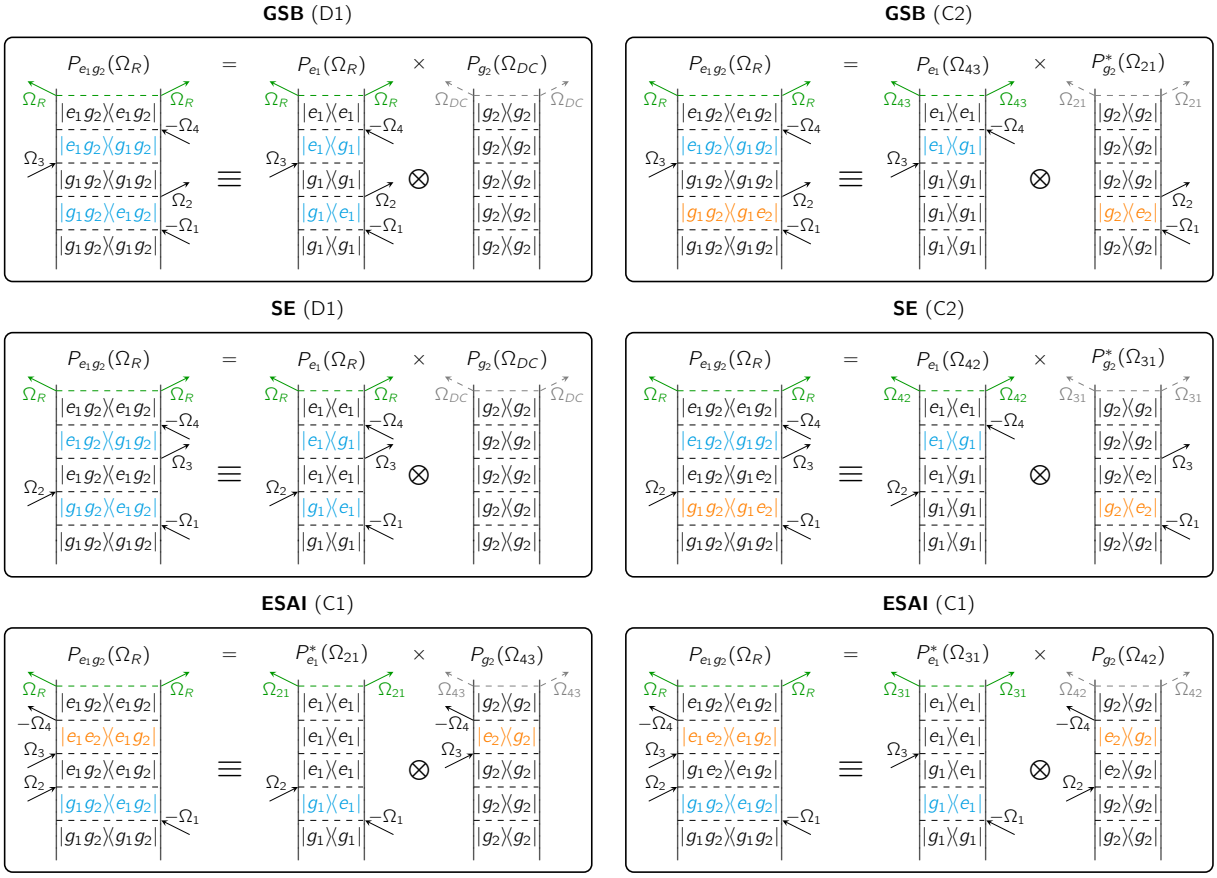

Fig. 4.C.5: Feynman diagrams for the rephasing signal emitted from $P_{e_1g_2}$ population in the one- and two-particle representations.

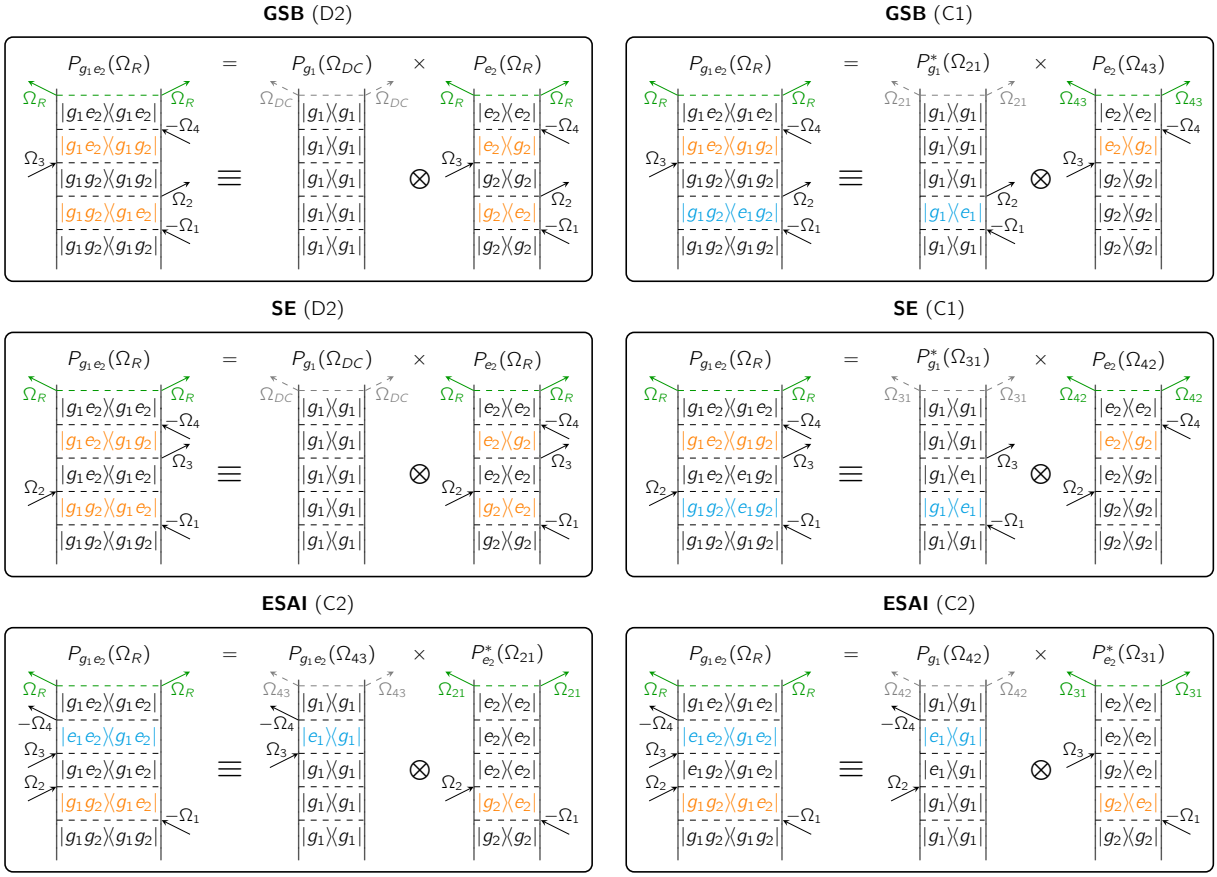

Fig. 4.C.6: Feynman diagrams for the rephasing signal emitted from $P_{g_1e_2}$ population in the one- and two-particle representations.

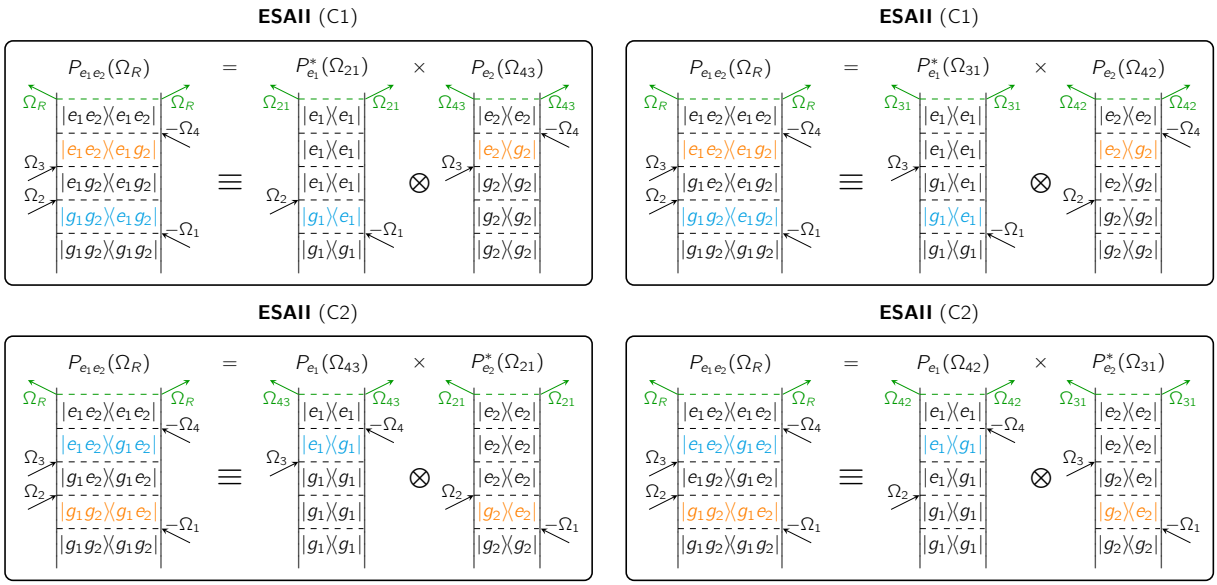

Fig. 4.C.7: Feynman diagrams for the rephasing signal emitted from $P_{e_1e_2}$ population in the one- and two-particle representations.

4.D. Kinetic Scheme for Populations and Incoherent Signal

In this appendix, we present a kinetic scheme for the one- and two-particle populations during the detection-time T_d. As a result of the kinetic scheme, we obtain the time-resolved populations along the detection-time T_d. These can then be further integrated to obtain the time-integrated populations which are used to construct the total signal.

The kinetic scheme is defined by the following rates: α_n is the exciton recombination rate, β_n and γ_{12} are the rates of exciton-exciton annihilation leading respectively to the annihilation of one and two excitons. Then, the incoherent signal is defined by the emission rates of the states which are Γ_1, Γ_2 and Γ_{12}.

4.D.1. Two-Particle Populations

The following kinetic scheme for the two-particle populations is assumed:

$$\begin{cases} \dfrac{d}{dt}P_{e_1g_2}(t) = -\alpha_1 P_{e_1g_2}(t) + (\alpha_2+\beta_2)P_{e_1e_2}(t) \\ \dfrac{d}{dt}P_{g_1e_2}(t) = -\alpha_2 P_{g_1e_2}(t) + (\alpha_1+\beta_1)P_{e_1e_2}(t) \\ \dfrac{d}{dt}P_{e_1e_2}(t) = -(\alpha_1+\beta_1+\alpha_2+\beta_2+\gamma_{12})P_{e_1e_2}(t) \end{cases} \tag{4.D.25}$$

whose solution gives the time-resolved populations:

$$\begin{cases} P_{e_1g_2}(t) = P_{e_1g_2}(0)e^{-\alpha_1 t} + \dfrac{\alpha_2+\beta_2}{\beta_1+\alpha_2+\beta_2+\gamma_{12}}P_{e_1e_2}(0)e^{-\alpha_1 t}\left(1-e^{-(\beta_1+\alpha_2+\beta_2+\gamma_{12})t}\right) \\ P_{g_1e_2}(t) = P_{g_1e_2}(0)e^{-\alpha_2 t} + \dfrac{\alpha_1+\beta_1}{\alpha_1+\beta_1+\beta_2+\gamma_{12}}P_{e_1e_2}(0)e^{-\alpha_2 t}\left(1-e^{-(\alpha_1+\beta_1+\beta_2+\gamma_{12})t}\right) \\ P_{e_1e_2}(t) = P_{e_1e_2}(0)e^{-(\alpha_1+\beta_1+\alpha_2+\beta_2+\gamma_{12})t} \end{cases} \tag{4.D.26}$$

with $P_{e_1g_2}(0)$, $P_{g_1e_2}(0)$ and $P_{e_1e_2}(0)$ as initial conditions. The time-resolved signal along the detection-time T_d is defined on the basis of two-particle populations as:

$$\mathcal{S}(T_d) = \Gamma_1 P_{e_1g_2}(T_d) + \Gamma_2 P_{g_1e_2}(T_d) + \Gamma_{12}P_{e_1e_2}(T_d). \tag{4.D.27}$$

By integrating the time-resolved populations for finite detection-time T_d, the time-gated populations are obtained:

$$\begin{cases} \overline{P_{e_1g_2}(T_d)} &= P_{e_1g_2}(0)\dfrac{1-e^{-\alpha_1 T_d}}{\alpha_1} - \dfrac{\alpha_2+\beta_2}{\beta_1+\alpha_2+\beta_2+\gamma_{12}}P_{e_1e_2}(0)\left(\dfrac{1-e^{-(\alpha_1+\beta_1+\alpha_2+\beta_2+\gamma_{12})T_d}}{\alpha_1+\beta_1+\alpha_2+\beta_2+\gamma_{12}} - \dfrac{1-e^{-\alpha_1 T_d}}{\alpha_1}\right) \\ \overline{P_{g_1e_2}(T_d)} &= P_{g_1e_2}(0)\dfrac{1-e^{-\alpha_2 T_d}}{\alpha_2} - \dfrac{\alpha_1+\beta_1}{\alpha_1+\beta_1+\beta_2+\gamma_{12}}P_{e_1e_2}(0)\left(\dfrac{1-e^{-(\alpha_1+\beta_1+\alpha_2+\beta_2+\gamma_{12})T_d}}{\alpha_1+\beta_1+\alpha_2+\beta_2+\gamma_{12}} - \dfrac{1-e^{-\alpha_2 T_d}}{\alpha_2}\right) \\ \overline{P_{e_1e_2}(T_d)} &= P_{e_1e_2}(0)\dfrac{1-e^{-(\alpha_1+\beta_1+\alpha_2+\beta_2+\gamma_{12})T_d}}{\alpha_1+\beta_1+\alpha_2+\beta_2+\gamma_{12}} \end{cases}$$

(4.D.28)

which can be used to calculate the time-gated signal:

$$\overline{\mathcal{S}(T_d)} = \Gamma_1\overline{P_{e_1g_2}(T_d)} + \Gamma_2\overline{P_{g_1e_2}(T_d)} + \Gamma_{12}\overline{P_{e_1e_2}(T_d)}. \tag{4.D.29}$$

By fully integrating along the detection-time T_d, the time-integrated populations are obtained:

$$\begin{cases} \overline{P_{e_1g_2}} = \dfrac{1}{\alpha_1}P_{e_1g_2}(0) + \dfrac{\alpha_2+\beta_2}{\alpha_1(\alpha_1+\beta_1+\alpha_2+\beta_2+\gamma_{12})}P_{e_1e_2}(0) \\ \overline{P_{g_1e_2}} = \dfrac{1}{\alpha_2}P_{g_1e_2}(0) + \dfrac{\alpha_1+\beta_1}{\alpha_2(\alpha_1+\beta_1+\alpha_2+\beta_2+\gamma_{12})}P_{e_1e_2}(0) \\ \overline{P_{e_1e_2}} = \dfrac{1}{\alpha_1+\beta_1+\alpha_2+\beta_2+\gamma_{12}}P_{e_1e_2}(0) \end{cases} \tag{4.D.30}$$

which are used to define the time-integrated signal:

$$\begin{aligned} \overline{\mathcal{S}} &= \Gamma_1\overline{P_{e_1g_2}} + \Gamma_2\overline{P_{g_1e_2}} + \Gamma_{12}\overline{P_{e_1e_2}} \\ &= \frac{\Gamma_1}{\alpha_1}P_{e_1g_2}(0) + \frac{\Gamma_2}{\alpha_2}P_{g_1e_2}(0) + \frac{\Gamma_1\alpha_2(\alpha_2+\beta_2)+\Gamma_2\alpha_1(\alpha_1+\beta_1)+\Gamma_{12}\alpha_1\alpha_2}{\alpha_1\alpha_2(\alpha_1+\beta_1+\alpha_2+\beta_2+\gamma_{12})}P_{e_1e_2}(0) \\ &= \Phi_1 P_{e_1g_2}(0) + \Phi_2 P_{g_1e_2}(0) + \left(\Phi_1\cdot\Pi_{e_1e_2\to e_1g_2} + \Phi_2\cdot\Pi_{e_1e_2\to g_1e_2} + \Phi_{12}\right)P_{e_1e_2}(0) \end{aligned}$$

(4.D.31)

where $\Phi_1 = \frac{\Gamma_1}{\alpha_1}$ and $\Phi_2 = \frac{\Gamma_2}{\alpha_2}$ are the quantum yields of the one-exciton states, $\Phi_{12} = \frac{\Gamma_{12}}{\alpha_1+\beta_1+\alpha_2+\beta_2+\gamma_{12}}$ is the quantum yield of the two-exciton state, while $\Pi_{e_1e_2\to e_1g_2} = \frac{\alpha_2+\beta_2}{\alpha_1+\beta_1+\alpha_2+\beta_2+\gamma_{12}}$ and $\Pi_{e_1e_2\to g_1e_2} = \frac{\alpha_1+\beta_1}{\alpha_1+\beta_1+\alpha_2+\beta_2+\gamma_{12}}$ are the probabilities that the two-exciton state converts

to one or the other one-exciton state during the detection-time T_d.

4.D.2. One-Particle Populations

The equivalent kinetic scheme for the one-particle populations is:

$$\begin{cases} \dfrac{d}{dt}P_{e_1}(t) = -\alpha_1 P_{e_1}(t) - (\beta_1 + \gamma_{12})P_{e_1e_2}(t) \\ \dfrac{d}{dt}P_{e_2}(t) = -\alpha_2 P_{e_2}(t) - (\beta_2 + \gamma_{12})P_{e_1e_2}(t) \end{cases} \tag{4.D.32}$$

which explicitly depends on the two-exciton population $P_{e_1e_2}(t)$. The kinetic scheme can be solved by using the solution for $P_{e_1e_2}(t)$ (Eq. 4.D.26) to obtain:

$$\begin{cases} P_{e_1}(t) = P_{e_1}(0)e^{-\alpha_1 t} - \dfrac{\beta_1 + \gamma_{12}}{\beta_1 + \alpha_2 + \beta_2 + \gamma_{12}} P_{e_1}(0) \times P_{e_2}(0)e^{-\alpha_1 t}\Big(1 - e^{-(\beta_1+\alpha_2+\beta_2+\gamma_{12})t}\Big) \\ P_{e_2}(t) = P_{e_2}(0)e^{-\alpha_2 t} - \dfrac{\beta_2 + \gamma_{12}}{\alpha_1 + \beta_1 + \beta_2 + \gamma_{12}} P_{e_1}(0) \times P_{e_2}(0)e^{-\alpha_2 t}\Big(1 - e^{-(\alpha_1+\beta_1+\beta_2+\gamma_{12})t}\Big) \end{cases}$$

(4.D.33)

where we have assumed the initial factorization of the two-exciton population $P_{e_1e_2}(0) = P_{e_1}(0) \times P_{e_2}(0)$ (Eq. 4.B.14). By imposing the condition $\Gamma_{12} = \Gamma_1 + \Gamma_2$, the time-resolved signal along the detection-time T_d is defined on the basis of one-particle populations as:

$$\mathcal{S}(T_d) = \Gamma_1 P_{e_1}(T_d) + \Gamma_2 P_{e_2}(T_d). \tag{4.D.34}$$

By integrating the time-resolved populations for finite detection-time T_d, the time-gated populations are obtained:

$$\begin{cases} \overline{P_{e_1}(T_d)} = P_{e_1}(0)\dfrac{1 - e^{-\alpha_1 T_d}}{\alpha_1} - \dfrac{\beta_1 + \gamma_{12}}{\beta_1 + \alpha_2 + \beta_2 + \gamma_{12}} P_{e_1}(0) \times P_{e_2}(0)\Big(\dfrac{1 - e^{-\alpha_1 T_d}}{\alpha_1} - \dfrac{1 - e^{-(\alpha_1+\beta_1+\alpha_2+\beta_2+\gamma_{12})T_d}}{\alpha_1 + \beta_1 + \alpha_2 + \beta_2 + \gamma_{12}}\Big) \\ \overline{P_{e_2}(T_d)} = P_{e_2}(0)\dfrac{1 - e^{-\alpha_2 T_d}}{\alpha_2} - \dfrac{\beta_2 + \gamma_{12}}{\alpha_1 + \beta_1 + \beta_2 + \gamma_{12}} P_{e_1}(0) \times P_{e_2}(0)\Big(\dfrac{1 - e^{-\alpha_2 T_d}}{\alpha_2} - \dfrac{1 - e^{-(\alpha_1+\beta_1+\alpha_2+\beta_2+\gamma_{12})T_d}}{\alpha_1 + \beta_1 + \alpha_2 + \beta_2 + \gamma_{12}}\Big) \end{cases}$$

(4.D.35)

which can be used to calculate the time-gated signal:

$$\overline{\mathcal{S}(T_d)} = \Gamma_1 \overline{P_{e_1}(T_d)} + \Gamma_2 \overline{P_{e_2}(T_d)}. \tag{4.D.36}$$

By fully integrating along the detection-time T_d, the time-integrated populations are obtained:

$$\begin{cases} \overline{P_{e_1}} = \dfrac{1}{\alpha_1} P_{e_1}(0) - \dfrac{\beta_1 + \gamma_{12}}{\alpha_1(\alpha_1 + \beta_1 + \alpha_2 + \beta_2 + \gamma_{12})} P_{e_1}(0) \times P_{e_2}(0) \\ \overline{P_{e_2}} = \dfrac{1}{\alpha_2} P_{e_2}(0) - \dfrac{\beta_2 + \gamma_{12}}{\alpha_2(\alpha_1 + \beta_1 + \alpha_2 + \beta_2 + \gamma_{12})} P_{e_1}(0) \times P_{e_2}(0) \end{cases} \tag{4.D.37}$$

which are used to calculate the time-integrated signal:

$$\begin{aligned} \overline{\mathcal{S}} &= \Gamma_1 \overline{P_{e_1}} + \Gamma_2 \overline{P_{e_2}} \\ &= \frac{\Gamma_1}{\alpha_1} P_{e_1}(0) + \frac{\Gamma_2}{\alpha_2} P_{e_2}(0) - \frac{\Gamma_1 \alpha_2(\beta_1 + \gamma_{12}) + \Gamma_2 \alpha_1(\beta_2 + \gamma_{12})}{\alpha_1 \alpha_2(\alpha_1 + \beta_1 + \alpha_2 + \beta_2 + \gamma_{12})} P_{e_1}(0) \times P_{e_2}(0) \\ &= \Phi_1 P_{e_1}(0) + \Phi_2 P_{e_2}(0) - \left(\Phi_1 \cdot \Pi^{EEA}_{e_1 \to g_1} + \Phi_2 \cdot \Pi^{EEA}_{e_2 \to g_2} \right) P_{e_1}(0) \times P_{e_2}(0) \end{aligned} \tag{4.D.38}$$

where $\Pi^{EEA}_{e_1 \to g_1} = \frac{\beta_1 + \gamma_{12}}{\alpha_1 + \beta_1 + \alpha_2 + \beta_2 + \gamma_{12}}$ and $\Pi^{EEA}_{e_2 \to g_2} = \frac{\beta_2 + \gamma_{12}}{\alpha_1 + \beta_1 + \alpha_2 + \beta_2 + \gamma_{12}}$ represent the probabilities to convert from the excited to the ground-state through EEA process during the detection-time T_d.

4.E. Generalized Kinetic Scheme

In this appendix, we report a generalized kinetic scheme based on the classical master equation. We consider the system composed by $N + 1$ states $|n\rangle$, with $n = 0, 1, \ldots, N$. The state $|n = 0\rangle$ represents the collective ground-state, while the remaining N states $|n \neq 0\rangle$ are excited-states. The populations are assumed to follow the classical master equation:

$$\frac{d}{dt} \vec{P}(t) = -\boldsymbol{K} \vec{P}(t) \tag{4.E.39}$$

where $\vec{P}(t) = \sum_{n=0}^{N} P_n(t) |n\rangle$ is the population vector, with $P_n(t)$ population of the n-th state, and $\boldsymbol{K}$ is the kinetic matrix whose elements are defined as:

$$K_{nm} = -(1 - \delta_{nm}) k_{n \leftarrow m} + \delta_{nm} \sum_{l \neq m} k_{l \leftarrow m} \tag{4.E.40}$$

where the first terms is responsible for the gain in population from state $|m\rangle$ to state $|n\rangle$ with rate $k_{n \leftarrow m}$, while the second term accounts for the loss in population from state $|m\rangle$ to state $|l\rangle$ with rate $k_{l \leftarrow m}$. The formal solution of the classical master equation is:

$$\vec{P}(t) = e^{-\boldsymbol{K} t} \vec{P}(0) \tag{4.E.41}$$

with population vector $\vec{P}(0)$ as initial condition. By using the spectral decomposition, the kinetic matrix can be written as $\boldsymbol{K} = \boldsymbol{V}\boldsymbol{\Lambda}\boldsymbol{V}^{-1}$, where $\boldsymbol{\Lambda} = \sum_{k=0}^{N} \lambda_k \left|k\right\rangle\!\left\langle k\right|$ is the eigenvalue matrix and $\boldsymbol{V} = \sum_{n,k} V_{nk} \left|n\right\rangle\!\left\langle k\right|$ is the eigenvector matrix. Each eigenvector $\left|k\right\rangle = \sum_{n=0}^{N} V_{nk} \left|n\right\rangle$ is associated with a real eigenvalue $\lambda_k \geq 0$. The solution of the master equation can thus be rewritten as:

$$\vec{P}(t) = \boldsymbol{V} e^{-\boldsymbol{\Lambda} t} \boldsymbol{V}^{-1} \vec{P}(0) \tag{4.E.42}$$

where the matrix exponential is $e^{-\boldsymbol{\Lambda} t} = \sum_{k=0}^{N} e^{-\lambda_k t} \left|k\right\rangle\!\left\langle k\right|$.

We now assume that the kinetic scheme admits one equilibrium state corresponding to the eigenstate $\left|k=0\right\rangle$ with eigenvalue $\lambda_0 = 0$. In the context of optical spectroscopy, $\left|k=0\right\rangle$ coincides with the collective ground-state $\left|n=0\right\rangle$. Therefore, the elements of the matrix exponential are:

$$\left[e^{-\boldsymbol{\Lambda} t}\right]_{kk} = \begin{cases} 1 & \text{for } \lambda_0 = 0 \\ e^{-\lambda_k t} & \text{for } \lambda_k > 0 \end{cases} \tag{4.E.43}$$

depending on the eigenvalue λ_k. We now introduce the emission matrix $\boldsymbol{\Gamma} = \sum_n \Gamma_n \left|n\right\rangle\!\left\langle n\right|$, where Γ_n is the emission rate of the n-th state. In the following, we assume that the collective ground-state do not emit signal $\Gamma_0 = 0$, while for the other excited-states $\Gamma_n \geq 0$ in general.

The time-resolved signal vector along the detection-time T_d is defined as:

$$\vec{S}(T_d) = \boldsymbol{\Gamma} \cdot \vec{P}(T_d) \tag{4.E.44}$$

with population vector defined in Eq. 4.E.42. The time-integrated population vector is given by:

$$\overline{\vec{P}} = \int_0^\infty dT_d \ \vec{P}(T_d) = \boldsymbol{V} \left[\int_0^\infty dT_d \ e^{-\boldsymbol{\Lambda} T_d} \right] \boldsymbol{V}^{-1} \vec{P}(0) \tag{4.E.45}$$

where the integral of the elements of the matrix exponential is:

$$\int_0^\infty dT_d \ \left[e^{-\boldsymbol{\Lambda} T_d}\right]_{kk} = \int_0^\infty dT_d \ e^{-\lambda_k T_d} = \begin{cases} +\infty & \text{if } \lambda_0 = 0 \\ \frac{1}{\lambda_n} & \text{if } \lambda_k > 0. \end{cases} \tag{4.E.46}$$

Therefore, the time-integrated signal vector can be obtained as:

$$\overline{\vec{S}} = \boldsymbol{\Gamma} \cdot \overline{\vec{P}} \tag{4.E.47}$$

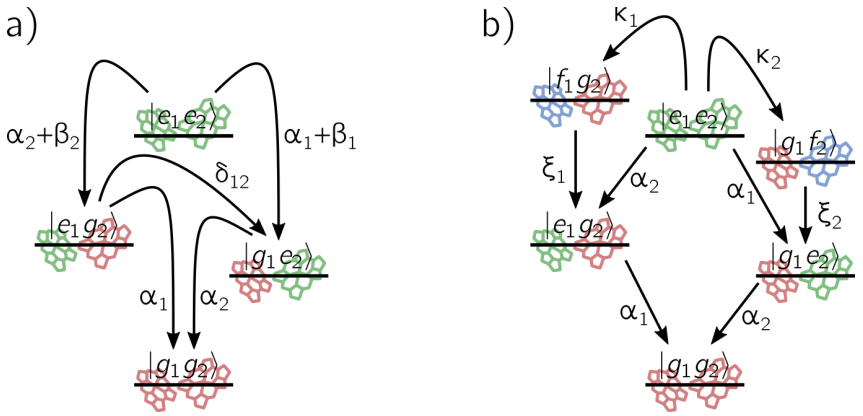

Fig. 4.F.8: Alternative kinetic schemes for two-particle populations during the detection-time T_d. Scheme a) includes EET process between one-exciton states at rate δ_{12}. Scheme b) describes EEA process explicitly, accounting for EET between two-exciton state and localized double-excited states at rate κ_n, followed by rapid internal conversion to one-exciton states at rate ξ_n.

by inserting the time-integrated population vector (Eq. 4.E.45).

4.F. Chromophoric Pair of Two-Level Systems

In this appendix, we report additional results regarding the model of chromophoric pair of two-level systems.

In Fig. 4.F.9, we report the Incoherent Mixing Factor (coefficient of the population product in Eq. 4.D.38) and the cross peak amplitude as a function of β_n/α_n for different values of γ_{12}.

Furthermore, we investigated the effects on the spectra of Exciton Energy Transfer (EET) during the detection-time T_d. By using the generalized kinetic scheme in App. 4.E, in addition to the EEA, we include the EET process between the two chromophores with rate δ_{12}, as depicted in Fig. 4.F.8a. In Fig. 4.F.10 are reported the time-integrated spectra of the individual contributions and the total signal for increasing EET rates δ_{12}. We observe that, while the presence of the EET process does not affect the total spectra, it may affect the individual contributions. Specifically, we notice that pathways ending in $P_{e_1 g_2}$ population at $T_d = 0$ fs are transferred to the $P_{g_1 e_2}$ population during the detection-time, resulting in the appearance of the corresponding features in the spectrum.

In Fig. 4.F.11, we report the time-integrated spectra for different quantum yields Φ_n of the two chromophores. In addition to the enhancement/depletion of spectral features associated with either chromophore, we point out how variations in the relative quantum yields can also affect the amplitude of cross peaks.

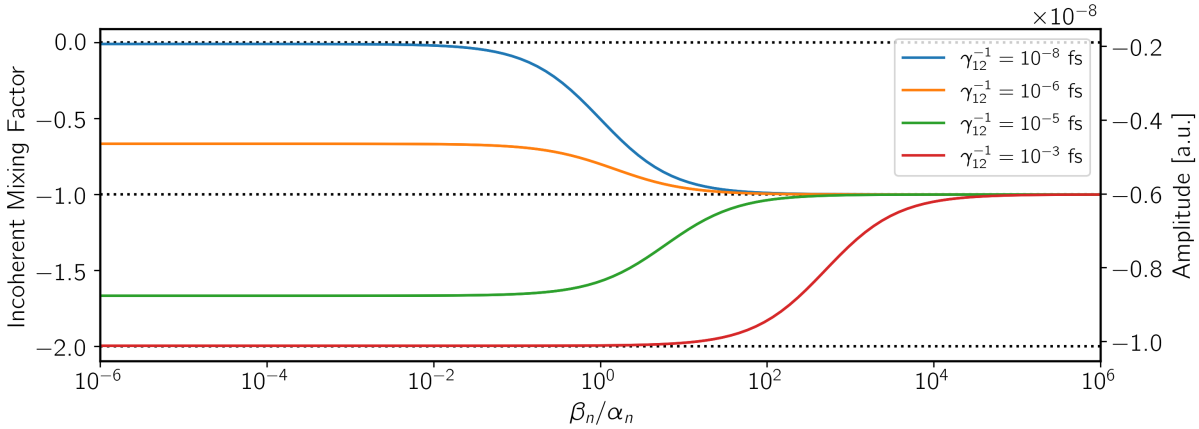

Fig. 4.F.9: Dependence of the Incoherent Mixing Factor in Eq. 4.D.38 and cross peaks amplitude for different values of EEA rates β_n, and γ_{12}. Exciton recombination rates $\alpha_n = 1$ ns^{-1}, emission rates $\Gamma_n = 1$ ns^{-1} and $\Gamma_{12} = \Gamma_1 + \Gamma_2$ are kept constant.

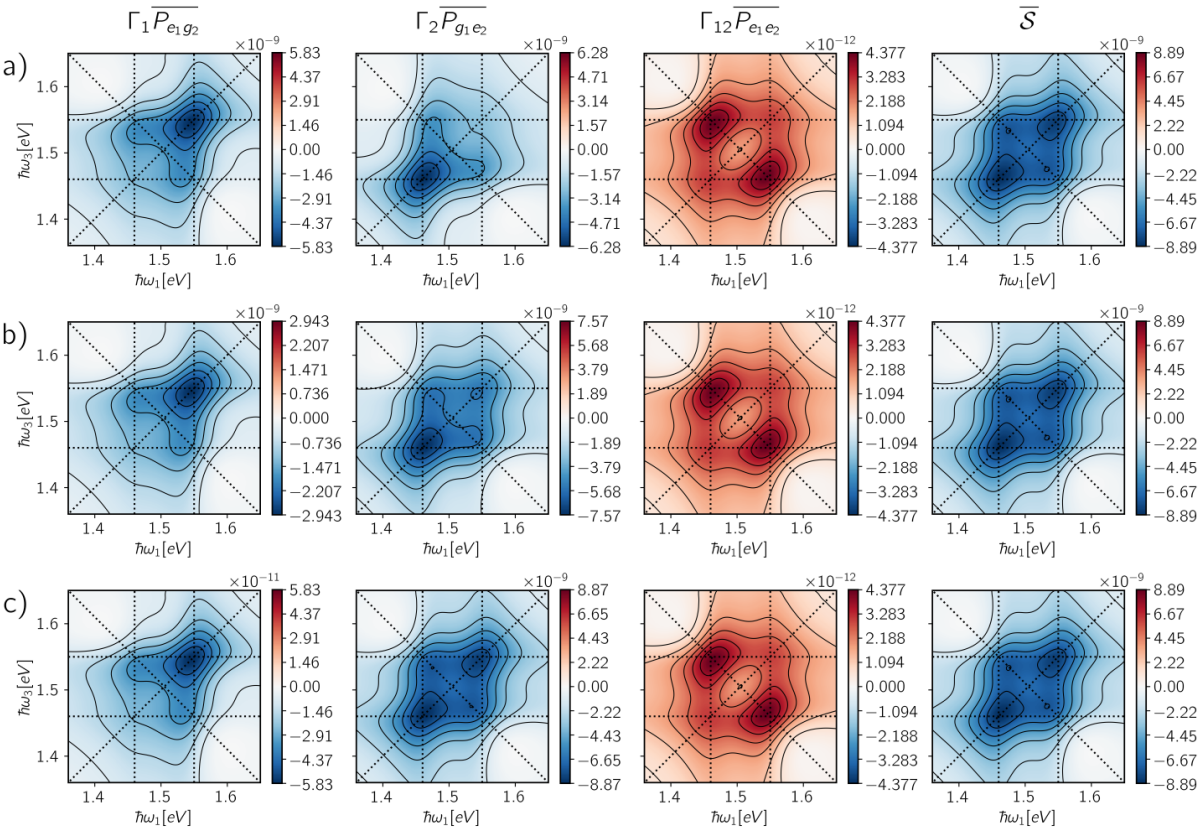

Fig. 4.F.10: Time-integrated rephasing spectra obtained using Eq. 4.E.45 for different EET rates: a) $\delta_{12}^{-1} = 100$ ns, b) $\delta_{12}^{-1} = 1$ ns, c) $\delta_{12}^{-1} = 10$ ps. Exciton recombination rates $\alpha_n^{-1} = 10$ ns, EEA annihilation rates $\beta_n^{-1} = 1$ ps and $\gamma_{12}^{-1} = 1$ μs, and emission rates $\Gamma_n = 1$ ns^{-1} and $\Gamma_{12} = \Gamma_1 + \Gamma_2$ are kept constant.

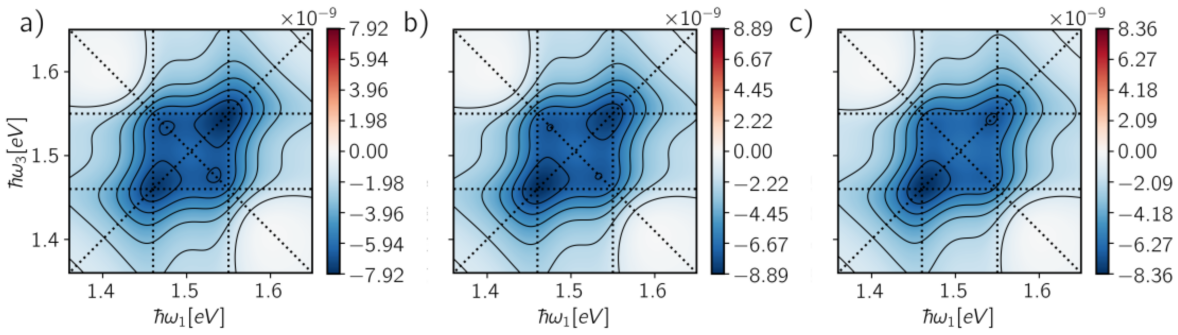

Fig. 4.F.11: Time-integrated rephasing spectra for different emission rates: a) $\Gamma_1^{-1} = 0.8$ ns and $\Gamma_2^{-1} = 1.0$ ns, b) $\Gamma_1^{-1} = 1.0$ ns and $\Gamma_2^{-1} = 1.0$ ns, c) $\Gamma_1^{-1} = 1.0$ ns and $\Gamma_2^{-1} = 0.8$ ns, assuming $\Gamma_{12} = \Gamma_1 + \Gamma_2$. Exciton recombination rates $\alpha_n^{-1} = 1$ ns, EEA rates $\beta_n^{-1} = 1$ ps and $\gamma_{12}^{-1} = 1$ μs are kept constant.

4.G. Chromophoric Pair of Three-Level Systems

In this appendix, we extend the model of chromophoric pair by treating each chromophore as a three-level system (Fig. 4.F.8b), i.e., composed by a ground state $|g_n\rangle$, a one-exciton state $|e_n\rangle$ and a two-exciton state $|f_n\rangle$. The energy of two-exciton states is assumed to be twice the energy of one-exciton states, with $\epsilon_{f_1} = 3.10$ eV and $\epsilon_{f_2} = 2.92$ eV, respectively.

In Fig. 4.G.12, we report the additional Feynman diagrams for the rephasing signal, corresponding to ESAI and ESAII self-population pathways. In Fig. 4.G.13, we show the spectra at $T_d = 0$ fs from two-particle populations corresponding to the states in the one-exciton manifold (Fig. 4.G.13a,b), two-exciton manifold (Fig. 4.G.13c-e), three-exciton manifold (Fig. 4.G.13g,h) and four-exciton manifold (Fig. 4.G.13i). Notice how the spectra from the states in the three- and four-exciton manifolds have smaller amplitudes compared to the others, as they arise from higher-order contributions in the light-matter interaction. For simplicity, we neglect those contributions in the definition of the time-integrated signal:

$$\overline{\mathcal{S}} = \Gamma_{e_1}\overline{P_{e_1 g_2}} + \Gamma_{e_2}\overline{P_{g_1 e_2}} + (\Gamma_{e_1} + \Gamma_{e_2})\overline{P_{e_1 e_1}} + \Gamma_{f_1}\overline{P_{f_1 g_2}} + \Gamma_{f_2}\overline{P_{g_1 f_2}}. \tag{4.G.48}$$

where the time-integrated populations are weighted by the emission rate of the states.

By using the generalized kinetic scheme reported in App. 4.E, we report the time-integrated spectra for different emission rates of the two-exciton states Γ_{f_n} compared to the one-exciton states Γ_{e_n} in Fig. 4.G.14. We notice that, as $\Gamma_{f_n} > \Gamma_{e_n}$, positive spectral features start to arise in the spectrum: diagonal-peaks result from ESAII self-population pathways (Fig. 4.G.12), appearing in Fig. 4.G.13d,e, while cross peaks are related to ESAII cross-population pathways (Fig. 4.C.7), appearing in Fig. 4.G.13c, which can be regarded as incoherent mixing contributions. We point out that fast radiative processes from higher excited-states are not usually present in molecular systems but these processes may take place in nanostructures, especially in photocurrent detection [13].

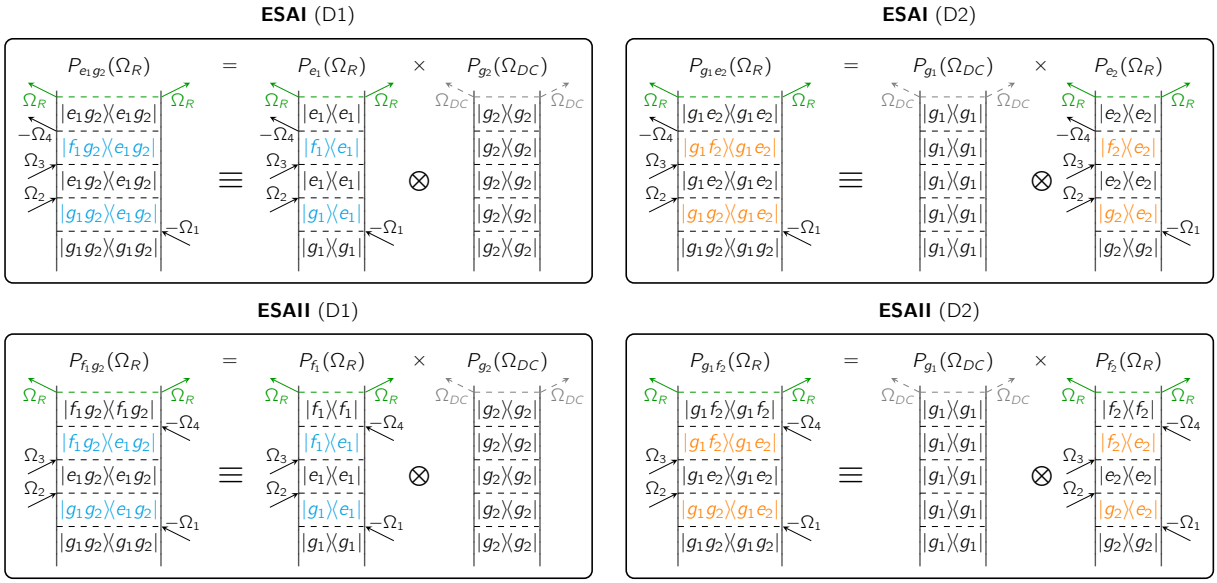

Fig. 4.G.12: (left) Feynman diagrams for the rephasing signal modulated at Ω_R emitted from the two-particle population $P_{e_1e_2}$ and (right) the equivalent Feynman diagrams for the one-particle populations.

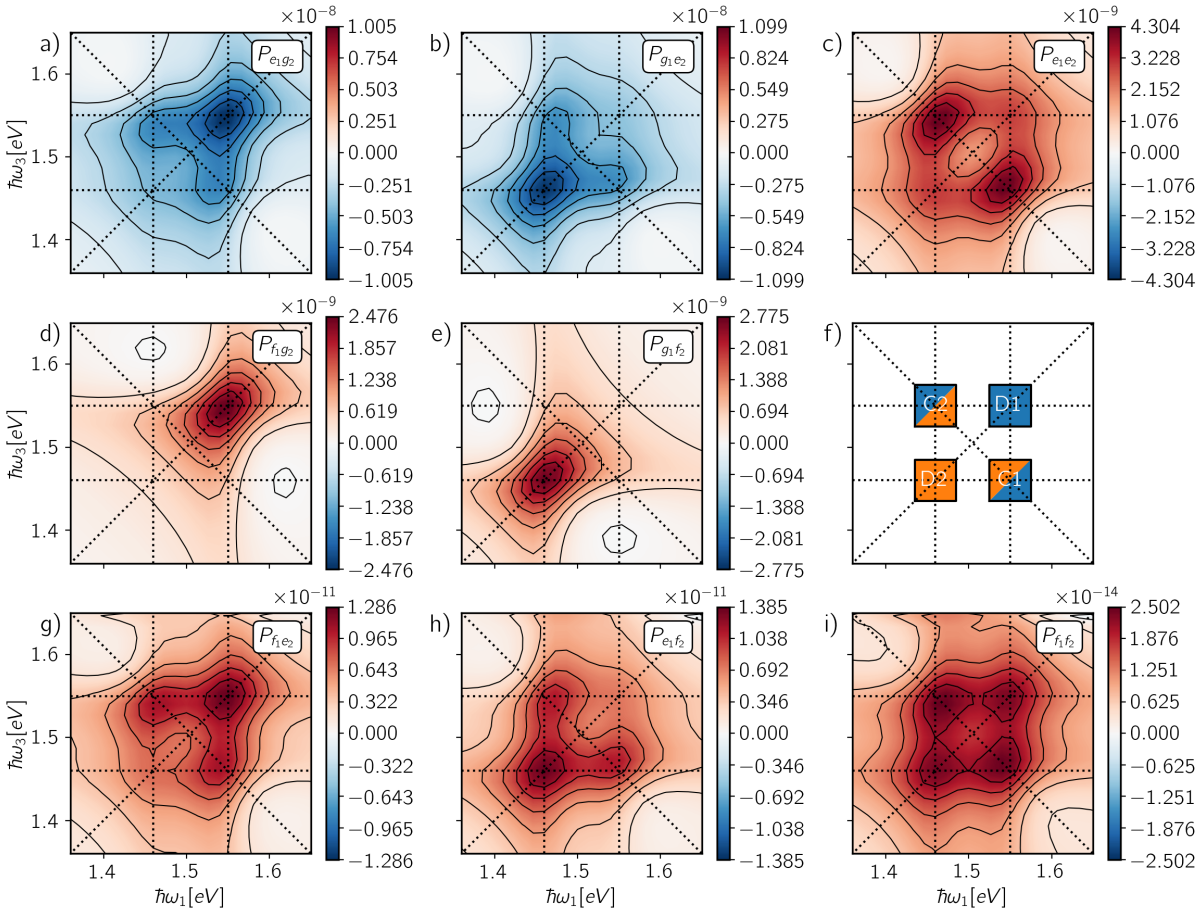

Fig. 4.G.13: Rephasing spectra from two-particle populations in the one-exciton manifold a) $P_{e_1g_2}$, b) $P_{g_1e_2}$, and two-exciton manifold c) $P_{e_1e_2}$, d) $P_{f_1g_2}$, e) $P_{g_1f_2}$, at detection-time $T_d = 0$ fs. In f) are reported the spectral positions of diagonal peaks (D1 and D2) and cross peaks (C1 and C2). We also report the two-particle populations for the three-exciton manifold g) $P_{f_1e_2}$, h) $P_{e_1f_2}$ and for the four-exciton manifold i) $P_{f_1f_2}$.

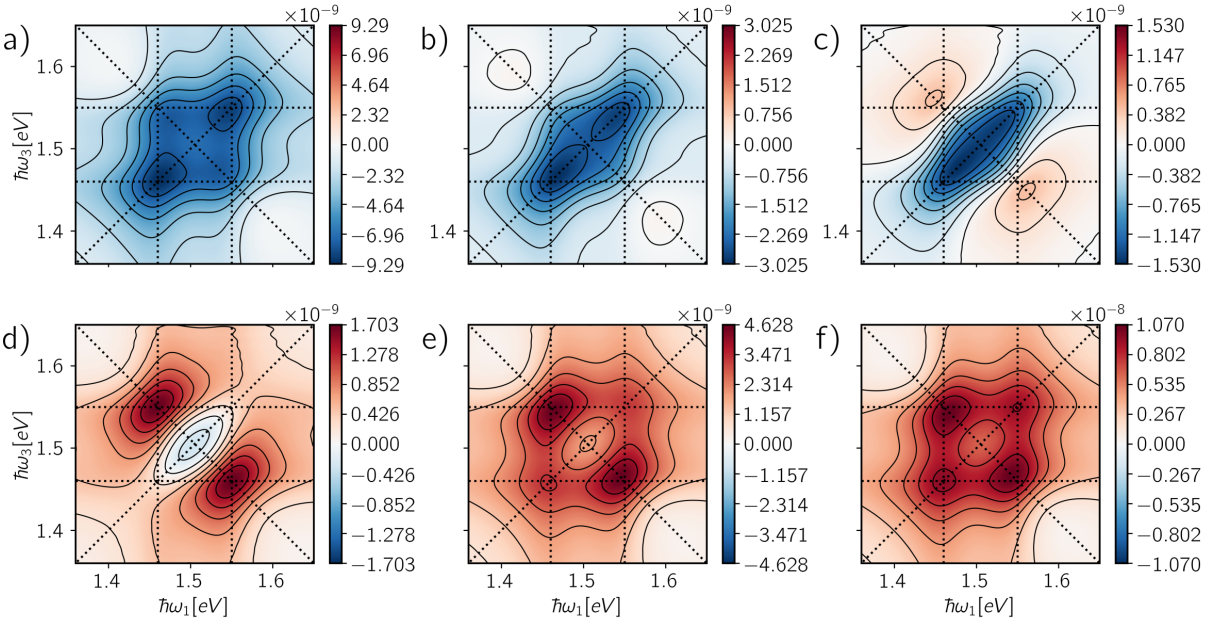

Fig. 4.G.14: Time-integrated rephasing spectra for different $\Gamma_{f_n}/\Gamma_{e_n}$ ratios: a) 0.0, b) 1.0, c) 1.25, d) 1.5, e) 2.0, f) 3.0. The emission rate of the single-excited state $\Gamma_{e_n} = 1$ ns^{-1} is kept fixed.

References

(1) Fuller, F. D.; Ogilvie, J. P. Experimental Implementations of Two-Dimensional Fourier Transform Electronic Spectroscopy. *Annu. Rev. Phys. Chem.* **2015**, *66*, 667–690.

(2) Collini, E. 2D Electronic Spectroscopic Techniques for Quantum Technology Applications. *J. Phys. Chem. C* **2021**, *125*, 13096–13108.

(3) Biswas, S.; Kim, J.; Zhang, X.; Scholes, G. D. Coherent Two-Dimensional and Broadband Electronic Spectroscopies. *Chem. Rev.* **2022**, *122*, 4257–4321.

(4) Tiwari, V. Multidimensional Electronic Spectroscopy in High-Definition - Combining Spectral, Temporal, and Spatial Resolutions. *J. Chem. Phys.* **2021**, *154*, 230901.

(5) Karki, K. J.; Ciappina, M. F. Advances in Nonlinear Spectroscopy using Phase Modulated Light Fields: Prospective Applications in Perturbative and Non-Perturbative Regimes. *Adv. Phys.: X* **2022**, *7*, 2090856.

(6) Tian, P.; Keusters, D.; Suzaki, Y.; Warren, W. S. Femtosecond Phase-Coherent Two-Dimensional Spectroscopy. *Science* **2003**, *300*, 1553–1555.

(7) Tan, H.-S. Theory and Phase-Cycling Scheme Selection Principles of Collinear Phase Coherent Multi-Dimensional Optical Spectroscopy. *J. Chem. Phys.* **2008**, *129*, 124501.

(8) Tekavec, P. F.; Lott, G. A.; Marcus, A. H. Fluorescence-Detected Two-Dimensional Electronic Coherence Spectroscopy by Acousto-Optic Phase Modulation. *J. Chem. Phys.* **2007**, *127*, 214307.

(9) Lott, G. A.; Perdomo-Ortiz, A.; Utterback, J. K.; Widom, J. R.; Aspuru-Guzik, A.; Marcus, A. H. Conformation of Self-Assembled Porphyrin Dimers in Liposome Vesicles by Phase-Modulation 2D Fluorescence Spectroscopy. *Proc. Natl. Acad. Sci. USA* **2011**, *108*, 16521–16526.

(10) Tiwari, V.; Matutes, Y. A.; Konar, A.; Yu, Z.; Ptaszek, M.; Bocian, D. F.; Holten, D.; Kirmaier, C.; Ogilvie, J. P. Strongly Coupled Bacteriochlorin Dyad Studied using Phase-Modulated Fluorescence-Detected Two-Dimensional Electronic Spectroscopy. *Opt. Express* **2018**, *26*, 22327–22341.

(11) Karki, K. J.; Chen, J.; Sakurai, A.; Shi, Q.; Gardiner, A. T.; Kühn, O.; Cogdell, R. J.; Pullerits, T. Before Förster. Initial Excitation in Photosynthetic Light Harvesting. *Chem. Sci.* **2019**, *10*, 7923–7928.

(12) Nardin, G.; Autry, T. M.; Silverman, K. L.; Cundiff, S. T. Multidimensional Coherent Photocurrent Spectroscopy of a Semiconductor Nanostructure. *Opt. Express* **2013**, *21*, 28617–28627.

(13) Karki, K. J.; Widom, J. R.; Seibt, J.; Moody, I.; Lonergan, M. C.; Pullerits, T.; Marcus, A. H. Coherent Two-Dimensional Photocurrent Spectroscopy in a PbS Quantum Dot Photocell. *Nat. Commun.* **2014**, *5*, 5869.

(14) Bolzonello, L.; Bernal-Texca, F.; Gerling, L. G.; Ockova, J.; Collini, E.; Martorell, J.; van Hulst, N. F. Photocurrent-Detected 2D Electronic Spectroscopy Reveals Ultrafast Hole Transfer in Operating PM6/Y6 Organic Solar Cells. *J. Phys. Chem. Lett.* **2021**, *12*, 3983–3988.

(15) Roeding, S.; Brixner, T. Coherent Two-Dimensional Electronic Mass Spectrometry. *Nat. Commun.* **2018**, *9*, 2519.

(16) Uhl, D.; Bangert, U.; Bruder, L.; Stienkemeier, F. Coherent optical 2D photoelectron spectroscopy. *Optica* **2021**, *8*, 1316–1324.

(17) Bakulin, A. A.; Silva, C.; Vella, E. Ultrafast Spectroscopy with Photocurrent Detection: Watching Excitonic Optoelectronic Systems at Work. *J. Phys. Chem. Lett.* **2016**, *7*, 250–258.

(18) Wang, C.; Cai, J.; Liu, X.; Chen, C.; Chen, X.; Karki, K. J. In Operando Quantification of Single and Multiphoton Photocurrents in GaP and InGaN Photodetectors with Phase-Modulated Femtosecond Light Pulses. *ACS Photonics* **2023**, *10*, 1119–1125.

(19) Tiwari, V.; Matutes, Y. A.; Gardiner, A. T.; Jansen, T. L. C.; Cogdell, R. J.; Ogilvie, J. P. Spatially-Resolved Fluorescence-Detected Two-Dimensional Electronic Spectroscopy Probes Varying Excitonic Structure in Photosynthetic Bacteria. *Nat. Commun.* **2018**, *9*, 4219.

(20) Bangert, U.; Stienkemeier, F.; Bruder, L. High-Resolution Two-Dimensional Electronic Spectroscopy Reveals the Homogeneous Line Profile of Chromophores Solvated in Nanoclusters. *Nat. Commun.* **2022**, *13*, 3350.

(21) Fersch, D.; Malý, P.; Rühe, J.; Lisinetskii, V.; Hensen, M.; Würthner, F.; Brixner, T. Single-Molecule Ultrafast Fluorescence-Detected Pump–Probe Microscopy. *J. Phys. Chem. Lett.* **2023**, *14*, 4923–4932.

(22) Perdomo-Ortiz, A.; Widom, J. R.; Lott, G. A.; Aspuru-Guzik, A.; Marcus, A. H. Conformation and Electronic Population Transfer in Membrane-Supported Self-Assembled Porphyrin Dimers by 2D Fluorescence Spectroscopy. *J. Phys. Chem. B* **2012**, *116*, 10757–10770.

(23) Kjellberg, P.; Brüggemann, B.; Pullerits, T. Two-Dimensional Electronic Spectroscopy of an Excitonically Coupled Dimer. *Phys. Rev. B* **2006**, *74*, 024303.

(24) Cipolloni, M.; Fresch, B.; Occhiuto, I.; Rukin, P.; Komarova, K. G.; Cecconello, A.; Willner, I.; Levine, R. D.; Remacle, F.; Collini, E. Coherent Electronic and

Nuclear Dynamics in a Rhodamine Heterodimer–DNA Supramolecular Complex. *Phys. Chem. Chem. Phys.* **2017**, *19*, 23043–23051.

(25) Malý, P.; Lüttig, J.; Mueller, S.; Schreck, M. H.; Lambert, C.; Brixner, T. Coherently and Fluorescence-Detected Two-Dimensional Electronic Spectroscopy: Direct Comparison on Squaraine Dimers. *Phys. Chem. Chem. Phys.* **2020**, *22*, 21222–21237.

(26) Malý, P.; Mančal, T. Signatures of Exciton Delocalization and Exciton–Exciton Annihilation in Fluorescence-Detected Two-Dimensional Coherent Spectroscopy. *J. Phys. Chem. Lett.* **2018**, *9*, 5654–5659.

(27) Schröter, M.; Pullerits, T.; Kühn, O. Using Fluorescence Detected Two-Dimensional Spectroscopy to Investigate Initial Exciton Delocalization between Coupled Chromophores. *J. Chem. Phys.* **2018**, *149*, 114107.

(28) Kunsel, T.; Tiwari, V.; Matutes, Y. A.; Gardiner, A. T.; Cogdell, R. J.; Ogilvie, J. P.; Jansen, T. L. C. Simulating Fluorescence-Detected Two-Dimensional Electronic Spectroscopy of Multichromophoric Systems. *J. Phys. Chem. B* **2019**, *123*, 394–406.

(29) Kühn, O.; Mančal, T.; Pullerits, T. Interpreting Fluorescence Detected Two-Dimensional Electronic Spectroscopy. *J. Phys. Chem. Lett.* **2020**, *11*, 838–842.

(30) Bruschi, M.; Gallina, F.; Fresch, B. Simulating Action-2D Electronic Spectroscopy of Quantum Dots: Insights on the Exciton and Biexciton Interplay from Detection-Mode and Time-Gating. *Phys. Chem. Chem. Phys.* **2022**, *24*, 27645–27659.

(31) Grégoire, P.; Srimath Kandada, A. R.; Vella, E.; Tao, C.; Leonelli, R.; Silva, C. Incoherent Population Mixing Contributions to Phase-Modulation Two-Dimensional Coherent Excitation Spectra. *J. Chem. Phys.* **2017**, *147*, 114201.

(32) Bargigia, I.; Gutiérrez-Meza, E.; Valverde-Chávez, D. A.; Marques, S. R.; Srimath Kandada, A. R.; Silva, C. Identifying Incoherent Mixing Effects in the Coherent Two-Dimensional Photocurrent Excitation Spectra of Semiconductors. *J. Chem. Phys.* **2022**, *157*, 204202.

(33) Kalaee, A. A. S.; Damtie, F.; Karki, K. J. Differentiation of True Nonlinear and Incoherent Mixing of Linear Signals in Action-Detected 2D Spectroscopy. *J. Phys. Chem. A* **2019**, *123*, 4119–4124.

(34) Mukamel, S. Communication: The Origin of Many-Particle Signals in Nonlinear Optical Spectroscopy of Non-Interacting Particles. *J. Chem. Phys.* **2016**, *145*, 041102.

(35) Damtie, F. A.; Wacker, A.; Pullerits, T.; Karki, K. J. Two-Dimensional Action Spectroscopy of Excitonic Systems: Explicit Simulation using a Phase-Modulation Technique. *Phys. Rev. A* **2017**, *96*, 053830.

(36) Anda, A.; Cole, J. H. Two-Dimensional Spectroscopy Beyond the Perturbative Limit: The Influence of Finite Pulses and Detection Modes. *J. Chem. Phys.* **2021**, *154*, 114113.

(37) van Grondelle, R. Excitation Energy Transfer, Trapping and Annihilation in Photosynthetic Systems. *Biochim. Biophys. Acta - Bioenerg.* **1985**, *811*, 147–195.

(38) Van Amerongen, H.; van Grondelle, R.; Valkunas, L., *Photosynthetic Excitons*; World Scientific: Singapore, 2000.

(39) May, V.; Kühn, O., *Charge and Energy Transfer Dynamics in Molecular Systems*; Wiley-VCH: Weinheim, 2011.

(40) Mukamel, S., *Principles of Nonlinear Optical Spectroscopy*; Oxford University Press: Oxford, 1995.

(41) Yang, M.; Fleming, G. R. Third-Order Nonlinear Optical Eesponse of Energy Transfer Systems. *J. Chem. Phys.* **1999**, *111*, 27–39.

(42) McNamee, M. G.; Ouyang, Z.; Yan, L.; Gan, Z.; Zhou, N.; Williams, O. F.; You, W.; Moran, A. M. Uncovering Transport Mechanisms in Perovskite Materials and Devices with Recombination-Induced Action Spectroscopies. *J. Phys. Chem. C* **2023**, *127*, 2782–2791.

(43) Zhou, N.; Ouyang, Z.; Hu, J.; Williams, O. F.; Yan, L.; You, W.; Moran, A. M. Distinguishing Energy- and Charge-Transfer Processes in Layered Perovskite Quantum Wells with Two-Dimensional Action Spectroscopies. *J. Phys. Chem. Lett.* **2020**, *11*, 4570–4577.

(44) Ouyang, Z.; Zhou, N.; McNamee, M. G.; Yan, L.; Williams, O. F.; You, W.; Moran, A. M. Multidimensional Time-of-Flight Spectroscopy. *J. Chem. Phys.* **2021**, *154*, 220901.

(45) Malý, P.; Mueller, S.; Lüttig, J.; Lambert, C.; Brixner, T. Signatures of Exciton Dynamics and Interaction in Coherently and Fluorescence-Detected Four- and Six-Wave-Mixing Two-Dimensional Electronic Spectroscopy. *J. Chem. Phys.* **2020**, *153*, 144204.

(46) May, V. Kinetic Theory of Exciton–Exciton Annihilation. *J. Chem. Phys.* **2014**, *140*, 054103.

(47) Kiessling, A. J.; Cina, J. A. Monitoring the Evolution of Intersite and Interexciton Coherence in Electronic Excitation Transfer via Wave-Packet Interferometry. *J. Chem. Phys.* **2020**, *152*, 244311.

5 | Multiple Pathways to Non-Linearity in A-2DES

5.1. Introduction

Action-2D Electronic Spectroscopy (A-2DES) has been attracting significant attention due to its advantages compared to conventional Coherent-2D Electronic Spectroscopy (C-2DES). Both techniques are employed to investigate the dynamics of complex multi-chromophoric systems. In C-2DES, the observable is a *coherent* electric field originating from the macroscopic polarization of the sample induced by a sequence of laser pulses [1, 2]. Conversely, in A-2DES, the observable is an *incoherent* signal proportional to the excited-state population generated by the light-matter interaction [3, 4]. The nature of this incoherent observable connects 2DES to almost any kind of signal, i.e., fluorescence [5], photocurrent [6–8], photoions [9], and photoelectrons [10, 11], allowing for the study of a wide range of systems under *operando* conditions [12]. Furthermore, A-2DES can be combined with microscopy techniques [13] or even single-molecule detection [14].

However, the difference between the information obtained from the two techniques is a matter of debate. Indeed, the third-order polarization detected in C-2DES cannot be simply reconstructed from the fourth-order population generated in A-2DES. Indeed, while in C-2DES, the signal is emitted over an ultrafast timescale (ps) limited by the dephasing of the optical coherence, in A-2DES, the incoherent signal is collected over a longer timescale (>ns) during which the excited-state population may undergo several processes during the detection.

Among these processes, we recognize the internal conversion from excited states with higher energy to those with lower energy, from which fluorescence occurs according to Kasha's rule [15]. Another example is represented by Exciton-Exciton Annihilation (EEA) in multichromophoric systems [5, 13, 16] and Auger recombination in nanostructures [7,

Adapted from Bolzonello, L.; Bruschi, M.; Fresch, B., van Hulst, N.F. *manuscript under revision*.

17, 18], both resulting in the net loss of an exciton. These processes underlie the emergence of cross-peaks in the spectrum at early waiting times [19–21]. Furthermore, it has been reported how the phenomenon of incoherent mixing can affect A-2DES spectra [22]. In this case, due to non-linear population dynamics [22], e.g., exciton-exciton annihilation, Auger recombination, or to non-linearities in the detection process [23], linear responses can mix during the detection entering the signal and potentially masking the non-linear response of the system [22, 24, 25].

The equivalence between the origin of cross-peaks at early waiting times and the phenomenon of incoherent mixing was recently demonstrated for a weakly interacting molecular dimer in the presence of EEA [25]. However, it is not yet clear how incoherent mixing affects the response in the case of multichromophoric systems and whether other mechanisms beyond EEA may lead to the same spectral features. This work clarifies these aspects. Specifically, we will show that, in the case of molecular assemblies, i) cross-peaks related to incoherent mixing translates into the dominance of the ground-state bleaching over the stimulated emission contribution of the signal and ii) the effect does not necessarily require *direct* interaction between excitons, e.g., EEA or Auger recombination, but it can result from other *indirect* interactions. To give a concrete example, natural photosynthetic proteins, such as Photosystem I and II or Light Harvesting complex 1 (LH1), contain a high number of chromophores but only one reaction center [26]. If two excitations are generated, they can directly interact leading to EEA. However, if one excitation reaches the reaction center, it influences the fate of the second excitation in a very indirect way. Indeed, as long as the charge separation step is slower than the exciton lifetime, the second excitation will eventually relax to the ground state because of the impossibility of reaching the reaction center. These additional non-linearities are characteristic of action detection schemes implying a mismatch between action- and coherent-detected spectra.

The light-matter interaction is commonly described in the framework of response theory [27]. The non-linear signal is given by higher-order terms in the response that allow a comprehensive explanation of the quantum dynamics of the system. At the same time, these theoretical tools could drive the spectroscopist far from a more practical and experimental approach. For this reason, here we examine the contributions to the signal using two approaches. The first approach involves the probabilistic description of light-matter interaction considering an assembly of N molecules. This approach aims to identify the sources of non-linearity in cases where the number of readable outputs differs from the number of molecules excited. In other words, we are referring to those systems where more than one exciton can be excited, such as multichromophoric systems as well as quantum

dots, but a smaller number of excitons can be detected, because of exciton-exciton annihilation, Auger recombination, internal conversion or limited charge separation. The second approach translates these findings into the framework of response theory. The non-linear signal is given by several contributions related to the different pathways followed by the system upon light-matter interaction. For the third-order polarization, these contributions are Ground-State Bleaching (GSB), Stimulated Emission (SE), and Excited-State Absorption (ESA), commonly used to describe the signal in pump-probe spectroscopy and 2DES. As anticipated, in the context of action-detected techniques, the readout involves the detection of the fourth-order population, i.e., the number of excitons after the pulse train. If populations decay through different processes other than the emission, the signal could suffer from non-linearities beyond the optical one. To include these, it is useful to distinguish between the non-linear terms involving a single molecule and the ones involving different molecules in the same assembly. Throughout our discussion, we assume excitations with a local character and therefore weak coupling between distinct absorbing units.

5.2. Results and Discussion

Let us start by considering an assembly of N identical molecules, each described by a ground state $|g\rangle$ and an excited state $|e\rangle$ (Fig. 5.1a). In the multi-particle basis, the state of the assembly is given by accounting for the state of each molecule simultaneously [21, 25, 28]. The states can be distinguished into different manifolds which differ by the number of excited molecules (Fig. 5.1b). The number of states in each manifold $|k\rangle$ scales as the binomial coefficient:

$$\binom{N}{k} = \frac{N!}{k!(N-k)!} \tag{5.1}$$

where k is the number of excitons. In the following, each assembly is assumed to contribute to the signal with a single output, i.e., one photon emission or one charge separation. We stress that this simple assumption mimics indistinctly very different scenarios: the presence of non-linear population dynamics, e.g., EEA or Auger recombination, non-linear signal generation, e.g., charge separation in photosynthetic systems, or non-linearities in the detection, e.g., single-photon detector.

Initially, all the molecules are in their ground state. Then, they interact subsequently with two identical laser pulses, referred to as pump and probe in analogy with spectroscopy. At each pulse, a molecule can undergo an electronic transition with probability $p = I\sigma$, where I is the photon fluence and σ is its cross-section, or remain in the same state

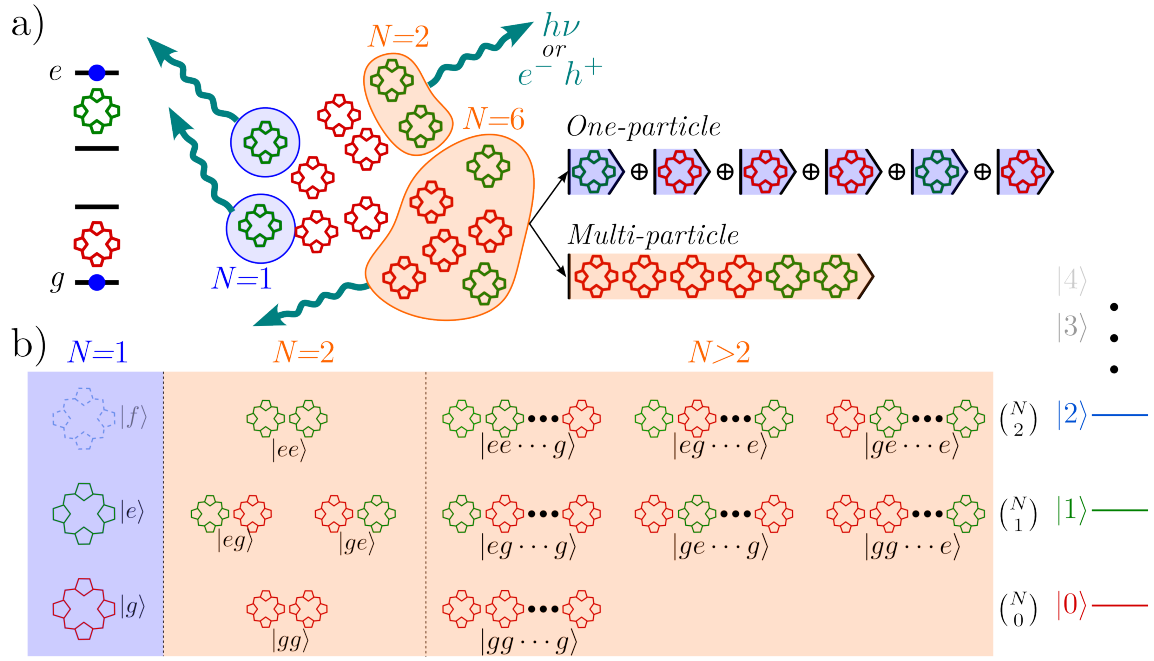

Fig. 5.1: In action spectroscopy, the detected signal is proportional to the excited-state population. a) In an ensemble of identical molecules, represented as two-level systems, the signal is proportional to the number of excited molecules. The molecules can be independent (blue-circled) or grouped in assemblies of N molecules (orange-circled) emitting a single output. The state of the assembly can be represented using a single-particle or a multi-particle description. b) From the multi-particle perspective, the states can be distinguished into different manifolds $|k\rangle$, depending on the number of excitons k. The number of states in each manifold is determined by the binomial coefficient $\binom{N}{k}$.

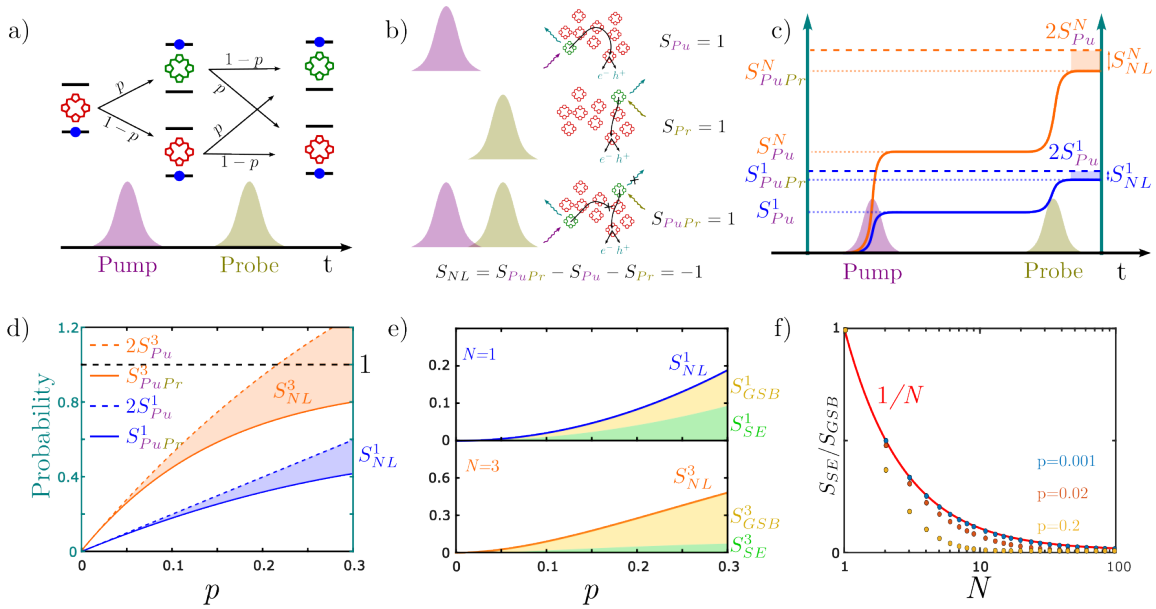

Fig. 5.2: Simulation of action-detected pump-probe experiment for a molecular assembly. a) An assembly interacts with two pulses, namely pump and probe. For each pulse, a molecule can either undergo a transition with probability p or remain in the same state with probability $1-p$. b) The non-linear signal is given by the difference between the pump-probe signal S_{PuPr} and that of independent pump and probe S_{Pu} and S_{Pr}. The depiction of an assembly shows how part of the non-linear signal originates from the excitation of distinct molecules by different pulses, which happens if the two excitations undergo annihilation or share the same reaction center for charge separation. c) A schematic representation illustrating the pump-probe experiment. The interaction with the pump excites molecules in the assembly with a certain probability. By finding the assembly in a different population state, the interaction with the probe does not double the probability of molecules being in the excited state, giving rise to the non-linear signal. d) Signal from the pump-probe (solid line), signal from two independent pulses (dashed line) and non-linear signal (infill area) as a function of the transition probability p for an assembly with $N=1$ (blue) and $N=3$ (orange). e) Decomposition of the non-linear signal in GSB and SE contributions for $N=1$ and $N=3$. f) The ratio between SE and GSB contributions follows $1/N$ for $p\to 0$, while it decreases for higher values.

with probability $1-p$ (Fig. 5.2a). In a realistic assembly, molecules can have different orientations, thus p would be different for each molecule. For the sake of simplicity, we keep p equal for all molecules, however the main conclusions hold in the more general case.

After the pump pulse, the probability of having a certain number of molecules in the excited state $P_{N,k}$ follows the binomial distribution:

$$P_{N,k}=\binom{N}{k}p^k(1-p)^{N-k}. \tag{5.2}$$

We define the probability of detecting a signal after the pump pulse as the probability of

having at least one molecule excited in the assembly:

$$S_{Pu}^{N} = 1 - P_{N,0} = 1 - (1-p)^{N} \tag{5.3}$$

where $(1-p)^N$ represents the probability that none of the N molecules get excited. Notice that for $N = 1$, the signal simply reduces to $S_{Pu}^{1} = p = I\sigma$, that is the probability of exciting an independent molecule. Within the same detection setting, the signal after the pump-probe sequence is again proportional to the probability of having at least one excitation in the system. This can be evaluated from the probability of the complementary event, that is every molecule is in the ground state. This is true if each molecule undergoes either no transition $(1-p)^2$ or two transitions p^2 :

$$S_{PuPr}^{N} = 1 - \left[(1-p)^2 + p^2\right]^{N}. \tag{5.4}$$

The non-linear signal is obtained by subtracting the pump-probe signal from that of the independent pump and probe pulses (Fig. 5.2c):

$$\begin{aligned} S_{NL}^{N} &= 2S_{Pu}^{N} - S_{PuPr}^{N} \\ &= 2\left[1-(1-p)^{N}\right] - \left\{1 - \left[(1-p)^2 + p^2\right]^{N}\right\}. \end{aligned} \tag{5.5}$$

From the spectroscopic point of view, the non-linear signal can be extracted by modulating the amplitude of the pulses using a chopper (Fig. 5.2b), as done in two-pulse action-detected experiments [29–32].

In Fig. 5.2d, we report the non-linear signal for two assemblies with different numbers of molecules, $N = 1$ and $N = 3$. We notice that, for $N = 1$, the non-linearity comes only from the double interaction with the pulses as S_p^1 is linear with p, while for $N > 1$, even the signal from the single pulse is non-linear, according to Eq. 5.3. Notice that, since a single output is detected, the non-linear signal saturates at 1 for any value of N. However, the probability of measuring an output increases steeper as N becomes larger. Therefore, at this stage, we can already highlight two different sources of non-linearity: the optical non-linearity due to the interaction with the two laser pulses and the non-linearity in the signal detection due to the measurement of a single output.

However, before aiming at these classifications, it is convenient to identify two complementary non-linear contributions: the Stimulated Emission (SE) and the Ground-State Bleaching (GSB). The SE signal is given by the process in which the probe de-excites a molecule that has been excited by the pump. Since this event is detected only when

it leads to a change in the signal, if another molecule in the assembly gets excited, the double transition would result unmeasured. Thus, in our model, SE signal is defined as the probability that at least one molecule in the assembly undergoes two transitions and the final output is vanishing:

$$S_{SE}^{N} = \left[(1-p)^2 + p^2\right]^N - (1-p)^{2N} \tag{5.6}$$

where $[(1-p)^2 + p^2]^N$ is the probability of vanishing output from the assembly, while $(1-p)^{2N}$ is the probability that all molecules undergo no transitions.

Instead, the GSB signal is given by the probability that the probe excites at least one molecule in the assembly, given that the pump has already excited another molecule, as this would give no additional signal:

$$S_{GSB}^{N} = [1-(1-p)^N]^2. \tag{5.7}$$

In other words, this is the lack of signal because the assembly has been excited by the pump. The non-linear signal corresponds to the sum of GSB and SE contributions:

$$S_{NL}^{N} \equiv S_{GSB}^{N} + S_{SE}^{N}. \tag{5.8}$$

In Fig. 5.2e, we show the decomposition of the non-linear signal into SE and GSB contributions. For $N = 1$, the two contributions are equal $S_{SE}^{1} = S_{GSB}^{1}$ as expected for independent molecules, while for $N > 1$, S_{GSB}^{N} becomes larger than S_{SE}^{N}. As shown in Fig. 5.2f, their ratio is:

$$\frac{S_{SE}^{N}}{S_{GSB}^{N}} \leq \frac{1}{N} \tag{5.9}$$

where the equality holds in the limit of small transition probabilities, $p \to 0$.

The probabilistic approach can be connected to the perturbative framework of non-linear response theory, thus enabling the analysis of action-detected 2D experiments. In four-pulse A-2DES, the components of the fourth-order signal are typically selected using phase-cycling [33, 34] or phase-modulation [35] schemes. The pulses are separated by delay times t_1, t_2 and t_3, while the emission of the incoherent signal occurs during t_4. At each light-matter interaction, the state of the system changes from population to coherence and *vice versa*. Therefore, each second-order interaction, which occurs with probability p in the pump-probe picture discussed above, is replaced by two first-order interactions in the four-pulse setting (Fig. 5.3a).

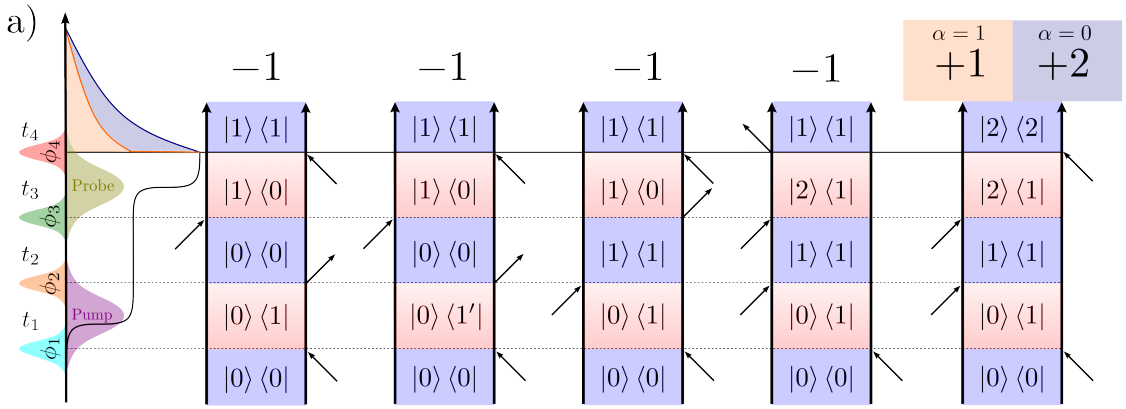

b)

α	$\mathbf{GSB}^s$	$\mathbf{GSB}^c$	$\mathbf{SE}^s$	$\mathbf{ESAI}^c$	$\mathbf{ESAII}^c$
0	$-N$	$-N(N-1)$	$-N$	$-N(N-1)$	$2N(N-1)$
$(0,1)$	$-N$	$-N(N-1)$	$-N$	$-N(N-1)$	$(2-\alpha)N(N-1)$
1	$-N$	$-N(N-1)$	$-N$	$-N(N-1)$	$N(N-1)$

Fig. 5.3: a) Feynman diagrams for Ground-State Bleaching (GSB), Stimulated Emission (SE), Excited-State Absorption I (ESAI) and Excited-State Absorption II (ESAII) of the rephasing signal in A-2DES. The diagrams are distinguished into self-population pathways “s", if the four pulses interact with the same chromophore, and cross-population pathways “c", if each pair of pulses interacts with different chromophores. b) Table reporting the number of contributions to the signal for each kind of pathway, in the case of different values of the coefficient α. For $\alpha = 0$, there is mutual cancellation between cross-population pathways, while for $\alpha = 1$, only ESA-type pathways mutually cancel.

Without loss of generality, we limit our analysis to the case where only one- and two-exciton manifolds, denoted as $|1\rangle$ and $|2\rangle$ in Fig. 5.1b, are populated with a non-negligible probability at the end of the pulse train. As shown in Fig. 5.1b, these manifolds consist of all the states in which one or two molecules are excited. We define $P_{e_n g}$ as the probability that the system is in the collective state $|g_1 \dots e_n \dots g_N\rangle$ in the one-exciton manifold and $P_{e_n e_m}$ as the probability of being in the state $|g_1 \dots e_n \dots e_m \dots g_N\rangle$ in the two-exciton manifold.

In experiments, the incoherent signal is typically integrated along the detection time t_4. The time-integrated signal results proportional to the population of one- and two-exciton manifolds at $t_4 = 0$, which in turn depend on the delay times t_1, t_2 and t_3 and the phases of the pulses. By selecting a certain phase combination, e.g. rephasing, non-rephasing or double-quantum coherence, and assuming that all chromophores have identical quantum yield Φ, the time-integrated signal can be written as

$$\overline{S} = \Phi \sum_{n=1} P_{e_n g}(0) + (2-\alpha)\Phi \sum_{n=1} \sum_{m>n} P_{e_n e_m}(0) \tag{5.10}$$

where the parameter α quantifies the deviation of the contribution of the two-exciton manifold from twice that of the one-exciton manifold. In the App. 5.A, we derive Eq. 5.10 from a kinetic model for the populations during the detection time, including exciton recombination, EEA and different signal generation rates of the one- and two-exciton manifolds.

The different pathways that generate populations on the one- and two-exciton manifold upon light-matter interaction can be visualized in terms of Feynman Diagrams (FDs). In Fig. 5.3a, we report FDs for the rephasing signal considering the ground state $|0\rangle$, the one-exciton state $|1\rangle$ and the two-exciton state $|2\rangle$. Notice that pathways that are in a coherence during the waiting time t_2 have been neglected. In the weak coupling limit, this coherence is established between (localized) site states rather than (delocalized) excitonic states. Since this coherence dephases at twice the rate of the optical coherence, these pathways can be neglected when the dephasing time is comparable to the pulse duration.

The pathways are distinguished into Ground-State Bleaching (GSB), Stimulated Emission (SE), and Excited-State Absorption (ESA) processes. While both GSB and SE pathways end in a one-exciton population, the presence of a fourth pulse gives rise to two kinds of ESA pathways, ending either in a one-exciton (ESAI) or in a two-exciton (ESAII) population. Each pathway contributes to the signal with a sign $(-1)^{n_B}$, where n_B is the number

of interactions on the *bra* side of the FD. Therefore, GSB, SE and ESAI contribute with negative features to the spectrum, while ESAII comes with positive sign. Depending on their sign, spectral features associated with different pathways may interfere constructively or destructively in the spectrum, eventually leading to partial or complete cancellation.

In weakly interacting systems, FDs can be differentiated into self- and cross-population pathways [25], respectively identified by the superscript “s" and “c" in Fig. 5.3a. In self-population pathways, the four pulses interact with the same chromophore, while in cross-population pathways, each pair of pulses interacts with different chromophores. Since self- and cross-population pathways have the same phase relation, they are extracted together in the signal. To comprehend their contribution to the final spectrum, we need to understand how the different pathways combine in the signal. Notice that in the present model, ESA-type contributions are all cross-population pathways simply because we have assumed that each molecule is described as a two-level system. While this assumption simplifies the analysis of the signal, it can be relaxed by including the double excited state of each molecule.

First, consider the ideal case where the two-exciton state contributes twice as much as the one-exciton state to the signal, corresponding to $\alpha = 0$ in Eq. 5.10. This is realized in the absence of EEA and when the signal generation rate of the two-exciton manifold is twice that of the one-exciton manifold. Under these conditions, the signal reduces to the sum of the non-linear response of independent chromophores, that is:

$$\overline{S} = \Phi \sum_{n=1} P_{e_n}(0) \tag{5.11}$$

where the single chromophore population results from the sum over that of the collective states, $P_{e_n} = P_{e_n g} + \sum_{m \neq n} P_{e_n e_m}$. In this case, only the GSB and SE self-population pathways contribute to the spectrum, meaning that the ESAII cross-population pathways exactly cancel the GSB and ESAI cross-population pathways. This corresponds to the situation with $N = 1$ in Eqs. 5.6 and 5.7, recovering an equal intensity of GSB and SE contributions to the non-linear signal while other sources of non-linearity are absent.

The situation changes when $\alpha > 0$. Let us consider the case where the assembly of N molecules generates the same signal independently of the number of excitations so that the one- and two-exciton manifold contributes equally, corresponding to $\alpha = 1$ in Eq. 5.10. In the App. 5.A, we show that this situation can result either because of fast EEA during t_4 or when the two-exciton manifold generates the signal at the same rate as the

one-exciton manifold, in the absence of EEA. In this case, which identifies the limit of complete annihilation, the signal can be written as

$$\begin{aligned}\overline{S} &= \Phi \sum_{n=1} P_{e_n g}(0) + \Phi \sum_{n=1} \sum_{m>n} P_{e_n e_m}(0) \\ &= \Phi \sum_{n=1} P_{e_n}(0) - \Phi \sum_{n=1} \sum_{m>n} P_{e_n}(0) \times P_{e_m}(0).\end{aligned} \tag{5.12}$$

Notice that the contribution of the two-exciton state to the signal is reduced, resulting in the mutual cancellation between the ESAII and ESAI cross-population pathways. Therefore, in addition to the self-population pathways from GSB and SE, also the GSB cross-population pathways contribute to the spectrum. This contribution to the signal corresponds to the non-linearity due to the reduced response of the assembly, resulting from Eqs. 5.6 and 5.7 for $N > 1$.

The second equality in Eq. 5.12 shows that, in the case of weak coupling between different chromophores, the population of the two-exciton manifold at $t_4 = 0$ can be factorized as $P_{e_n e_m}(0) = P_{e_n}(0) \times P_{e_m}(0)$. Therefore, the additional signal boils down to the product of the linear signals of the individual molecules. This is analogous to the phenomenon of incoherent mixing [22, 24, 25] as we will further discuss below.

A key point to note is the different scaling in the number of self- and cross-population pathways: GSB involves N self-population pathways and $N \cdot (N-1)$ cross-population pathways, while SE involves N self-population pathways (Fig. 5.3b). This is reflected in the number of linear and product terms contributing to the signal in Eq. 5.12. As N increases, the striking consequence in the spectrum is the dominance of GSB cross-population contributions over the self-population signal, in analogy with the ratio resulting from the probabilistic analysis in Eq. 5.9. Indeed, the ratio between the number of SE and GSB pathways is:

$$\frac{SE}{GSB} = \frac{SE^s}{GSB^s + GSB^c} = \frac{N}{N + N(N-1)} = \frac{1}{N} \tag{5.13}$$

resulting that, for large N, the GSB contribution can completely dominate over the SE contribution, in the limiting case of $\alpha = 1$. Furthermore, we also notice that the ratio between the number of self- and cross-population pathways is:

$$\frac{\text{self}}{\text{cross}} = \frac{GSB^s + SE^s}{GSB^c} = \frac{2N}{N(N-1)} = \frac{2}{N-1} \tag{5.14}$$

meaning that, for large N, the non-linear signal is dominated by cross-population pathways.

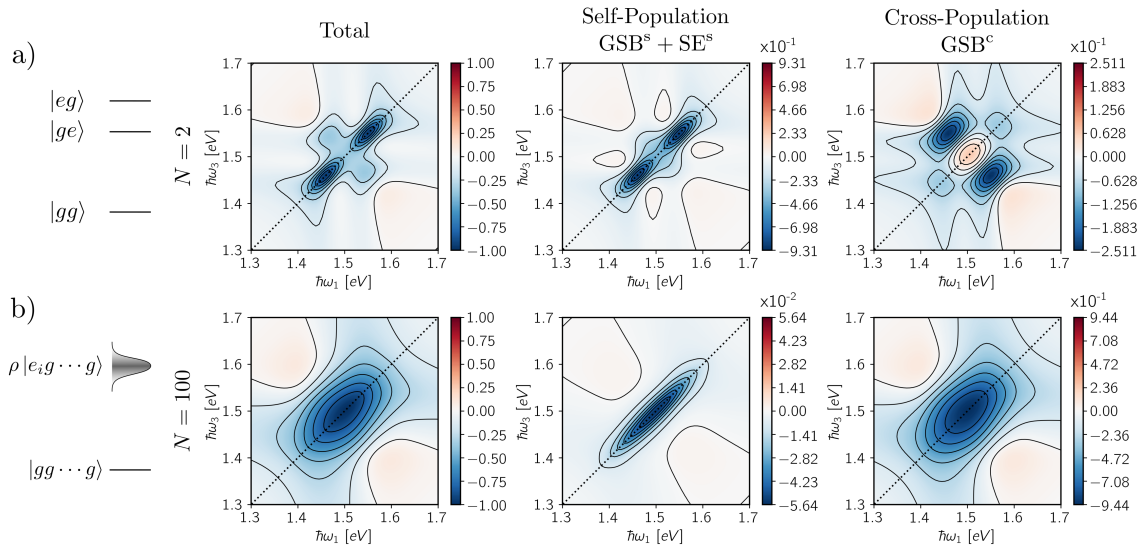

Fig. 5.4: Total (first column), self-population contribution (second column) and cross-population contribution (third column) for the rephasing signal of two different assemblies with a) $N = 2$ and b) $N = 100$. On the left, a schematic representation of the energy levels for the two systems.

These ratios are important to assess the information content in the spectra as SE is the only pathway containing information about the excited-state dynamics along t_2 and self-population pathways are the pathways containing the non-linear response of the chromophores. As N increases, the contribution of cross-population pathways becomes more significant, reducing the amount of dynamical information. In other words, both self- and cross-population pathways contribute to the spectra, but only the former actually provides information about the excited-state dynamics in the system, while the latter simply reduces to the product of linear responses of the two molecules with no evolution along t_2.

We now consider the interplay between self- and cross-population pathways to the A-2DES spectra at waiting time $t_2 = 0$ fs by varying the number of chromophores N. Assuming $\Phi = 1$ and $\alpha = 1$, in Fig. 5.4 we report the rephasing spectra for $N = 2$ (Fig. 5.4a) and $N = 100$ (Fig. 5.4b), along with the isolated contributions from self- and cross-population pathways. For $N = 2$, we consider two chromophores with different excitation energies so that the net effect is the appearance of well-defined cross-peaks. The transition energies of the two molecules are respectively $\epsilon_1 = 1.55$ eV and $\epsilon_2 = 1.46$ eV. Instead, the energies of the chromophores for $N = 100$ are drawn from a Gaussian distribution with mean $\mu = 1.5$ eV and standard deviation $\sigma = 45$ meV. In both cases, we consider a Voigt lineshape $g(t) = \Gamma t + \Delta^2 t^2$, which accounts for homogeneous ($\Delta = 20$ meV) and inhomogeneous ($\Gamma = 20$ meV) broadenings.

In the case of $N = 2$, the spectrum exhibits two diagonal peaks and two cross-peaks, corresponding to the self- and cross-population contributions, respectively. In this case, the amount of signal associated with cross-population pathways is smaller than the self-population one, meaning that the dynamical information brought by the SE contribution is not hidden. On the contrary, for $N = 100$, the spectrum is dominated by a single broad peak mainly due to the contribution of cross-population pathways. By recalling that cross-population contributions in the weak coupling limit reduce to the product of linear signals (incoherent mixing), a rather unexpected result of our analysis is that such mixing can happen even in the absence of direct interaction between excitons. Indeed, the emergence of the GSB cross-population contribution is related to the reduced signal generated by the two-exciton manifold, as resulting from Eqs. 5.10 and 5.12. This is reduced because of dynamical processes, e.g., EEA, but also for other intrinsic mechanisms limiting the emission to a single output. In this sense, the case of the reaction center generating charges on a timescale slower than the exciton lifetime is paradigmatic because $\alpha = 1$ even when two independent excitations are generated. Therefore, the emergence of cross-peaks does not necessarily reflect the presence of coupling between molecules nor the annihilation between different excitations.

The spectra in Fig. 5.4 refers to $t_2 = 0$. Since we are looking at the rephasing signal, self-population pathways are diagonally elongated whereas cross-population pathways result in inhomogeneously broadened spectra. The different lineshape reflects the fact that fluctuations on the same molecule are correlated, while those on different molecules are uncorrelated [36]. A discussion about the lineshape of self- and cross-population pathways in the presence of homogeneous and inhomogeneous broadening is reported in the App. 5.B. The evolution of the spectral lineshapes for longer t_2 is not considered explicitly here, however, while the lineshape of the self-population pathways reflects the evolution of the wavepacket during t_2, the GSB cross-population pathway only reflects the recovery of the ground state as much as the overall non-linear signal. Moreover, as t_2 increases, energy transfer between different molecules can take place resulting in cross-peaks carrying information about the excited-state dynamics. However, since these pathways would have the same weight as the self-population pathways from which they originate, we also expect them to be hidden by cross-population pathways when N is large.

In summary, we considered the different sources of non-linearity in the response of a molecular assembly excited by multiple pulses in the case of action detection. The probabilistic analysis offers a practical interpretation of the signal contributions described by response theory. For example, cancellation of the ESA pathways in the fourth-order re-

sponse simply corresponds to the fact that, when only one excitation can be detected, the number of excitation events does not change the output.

Therefore, we can conclude that when the output is not proportional to the number of excited molecules, action-detected spectroscopy cannot isolate pathways in which the interaction occurs on the same molecule (self-population pathways) or on different molecules (cross-population pathways). In the worst-case scenario of complete annihilation, i.e., $\alpha = 1$, the ratio between self- and cross-population pathways is $2/(N-1)$, where only the former bring dynamical information. Moreover, we highlight that the excited-state dynamics along t_2 is exclusively present in the SE contribution. Since the ratio SE/GSB has $1/N$ as an upper limit, the SE contribution is likely to be hidden or negligible for large N.

As a result, we are able to identify the origin of incoherent mixing as due to the fourth-order terms that correspond to GSB cross-population pathways, where the two coherences along the t_1 and t_3 occur on different molecules but result in a single output. In a 2D spectrum of a weakly interacting assembly, GSB^c pathways correspond to the product of the two linear signals and do not show evolution along t_2 beyond the ground-state recovery. Thus, for large N, A-2DES measurements would likely provide equivalent information to linear absorption. We can apply this argument to different systems as the key factor is the ratio between the number of output and excitation sites, which is $1/N$ in the case of equal contribution of the one- and two-exciton manifolds in the weak coupling scenario.

We report that excitonic coupling may change the result and play a positive role. Indeed, while the contribution of the two-exciton manifold can still be suppressed by efficient EEA or by non-linear signal generation mechanisms, the number of optically active GSB cross-population contributions may be reduced because of dipole moment redistribution. In this more general setting, N should be identified with the number of absorbing states rather than the number of independent chromophores. Moreover, in the case of strong excitonic coupling, cross-population pathways reflect the presence of delocalization in the system [16, 37]. An unexpected mitigation of the unfavorable scaling of self-population pathways comes from disorder. Indeed, the presence of inhomogeneous broadening improves the visibility of self-population pathways compared to cross-population pathways. This aspect is linked to the rephasing capability of the non-linear response, as shown explicitly in the App. 5.B.

When it is known that the signal corresponds to the case of complete annihilation ($\alpha = 1$), a potential advantage comes from the possibility of estimating N itself. N could be

an indicator of how many chromophores are connected to the output, such as the number of chlorophylls linked to the reaction center in a photosynthetic system. The estimation of N would become feasible if SE and GSB can be measured independently. For example, it is possible to design an experiment where the pump pulse overlaps only with the lower energies of the absorption band and the probe with the full band. Close to $t_2 = 0$, the A-2DES signal would exhibit both SE and GSB components at the pump frequencies, whereas only the GSB component at higher frequency, where the probe does not overlap with the pump. Nevertheless, action spectroscopies have strong limits in their use on a wide range of materials. For this reason, it is then crucial to be aware of the kind of samples to be studied with action-detected spectroscopies. Grégoire et al. showed that incoherent mixing can contribute differently depending on the amount of EEA in the sample [22]. Indeed, it has been found that incoherent mixing does not contribute significantly to the A-2DES spectrum of organic solar cells, while it dominates over the non-linear response in perovskite samples. Additionally, cross-peak dynamics has been observed in heterojunction photovoltaic cells [8]. This is possible because a working cell tries to achieve high internal quantum efficiency, implying that from every exciton a charge is produced, meaning a detection for every absorption ($\alpha = 0$ or $N = 1$).

The results reported in this work highlight the importance of strategies to minimize the incoherent mixing contributions to A-2DES. Recently, 2D-FLEX has been proposed, which can selectively measure the SE pathway in fluorescence-detected experiments [38]. Furthermore, the possibility of time-gating the fluorescence signal during the detection time can help to reduce the extent of incoherent mixing [18–20]. However, a time-gating approach is far-fetched to be applied in photocurrent detection.

5.3. Conclusions

In this work, we provided a different perspective to the problem of incoherent mixing in action-detected spectroscopy. Our argument explicitly refers to an assembly of weakly coupled molecules and it does not explicitly account for the presence of vibrational degrees of freedom. Future work is needed to understand how strong excitonic coupling may change the relative weight of the different contributions to the signal and to further elucidate the dynamics along the waiting time t_2. On the other hand, the inclusion of higher excited states $|f\rangle$ of each molecule introduces ESA self-population pathways providing additional spectral features, without affecting the scaling between SE and GSB contributions. A further step will be to consider higher-order response in the light-matter interaction in

order to investigate the signal coming from multi-exciton states [39, 40].

5.A. Populations and Incoherent Signal

In A-2DES, the time-resolved signal emitted during the detection time t is:

$$S(t) = k_S \sum_n P_{e_n g}(t) + (2k_S + \delta) \sum_n \sum_{m>n} P_{e_n e_m}(t) \tag{5.A.15}$$

where $P_{e_n g}(t)$ and $P_{e_n e_m}(t)$ are the populations of one- and two-exciton states, k_S represents the signal generation rate, while δ quantifies the difference in the signal generation rate between the two-exciton states and twice that of the one-exciton states. The populations are assumed to evolve according to the following kinetic scheme:

$$\begin{cases} \dfrac{d}{dt} P_{e_n g}(t) = -k_R P_{e_n g}(t) + (k_R + k_A) \displaystyle\sum_{m \neq n} P_{e_n e_m}(t) \\ \dfrac{d}{dt} P_{e_n e_m}(t) = -\left(2k_R + 2k_A + k_{AA}\right) P_{e_n e_m}(t) \end{cases} \tag{5.A.16}$$

where k_R is the exciton recombination rate, while k_A and k_{AA} are the exciton-exciton annihilation rates resulting in the net loss of one and two excitons, respectively. By solving the kinetic scheme, the time-resolved populations are obtained:

$$\begin{cases} P_{e_n g}(t) = P_{e_n g}(0) e^{-k_R t} + \dfrac{k_R + k_A}{k_R + 2k_A + k_{AA}} \left(e^{-k_R t} - e^{-(2k_R + 2k_A + k_{AA})t}\right) \displaystyle\sum_{m \neq n} P_{e_n e_m}(0) \\ P_{e_n e_m}(t) = P_{e_n e_m}(0) e^{-(2k_R + 2k_A + k_{AA})t} \end{cases} \tag{5.A.17}$$

where $P_{e_n g}(0)$ and $P_{e_n e_m}(0)$ are the populations at the end of the train of pulses. In an experiment, the signal is commonly integrated during the detection time. The time-integrated signal results:

$$\overline{S} = k_S \sum_n \overline{P_{e_n g}} + (2k_S + \delta) \sum_n \sum_{m>n} \overline{P_{e_n e_m}} \tag{5.A.18}$$

where the time-integrated populations are:

$$\begin{cases} \overline{P_{e_n g}} = \dfrac{1}{k_R} P_{e_n g}(0) + \dfrac{k_R + k_A}{k_R(2k_R + 2k_A + k_{AA})} \displaystyle\sum_{m \neq n} P_{e_n e_m}(0) \\ \overline{P_{e_n e_m}} = \dfrac{1}{2k_R + 2k_A + k_{AA}} P_{e_n e_m}(0). \end{cases} \tag{5.A.19}$$

Substituting Eq. 5.A.19 in Eq. 5.A.18, we obtain:

$$\begin{aligned}\overline{S} &= \frac{k_S}{k_R}\sum_n P_{e_n g}(0) + \frac{2k_S(2k_R+k_A)+\delta k_R}{k_R(2k_R+2k_A+k_{AA})}\sum_n\sum_{m>n} P_{e_n e_m}(0) \\ &= \Phi\sum_n P_{e_n g}(0) + (2-\alpha)\Phi\sum_n\sum_{m>n} P_{e_n e_m}(0)\end{aligned} \tag{5.A.20}$$

where $\Phi = \frac{k_S}{k_R}$ is the quantum yield, while $\alpha = \frac{2k_S(k_A+k_{AA})-\delta k_R}{k_S(2k_R+2k_A+k_{AA})}$ is a parameter which quantifies the deviation of the signal from that of independent molecules. Since $P_{e_n}(0) = P_{e_n g}(0) + \sum_{m\neq n} P_{e_n e_m}(0)$, the signal can be rewritten as:

$$\begin{aligned}\overline{S} &= \frac{k_S}{k_R}\sum_n P_{e_n}(0) - \frac{2k_S(k_A+k_{AA})-\delta k_R}{k_R(2k_R+2k_A+k_{AA})}\sum_n\sum_{m>n} P_{e_n}(0)\times P_{e_m}(0) \\ &= \Phi\sum_n P_{e_n}(0) - \alpha\Phi\sum_n\sum_{m>n} P_{e_n}(0)\times P_{e_m}(0)\end{aligned} \tag{5.A.21}$$

where we assumed that the initial population of the two-exciton can be factorized as $P_{e_n e_m}(0) = P_{e_n}(0)\times P_{e_m}(0)$. Eq. 5.A.21 is the generalization of Eq. 5.12 where α is assumed to be 1.

Considering the case where the signal generation rate of the two-exciton manifold is twice that of the one-exciton manifold ($\delta = 0$), the parameter $\alpha = 0$ when the exciton recombination is faster than annihilation $k_R \gg k_A, k_{AA}$, while the parameter $\alpha = 1$ when exciton-exciton annihilation is faster than exciton recombination $k_A \gg k_R, k_{AA}$. In contrast, in the case where the signal generation rate of the one- and two-exciton manifold is equal ($\delta = -k_S$), the parameter $\alpha = 1$ when exciton recombination rate is equal that of the loss of two excitons, $k_R = k_{AA} \gg k_A$ and $\delta = -k_S$.

5.B. Response Function and Lineshape

Considering the rephasing signal, the fourth-order response functions for self-population pathways are:

$$R_{GSB^s}(t_1,t_2,t_3) = -\left(\frac{i}{\hbar}\right)^4\sum_n |\mu_n|^4 e^{+i\omega_n t_1} e^{-i\omega_n t_3} F_S(t_1,t_2,t_3) \tag{5.B.22}$$

$$R_{SE^s}(t_1,t_2,t_3) = -\left(\frac{i}{\hbar}\right)^4\sum_n |\mu_n|^4 e^{+i\omega_n t_1} e^{-i\omega_n t_3} F_S(t_1,t_2,t_3) \tag{5.B.23}$$

and for cross-population pathways are:

$$R_{GSB^c}(t_1, t_2, t_3) = -\left(\frac{i}{\hbar}\right)^4 \sum_n \sum_{m\neq n} |\mu_n|^2 |\mu_m|^2 e^{+i\omega_n t_1} e^{-i\omega_m t_3} F_C(t_1, t_2, t_3) \tag{5.B.24}$$

$$R_{ESAI^c}(t_1, t_2, t_3) = -\left(\frac{i}{\hbar}\right)^4 \sum_n \sum_{m\neq n} |\mu_n|^2 |\mu_m|^2 e^{+i\omega_n t_1} e^{-i\omega_m t_3} F_C(t_1, t_2, t_3) \tag{5.B.25}$$

$$R_{ESAII^c}(t_1, t_2, t_3) = +\left(\frac{i}{\hbar}\right)^4 \sum_n \sum_{m\neq n} |\mu_n|^2 |\mu_m|^2 e^{+i\omega_n t_1} e^{-i\omega_n t_3} F_C(t_1, t_2, t_3) \tag{5.B.26}$$

where ω_n and μ_n are the transition frequency and transition dipole moment of the n-th molecule, respectively. According to the stochastic theory of lineshape, the dephasing function for self-population pathways is:

$$F_s(t_1, t_2, t_3) = e^{-g(t_1)+g(t_2)-g(t_3)-g(t_1+t_2)-g(t_2+t_3)+g(t_1+t_2+t_3)} \tag{5.B.27}$$

while for cross-population pathways is:

$$F_c(t_1, t_2, t_3) = e^{-g(t_1)-g(t_3)} \tag{5.B.28}$$

where we assumed that the fluctuations on different molecules are independent [36, 41]. In the following, we consider a Voigt lineshape function [41]:

$$g(t) = \Gamma t + \Delta^2 t^2 \tag{5.B.29}$$

where Γ and Δ are the parameter related to homogeneous and inhomogeneous broadening, respectively. In this scenario, the dephasing functions for self- and cross-population pathways become:

$$F_s(t_1, t_2, t_3) = e^{-\Gamma(t_1+t_3)} e^{-\Delta^2(t_1^2+t_3^2-2t_1t_3)} \tag{5.B.30}$$

$$F_c(t_1, t_2, t_3) = e^{-\Gamma(t_1+t_3)} e^{-\Delta^2(t_1^2+t_3^2)}. \tag{5.B.31}$$

Notice the different behaviour of self- and cross-population pathways in the presence of inhomogeneous disorder. While the former give rise to photon echo for $t_1 = t_3$, the latter result in free-induction decay.

In Fig. 5.B.5, we show the ratio between the maxima of the spectral amplitudes of self- and cross-population features for different values of inhomogeneous broadening. Notice

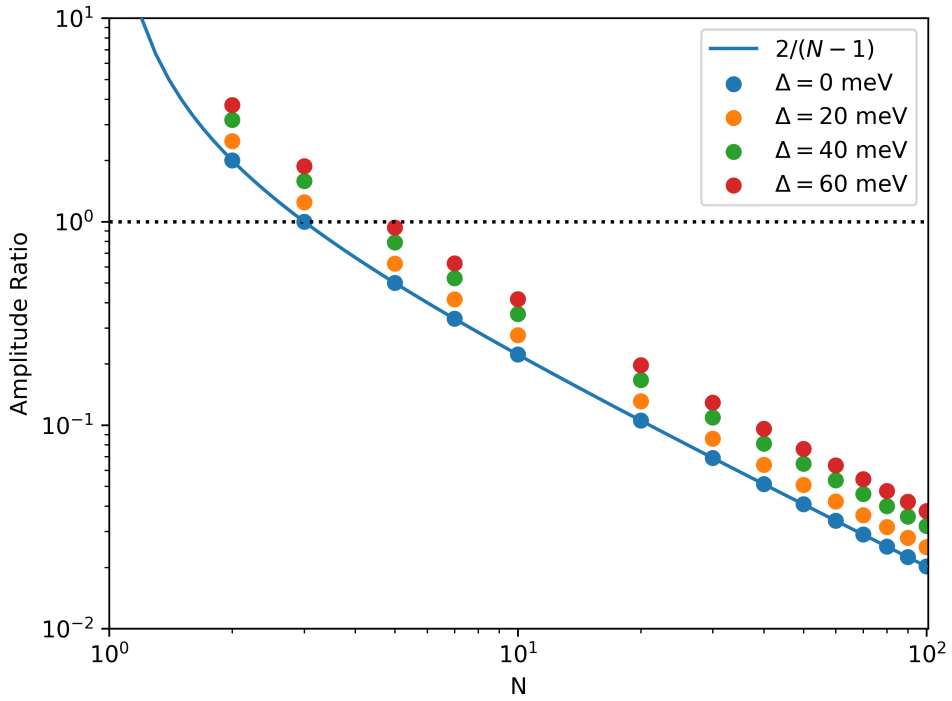

Fig. 5.B.5: Ratio between maxima of spectral amplitudes of self- and cross-population contributions for different values of inhomogeneous broadening Δ, while homogeneous broadening is kept constant ($\Gamma = 40$ meV). In this case, the transition energies of the molecules are assumed to be equal.

that only when $\Delta = 0$ meV, the ratio results:

$$\frac{\text{self}}{\text{cross}} = \frac{2}{N-1} \tag{5.B.32}$$

corresponding to Eq. 5.14. In the presence of inhomogeneous broadening, the ratio results higher due to the rephasing capability of self-population pathways compared to cross-population pathways.

References

(1) Collini, E. 2D Electronic Spectroscopic Techniques for Quantum Technology Applications. *J. Phys. Chem. C* **2021**, *125*, 13096–13108.

(2) Biswas, S.; Kim, J.; Zhang, X.; Scholes, G. D. Coherent two-dimensional and broadband electronic spectroscopies. *Chem. Rev.* **2022**, *122*, 4257–4321.

(3) Tiwari, V. Multidimensional Electronic Spectroscopy in High-Definition - Combining Spectral, Temporal, and Spatial Resolutions. *J. Chem. Phys.* **2021**, *154*, 230901.

(4) Karki, K. J.; Ciappina, M. F. Advances in Nonlinear Spectroscopy using Phase Modulated Light Fields: Prospective Applications in Perturbative and Non-Perturbative Regimes. *Adv. Phys.: X* **2022**, *7*, 2090856.

(5) Karki, K. J.; Chen, J.; Sakurai, A.; Shi, Q.; Gardiner, A. T.; Kühn, O.; Cogdell, R. J.; Pullerits, T. Before Förster. Initial Excitation in Photosynthetic Light Harvesting. *Chem. Sci.* **2019**, *10*, 7923–7928.

(6) Bakulin, A. A.; Rao, A.; Pavelyev, V. G.; van Loosdrecht, P. H. M.; Pshenichnikov, M. S.; Niedzialek, D.; Cornil, J.; Beljonne, D.; Friend, R. H. The Role of Driving Energy and Delocalized States for Charge Separation in Organic Semiconductors. *Science* **2012**, *335*, 1340–1344.

(7) Karki, K. J.; Widom, J. R.; Seibt, J.; Moody, I.; Lonergan, M. C.; Pullerits, T.; Marcus, A. H. Coherent Two-Dimensional Photocurrent Spectroscopy in a PbS Quantum Dot Photocell. *Nat. Commun.* **2014**, *5*, 5869.

(8) Bolzonello, L.; Bernal-Texca, F.; Gerling, L. G.; Ockova, J.; Collini, E.; Martorell, J.; van Hulst, N. F. Photocurrent-Detected 2D Electronic Spectroscopy Reveals Ultrafast Hole Transfer in Operating PM6/Y6 Organic Solar Cells. *J. Phys. Chem. Lett.* **2021**, *12*, 3983–3988.

(9) Roeding, S.; Brixner, T. Coherent Two-Dimensional Electronic Mass Spectrometry. *Nat. Commun.* **2018**, *9*, 2519.

(10) Aeschlimann, M.; Brixner, T.; Fischer, A.; Kramer, C.; Melchior, P.; Pfeiffer, W.; Schneider, C.; Strüber, C.; Tuchscherer, P.; Voronine, D. V. Coherent Two-Dimensional Nanoscopy. *Science* **2011**, *333*, 1723–1726.

(11) Uhl, D.; Bangert, U.; Bruder, L.; Stienkemeier, F. Coherent Optical 2D Photoelectron Spectroscopy. *Optica* **2021**, *8*, 1316.

(12) Bakulin, A. A.; Silva, C.; Vella, E. Ultrafast Spectroscopy with Photocurrent Detection: Watching Excitonic Optoelectronic Systems at Work. *J. Phys. Chem. Lett.* **2016**, *7*, 250–258.

(13) Tiwari, V.; Matutes, Y. A.; Gardiner, A. T.; Jansen, T. L.; Cogdell, R. J.; Ogilvie, J. P. Spatially-Resolved Fluorescence-Detected Two-Dimensional Electronic Spectroscopy Probes Varying Excitonic Structure in Photosynthetic Bacteria. *Nat. Commun.* **2018**, *9*, 4219.

(14) Fersch, D.; Malý, P.; Rühe, J.; Lisinetskii, V.; Hensen, M.; Würthner, F.; Brixner, T. Single-Molecule Ultrafast Fluorescence-Detected Pump–Probe Microscopy. *J. Phys. Chem. Lett.* **2023**, *14*, 4923–4932.

(15) Mueller, S.; Draeger, S.; Ma, X.; Hensen, M.; Kenneweg, T.; Pfeiffer, W.; Brixner, T. Fluorescence-Detected Two-Quantum and One-Quantum–Two-Quantum 2D Electronic Spectroscopy. *J. Phys. Chem. Lett.* **2018**, *9*, 1964–1969.

(16) Malý, P.; Lüttig, J.; Mueller, S.; Schreck, M. H.; Lambert, C.; Brixner, T. Coherently and Fluorescence-Detected Two-Dimensional Electronic Spectroscopy: Direct Comparison on Squaraine Dimers. *Phys. Chem. Chem. Phys.* **2020**, *22*, 21222–21237.

(17) Mueller, S.; Lüttig, J.; Brenneis, L.; Oron, D.; Brixner, T. Observing Multiexciton Correlations in Colloidal Semiconductor Quantum Dots via Multiple-Quantum Two-Dimensional Fluorescence Spectroscopy. *ACS Nano* **2021**, *15*, 4647–4657.

(18) Bruschi, M.; Gallina, F.; Fresch, B. Simulating Action-2D Electronic Spectroscopy of Quantum Dots: Insights on the Exciton and Biexciton Interplay from Detection-Mode and Time-Gating. *Phys. Chem. Chem. Phys.* **2022**, *24*, 27645–27659.

(19) Malý, P.; Mančal, T. Signatures of Exciton Delocalization and Exciton–Exciton Annihilation in Fluorescence-Detected Two-Dimensional Coherent Spectroscopy. *J. Phys. Chem. Lett.* **2018**, *9*, 5654–5659.

(20) Kunsel, T.; Tiwari, V.; Matutes, Y. A.; Gardiner, A. T.; Cogdell, R. J.; Ogilvie, J. P.; Jansen, T. L. C. Simulating Fluorescence-Detected Two-Dimensional Electronic Spectroscopy of Multichromophoric Systems. *J. Phys. Chem. B* **2019**, *123*, 394–406.

(21) Kühn, O.; Mančal, T.; Pullerits, T. Interpreting Fluorescence Detected Two-Dimensional Electronic Spectroscopy. *J. Phys. Chem. Lett.* **2020**, *11*, 838–842.

(22) Grégoire, P.; Srimath Kandada, A. R.; Vella, E.; Tao, C.; Leonelli, R.; Silva, C. Incoherent Population Mixing Contributions to Phase-Modulation Two-Dimensional Coherent Excitation Spectra. *J. Chem. Phys.* **2017**, *147*, 114201.

(23) Bargigia, I.; Gutiérrez-Meza, E.; Valverde-Chávez, D. A.; Marques, S. R.; Srimath Kandada, A. R.; Silva, C. Identifying Incoherent Mixing Effects in the Coherent Two-Dimensional Photocurrent Excitation Spectra of Semiconductors. *J. Chem. Phys.* **2022**, *157*, 204202.

(24) Kalaee, A. A. S.; Damtie, F.; Karki, K. J. Differentiation of True Nonlinear and Incoherent Mixing of Linear Signals in Action-Detected 2D Spectroscopy. *J. Phys. Chem. A* **2019**, *123*, 4119–4124.

(25) Bruschi, M.; Bolzonello, L.; Gallina, F.; Fresch, B. Unifying Nonlinear Response and Incoherent Mixing in Action-2D Electronic Spectroscopy. *J. Phys. Chem. Lett.* **2023**, *14*, 6872–6879.

(26) Croce, R.; Amerongen, H. V. Light-Harvesting in Photosystem I. *Photosynth. Res.* **2013**, *116*, 153–166.

(27) Mukamel, S., *Principles of Nonlinear Optical Spectroscopy*; 6; Oxford University Press: 1995.

(28) Mukamel, S. Communication: The Origin of Many-Particle Signals in Nonlinear Optical Spectroscopy of Non-Interacting Particles. *J. Chem. Phys.* **2016**, *145*, 041102.

(29) Zhou, N.; Ouyang, Z.; Hu, J.; Williams, O. F.; Yan, L.; You, W.; Moran, A. M. Distinguishing Energy- and Charge-Transfer Processes in Layered Perovskite Quantum Wells with Two-Dimensional Action Spectroscopies. *J. Phys. Chem. Lett.* **2020**, *11*, 4570–4577.

(30) Ouyang, Z.; Zhou, N.; McNamee, M. G.; Yan, L.; Williams, O. F.; You, W.; Moran, A. M. Multidimensional Time-of-Flight Spectroscopy. *J. Chem. Phys.* **2021**, *154*, 220901.

(31) McNamee, M. G.; Ouyang, Z.; Yan, L.; Gan, Z.; Zhou, N.; Williams, O. F.; You, W.; Moran, A. M. Uncovering Transport Mechanisms in Perovskite Materials and Devices with Recombination-Induced Action Spectroscopies. *J. Phys. Chem. C* **2023**, *127*, 2782–2791.

(32) Rojas-Gatjens, E.; Yallum, K. M.; Shi, Y.; Zheng, Y.; Bills, T.; Perini, C. A. R.; Correa-Baena, J.-P.; Ginger, D. S.; Banerji, N.; Silva-Acuña, C. Resolving Nonlinear Recombination Dynamics in Semiconductors via Ultrafast Excitation Correlation Spectroscopy: Photoluminescence versus Photocurrent Detection. *J. Phys. Chem. C* **2023**, *127*, 15969–15977.

(33) Tian, P.; Keusters, D.; Suzaki, Y.; Warren, W. S. Femtosecond Phase-Coherent Two-Dimensional Spectroscopy. *Science* **2003**, *300*, 1553–1555.

(34) Tan, H.-S. Theory and Phase-Cycling Scheme Selection Principles of Collinear Phase Coherent Multi-Dimensional Optical Spectroscopy. *J. Chem. Phys.* **2008**, *129*, 124501.

(35) Tekavec, P. F.; Lott, G. A.; Marcus, A. H. Fluorescence-Detected Two-Dimensional Electronic Coherence Spectroscopy by Acousto-Optic Phase Modulation. *J. Chem. Phys.* **2007**, *127*, 214307.

(36) Yang, M.; Fleming, G. R. Third-Order Nonlinear Optical Response of Energy Transfer Systems. *J. Chem. Phys.* **1999**, *111*, 27–39.

(37) Schröter, M.; Pullerits, T.; Kühn, O. Using Fluorescence Detected Two-Dimensional Spectroscopy to Investigate Initial Exciton Delocalization between Coupled Chromophores. *J. Chem. Phys.* **2018**, *149*, 114107.

(38) Yang, J.; Gelin, M. F.; Chen, L.; Šanda, F.; Thyrhaug, E.; Hauer, J. Two-Dimensional Fluorescence Excitation Spectroscopy: A Novel Technique for Monitoring Excited-State Photophysics of Molecular Species with High Time and Frequency Resolution. *J. Chem. Phys.* **2023**, *159*, 074201.

(39) Malý, P.; Lüttig, J.; Rose, P. A.; Turkin, A.; Lambert, C.; Krich, J. J.; Brixner, T. Separating Single- from Multi-Particle Dynamics in Nonlinear Spectroscopy. *Nature* **2023**, 1–8.

(40) Lüttig, J.; Rose, P. A.; Malý, P.; Turkin, A.; Bühler, M.; Lambert, C.; Krich, J. J.; Brixner, T. High-Order Pump–Probe and High-Order Two-Dimensional Electronic Spectroscopy on the Example of Squaraine Oligomers. *J. Chem. Phys.* **2023**, *158*, 234201.

(41) Hamm, P.; Zanni, M., *Concepts and Methods of 2D Infrared Spectroscopy*; Cambridge University Press: 2011.

6 | Witnessing Annihilation and Delocalization in A-2DES

6.1. Introduction

Action-2D Electronic Spectroscopy (A-2DES) is recently gaining considerable attention for the study of complex excitonic systems [1, 2]. In this technique, the sample interacts with a sequence of multiple laser pulses, then emitting an incoherent signal proportional to the excited-state population. Depending on the sample, different kinds of incoherent signals can be detected, e.g., fluorescence [3–5], photocurrent [6, 7], photoions [8] and photoelectrons [9]. The variety of signals that can be measured gives technique a function-oriented role, allowing systems to be studied under working conditions [10]. Furthermore, when combined with microscopy [11] and single-molecule [12] techniques, high spatial resolution can be achieved, thus preventing inhomogeneities in the sample. Furthermore, the technique offers a unique lens to unveil many-particle interactions as encoded in higher-order signals [13].

However, to take full advantage of the opportunities offered by the technique, it is essential to correctly interpret the spectral features. From the theoretical perspective, great efforts have been devoted to establish the nature of the cross-peaks appearing in the spectrum at early waiting-times [14–19]. In general, cross-peaks emerge due to the presence of Exciton-Exciton Annihilation (EEA) process occurring during signal detection. In the language of non-linear response theory, EEA leads to a reduced contribution of the positive ESAII pathway, resulting in the incomplete cancellation of negative features arising from GSB, SE and ESAI pathways in cross-peaks position. On the one hand, for weakly interacting systems, the emergence of cross-peaks can be equivalently interpreted in the framework of incoherent mixing [17, 19, 20]. In this context, cross-peaks simply reflect the annihilation process of excitons generated on different molecules, without conveying non-linear information. Indeed, the amplitude and lineshape are simply determined by the product of linear responses of independent chromophores [18, 19]. On the other hand,

for strongly interacting systems, it is no longer appropriate to consider chromophores as independent entities, since excitonic delocalization induces dipole moment redistribution and excitonic splitting. In such situation, cross-peaks are an essential part of the non-linear response of the coupled system [14–16]. Therefore, the current issue with A-2DES is to assess whether the cross-peaks only reflect the occurrence of exciton-exciton annihilation within the system or whether they also provide insights about the presence of excitonic delocalization among chromophores.

Answering this important question first requires to account for the relation between the EEA process and exciton delocalization. EEA is often described as an incoherent process arising from the stochastic encounter of two excitons within the system. It is typically modeled phenomenologically as a bimolecular process involvng the exciton density [21]. Besides this macroscopic description, there has been few attempts to describe the EEA phenomenon from a microscopic theory [22–25]. Recent evidences has highlighted the existence of coherent effects in the annihilation process [26–28].

In this work, we investigate the optical response of a molecular dimer in different coupling regimes by simulating A-2DES spectra. The EEA process in our model results from the mixing of the local states, as suggested in refs. [29, 30], allowing the characterization of the interplay between the EEA and exciton delocalization in shaping the A-2DES spectra. The most relevant result is the characterization of the nature of cross-peaks as a function of the excitonic coupling strength. For very small excitonic coupling, cross-peaks appear because of exciton-exciton annihilation which become effective even in the absence of any relevant delocalization in the one-exciton manifold. In this regime, cross-peaks can be regarded as incoherent mixing contributions [19]. On the other hand, for increasing coupling strengths, cross-peaks start to reflect the presence of excitonic delocalization.

We also consider the dynamics of spectral features along the waiting-time, observing oscillations at frequencies equal to the excitonic splitting between the states of the one-exciton manifold. Nevertheless, further work is required in this direction to comprehensively characterize the strong coupling regime.

6.2. Theory and Simulations

6.2.1. Model System

In the following, we consider a molecular dimer where each chromophore is treated as a three-level electronic system, consisting of a ground state $|g_n\rangle$, a first-excited state $|e_n\rangle$

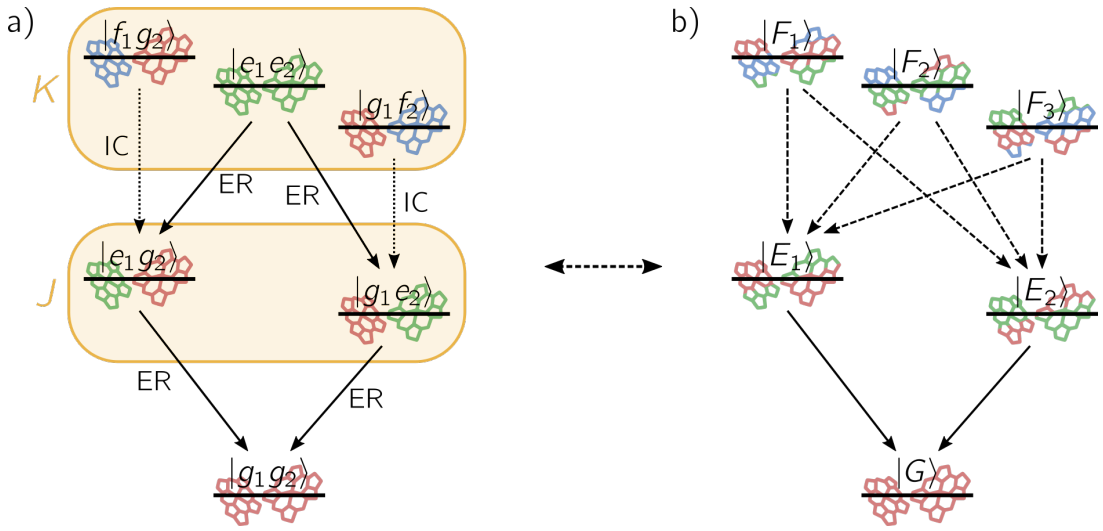

Fig. 6.1: Model of a molecular dimer, where each chromophore is described as a three-level electronic system. Representation of the states in the a) (localized) site basis and b) (delocalized) excitonic basis.

and a second-excited state $|f_n\rangle$, with $n = 1, 2$. The Hamiltonian of the n-th chromophore is:

$$\hat{H}_n = \epsilon_{g_n} |g_n\rangle\langle g_n| + \epsilon_{e_n} |e_n\rangle\langle e_n| + \epsilon_{f_n} |f_n\rangle\langle f_n| \tag{6.1}$$

where ϵ_{g_n}, ϵ_{e_n}, ϵ_{f_n} are the energies of the ground, first- and second-excited states, respectively.

Depending on the number of excitons, the states of the molecular dimer can be distinguished into different manifolds. In the (localized) site basis (Fig. 6.1a), the manifolds are: the collective ground state, where both molecules are in their ground state $|g_1 g_2\rangle$, the one-exciton manifold, where one molecule is the first-excited state and the other is in the ground state $|e_1 g_2\rangle$ and $|g_1 e_2\rangle$, and the two-exciton manifold, where both molecules are in their first-excited state $|e_1 e_2\rangle$ or one molecule is in the second-excited state and the other is in the ground state $|f_1 g_2\rangle$ and $|g_1 f_2\rangle$. In the site basis, the energy of the dimer states is given by the sum of the energies of the constituent monomer states $\epsilon_{a_1 b_2} = \epsilon_{a_1} + \epsilon_{b_2}$, where $a, b = g, e, f$. Notice that states beyond the two-exciton manifold are neglected in this description.

Since the interaction between states belonging to different manifolds can be assumed to be negligible, the Hamiltonian of the molecular dimer results to be block diagonal:

$$\hat{H} = \hat{H}^{(0)} + \hat{H}^{(1)} + \hat{H}^{(2)} \tag{6.2}$$

with the ground-state Hamiltonian:

$$\hat{H}^{(0)} = \epsilon_{g_1 g_2} |g_1 g_2\rangle\langle g_1 g_2| \tag{6.3}$$

the one-exciton Hamiltonian:

$$\begin{aligned}\hat{H}^{(1)} =& \epsilon_{e_1 g_2} |e_1 g_2\rangle\langle e_1 g_2| + \epsilon_{g_1 e_2} |g_1 e_2\rangle\langle g_1 e_2| + \\ &+ J\left(|e_1 g_2\rangle\langle g_1 e_2| + h.c.\right)\end{aligned} \tag{6.4}$$

and the two-exciton Hamiltonian:

$$\begin{aligned}\hat{H}^{(2)} =& \epsilon_{e_1 e_2} |e_1 e_2\rangle\langle e_1 e_2| + \epsilon_{f_1 g_2} |f_1 g_2\rangle\langle f_1 g_2| + \epsilon_{g_1 f_2} |g_1 f_2\rangle\langle g_1 f_2| + \\ &+ K\left(|e_1 e_2\rangle\langle f_1 g_2| + |e_1 e_2\rangle\langle g_1 f_2| + h.c.\right)\end{aligned} \tag{6.5}$$

where J and K represent the excitonic coupling between states in the one- and two-exciton manifold, respectively. In general, they can be assumed to be proportional $K = \alpha J$, where α is a proportionality factor [30].

Due to the structure of the Hamiltonian, each block can be diagonalized independently to obtain the eigenstates of the system, which represent (delocalized) excitonic states given by the combination of localized excitations (Fig. 6.1b). For the ground-state manifold, the eigenstate is directly available:

$$|G\rangle = |g_1 g_2\rangle \tag{6.6}$$

while for the one-exciton manifold are:

$$|E_k\rangle = c_{1k} |e_1 g_2\rangle + c_{2k} |g_1 e_2\rangle \tag{6.7}$$

with $k = 1, 2$, and for the two-exciton manifold are:

$$|F_l\rangle = c_{1l} |e_1 e_2\rangle + c_{2l} |f_1 g_2\rangle + c_{3l} |g_1 f_2\rangle \tag{6.8}$$

with $l = 1, 2, 3$.

In the calculations, the energies of the first-excited state of each chromophore are $\epsilon_{e_1} = 1.55$ eV and $\epsilon_{e_2} = 1.46$ eV, while that of the second-excited state are $\epsilon_{f_1} = 2\epsilon_{e_1} = 3.10$ eV and $\epsilon_{f_2} = 2\epsilon_{e_2} = 2.92$ eV. For simplicity, the excitonic couplings between localized states in the one- and two-exciton manifolds are assumed to be equal $J = K$.

In Fig. 6.A.7 of App. 6.A, we report the modulus square of the expansion coefficients in the localized basis for the eigenstates in Eqs. 6.7 and 6.8, by varying the excitonic coupling. Furthermore, we consider the amount of excitonic delocalization as quantified by the inverse of the Inverse Participation Ratio $IPR(k) = \sum_n |c_{nk}|^4$.

6.2.2. Light-Matter Interaction

Light-matter interaction induces transitions between states of different manifolds. In the dipole approximation, the interaction Hamiltonian is:

$$\hat{H}'(t) = -\hat{\mu} \cdot E(t) \tag{6.9}$$

with dipole moment operator $\hat{\mu}$ and electric field $E(t)$. In the site basis, the dipole moment operator of the dimer is:

$$\begin{aligned}\hat{\mu} =&\mu_{e_1g_1}(|e_1g_2\rangle\langle g_1g_2| + |e_1e_2\rangle\langle g_1e_2| + h.c.) + \mu_{f_1e_1}(|f_1g_2\rangle\langle e_1g_2| + h.c.)+ \\ &\mu_{e_2g_2}(|g_1e_2\rangle\langle g_1g_2| + |e_1e_2\rangle\langle e_1g_2| + h.c.) + \mu_{f_2e_2}(|g_1f_2\rangle\langle g_1g_2| + h.c.)\end{aligned} \tag{6.10}$$

with transition dipole moment of the monomers is $\mu_{e_ng_n}$, from the ground to the first-excited state, and $\mu_{f_ne_n}$, from the first- to the second-excited state. In the calculations, the transition dipole moment of the transitions are assumed to be parallel and equal $\mu_{e_ng_n} = \mu_{f_ne_n}$.

6.2.3. Quantum Dynamics

The system is assumed to evolve according to the Lindblad Quantum Master Equation (QME) [31, 32]:

$$\frac{d}{dt}\rho(t) = -\frac{i}{\hbar}[\hat{H}(t), \rho(t)] + \sum_\alpha \frac{k_\alpha}{\hbar}\left(\hat{L}_\alpha \rho(t) \hat{L}_\alpha^\dagger - \frac{1}{2}\left\{\hat{L}_\alpha^\dagger \hat{L}_\alpha, \rho(t)\right\}\right) \tag{6.11}$$

where $[\cdot,\cdot]$ is the commutator and $\{\cdot,\cdot\}$ is the anti-commutator. The total Hamiltonian $\hat{H}(t) = \hat{H} + \hat{H}'(t)$ is given by sum of the system Hamiltonian (Eq. 6.2) and the interaction Hamiltonian (Eq. 6.9). The Lindblad operators $\hat{L}_\alpha$ represent dephasing or relaxation processes induced by the interaction with the environment, i.e., vibrations and solvent, with associated rates k_α.

Initially, the system is assumed to be in the ground state, described by the density matrix $\rho(t_0) = |G\rangle\langle G|$. In the following, we assume that each chromophore has an independent

environment. In the site basis, relaxation between states of different manifolds is described by $\hat{L}_{g_n e_n} = |g_n\rangle\langle e_n|$ for the Exciton Recombination (ER) mechanism and $\hat{L}_{e_n f_n} = |e_n\rangle\langle f_n|$ for the Internal Conversion (IC) mechanism (Fig. 6.1a). Furthermore, we introduce site-dephasing using $\hat{L}_{g_1 g_1} = |g_n\rangle\langle g_n|$, $\hat{L}_{e_n e_n} = |e_n\rangle\langle e_n|$ and $\hat{L}_{f_n f_n} = |f_n\rangle\langle f_n|$. These operators represent fluctuations of the site energies and are responsible for the dephasing of coherences between different sites. In the excitonic basis, these operators also promote transitions between states within the same manifold, leading to a quasi-equilibrium state in the high-temperature limit. Decoherence between different local sites is the non-unitary evolution channel in the Haken-Strobl QME [33] which had success in modelling exciton dynamics across different coupling regimes, bridging the transition from coherent to incoherent transport within the single exciton manifold [34–36]. Although giving rise to the high-temperature limit, it is known to be valid for arbitrary excitonic coupling [37].

In the site basis, EEA mechanism can be visualized as a two-step process: first, exciton transfer occurs from the two-exciton state $|e_1 e_2\rangle$ to second-excited states $|f_1 g_2\rangle$ and $|g_1 f_2\rangle$, followed by a rapid IC to the one-exciton states $|e_1 g_2\rangle$ and $|g_1 e_2\rangle$, with the net loss of one exciton (Fig. 6.1a). From the perspective of excitonic states, EEA process arises from the delocalization within the two-exciton manifold (Eq. 6.8): the two-exciton state $|e_1 e_2\rangle$ mixes with second-excited states $|f_1 g_2\rangle$ and $|g_1 f_2\rangle$, inheriting the rapid IC character (Fig. 6.1b).

Indeed, due to the delocalization, the eigenstates may have a different relaxation rates compared to localized states [38]. In the excitonic basis, the relaxation rates from one-exciton states to the ground-state are:

$$k_{GE_k} = k_{g_1 e_1} |\langle E_k | e_1 g_2\rangle|^2 + k_{g_2 e_2} |\langle E_k | g_1 e_2\rangle|^2 \tag{6.12}$$

while from the two-exciton states to the one-exciton states are:

$$\begin{aligned} k_{E_k F_l} =& k_{g_1 e_1} |\langle g_1 e_2 | E_k\rangle|^2 |\langle F_l | e_1 e_2\rangle|^2 + k_{g_2 e_2} |\langle e_1 g_2 | E_k\rangle|^2 |\langle F_l | e_1 e_2\rangle|^2 \\ &+ k_{e_1 f_1} |\langle e_1 g_2 | E_k\rangle|^2 |\langle F_l | f_1 g_2\rangle|^2 + k_{e_2 f_2} |\langle g_1 e_2 | E_k\rangle|^2 |\langle F_l | g_1 f_2\rangle|^2. \end{aligned} \tag{6.13}$$

In the calculations, unless otherwise stated, we considered the Exciton Recombination (ER) rate $k_{ER}/h = k_{g_1 e_1}/h = k_{g_2 e_2}/h = 1/10$ ns^{-1} and the Internal Conversion (IC) rate $k_{IC}/h = k_{e_1 f_1}/h = k_{e_2 f_2}/h = 1/100$ fs^{-1}, while for site-dephasing rate $k_d/h = k_{g_n g_n}/h = k_{e_n e_n}/h = k_{f_n f_n}/h = 1/100$ fs^{-1}.

6.2.4. Action-2D Electronic Spectroscopy

The optical response of the molecular dimer is probed using A-2DES. In A-2DES, the system interacts with a train of four collinear laser pulses. The electric field is given by:

$$E(t) = \sum_{i=1}^{4} E_i(t) \tag{6.14}$$

where each pulse is described as:

$$E_i(t) = E_i^0 \exp\left\{ -\frac{(t-\mathcal{T}_i)^2}{2\sigma_i^2} \right\} \cos[\omega_i(t-\mathcal{T}_i) + \phi_i]. \tag{6.15}$$

with amplitude E_i^0, pulse duration σ_i, frequency ω_i and phase ϕ_i. The first pulse is centered at time $T_0 = t_1$, while the following pulses are separated from the previous one by delay-times $T_1 = t_2 - t_1$, $T_2 = t_3 - t_2$, and $T_3 = t_4 - t_3$. For convenience, we use the cumulative delay-time: $\mathcal{T}_i = \sum_{j=0}^{i-1} T_j$. After the interaction, the incoherent signal $\mathcal{S}(T_d)$ is collected during the detection-time T_d.

In order to isolate the different contributions to the optical response, the phase-cycling scheme is employed [39]. In phase cycling, the relative phase between the pulses $\phi_{ij} = \phi_i - \phi_j$ is varied independently by an interval $\Delta\phi_{ij}$ from a train to another. The specific contributions to the signal are extracted by taking combinations of the phase-dependent signal:

$$\mathcal{S}(\beta,\gamma,\delta) = \frac{1}{LMN} \sum_{l=0}^{L-1} \sum_{m=0}^{M-1} \sum_{n=0}^{N-1} \mathcal{S}(l,m,n) e^{-i\beta l \Delta\phi_{21}} e^{-i\gamma m \Delta\phi_{31}} e^{-i\delta n \Delta\phi_{41}}. \tag{6.16}$$

where L, M, and N are the number of steps in which the phases are cycled. In the following, a 27-fold phase-cycling scheme is employed ($L = M = N = 3$), which allows the simultaneous isolation of rephasing ($\beta = +1$, $\gamma = +1$, $\delta = -1$), non-rephasing ($\beta = -1$, $\gamma = +1$, $\delta = -1$) and double-quantum coherence ($\beta = +1$, $\gamma = -1$, $\delta = -1$) signals. We focus our analysis on the rephasing signal. By taking the Fourier transform along delay-times T_1 and T_3, 2D spectra are displayed as a function of $\hbar\omega_1$ and $\hbar\omega_2$ for each value of the waiting-time T_2.

The parameters used for the simulations are: $\sigma_i = 5$ fs, $\hbar\omega_i = 1.50$ eV and $\mu_{e_n g_n} E_i^0 = \mu_{f_n e_n} E_i^0 = 8$ meV. The delay-times T_1 and T_3 are scanned from 0 to 300 fs in steps of 10 fs, while the waiting-time T_2 is scanned from 0 to 100 fs in steps of 5 fs. The signal is collected in the rotating-frame at angular frequency $\omega_{RF} = 2.28$ [rad]/fs. Furthermore,

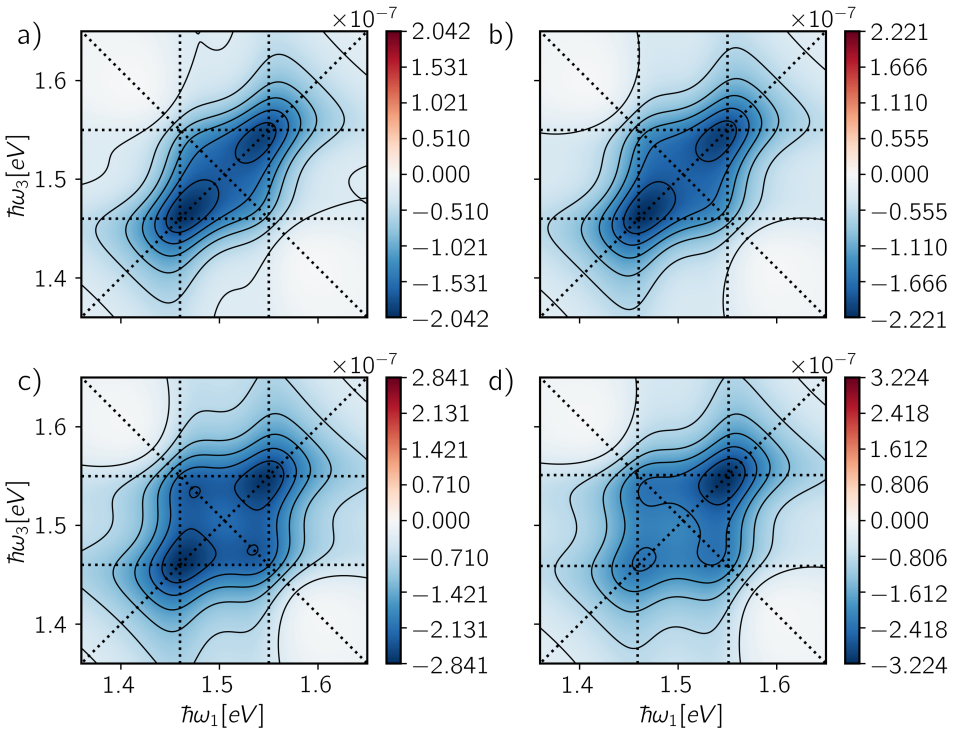

Fig. 6.2: Total spectra obtained for different excitonic couplings: a) $J = +10^{-4}$ eV, b) $J = +10^{-3}$ eV, c) $J = +10^{-2}$ eV.

the temporal signal is zero-padded in order to smooth the spectra.

6.2.5. Incoherent Signal

The time-resolved signal along the detection-time T_d is given by the sum over the eigenstate populations extracted from the density matrix after the train of pulses:

$$\begin{aligned}\mathcal{S}(T_d) =& k^{(r)}_{G_1E_1} P_{E_1}(T_d) + k^{(r)}_{G_2E_2} P_{E_2}(T_d) + \left(k^{(r)}_{E_1F_1} + k^{(r)}_{E_2F_1}\right) P_{F_1}(T_d) + \\ & \left(k^{(r)}_{E_1F_2} + k^{(r)}_{E_2F_2}\right) P_{F_2}(T_d) + \left(k^{(r)}_{E_1F_3} + k^{(r)}_{E_2F_3}\right) P_{F_3}(T_d)\end{aligned} \tag{6.17}$$

weighted by the radiative relaxation rate. These rates are obtained using Eqs. 6.12 and 6.13 considering the radiative relaxation rates of the monomers $k^{(r)}_{g_1e_1}/h = k^{(r)}_{g_2e_2}/h = 1/10$ ns^{-1} and $k^{(r)}_{e_1f_1}/h = k^{(r)}_{e_2f_2}/h = 0$ fs. However, in an experiment, the signal emission is not time-resolved and the spectroscopic observable is represented by the time-integrated signal along the detection-time:

$$\overline{\mathcal{S}} = \int_0^{+\infty} dT_d \; \mathcal{S}(T_d) \tag{6.18}$$

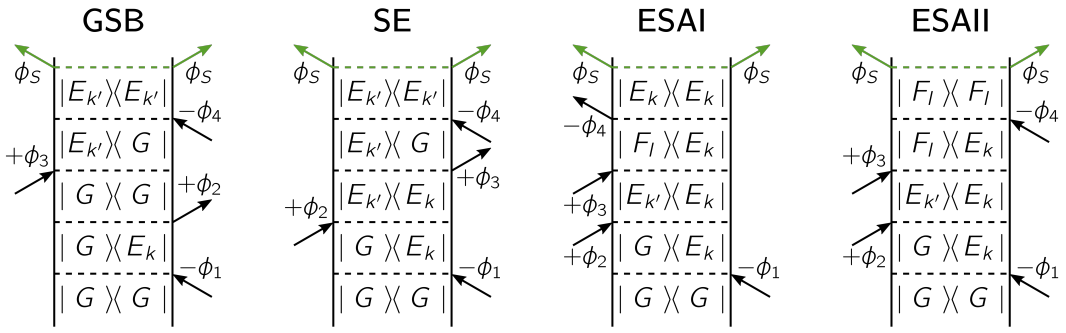

Fig. 6.3: Feynman diagrams for the considered system relative to Ground-State Bleaching (GSB), Stimulated Emission (SE), Excited-State Absorption I (ESAI) and Excited-State Absorption II (ESAII) pathways.

which can be expressed in terms of the time-integrated populations:

$$\begin{aligned}\overline{\mathcal{S}} =& k^{(r)}_{G_1E_1}\overline{P_{E_1}} + k^{(r)}_{G_2E_2}\overline{P_{E_2}} + \left(k^{(r)}_{E_1F_1} + k^{(r)}_{E_2F_1}\right)\overline{P_{F_1}} + \\ & \left(k^{(r)}_{E_1F_2} + k^{(r)}_{E_2F_2}\right)\overline{P_{F_2}} + \left(k^{(r)}_{E_1F_3} + k^{(r)}_{E_2F_3}\right)\overline{P_{F_3}}.\end{aligned} \tag{6.19}$$

6.3. Results and Discussion

As a starting point, we consider the changes in the spectral features of the rephasing signal at waiting-time $T_2 = 0$ fs for different values of the excitonic coupling J (Fig. 6.2).

In the case of null (Fig. 6.2a) or negligible excitonic coupling (Fig. 6.2b), only diagonal peaks appear in the spectra, which are related to the optical response of individual chromophores. As the excitonic coupling increases, two different changes are observed in the spectra. The first is related to the emergence of cross-peaks (Fig. 6.2c) as a result of the EEA process. This fact is commonly interpreted in terms of the incomplete cancellation of spectral features of opposite sign [14–16, 19]. Indeed, the presence of EEA leads to a reduction in the positive ESAII contribution, which no longer compensates the contributions from negative GSB, SE and ESAI pathways in these positions (Fig. 6.3). Instead, the second is represented by the variation in the relative amplitude of the peaks (Fig. 6.2d) resulting from the dipole moment redistribution. Indeed, due to excitonic delocalization, one state in the one-exciton manifold becomes increasingly bright while the other becomes dark. In addition, the increase in excitonic coupling leads to a progressive shift in peak position that reflects the splitting between states in the one-exciton manifold.

To gain further insights, we analyze the amplitude of the spectral features over a range of

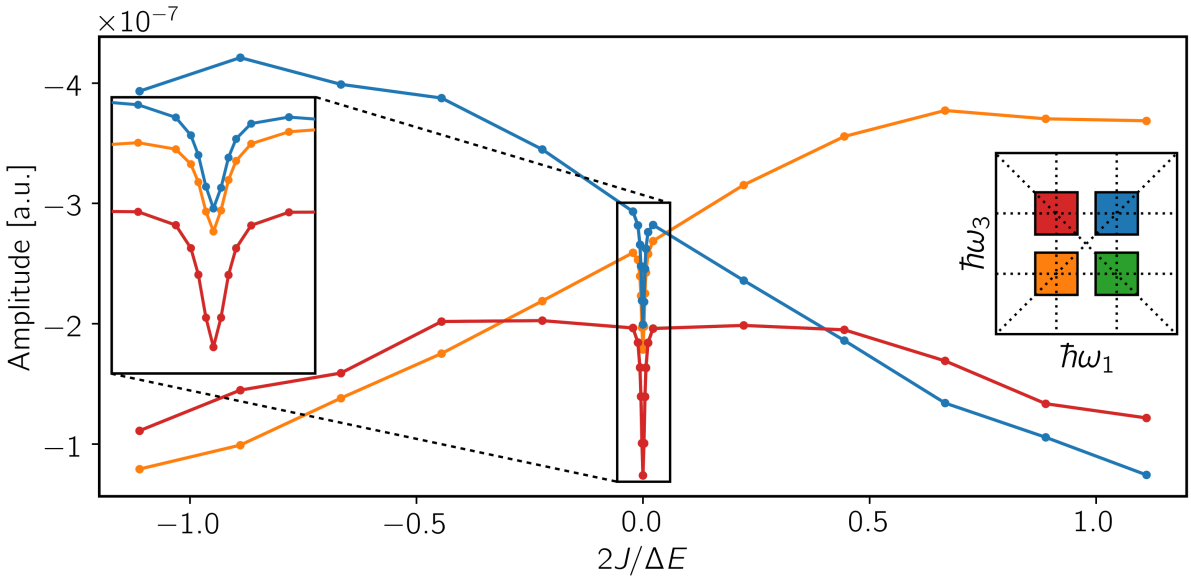

Fig. 6.4: Amplitude of diagonal peaks (blue and orange) and cross-peaks (red and green) as a function of the excitonic coupling J. Right inset: relative positions of the spectral features and the associated colors. Left inset: enlargement of the region of negligible excitonic coupling ($J \simeq 0$).

positive and negative excitonic couplings (Fig. 6.4). We notice that the peaks amplitude exhibits a non-monotonic behaviour as a function of the excitonic coupling, which can distinguished into three different regions: positive excitonic coupling ($J > 0$), negative excitonic coupling ($J < 0$), and negligible excitonic coupling ($J \simeq 0$). In the positive and negative regions, changes in the peak amplitudes can be attributed to the dipole moment redistribution (Fig. 6.2d). While for positive excitonic coupling ($J > 0$), the amplitude of the upper diagonal peak increases and that of the lower diagonal peak decreases, for negative excitonic coupling ($J < 0$), the opposite trend occurs. Conversely, the amplitude of cross-peaks is less affected by the excitonic coupling and their behaviour result mirrored with respect to $J = 0$. These findings are in agreement with previous studies of A-2DES [14, 15], which has shown that the amplitude of the diagonal peaks scales as $|\mu_{E_n}|^4$ while that of the cross-peaks scales as $|\mu_{E_1}|^2|\mu_{E_2}|^2$.

On the other hand, in the region of negligible excitonic coupling ($J \simeq 0$), we observe a prominent cusp in the amplitude of the spectral features (left inset of Fig. 6.4). For null excitonic coupling ($J = 0$), we observe a minimum in the amplitude since, as a result of the perfect cancellation of pathways with opposite sign, cross-peaks are not present (Fig. 6.2a). As soon as the excitonic coupling $J \neq 0$, EEA process start to become effective and the pathway cancellation is not anymore complete. As a result, the amplitude of cross-peaks starts to increase (Fig. 6.2b), until their appearance in the spectrum (Fig.

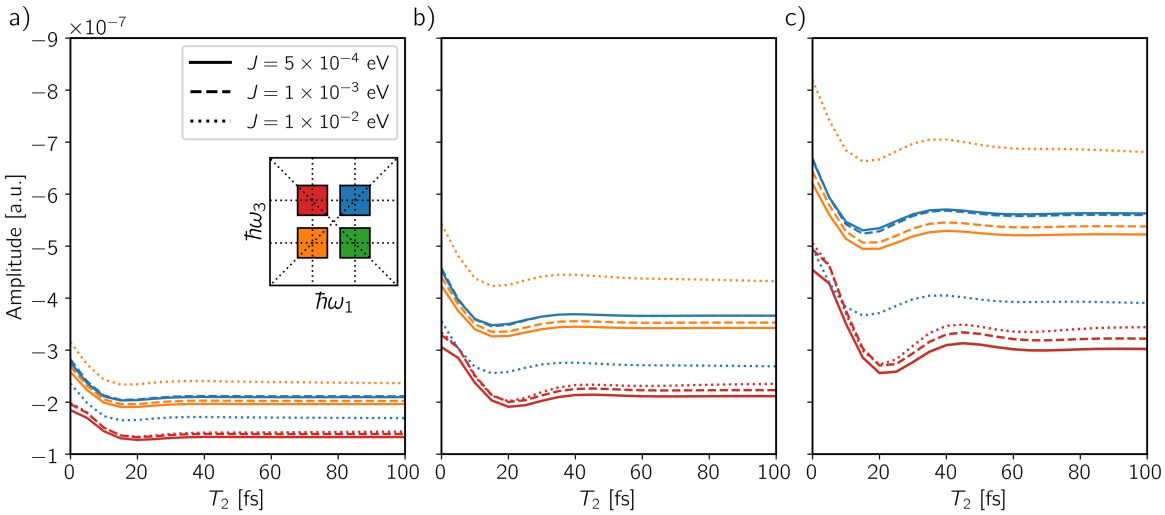

Fig. 6.5: Evolution of the spectral features as a function of the waiting-time T_2 site-dephasing rates a) $k_d/h = 1/100$ fs^{-1}, b) $k_d/h = 1/150$ fs^{-1} and c) $k_d/h = 1/200$ fs^{-1} and different excitonic coupling (solid line) $J = 5 \cdot 10^{-4}$ eV, (dashed line) $J = 1 \cdot 10^{-3}$ eV and (dotted line) $J = 1 \cdot 10^{-2}$ eV.

6.2c). This particular region has not been considered in previous studies of A-2DES, since EEA was introduced as an incoherent transfer mechanism without explicitly accounting for excitonic delocalization within the states in the two-exciton manifold [14, 15].

Furthermore, we notice that the amplitude of the diagonal peaks also increases with the excitonic coupling in this region. This effect can be ascribed due to the constructive interference of diagonal peaks with the emerging cross-peaks in the spectrum. We highlight that within this region, the presence of excitonic coupling is such that it induces the EEA process but does not give rise to any significant redistribution of the dipole moment.

On the basis of the presented analysis, we propose to distinguish the nature of cross-peaks in A-2DES. While in the region of negligible excitonic coupling, cross-peaks merely represent a signature of exciton-exciton annihilation and can be regarded as incoherent mixing contributions [19], outside this region, they start to reflect the presence of excitonic delocalization.

Furthermore, we investigated the evolution of the spectral features during the waiting-time T_2 (Fig. 6.5) considering three different values of excitonic coupling J and site-dephasing rates k_d.

According to the analysis of the dynamical pathways contributing to the rephasing signal of an excitonic dimer, the oscillation of the cross-peak amplitude as a function of t_2 reflects the coherent superposition of the two one-exciton states $|E_1\rangle$ and $|E_2\rangle$. The amplitude

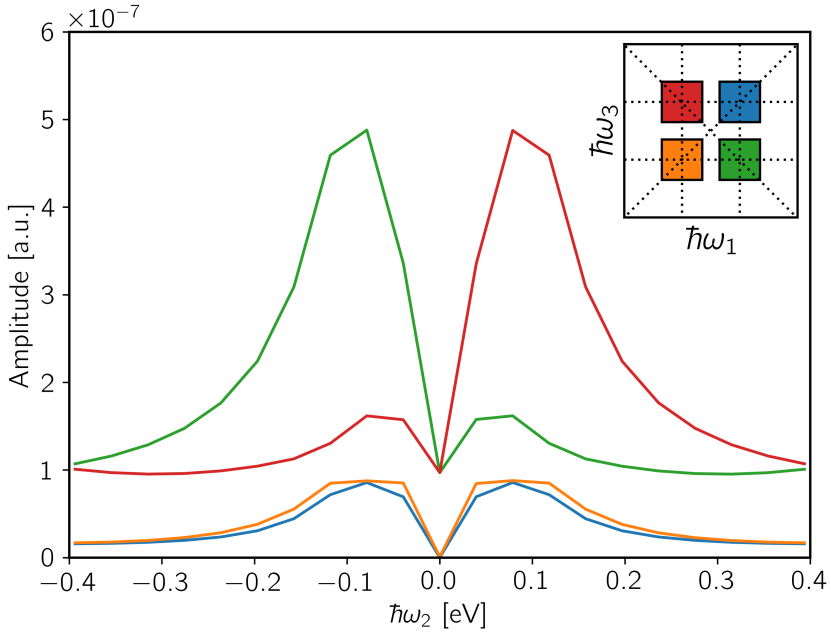

Fig. 6.6: Absolute value of the coherence spectrum along $\hbar\omega_2$ for excitonic coupling $J = 10^{-2}$ eV and site-dephasing rates $k_d/h = 1/200$ fs^{-1}.

of the peaks in the simulated spectra for different excitonic couplings are reported in Fig. 6.5. As reported in Fig. 6.A.8a of App. 6.A, the coupling range investigated here does not imply a significant variation of the excitonic splitting, therefore the oscillation frequency as a function of t_2 are about the same in the three cases. Higher oscillation frequency should be expected for increasing excitonic couplings. However, due to the reduction of the cross-peaks amplitude caused by the dipole moment redistribution, the strong coupling regime is not observable in this model. Further investigation with a different relative configurations of the transition dipole moments are necessary to extend the study to the strong coupling regime. We also considered changes in the evolution with the site-dephasing rate. For the case of fast site-dephasing rate, the peaks amplitude exhibits a rapid decay in the timescale of 10 fs (Fig. 6.5a), which can be ascribed to the *coherent artifact* [40]. Since the pulses overlap significantly at early waiting-times, different time-ordering of light-matter interactions are possible [41]. This leads to an increase in the number of pathways contributing to the signal, resulting in a larger amplitude of spectral features in this region. As the waiting-time increases and the pulses no longer overlap, a decrease in peaks amplitude is observed as these pathways become unavailable.

As site-dephasing rate decreases, both diagonal and cross-peaks exhibit more pronounced beatings (Fig. 6.5b,c). To analyze these oscillations, we considered the absolute value of the Fourier transform of the signal along the waiting-time T_2 (Fig. 6.6). In this case,

the temporal trace was fitted with an exponential decay and subtracted to the signal. We notice that all spectral features exhibit frequency components around 0.1eV, which is compatible with the energy splitting between states in the one-exciton manifold. As the analysis suggests, diagonal peaks preset both positive and negative frequency components because their temporal trace is real. In contrast, cross-peaks predominantly display either a positive or negative frequency component, since the temporal trace is complex, meaning that they oscillates with opposite phases.

We highlight that these beatings may not necessarily represent a signature of coherent excitonic behaviour, as the weak excitonic coupling cannot induce sufficient excitonic delocalization in the considered cases. In this situations, the presence of beatings may represent inter-site coherences rather than inter-exciton coherences [42].

6.4. Conclusions

In this work, we investigated the effects of the excitonic coupling in the spectral features of A-2DES, considering a molecular dimer. We observed that, in the case of weak coupling, cross-peaks primarily reflect the presence of exciton-exciton annihilation between chromophores. In this limit, cross-peaks can be rationalized within the incoherent mixing mechanism involving the linear responses of individual chromophores during the detection-time. Conversely, for stronger coupling, we noted that spectral features start to reflect excitonic delocalization between chromophores, as evidenced by the redistribution of the dipole moment.

In the analysis of the waiting-time dynamics, we identified the presence of oscillations in the amplitude of the spectral features, which can be attributed to coherences between the states of the one-exciton manifold. However, we highlight that these are not necessarily inter-exciton coherences, but can also be inter-site in nature.

Given the considered parameters, we could not detect significant changes in the dephasing time for increasing excitonic coupling. Due to the large redistribution of the dipole moment in the limit of strong coupling, the amplitude of the spectral features results suppressed, thus precluding the investigation. However, the effect of the redistribution can be mitigated by considering a perpendicular orientation of the dipole moments of the two chromophores.

6.A. Additional Figures

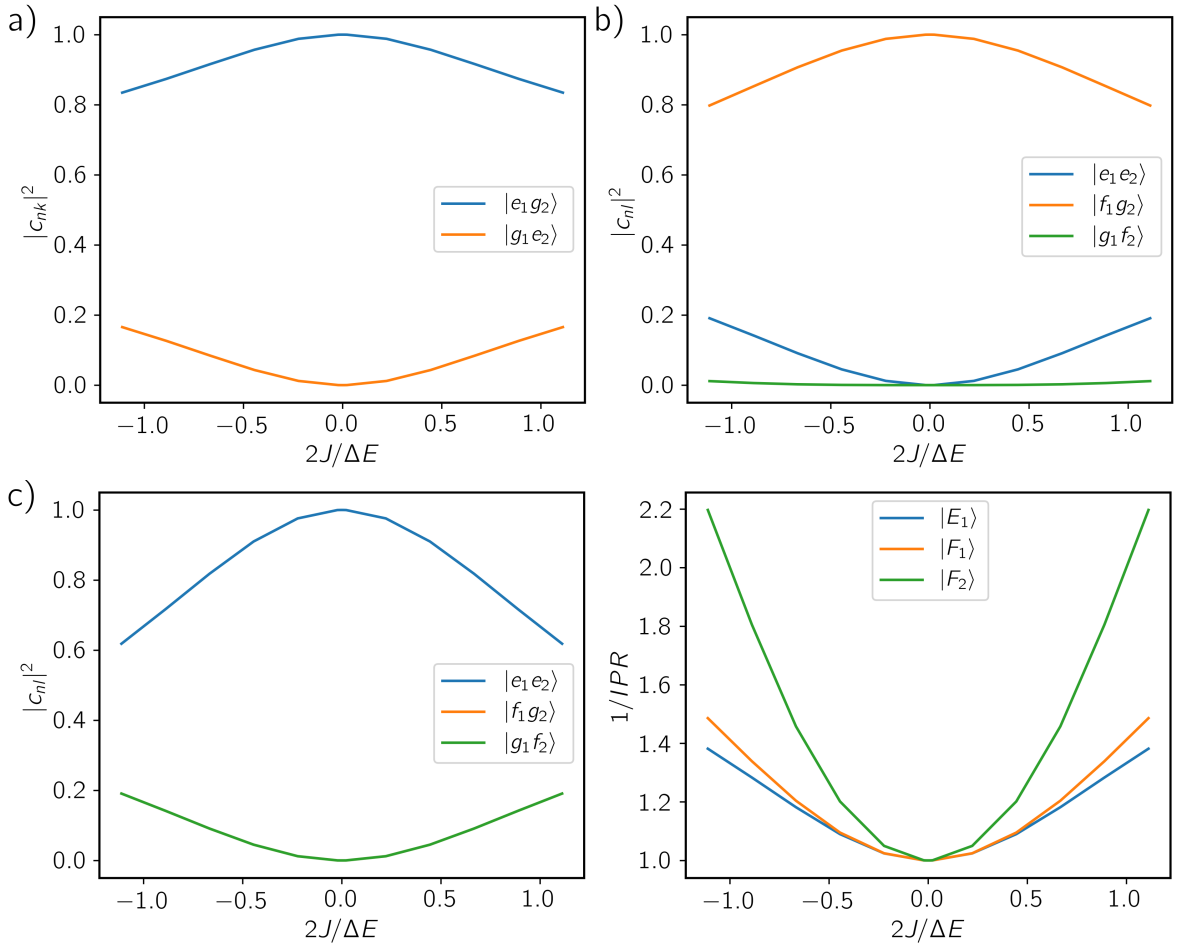

Fig. 6.A.7: Modulus square of the expansion coefficients for a) the eigenstate $|E_1\rangle$ in the one-exciton manifold (Eq. 6.7), b) the eigenstates $|F_1\rangle$ and c) $|F_2\rangle$ in the two-exciton manifold (Eq. 6.8). d) The inverse of the Inverse Partecipation Ratio (IPR) which quantifies the amount of excitonic delocalization for the eigenstates $|E_1\rangle$, $|F_1\rangle$ and $|F_2\rangle$.

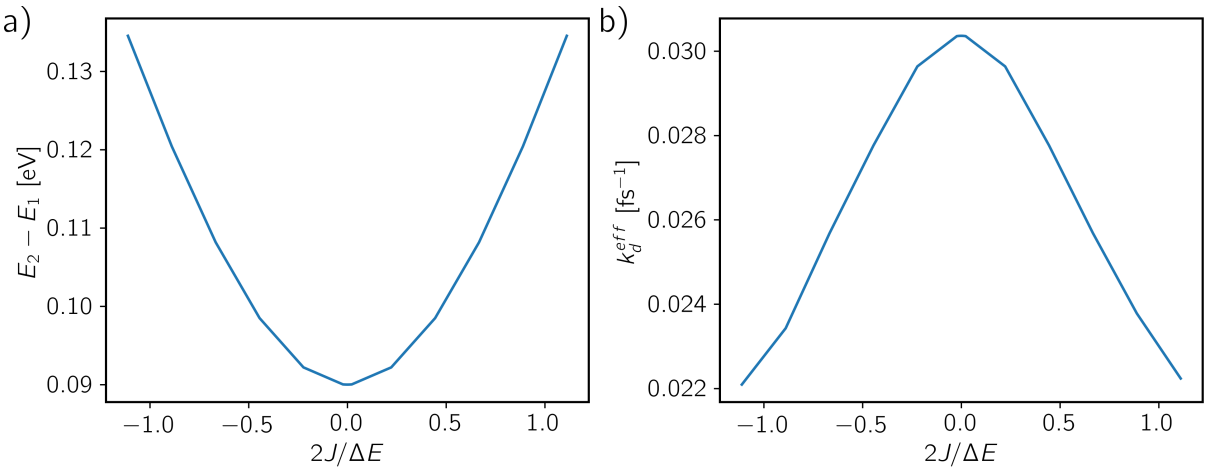

Fig. 6.A.8: a) Excitonic splitting and b) effective dephasing rate as a function of the excitonic coupling.

References

(1) Tiwari, V. Multidimensional Electronic Spectroscopy in High-Definition - Combining Spectral, Temporal, and Spatial Resolutions. *J. Chem. Phys.* **2021**, *154*, 230901.

(2) Karki, K. J.; Ciappina, M. F. Advances in Nonlinear Spectroscopy using Phase Modulated Light Fields: Prospective Applications in Perturbative and Non-Perturbative Regimes. *Adv. Phys.: X* **2022**, *7*, 2090856.

(3) Lott, G. A.; Perdomo-Ortiz, A.; Utterback, J. K.; Widom, J. R.; Aspuru-Guzik, A.; Marcus, A. H. Conformation of Self-Assembled Porphyrin Dimers in Liposome Vesicles by Phase-Modulation 2D Fluorescence Spectroscopy. *Proc. Natl. Acad. Sci. U.S.A.* **2011**, *108*, 16521–16526.

(4) Tiwari, V.; Matutes, Y. A.; Konar, A.; Yu, Z.; Ptaszek, M.; Bocian, D. F.; Holten, D.; Kirmaier, C.; Ogilvie, J. P. Strongly Coupled Bacteriochlorin Dyad Studied using Phase-Modulated Fluorescence-Detected Two-Dimensional Electronic Spectroscopy. *Opt. Express* **2018**, *26*, 22327–22341.

(5) Karki, K. J.; Chen, J.; Sakurai, A.; Shi, Q.; Gardiner, A. T.; Kühn, O.; Cogdell, R. J.; Pullerits, T. Before Förster. Initial Excitation in Photosynthetic Light Harvesting. *Chem. Sci.* **2019**, *10*, 7923–7928.

(6) Karki, K. J.; Widom, J. R.; Seibt, J.; Moody, I.; Lonergan, M. C.; Pullerits, T.; Marcus, A. H. Coherent Two-Dimensional Photocurrent Spectroscopy in a PbS Quantum Dot Photocell. *Nat. Commun.* **2014**, *5*, 5869.

(7) Bolzonello, L.; Bernal-Texca, F.; Gerling, L. G.; Ockova, J.; Collini, E.; Martorell, J.; van Hulst, N. F. Photocurrent-Detected 2D Electronic Spectroscopy Reveals Ultrafast Hole Transfer in Operating PM6/Y6 Organic Solar Cells. *J. Phys. Chem. Lett.* **2021**, *12*, 3983–3988.

(8) Roeding, S.; Brixner, T. Coherent Two-Dimensional Electronic Mass Spectrometry. *Nat. Commun.* **2018**, *9*, 2519.

(9) Uhl, D.; Bangert, U.; Bruder, L.; Stienkemeier, F. Coherent Optical 2D Photoelectron Spectroscopy. *Optica* **2021**, *8*, 1316–1324.

(10) Bakulin, A. A.; Silva, C.; Vella, E. Ultrafast Spectroscopy with Photocurrent Detection: Watching Excitonic Optoelectronic Systems at Work. *J. Phys. Chem. Lett.* **2016**, *7*, 250–258.

(11) Tiwari, V.; Matutes, Y. A.; Gardiner, A. T.; Jansen, T. L. C.; Cogdell, R. J.; Ogilvie, J. P. Spatially-Resolved Fluorescence-Detected Two-Dimensional Electronic Spectroscopy Probes Varying Excitonic Structure in Photosynthetic Bacteria. *Nat. Commun.* **2018**, *9*, 4219.

(12) Fersch, D.; Malý, P.; Rühe, J.; Lisinetskii, V.; Hensen, M.; Würthner, F.; Brixner, T. Single-Molecule Ultrafast Fluorescence-Detected Pump–Probe Microscopy. *J. Phys. Chem. Lett.* **2023**, *14*, 4923–4932.

(13) Lüttig, J.; Mueller, S.; Malý, P.; Krich, J. J.; Brixner, T. Higher-Order Multidimensional and Pump–Probe Spectroscopies. *J. Phys. Chem. Lett.* **2023**, *14*, 7556–7573.

(14) Malý, P.; Mancal, T. Signatures of Exciton Delocalization and Exciton–Exciton Annihilation in Fluorescence-Detected Two-Dimensional Coherent Spectroscopy. *J. Phys. Chem. Lett.* **2018**, *9*, 5654–5659.

(15) Schröter, M.; Pullerits, T.; Kühn, O. Using Fluorescence Detected Two-Dimensional Spectroscopy to Investigate Initial Exciton Delocalization between Coupled Chromophores. *J. Chem. Phys.* **2018**, *149*, 114107.

(16) Kunsel, T.; Tiwari, V.; Matutes, Y. A.; Gardiner, A. T.; Cogdell, R. J.; Ogilvie, J. P.; Jansen, T. L. C. Simulating Fluorescence-Detected Two-Dimensional Electronic Spectroscopy of Multichromophoric Systems. *J. Phys. Chem. B* **2019**, *123*, 394–406.

(17) Kalaee, A. A. S.; Damtie, F.; Karki, K. J. Differentiation of True Nonlinear and Incoherent Mixing of Linear Signals in Action-Detected 2D Spectroscopy. *J. Phys. Chem. A* **2019**, *123*, 4119–4124.

(18) Kühn, O.; Mančal, T.; Pullerits, T. Interpreting Fluorescence Detected Two-Dimensional Electronic Spectroscopy. *J. Phys. Chem. Lett.* **2020**, *11*, 838–842.

(19) Bruschi, M.; Bolzonello, L.; Gallina, F.; Fresch, B. Unifying Nonlinear Response and Incoherent Mixing in Action-2D Electronic Spectroscopy. *J. Phys. Chem. Lett.* **2023**, *14*, 6872–6879.

(20) Grégoire, P.; Srimath Kandada, A. R.; Vella, E.; Tao, C.; Leonelli, R.; Silva, C. Incoherent Population Mixing Contributions to Phase-Modulation Two-Dimensional Coherent Excitation Spectra. *J. Chem. Phys.* **2017**, *147*, 114201.

(21) Bittner, T.; Irrgang, K.-D.; Renger, G.; Wasielewski, M. R. Ultrafast Excitation Energy Transfer and Exciton-Exciton Annihilation Processes in Isolated Light Harvesting Complexes of Photosystem II (LHC II) from Spinach. *J. Phys. Chem.* **1994**, *98*, 11821–11826.

(22) Renger, T.; May, V. Multiple Exciton Effects in Molecular Aggregates: Application to a Photosynthetic Antenna Complex. *Phys. Rev. Lett.* **1997**, *78*, 3406–3409.

(23) Malyshev, V.; Glaeske, H.; Feller, K.-H. Exciton–Exciton Annihilation in Linear Molecular Aggregates at Low Temperature. *Chem. Phys. Lett.* **1999**, *305*, 117–122.

(24) Brüggemann, B.; Herek, J. L.; Sundström, V.; Pullerits, T.; May, V. Microscopic Theory of Exciton Annihilation: Application to the LH2 Antenna System. *J. Phys. Chem. B* **2001**, *105*, 11391–11394.

(25) May, V. Kinetic Theory of Exciton–Exciton Annihilation. *J. Chem. Phys.* **2014**, *140*, 054103.

(26) Tempelaar, R.; Jansen, T. L. C.; Knoester, J. Exciton–Exciton Annihilation Is Coherently Suppressed in H-Aggregates, but Not in J-Aggregates. *J. Phys. Chem. Lett.* **2017**, *8*, 6113–6117.

(27) Kumar, S.; Dunn, I. S.; Deng, S.; Zhu, T.; Zhao, Q.; Williams, O. F.; Tempelaar, R.; Huang, L. Exciton Annihilation in Molecular Aggregates Suppressed through Quantum Interference. *Nat. Chem.* **2023**, *15*, 1118–1126.

(28) Malý, P.; Lüttig, J.; Rose, P. A.; Turkin, A.; Lambert, C.; Krich, J. J.; Brixner, T. Separating Single- from Multi-Particle Dynamics in Nonlinear Spectroscopy. *Nature* **2023**, *616*, 280–287.

(29) Süß, J.; Engel, V. A Wave Packet Picture of Exciton–Exciton Annihilation: Molecular Dimer Dynamics. *J. Chem. Phys.* **2020**, *152*, 174305.

(30) Malý, P.; Lüttig, J.; Mueller, S.; Schreck, M. H.; Lambert, C.; Brixner, T. Coherently and Fluorescence-Detected Two-Dimensional Electronic Spectroscopy: Direct Comparison on Squaraine Dimers. *Phys. Chem. Chem. Phys.* **2020**, *22*, 21222–21237.

(31) Lindblad, G. On the Generators of Quantum Dynamical Semigroups. *Commun. Math. Phys.* **1976**, *48*, 119–130.

(32) Gorini, V.; Kossakowski, A.; Sudarshan, E. C. G. Completely Positive Dynamical Semigroups of N-Level Systems. *J. Math. Phys.* **1976**, *17*, 821–825.

(33) Haken, H.; Strobl, G. An Exactly Solvable Model for Coherent and Incoherent Exciton Motion. *Z. Phys.* **1973**, *262*, 135–148.

(34) Rebentrost, P.; Mohseni, M.; Kassal, I.; Lloyd, S.; Aspuru-Guzik, A. Environment-Assisted Quantum Transport. *New J. Phys.* **2009**, *11*, 033003.

(35) Caruso, F.; Chin, A. W.; Datta, A.; Huelga, S. F.; Plenio, M. B. Highly Efficient Energy Excitation Transfer in Light-Harvesting Complexes: The Fundamental Role of Noise-Assisted Transport. *J. Chem. Phys.* **2009**, *131*, 105106.

(36) Zerah-Harush, E.; Dubi, Y. Universal Origin for Environment-Assisted Quantum Transport in Exciton Transfer Networks. *J. Phys. Chem. Lett.* **2018**, *9*, 1689–1695.

(37) Ishizaki, A.; Fleming, G. R. On the Adequacy of the Redfield Equation and Related Approaches to the Study of Quantum Dynamics in Electronic Energy Transfer. *J. Chem. Phys.* **2009**, *130*, 234110.

(38) Brüggemann, B.; May, V. Exciton Exciton Annihilation Dynamics in Chromophore Complexes. I. Multiexciton Density Matrix Formulation. *J. Chem. Phys.* **2002**, *118*, 746–759.

(39) Tan, H.-S. Theory and Phase-Cycling Scheme Selection Principles of Collinear Phase Coherent Multi-Dimensional Optical Spectroscopy. *J. Chem. Phys.* **2008**, *129*, 124501.

(40) Paleček, D.; Edlund, P.; Gustavsson, E.; Westenhoff, S.; Zigmantas, D. Potential Pitfalls of the Early-Time Dynamics in Two-Dimensional Electronic Spectroscopy. *J. Chem. Phys.* **2019**, *151*, 024201.

(41) Rose, P. A.; Krich, J. J. Automatic Feynman Diagram Generation for Nonlinear Optical Spectroscopies and Application to Fifth-Order Spectroscopy with Pulse Overlaps. *J. Chem. Phys.* **2021**, *154*, 034109.

(42) Kiessling, A. J.; Cina, J. A. Monitoring the Evolution of Intersite and Interexciton Coherence in Electronic Excitation Transfer via Wave-Packet Interferometry. *J. Chem. Phys.* **2020**, *152*, 244311.

7 | Digital Quantum Simulation of Two Dimensional Electronic Spectroscopy

7.1. Introduction

Defining how the quantum nature of the molecular scale reflects on mesoscopic properties, such as energy and charge transport, has been a central issue in the physical chemistry research of the last two decades [1, 2]. On the other hand, the efforts spent to turn quantum features into useful resources brought to our labs the first generation of quantum computers. Although in the near future, we should not expect systematic performance improvements in using this technology over high-performance classical architectures [3], there is a need to explore scientifically relevant problems amenable to quantum advantage and to carry out proof-of-principle calculations in currently available quantum processors. In this work, we present a quantum algorithm for the simulation of Two-Dimensional Electronic Spectroscopy (2DES).

2DES has played a pivotal role in the investigation of energy transfer in biological complexes [4–7] and artificial systems [8–11]. non-linear response theory [12] provides the conceptual framework for the interpretation of the technique and the computational simulation of the spectra [13–18] In this context, the response function is defined on the basis of the quantum dynamics of the molecular system in the absence of the external field. Such dynamical simulation can become a hard problem for classical computers due to the exponential scaling of the Hilbert space with the system size, e.g., including vibrational degrees of freedom which are coupled to electronic transitions. Here is where Quantum Computers (QCs) can give an advantage taming the so-called curse of dimensionality.

At the core of QCs lies the quantum processor, typically comprising a register of two-

Adapted from Bruschi, M.; Gallina, F.; Fresch, B. *manuscript under revision*.

level quantum systems called qubits. Computation within QCs is achieved by manipulating their quantum state with unitary operations, called quantum gates, and taking the measurements of one or more qubits. The ordered sequence of all operations is collected in a structure known as the quantum circuit. Simulating the dynamics of many-body quantum systems is one of the most anticipated applications of QCs [19] because of the potential to solve the problem in polynomial time and using polynomial resources. An early demonstration of quantum speed-up in the simulation of unitary quantum dynamics was proposed by Lloyd [20]. More recently, several sophisticated protocols have been developed for simulating the dynamics of molecular systems [21–24]. In this work, we build on the advantage of quantum simulation of the field-free Hamiltonian dynamics, and we focus on the algorithm connecting such dynamics to the simulation of spectral features in linear and non-linear optical techniques. To this aim, we leverage the structure of the response function as a combination of Time Correlation Functions (TCFs) of the dipole moment operator of the system. In non-linear optical spectroscopy, the contributions to the signal are commonly visualized in terms of (double-sided) Feynman Diagrams (FDs), which are graphical representations of the pathways followed by the system upon light-matter interactions. The central idea of this work is to translate FDs into quantum circuits.

A number of recent investigations have focused on the quantum simulation of correlation and response functions with digital (and analog [25, 26]) QCs, albeit focusing mainly on the linear response. Among the proposed methods, there are strategies based on the quantum linear system algorithm [27] or variational approaches [27–30]. However, most proposals rely on the so-called Hadamard test [31], which, opportunely modified, can return an estimation of a quantum TCFs [32–37]. By designing the quantum algorithms to implement the FDs, we arrive at a formulation that fits into this framework. In particular, we exploit an *ancilla* qubit to control the evolution of the system, recovering the contribution of a selected pathway by measuring its state. For the sake of completeness, we also mention the alternative formulation of molecular spectra in terms of excited state calculations together with the sum-over-state method. Quantum implementations of this approach have been presented based on well-developed VQE-like hybrid algorithms [38–41]. Although well suited to reproduce linear response, this method provides a static representation of the system and therefore cannot be applied to the calculation of time-resolved experiments, like 2DES, where exciton transfer, spectral diffusion, motional narrowing and peak shifts are important observables.

The work is organized as follows: we begin by recalling the standard perturbative framework of non-linear optical spectroscopy, from which FDs are defined. Using this framework,

we map the dynamical pathways followed by the system during excitation to a quantum algorithm. To illustrate the procedure, we first consider in detail the simplest case of one chromophore with a single excited state. By generalizing the algorithm to an arbitrary number of chromophores, both the number of circuits to be evaluated and the number of gates per circuit increase polynomially with the size of the system. Then, we present the simulation of non-linear spectra calculated with real quantum hardware and compare it with the results obtained with a simulator. In particular, the cases of the 2DES response of a single chromophore and an excitonic dimer are used as proofs of concept, showing excellent agreement with the expected result. The software used for the simulations is freely available as a Python package[42].

7.2. Results and Discussion

We frame our investigation within a semi-classical description of the light-matter interaction. The total energy is given by the Hamiltonian

$$\hat{H}(t) = \hat{H}_0 + \hat{V}(t) \tag{7.1}$$

where $\hat{H}_0$ is the Hamiltonian of the system (possibly containing nuclear and solvent degrees of freedom), while the interaction Hamiltonian in the dipole approximation can be defined as

$$\hat{V}(t) = -\hat{\boldsymbol{\mu}} \cdot \boldsymbol{E}(t) \tag{7.2}$$

with $\hat{\boldsymbol{\mu}}$ the dipole moment operator of the system and $\boldsymbol{E}(t)$ the external electric field. In time-resolved spectroscopy, the electric field is typically given by the summation over the M pulses used to probe the system

$$\boldsymbol{E}(t) = \sum_{m=1}^{M} \boldsymbol{E}_m(t) \tag{7.3}$$

where each pulse

$$\boldsymbol{E}_m(t) = E_m^0 \mathcal{E}_m(t - \tau_m) e^{i(\boldsymbol{k}_m \cdot \boldsymbol{r} - \omega_m t)} \boldsymbol{e}_m + h.c. \tag{7.4}$$

is characterized by amplitude E_m^0, envelope $\mathcal{E}_m(t)$, central time τ_m, wavevector $\boldsymbol{k}_m$, frequency ω_m, and polarization unit vector $\boldsymbol{e}_m$. During the experiment, the electric field interacts with the sample consisting of many replicas of the system. For simplicity, from now on, we drop the polarization of the fields so that the vectorial nature of the dipole moment becomes unimportant. For an isotropic sample, an additional orientational average

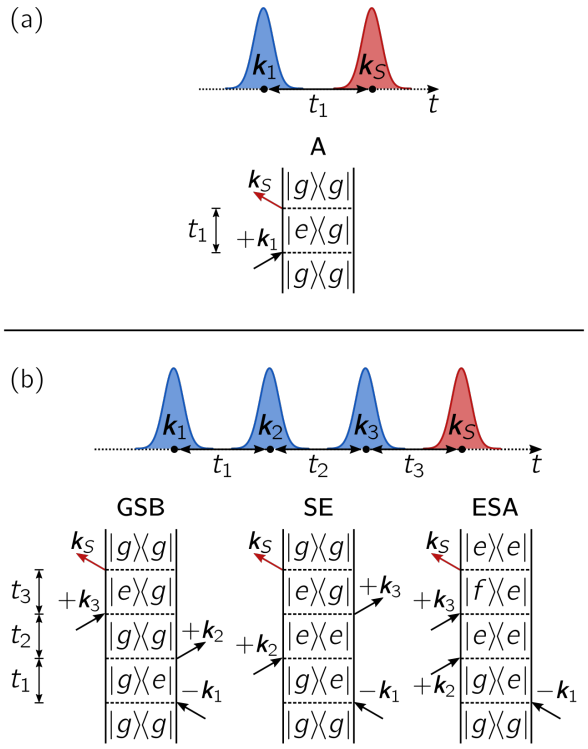

Fig. 7.1: Schematic representation of spectroscopic experiments and the associated (double-sided) Feynman diagrams. (a) Linear spectroscopy and Absorption (A) pathway and (b) 2D-electronic spectroscopy and rephasing signal contributions, namely the Ground-State Bleaching (GSB), Stimulated Emission (SE) and Excited-State Absorption (ESA) pathways.

should be performed [43].

As a result of the light-matter interaction, a macroscopic polarization $P(t)$ is induced in the sample which acts as a source of electric field, emitting a coherent signal $E_S(t) \propto iP(t)$. The total polarization can be expanded at different orders in the light-matter interaction $P(t) = \sum_{n=0}^{\infty} P^{(n)}(t)$. In the framework of non-linear response theory [12], the n-th order polarization is expressed as the convolution between the material response function and the external perturbation,

$$P^{(n)}(t) = \int_0^\infty dt_n \int_0^\infty dt_{n-1} \cdots \int_0^\infty dt_1 \, R^{(n)}(t_n, t_{n-1}, \ldots, t_1) \times E(t - t_n) E(t - t_n - t_{n-1}) \ldots E(t - t_n - t_{n-1} \cdots - t_1) \tag{7.5}$$

where the response function $R^{(n)}(t_n, t_{n-1}, ..., t_1)$ is a combination of $(n+1)$-TCFs of the dipole moment operator, with t_n the delay times between subsequent interactions with the electric field. The importance of this formulation lies in the separation between the material properties, namely the natural dynamics due to $\hat{H}_0$ and the dipole moment

operator $\hat{\mu}$, from the external fields. In the following, we focus on the material part of the response by assuming that electric fields are impulsive, i.e., short compared with any system timescale. In this limit, obtained formally by assuming a delta-function envelope for each pulse $\mathcal{E}_m(t-\tau_m) = \delta(t-\tau_m)$, the spectroscopic signals can be calculated directly from the response function $R^{(n)}(t_n, t_{n-1}, \ldots, t_1)$, where the time variables $t_n = \tau_{n+1} - \tau_n$ are the delay times between two subsequent pulses and a specific time-ordering of the interactions is assumed.

The response function is directly related to the perturbative expansion of the system density matrix at different orders of the light-matter interaction. At the n-th order, it includes terms with all possible combinations of interactions on the *ket* and the *bra* side of the system density matrix. By assuming a specific time-ordering of the pulses, each of these terms identifies a dynamical pathway corresponding to a particular sequence of excitation and de-excitation processes connecting different elements of the density matrix. However, spectroscopic signals are typically not calculated using the full perturbative expansion because only specific pathways give non-zero contributions to the measured signal. These pathways can be visualized using FDs [12, 44]. When the wavevectors of the applied laser pulses are non-collinear, signals originating from different FDs will be emitted in distinct phase-matching directions $\boldsymbol{k}_S = \sum_{m=1}^{M} \pm \boldsymbol{k}_m$.

In Fig. 7.1, we report the FDs relative to the Absorption (A) pathway for the linear signal (Fig. 7.1a) emitted along $\boldsymbol{k}_S = \boldsymbol{k}_1$ and the Ground-State Bleaching (GSB), Stimulated Emission (SE) and Excited-State Absorption (ESA) pathways contributing to the rephasing component of the third order signal (Fig. 7.1b) measured along $\boldsymbol{k}_S = -\boldsymbol{k}_1 + \boldsymbol{k}_2 + \boldsymbol{k}_3$. In these diagrams, time runs from the bottom to the top. The state of the system is indicated by two vertical lines, corresponding to the *ket* (left side) and *bra* (right side) components of the density matrix. Each black arrow corresponds to the interaction with a laser pulse, contributing with wavevector $+\boldsymbol{k}_m$ when it points to the right, or $-\boldsymbol{k}_m$ when it points to the left. The interaction results in an excitation when the arrow points towards the diagram or a de-excitation when it points outwards. Between two consecutive interactions, the state of the system freely evolves under the Hamiltonian $\hat{H}_0$. Finally, the red arrow at the top of the diagram represents the emission of the coherent signal with wavevector $\boldsymbol{k}_S$ according to the phase-matching condition.

The structure of FDs suggests an algorithmic representation of the corresponding dynamical process [45] according to the three blocks shown in Fig. 7.2: the state initialization, an interaction-evolution loop and the signal emission. Let us now elaborate on the details

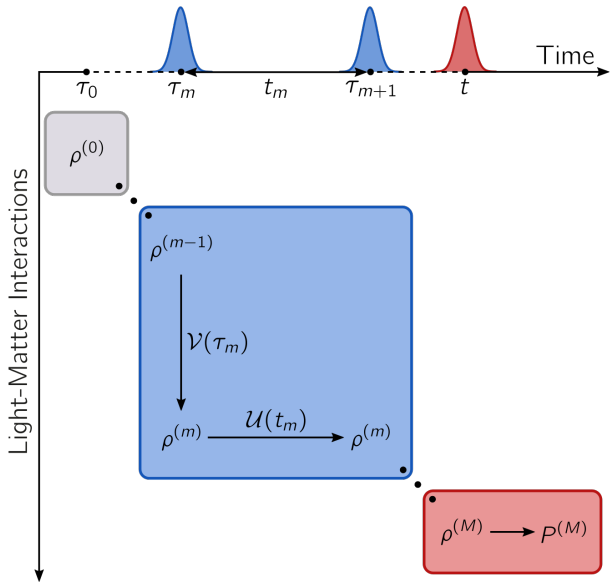

Fig. 7.2: Algorithmic representation of the non-linear optical response. In the beginning, the system state is initialized (grey block) and then updated to various orders of the light-matter interaction through the interaction-evolution loop (blue block). Finally, the total polarization at the M-th order is calculated, which is responsible for the signal emission (red block).

of these blocks for the simplest case study of a chromophore with a ground $|g\rangle$ and an excited $|e\rangle$ electronic state. The system Hamiltonian

$$\hat{H}_0 = -\frac{\epsilon}{2}\hat{\sigma}^z \tag{7.6}$$

and the dipole moment operator

$$\hat{\mu} = \mu\hat{\sigma}^x \tag{7.7}$$

can be written in terms of Pauli operators $\sigma^z = |g\rangle\langle g| - |e\rangle\langle e|$ and $\hat{\sigma}^x = |e\rangle\langle g| + |g\rangle\langle e|$, while ϵ is the excitation energy and μ is the transition dipole moment. Typically, at room temperature, the system is in the electronic ground state prior to any interaction, therefore the state is initialized in the pure-state density matrix $\rho^{(0)}(\tau_0) = |g\rangle\langle g|$ (grey block in Fig. 7.2).

To implement the interaction-evolution block, we proceed as follows. The interaction with the m-th pulse, occurring at time τ_m, is represented by the superoperator $\mathcal{V}_\alpha(\tau_m)$, where the subscript α identifies the pathway followed by the system during the coherent excitation (e.g., GSB, SE and ESA). According to each pathway, the state is updated at

the m-th order in the light-matter interaction through the relation

$$\begin{aligned}\rho_\alpha^{(m)}(\tau_m) &= \mathcal{V}_\alpha(\tau_m)\big[\rho_\alpha^{(m-1)}(\tau_m)\big] \\ &= \hat{V}_\alpha^{\mathrm{K}}(\tau_m)\rho_\alpha^{(m-1)}(\tau_m)\big(\hat{V}_\alpha^{\mathrm{B}}(\tau_m)\big)^\dagger\end{aligned} \tag{7.8}$$

where the second equality defines the Hilbert space operators acting on the right and the left of the density matrix. When the pulse acts on the *ket* component, $\hat{V}_\alpha^{\mathrm{K}}(\tau_m) = \mu E_m^0 \hat{\sigma}^x$ and $\hat{V}_\alpha^{\mathrm{B}}(\tau_m) = \hat{\mathbb{1}}$, while when it acts on the *bra* component, $\hat{V}_\alpha^{\mathrm{K}}(\tau_m) = \hat{\mathbb{1}}$ and $\hat{V}_\alpha^{\mathrm{B}}(\tau_m) = \mu E_m^0 \hat{\sigma}^x$. Subsequently, during the delay time between the pulses $t_m = \tau_{m+1} - \tau_m$, the system undergoes a free Hamiltonian evolution

$$\begin{aligned}\rho_\alpha^{(m)}(\tau_m + t_m) &= \mathcal{U}(t_m)\left[\rho_\alpha^{(m)}(\tau_m)\right] \\ &= \hat{U}(t_m)\rho_\alpha^{(m)}(\tau_m)\hat{U}^\dagger(t_m)\end{aligned} \tag{7.9}$$

where the time-evolution operators $\hat{U}(t_m) = \exp\big(-i\hat{H}_0 t_m\big)$ and $\hat{U}^\dagger(t_m)$ acts simultaneously on the *ket* and *bra* components, respectively. This interaction-evolution sequence (Eqs. 7.8 and 7.9) is repeated M times according to the target order of the response (blue block in Fig. 7.2).

Finally, the M-th order polarization is evaluated by summing the contributions of all the relevant pathways to obtain the signal of interest, that is

$$P^{(M)}(t) = \sum_\alpha P_\alpha^{(M)}(t) = \sum_\alpha s_\alpha \,\mathrm{Tr}\big\{\hat{\mu}\rho_\alpha^{(M)}(t)\big\} \tag{7.10}$$

where $s_\alpha = i^M(-1)^{m_{\mathrm{B}}}$ depends on the number of interactions m_{B} on the *bra* side of the FD corresponding to the α pathway.

The procedure of mapping FDs to quantum circuits is illustrated in Fig. 7.3 for the GSB pathway (Fig. 7.3a). The system is represented by a qubit, referred to as the *system* qubit, with the states $|0\rangle$ and $|1\rangle$ corresponding to the ground and excited state of the single chromophore, respectively. An additional qubit, known as the *ancilla* qubit, is introduced to perform the computation without representing any physical degree of freedom. By convention in quantum computing, the initial state of the quantum register is $|0\rangle \otimes |0\rangle_{\mathrm{a}}$, where the subscript identifies the *ancilla* qubit. In this case, the *system* qubit is already correctly initialized in the ground state of the chromophore. The first step of the circuit is to initialize the state of the *ancilla* into a superposition state. This is done by applying the

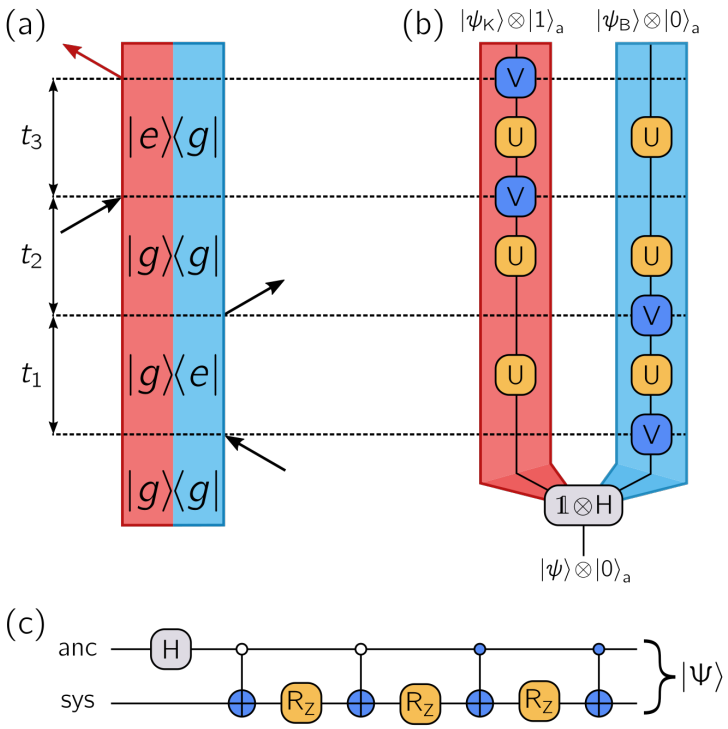

Fig. 7.3: Mapping procedure of a (double-sided) Feynman diagram onto a quantum circuit. (a) Feynman diagram corresponding to the ground-state bleaching pathway. (b) "Circuital" representation of the Feynman diagram. The left side corresponds to the $|1\rangle_a$ state of the *ancilla* qubit, while the right side corresponds to the $|0\rangle_a$ state. (c) Quantum circuit corresponding to the Feynman diagram. Involved gates are the Hadamard gate `H` (grey), which creates the initial superposition state, the single-qubit rotation R_Z (yellow), representing the Hamiltonian propagator of a two-level system, and the two-qubit `CNOT` gate (blue), representing the light-matter interaction.

	$\hat{K}_\alpha(1)$	$\hat{B}_\alpha(1)$	$\hat{K}_\alpha(2)$	$\hat{B}_\alpha(2)$	$\hat{K}_\alpha(3)$	$\hat{B}_\alpha(3)$
GSB	$\hat{\mathbb{1}}$	$\hat{\sigma}^x$	$\hat{\mathbb{1}}$	$\hat{\sigma}^x$	$\hat{\sigma}^x$	$\hat{\mathbb{1}}$
SE	$\hat{\mathbb{1}}$	$\hat{\sigma}^x$	$\hat{\sigma}^x$	$\hat{\mathbb{1}}$	$\hat{\mathbb{1}}$	$\hat{\sigma}^x$
ESA	$\hat{\mathbb{1}}$	$\hat{\sigma}^x$	$\hat{\sigma}^x$	$\hat{\mathbb{1}}$	$\hat{\sigma}^x$	$\hat{\mathbb{1}}$

Tab. 7.1: Operators $\hat{K}_\alpha(m)$ and $\hat{B}_\alpha(m)$ in Eq. 7.13 for the Ground-State Bleaching (GSB), Stimulated Emission (SE) and Excited-State Absorption (ESA) pathways of the rephasing signal.

so-called Hadamard gate, a one-qubit operation, which in the computational basis reads

$$\mathtt{H} = \frac{1}{\sqrt{2}} \begin{bmatrix} 1 & 1 \\ 1 & -1 \end{bmatrix}. \tag{7.11}$$

When the Hadamard gate is applied to the *ancilla* qubit, it leads to the superposition state

$$\left|\Psi^{(0)}\right\rangle = \frac{1}{\sqrt{2}}\left(|0\rangle \otimes |0\rangle_{\mathrm{a}} + |0\rangle \otimes |1\rangle_{\mathrm{a}} \right). \tag{7.12}$$

Here, we see the first role of the *ancilla*. In fact, by interpreting the *system* state associated with $|0\rangle_{\mathrm{a}}$ as corresponding to the *bra* side and that associated with $|1\rangle_{\mathrm{a}}$ as the *ket* side, the superposition of the *ancilla* allows us to distinguish the two sides of the FD (Fig. 7.3b).

Following this initialization step, the application of the interaction superoperator $\mathcal{V}_\alpha(\tau_m)$ of Eq. 7.8 is represented by the two-qubit operator

$$\hat{C}_\alpha(m) = \hat{B}_\alpha(m) \otimes |0\rangle\langle 0| + \hat{K}_\alpha(m) \otimes |1\rangle\langle 1| \,. \tag{7.13}$$

where $\hat{B}_\alpha(m) = \hat{\sigma}^x$ and $\hat{K}_\alpha(m) = \hat{\mathbb{1}}$ if the pulse acts on the *bra* side, or $\hat{B}_\alpha(m) = \hat{\mathbb{1}}$ and $\hat{K}_\alpha(m) = \hat{\sigma}^x$ if the pulse acts on the *ket* side. Operator $\hat{C}_\alpha$ corresponds to the so-called `CNOT` (controlled-`NOT` or controlled-`X`) gate, where the control state of the *ancilla* qubit can either be 0 or 1, depending on which side of the FD the pulse interacts with (see Tab. 7.1). Since quantum gates are unitary by definition, the factors μE_m^0 in the superoperator $\mathcal{V}_\alpha(\tau_m)$ (Eq. 7.8) have to be multiplied separately to the result at the end of the quantum computation.

After light-matter interaction, both branches of the density matrix evolve under the action of the system Hamiltonian (Eq. 7.9). In our quantum implementation, the operator for this unitary Hamiltonian propagation is straightforward,

$$\hat{U}(m) = \hat{U}(t_m) \otimes \hat{\mathbb{1}} \tag{7.14}$$

and, for a two-level system, it corresponds to the application of a rotation gate $\mathtt{R}_Z(\theta) = \exp\left(-i\frac{\theta}{2}\hat{\sigma}^z\right)$ to the *system* qubit, with $\theta = -\epsilon t_m$.

Overall, the sequential application of the field-interaction and free-evolution operators to the qubits reflects the update of the system state at the m-th order in the light-matter interaction

$$\begin{aligned}\left|\Psi^{(m)}\right\rangle =& \hat{U}(m)\hat{C}_\alpha(m)\left|\Psi^{(m-1)}\right\rangle \\ =& \frac{1}{\sqrt{2}}\ \left(\hat{U}(t_m)\hat{B}_\alpha(m)\left|\psi_{\mathrm{B}}^{(m-1)}\right\rangle \otimes |0\rangle_{\mathrm{a}}\right. \\ &\left. + \hat{U}(t_m)\hat{K}_\alpha(m)\left|\psi_{\mathrm{K}}^{(m-1)}\right\rangle \otimes |1\rangle_{\mathrm{a}}\right)\end{aligned} \tag{7.15}$$

where $\left|\psi_{\mathrm{B}}^{(m-1)}\right\rangle$ and $\left|\psi_{\mathrm{K}}^{(m-1)}\right\rangle$ are the states of the *system* qubit representing the *bra* and *ket* sides of the density matrix at the $(m-1)$-th order, respectively. M iterations of Eq. 7.15 defines the evolution block up to the M-th order.

In order to calculate the polarization, we have to apply a further `CNOT` gate

$$\hat{C}_{\mathrm{S}} = \hat{\mathbb{1}} \otimes |0\rangle\langle 0| + \hat{\sigma}^x \otimes |1\rangle\langle 1| \tag{7.16}$$

representing the dipole moment operator, which leads to the final state

$$\begin{aligned}\left|\Psi^{\mathrm{S}}\right\rangle &= \hat{C}_{\mathrm{S}}\left|\Psi^{(M)}\right\rangle \\ &= \frac{1}{\sqrt{2}}\left(\left|\psi_{\mathrm{B}}^{(M)}\right\rangle \otimes |0\rangle_{\mathrm{a}} + \hat{\sigma}^x\left|\psi_{\mathrm{K}}^{(M)}\right\rangle \otimes |1\rangle_{\mathrm{a}}\right).\end{aligned} \tag{7.17}$$

Note that also in this case we have to remember a multiplicative factor μ coming from Eq. 7.10. The quantum circuit that includes the discussed gates is reported in Fig. 7.3c for the GSB pathway.

Finally, to obtain the M-th order polarization, we exploit once again the *ancilla* qubit. In fact, as it follows from Eq. 7.17 and demonstrated in the App. 7.A, by measuring the expectation value of operator $\hat{O} = 2|0\rangle\langle 1|$ of the *ancilla*, we end up with an estimation of $\left\langle\psi_B^{(M)}\right|\hat{\sigma}^x\left|\psi_K^{(M)}\right\rangle$, which can be used to calculate the system response function. However, since operator $\hat{O}$ is non-unitary, in quantum computing its expectation value can be estimated by decomposing it into unitary contributions, $\hat{O} = \hat{\sigma}^x + i\hat{\sigma}^y$, with $\hat{\sigma}^y = i\left(|1\rangle\langle 0| - |0\rangle\langle 1|\right)$, and measuring their expectation values

$$\begin{aligned}\langle\hat{\sigma}^x\rangle_{\mathrm{a}} &= \left\langle\Psi^{\mathrm{S}}\right|\hat{\mathbb{1}} \otimes \hat{\sigma}^x\left|\Psi^{\mathrm{S}}\right\rangle \\ \langle\hat{\sigma}^y\rangle_{\mathrm{a}} &= \left\langle\Psi^{\mathrm{S}}\right|\hat{\mathbb{1}} \otimes \hat{\sigma}^y\left|\Psi^{\mathrm{S}}\right\rangle\end{aligned} \tag{7.18}$$

which are related to the real and imaginary parts, respectively, of the α component of the response function by

$$R_{\alpha}^{(M)} = s_{\alpha}\mu^{M}\left(\langle\hat{\sigma}^{x}\rangle_{\mathrm{a}} + i\,\langle\hat{\sigma}^{y}\rangle_{\mathrm{a}}\right). \tag{7.19}$$

Hence, the target polarization results as $P_{\alpha}^{(M)} = E_{M}^{0}E_{M-1}^{0}\ldots E_{1}^{0}R_{\alpha}^{(M)}$. We recall that both the response function and the polarization depend parametrically on the set of delay times probing the dynamics of the chromophore.

The generalization of the algorithm to a molecular aggregate composed of N interacting two-level systems is given in the App. 7.B. In this case, the number of *system* qubits is equal to the number of chromophores in the aggregate, yet only one *ancilla* qubit is necessary. Differently from the single chromophore case, in order to select the contributing pathways according to the rotating-wave approximation, the dipole moment operator must be decomposed as $\hat{\mu} = \hat{\mu}^{+} + \hat{\mu}^{-}$, where $\hat{\mu}^{+}$ and $\hat{\mu}^{-}$ are non-Hermitian operators responsible for excitation and de-excitation on the *ket* side of the density matrix, respectively. Since these operators are non-unitary, they do not correspond to quantum gates and must be further decomposed into the sum of unitary contributions.

It should be emphasized that no measurement of the *system* qubit is required as all the information regarding the response function is retrieved from the *ancilla*. The importance of this aspect of the readout procedure is evident when the system consists of multiple qubits since the number of measurements required by the circuit does not increase with the size of the system.

We tested the quantum algorithm on the Qiskit qasm_simulator and on the IBM quantum processors ibmq_manila [46]. Figs. 7.4 and 7.5 show the linear and non-linear optical response of a single chromophore and an excitonic dimer, respectively. Each optical response is calculated as the signal $E_{\mathrm{S}} \propto iP$ by running the algorithm for a set of delay times. For the third-order response, we set delay time $t_2 = 0$. In both the considered models, the GSB and SE pathways are identical. Thus, only one of them has been explicitly calculated. To reduce the burden of the time-scanning procedure, we performed an undersampling of the delay times and subsequently applied a rotating frame to the computed signals [47, 48]. To avoid artifacts due to the Fast Fourier Transform (FFT), the temporal responses are multiplied by an exponential window function and zero-padded, resulting in a Lorentzian lineshape of the peaks in the corresponding spectra. Standard measurement error mitigation is applied to the results of the quantum processor. Technical details about the simulations are reported in the App. 7.D.

As shown for the case of the single chromophore, the quantum algorithm provides the

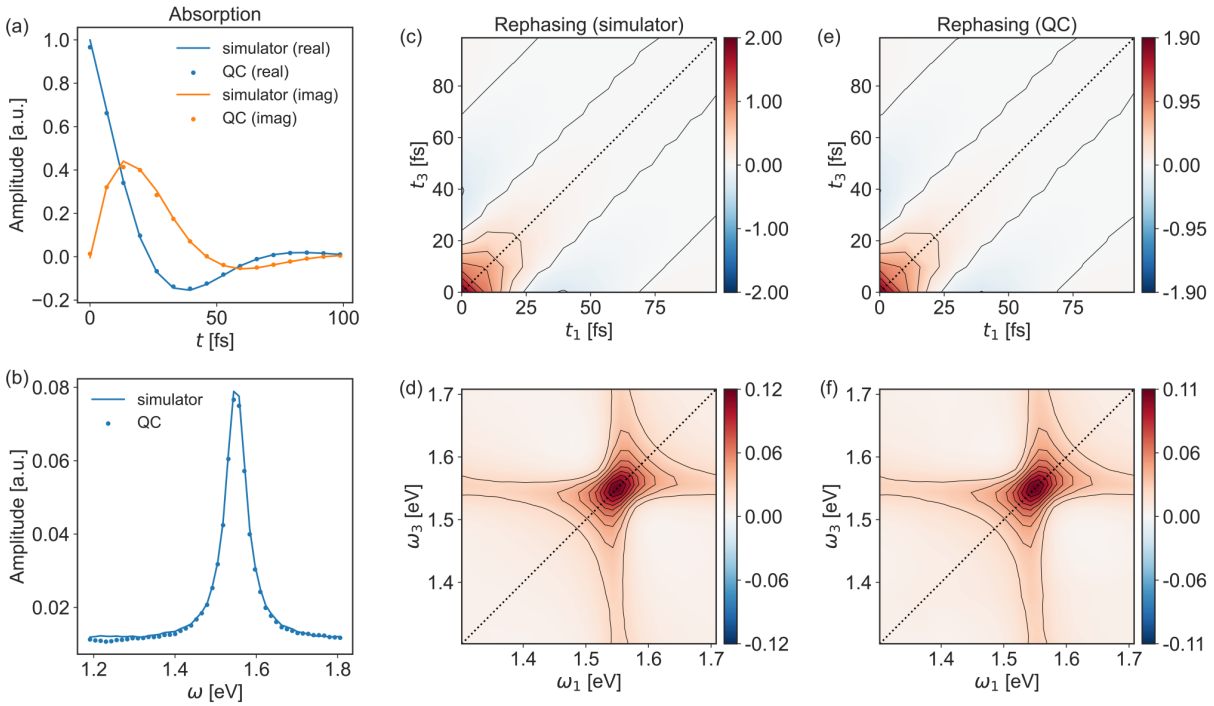

Fig. 7.4: Optical response of a single chromophore described as a two-level system. (a) Real and imaginary parts of the temporal linear signal ($\boldsymbol{k}_S = -\boldsymbol{k}_1$) obtained with Qiskit qasm_simulator and ibmq_manila quantum processor and (b) the corresponding absorption spectrum. (c, e) Real part of the rephasing third order signal ($\boldsymbol{k}_S = -\boldsymbol{k}_1 + \boldsymbol{k}_2 + \boldsymbol{k}_3$) obtained with Qiskit qasm_simulator and ibmq_manila quantum processor and (d, f) real part of the resulting 2D spectra.

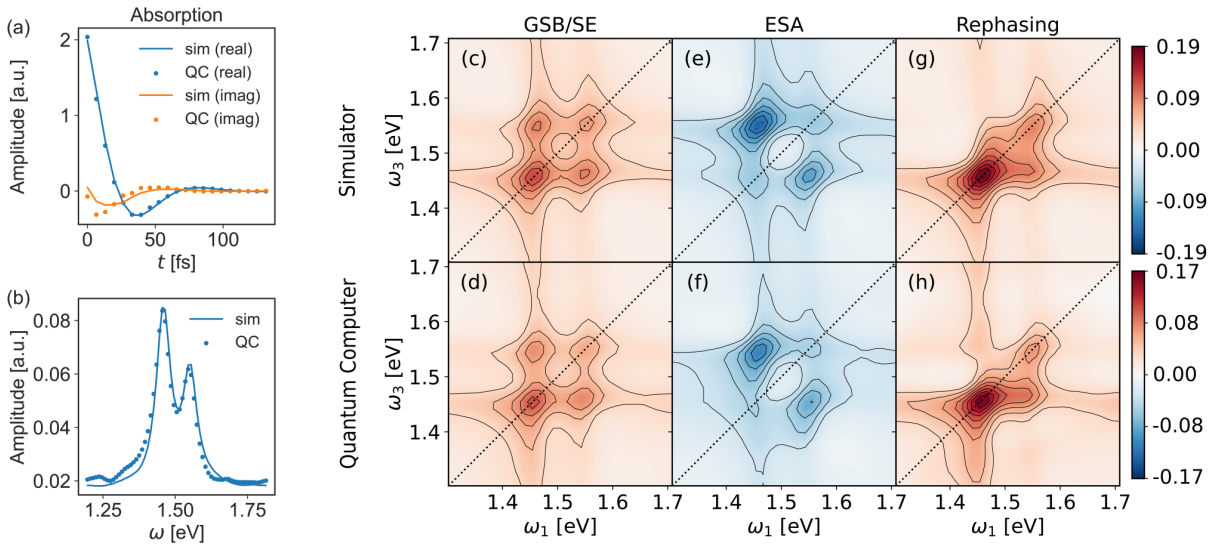

Fig. 7.5: Optical response of a dimer system. (a) Real and imaginary parts of the linear signal ($\boldsymbol{k}_S = -\boldsymbol{k}_1$) obtained with Qiskit qasm_simulator and ibmq_manila quantum processor and (b) the corresponding absorption spectra. Real parts of the 2D spectra for the (c, d) GSB (equal to the SE), (e, f) ESA and (g, h) total rephasing signal (obtained as the sum of GSB, SE and ESA spectra). Panels (c, e, g) are obtained from Qiskit qasm_simulator, while (d, f, h) result from ibmq_manila quantum processor.

first (Fig. 7.4a) and third order signals (Fig. 7.4c,e). Then, the linear (Fig. 7.4b) and 2D spectra (Fig. 7.4d,f) are obtained by taking the Fourier transform along suitable delay times. The results obtained with the QC closely reproduce those of the simulator in both shape and amplitude. This is not surprising since the quantum processor is in charge of executing quantum circuits with shallow depth, due to the small size and simple dynamics of the single chromophore case.

The number of qubits and complexity of the dynamics slightly increase in the case of an excitonic dimer. Nevertheless, even in this situation, the spectra obtained with the quantum processor match those of the simulator with encouraging accuracy. However, compared to the single chromophore case, we should note the appearance of some spurious features. In the linear spectrum (Fig. 7.5b), alongside the two main peaks, corresponding to the transition frequencies of the system, we observe the presence of some wiggles. These spectral features reflect noise in the data related to the temporal signal and are also affected by the post-processing procedure, like the rotating frame and zero-padding. In addition, a fictitious peak that used to emerge at zero frequency (see non-mitigated spectra in Fig. 7.E.7) can be eliminated with a mitigation protocol for the readout error. Concerning the 2D spectra, (temporal signal reported in Fig. 7.E.8), we computed the GSB (equivalent to the SE) and ESA contributions (Fig. 7.5c,d,e,f) and then the total rephasing

spectrum is obtained by summing up these contributions (Fig. 7.5g,h). The quantum processor correctly reproduces the peak positions and the overall shape of the spectral contributions. However, in the quantum hardware calculations, the relative amplitudes of the spectral features do not match exactly those obtained in the simulator, as they may vary in different runs of the algorithm. Because the total rephasing spectrum results from the fine balance between the positive (GSB and SE) and the negative (ESA) contributions, variations in the relative amplitude of the different contributions are reflected in the total spectrum (Fig. 7.5g,h) showing minimal differences with the simulated one.

In general, we trace the origin of these artifacts and deviations to two factors related to the scaling analysis of the algorithm whose details are reported in App. 7.C. One is the increased number of gates per circuit compared to the single chromophore, which is reflected in a longer circuit execution time. During this time, qubit relaxation dynamics occur, introducing noise in the quantum computation. The circuit complexity of the implementation mainly depends on the way the Hamiltonian propagator is executed, and scales as $\mathcal{O}\left(n_{\mathrm{T}}N^2\right)$ when 1-st order Trotterization is applied with n_{T} Trotter steps. The second factor to consider is the increased number of circuits to be computed, which scales as $\mathcal{O}\left(N^{M+1}\right)$. In fact, since these circuits are executed in different moments by the quantum processor, the noise level associated with the outcomes can be very different, causing asymmetries and artifacts in the spectra. In this regard, we report in Fig. 7.E.9 another independent simulation of the ESA contribution of the dimer. Although reproducing the same spectral features, the outcome of two independent runs is not exactly the same thus demonstrating how variability in the noise level of the circuit can influence the calculated spectra.

7.3. Conclusions

In summary, we have presented and discussed a quantum algorithm for the simulation of linear and non-linear optical responses of molecular systems based on quantum circuits calculating the terms of the corresponding response function. The quantum advantage stems from the efficient simulation of the quantum dynamics of the system evolution during the delay times (Eqs. 7.9 and 7.14), while the structure of the algorithm based on the independent computation of different FDs introduces flexibility in the kind of experiment to be simulated. The algorithm is naturally suited to include interaction with a complex environment. For example, it is possible to employ a stochastic propagation of the state vector exploiting the repetition of the quantum circuit due to sampling, as demonstrated

in the context of the simulation of exciton transport with digital QCs [49]. This method has already proven effective in the simulation of multidimensional optical spectroscopy on classical computer [50, 51]. Alternatively, other quantum algorithms to simulate open system dynamics of excitonic system have been proposed [52, 53] including an explicit representation of the environment through the use of a collision model [49] or by inserting vibrational degrees of freedom [54] to follow the wavepacket dynamics in the excited state [23, 55]. For multidimensional spectra, the scanning of delay times represents a demanding computational task both in classical and quantum implementations. To reduce the computational burden, strategies already implemented in experiments such as compressed sensing techniques [56–59], may aid in effectively reducing the number of sampled points. Although the focus of this work is on 2D electronic spectroscopy, the quantum algorithm can be easily adapted to simulate other coherent techniques in different spectral domains, from NMR to X-ray spectroscopy, sharing the common ground of response theory [60, 61].

7.A. Execution of the Quantum Algorithm for a Single Chromophore

In this appendix, we discuss step-by-step the evolution of the state of the quantum register during the algorithmic procedure discussed in the main text for the Ground-State Bleaching (GSB) pathway. At the beginning, the quantum register is initialized in

$$\left|\Psi^{(0)}\right\rangle = \frac{1}{\sqrt{2}}\left(\left|0\right\rangle \otimes \left|0\right\rangle_{\mathrm{a}} + \left|0\right\rangle \otimes \left|1\right\rangle_{\mathrm{a}}\right) \tag{7.A.20}$$

by applying a Hadamard gate to the *ancilla* qubit. Afterwards, the GSB pathway involves the interaction of the electric field with the *bra*, represented by the operator

$$\hat{C}_{\mathrm{GSB}}(1) = \hat{\sigma}^{x} \otimes \left|0\right\rangle\!\left\langle 0\right|_{\mathrm{a}} + \hat{\mathbb{1}} \otimes \left|1\right\rangle\!\left\langle 1\right|_{\mathrm{a}} \tag{7.A.21}$$

which leads, after Hamiltonian evolution $\hat{U}(t_1)$, to the following state of the quantum register

$$\left|\Psi^{(1)}\right\rangle = \frac{1}{\sqrt{2}}\left(\hat{U}(t_1)\hat{\sigma}^{x}\left|0\right\rangle \otimes \left|0\right\rangle_{\mathrm{a}} + \hat{U}(t_1)\left|0\right\rangle \otimes \left|1\right\rangle_{\mathrm{a}}\right). \tag{7.A.22}$$

This is repeated for a second interaction with the *bra*

$$\hat{C}_{\mathrm{GSB}}(2) = \hat{C}_{\mathrm{GSB}}(1) \tag{7.A.23}$$

and a third interaction with the *ket*

$$\hat{C}_{\mathrm{GSB}}(3) = \hat{\mathbb{1}} \otimes \left|0\right\rangle\!\left\langle 0\right|_{\mathrm{a}} + \hat{\sigma}^{x} \otimes \left|1\right\rangle\!\left\langle 1\right|_{\mathrm{a}} \tag{7.A.24}$$

leading to the state

$$\left|\Psi^{(3)}\right\rangle = \frac{1}{\sqrt{2}}\left(\hat{U}(t_3)\hat{U}(t_2)\hat{\sigma}^{x}\hat{U}(t_1)\hat{\sigma}^{x}\left|0\right\rangle \otimes \left|0\right\rangle_{\mathrm{a}} + \hat{U}(t_3)\hat{\sigma}^{x}\hat{U}(t_2)\hat{U}(t_1)\left|0\right\rangle \otimes \left|1\right\rangle_{\mathrm{a}}\right). \tag{7.A.25}$$

Then, the calculation of the polarization requires the application of the dipole moment operator on the *ket* side. This is represented by gate $\hat{C}_{\mathrm{S}}$ leading to the state

$$\left|\Psi^{\mathrm{S}}\right\rangle = \frac{1}{\sqrt{2}}\left(\left|\psi_{\mathrm{B}}^{(3)}\right\rangle \otimes \left|0\right\rangle_{\mathrm{a}} + \hat{\sigma}^{x}\left|\psi_{\mathrm{K}}^{(3)}\right\rangle \otimes \left|1\right\rangle_{\mathrm{a}}\right) \tag{7.A.26}$$

where

$$\begin{aligned}\left|\psi_{\mathrm{B}}^{(3)}\right\rangle &= \hat{U}(t_3)\hat{U}(t_2)\hat{\sigma}^x\hat{U}(t_1)\hat{\sigma}^x\left|0\right\rangle \\ \left|\psi_{\mathrm{K}}^{(3)}\right\rangle &= \hat{U}(t_3)\hat{\sigma}^x\hat{U}(t_2)\hat{U}(t_1)\left|0\right\rangle\end{aligned} \tag{7.A.27}$$

are the states of the *system* qubit representing the *bra* and *ket* sides of the density matrix at the third order, respectively. Finally, our interest is in measuring operator $\hat{O} = 2\left|0\right\rangle\!\left\langle 1\right|$ of the *ancilla* qubit since its expectation value is

$$\begin{aligned}2\,\mathrm{Tr}\left\{\hat{\mathbb{1}}\otimes\left|0\right\rangle\!\left\langle 1\right|\left|\Psi^{\mathrm{S}}\right\rangle\!\left\langle\Psi^{\mathrm{S}}\right|\right\} &= \mathrm{Tr}\left\{\hat{\sigma}^x\left|\psi_{\mathrm{K}}^{(3)}\right\rangle\!\left\langle\psi_{\mathrm{B}}^{(3)}\right|\right\} \\ &= \mathrm{Tr}\left\{\hat{\sigma}^x\hat{U}(t_3)\hat{\sigma}^x\hat{U}(t_2)\hat{U}(t_1)\left|0\right\rangle\!\left\langle 0\right|\hat{\sigma}^x\hat{U}^\dagger(t_1)\hat{\sigma}^x\hat{U}^\dagger(t_2)\hat{U}^\dagger(t_3)\right\} \\ &= \mathrm{Tr}\{\hat{\sigma}^x(t_3+t_2+t_1)\hat{\sigma}^x(t_2+t_1)\left|0\right\rangle\!\left\langle 0\right|\hat{\sigma}^x(0)\hat{\sigma}^x(t_1)\} \\ &= iR_{\mathrm{GSB}}^{(3)}(t)/\mu^3\end{aligned} \tag{7.A.28}$$

where we used the identity $\hat{U}(t)\hat{U}^\dagger(t) = \hat{\mathbb{1}}$ and the interaction picture to go from the second to the third line. However, since operator $\hat{O}$ is non-unitary, in quantum computing its expectation value can be estimated by decomposing it into unitary contributions, $\hat{O} = \hat{\sigma}^x + i\hat{\sigma}^y$, with $\hat{\sigma}^x = \left|1\right\rangle\!\left\langle 0\right| + \left|0\right\rangle\!\left\langle 1\right|$ and $\hat{\sigma}^y = i\left(\left|1\right\rangle\!\left\langle 0\right| - \left|0\right\rangle\!\left\langle 1\right|\right)$, and measuring their expectation values

$$\begin{aligned}\left\langle\hat{\sigma}^x\right\rangle_{\mathrm{a}} &= \left\langle\Psi^{\mathrm{S}}\right|\hat{\mathbb{1}}\otimes\hat{\sigma}^x\left|\Psi^{\mathrm{S}}\right\rangle \\ \left\langle\hat{\sigma}^y\right\rangle_{\mathrm{a}} &= \left\langle\Psi^{\mathrm{S}}\right|\hat{\mathbb{1}}\otimes\hat{\sigma}^y\left|\Psi^{\mathrm{S}}\right\rangle\end{aligned} \tag{7.A.29}$$

so that the final form of the GSB response function is

$$R_{\mathrm{GSB}}^{(3)} = -i\mu^3\left(\left\langle\hat{\sigma}^x\right\rangle_{\mathrm{a}} + i\left\langle\hat{\sigma}^y\right\rangle_{\mathrm{a}}\right). \tag{7.A.30}$$

7.B. Generalized Quantum Algorithm for Molecular Aggregates

In this appendix, we generalize the procedure to the case of a molecular aggregate composed of N interacting chromophores, each with a ground $\left|g_i\right\rangle$ and an excited $\left|e_i\right\rangle$

electronic state. The energy is described by the Frenkel Hamiltonian in the form

$$\hat{H}_0 = -\sum_{i=1}^{N} \frac{\epsilon_i}{2} \hat{\sigma}_i^z + \sum_{i=1}^{N} \sum_{\substack{j=1 \\ j \neq i}}^{N} J_{ij} \hat{\sigma}_i^+ \hat{\sigma}_j^- \tag{7.B.31}$$

where $\sigma_i^z = |g_i\rangle\langle g_i| - |e_i\rangle\langle e_i|$, $\sigma_i^+ = |e_i\rangle\langle g_i|$ and $\sigma_i^- = |g_i\rangle\langle e_i|$. The excitation energy gap of the i-th molecule is denoted by ϵ_i, while J_{ij} is the excitonic coupling between molecule i and j, which is assumed to be real in the following. Depending on the number of excitations in the aggregate, we can distinguish different exciton manifolds. In particular, in the following, we will use $|0\rangle \equiv \bigotimes_i |g_i\rangle$ for the collective ground state, $|i\rangle \equiv |e_i\rangle \bigotimes_{j \neq i} |g_j\rangle = \sigma_i^+ |0\rangle$ for one-exciton states and $|ij\rangle \equiv |e_i\rangle |e_j\rangle \bigotimes_{k \neq i,j} |g_k\rangle = \sigma_i^+ \sigma_j^+ |0\rangle$. The total dipole moment operator of the aggregate is

$$\hat{\mu} = \sum_{i=1}^{N} \mu_i \hat{\sigma}_i^x \tag{7.B.32}$$

where μ_i is the transition dipole moment of the i-th molecule. To pave the way for future approximations, it is convenient to distinguish the two non-Hermitian contributions to the dipole moment operator responsible for the excitation and de-excitation of the aggregate. We have thus

$$\hat{\mu} = \hat{\mu}^+ + \hat{\mu}^- \tag{7.B.33}$$

with

$$\hat{\mu}^\pm = \sum_{i=1}^{N} \mu_i \hat{\sigma}_i^\pm. \tag{7.B.34}$$

Assuming the RWA, either the rotating E_m^+ or counter-rotating E_m^- component of the electric field contributes to the signal. In this case, the light-matter interaction Hamiltonian $\hat{V}(t)$ can be decomposed as

$$\hat{V}(t) = \hat{V}^+(t) + \hat{V}^-(t) \tag{7.B.35}$$

where

$$\hat{V}^\pm(t) = \sum_{i=1}^{N} V_i^\pm(t) \hat{\sigma}_i^\pm \tag{7.B.36}$$

and

$$V_i^\pm(t) = -\sum_{i=1}^{N} \mu_i E^\pm(t). \tag{7.B.37}$$

The RWA introduces some substantial changes in the algorithmic implementation of FDs suggested in the main text. In particular, in Eq. 7.8 of the main text becomes

$$\rho_{\alpha}^{(m)}(\tau_m) = \hat{V}_{\alpha}^{\mathrm{K}}(\tau_m)\rho_{\alpha}^{(m-1)}(\tau_m)\big(\hat{V}_{\alpha}^{\mathrm{B}}(\tau_m)\big)^{\dagger} \tag{7.B.38}$$

the operators $\hat{V}_{\alpha}^{\mathrm{K}}(\tau_m)$ and $\hat{V}_{\alpha}^{\mathrm{B}}(\tau_m)$ are now defined as

$$\begin{cases} \hat{V}_{\alpha}^{\mathrm{K}}(\tau_m) = \hat{V}^{\pm}(\tau_m) \\ \hat{V}_{\alpha}^{\mathrm{B}}(\tau_m) = \hat{\mathbb{1}} \end{cases} \tag{7.B.39}$$

when the pulse acts as an excitation (+) or de-excitation (-) on the *ket* component, and

$$\begin{cases} \hat{V}_{\alpha}^{\mathrm{K}}(\tau_m) = \hat{\mathbb{1}} \\ \hat{V}_{\alpha}^{\mathrm{B}}(\tau_m) = \hat{V}^{\pm}(\tau_m) \end{cases} \tag{7.B.40}$$

when the pulse acts as an excitation (+) or de-excitation (-) on the *bra* component. We highlight that the action of $V^{\pm}(t)$ promotes a transition to a neighboring exciton manifold.

Similarly, the emission of the final signal is influenced by the RWA too. In particular, the M-th order polarization is obtained as

$$P^{(M)}(t) = \sum_{\alpha} s_{\alpha}\,\mathrm{Tr}\big\{\hat{\mu}^{-}\rho_{\alpha}^{(M)}(t)\big\} \tag{7.B.41}$$

where $s_{\alpha} = i^{M}(-1)^{m_{\mathrm{B}}}$ depends on the number of interactions m_{B} on the *bra* side of the FD corresponding to the α pathway.

7.B.1. Decomposition of Non-Unitary Operators

In contrast to the single chromophore case, operators appearing in Eq. 7.B.38 are non-unitary. Therefore, if we want to calculate the polarization components using a quantum computer, we have to tackle the problem of assembling the quantum circuit in terms of (unitary) quantum gates. To solve the issue, we must decompose the dipole moment operators as the sum of unitary contributions.

Let us take the GSB of a third-order rephasing signal as an example to illustrate the

procedure. First, we expand the trace in Eq. 7.B.41 by using Eqs. 7.B.34 and 7.B.36

$$\begin{aligned}\mathrm{Tr}\Big\{\hat{\mu}^{-}\rho^{(3)}_{\mathrm{GSB}}(t)\Big\} = \sum_{i,j,k,l=1}^{N} & V_i^{-}(\tau_1)V_j^{+}(\tau_2)V_k^{+}(\tau_3)\mu_l \\ & \mathrm{Tr}\big\{\hat{\sigma}_l^{-}\hat{U}(\tau_3)\hat{\sigma}_k^{+}\hat{U}(\tau_2+\tau_1)\rho^{(0)}(\tau_0)\hat{\sigma}_i^{-}\hat{U}^{\dagger}(\tau_1)\hat{\sigma}_j^{+}\hat{U}^{\dagger}(\tau_2+\tau_3)\big\}.\end{aligned} \tag{7.B.42}$$

The various TCFs in the summation consider the possible excitation and de-excitation pathways through the different chromophores in the aggregate. In fact, the first light-matter interaction excites the i-th chromophore. Subsequently, as a consequence of the exciton coupling, excitation is redistributed in the network during the free Hamiltonian evolution, so that the second interaction causes the de-excitation of a chromophore j. The same reasoning applies to the following interactions. Note that, in this case, up to four different chromophores can be involved.

Once we have Eq. 7.B.42, the argument inside the trace still contains non-unitary operators. Thus, we exploit the equivalence

$$\hat{\sigma}^{\pm} = \frac{\hat{\sigma}^{x} \mp i\hat{\sigma}^{y}}{2} \tag{7.B.43}$$

to rewrite the trace as

$$\begin{aligned}&\mathrm{Tr}\big\{\hat{\sigma}_l^{-}\hat{U}(\tau_3)\hat{\sigma}_k^{+}\hat{U}(\tau_2+\tau_1)\rho^{(0)}(\tau_0)\hat{\sigma}_i^{-}\hat{U}^{\dagger}(\tau_1)\hat{\sigma}_j^{+}\hat{U}^{\dagger}(\tau_2+\tau_3)\big\} = \\ &= \sum_{o,o',o'',o'''=x,y} \frac{1}{16} c_o c_{o'} c_{o''} c_{o'''}\, \mathrm{Tr}\big\{\hat{\sigma}_l^{o'''}\hat{U}(\tau_3)\hat{\sigma}_k^{o''}\hat{U}(\tau_2+\tau_1)\rho^{(0)}(\tau_0)\hat{\sigma}_i^{o}\hat{U}^{\dagger}(\tau_1)\hat{\sigma}_j^{o'}\hat{U}^{\dagger}(\tau_2+\tau_3)\big\}\end{aligned} \tag{7.B.44}$$

where

$$c_o = \begin{cases} 1 & \text{if } o = x \\ i & \text{if } o = y \end{cases} \quad c_{o'} = \begin{cases} 1 & \text{if } o' = x \\ -i & \text{if } o' = y \end{cases} \quad c_{o''} = \begin{cases} 1 & \text{if } o'' = x \\ -i & \text{if } o'' = y \end{cases} \quad c_{o'''} = \begin{cases} 1 & \text{if } o''' = x \\ i & \text{if } o''' = y \end{cases} \tag{7.B.45}$$

With Eq. 7.B.44, we finally got an expression in which all the operators acting on the density matrix are unitary operators. Therefore, we are ready for the composition of the quantum circuit.

7.B.2. Circuit Construction

In the circuit construction, the N chromophore aggregate is represented by N qubits of the *system* quantum register, while an *ancilla* qubit is used to identify the *ket* and *bra* sides of the FD as for the single chromophore case reported in the main text. The collective ground state of the aggregate $|0\rangle$ corresponds to the *system*-qubit state $|\mathbf{0}\rangle \equiv \bigotimes_{i=1}^{N} |0\rangle_i$. At the beginning of the circuit, the *ancilla* qubit is prepared into a superposition state by applying a Hadamard gate

$$\left|\Psi^{(0)}\right\rangle = \frac{1}{\sqrt{2}}\left(|\mathbf{0}\rangle \otimes |0\rangle_{\mathrm{a}} + |\mathbf{0}\rangle \otimes |1\rangle_{\mathrm{a}} \right) \tag{7.B.46}$$

which represents the two branches of the Feynman diagram by interpreting the *system* state associated with $|0\rangle_{\mathrm{a}}$ as corresponding to the *bra* side, and the other associated with $|1\rangle_{\mathrm{a}}$ as the *ket* side.

The target of the circuits is to calculate the TCFs at the right-hand side of Eq. 7.B.44. To do so, we make use of controlled gates to represent the light-matter interactions. We define the operator

$$\hat{C}^{o}_{\alpha}(m,i) = \hat{B}^{o}_{\alpha}(m,i) \otimes |0\rangle\langle 0|_{\mathrm{a}} + \hat{K}^{o}_{\alpha}(m,i) \otimes |1\rangle\langle 1|_{\mathrm{a}} \tag{7.B.47}$$

where

$$\begin{cases} \hat{B}^{o}_{\alpha}(m,i) = \hat{\sigma}^{o}_{i} \\ \hat{K}^{o}_{\alpha}(m,i) = \hat{\mathbb{1}} \end{cases} \tag{7.B.48}$$

if the pulse acts on the *bra* side, or

$$\begin{cases} \hat{B}^{o}_{\alpha}(m,i) = \hat{\mathbb{1}} \\ \hat{K}^{o}_{\alpha}(m,i) = \hat{\sigma}^{o}_{i} \end{cases} \tag{7.B.49}$$

if the pulse acts on the *ket* side. The index i denotes the target-qubit representing the i-th chromophore, while the superscript o can be either x or y depending on the TCF we are evaluating. The controlled gates correspond to `CNOT` (`CX`) and `CY` quantum gates, respectively, where the control state is the *ancilla* state 0 when we refer to Eq. 7.B.48 and 1 when we refer to Eq. 7.B.49.
For example, the first interaction in a GSB pathway is

$$\hat{C}^{o}_{\mathrm{GSB}}(m=1,i) = \hat{\sigma}^{o}_{i} \otimes |0\rangle\langle 0|_{\mathrm{a}} + \hat{\mathbb{1}} \otimes |1\rangle\langle 1|_{\mathrm{a}} \,. \tag{7.B.50}$$

After a controlled operation, which represents the light-matter interaction, the free Hamiltonian evolution is performed on the *system* qubits, represented by the unitary operator

$$\hat{U}(m) = \hat{U}(t_m) \otimes \hat{\mathbb{1}}. \tag{7.B.51}$$

Differently from the single chromophore case, $\hat{U}(m)$ is in general a multi-qubit gate and it must be decomposed into 1- and 2-qubit gates in order to be executed by a quantum processor. Various methods can be used for the scope. An effective method is to use Trotter decomposition [20] to write the operator in terms of simple gates

$$\hat{U}(t_m) \approx \left(\prod_{i=1}^{N} \mathrm{R}_{Z_i}\left(-2\epsilon_i \frac{t_m}{n_\mathrm{T}}\right) \prod_{i=1}^{N-1} \prod_{j=i+1}^{N} \mathrm{R}_{X_iX_j}\left(J_{ij}\frac{t_m}{n_\mathrm{T}}\right) \mathrm{R}_{Y_iY_j}\left(J_{ij}\frac{t_m}{n_\mathrm{T}}\right) \right)^{n_\mathrm{T}} \tag{7.B.52}$$

where

$$\begin{cases} \mathrm{R}_{Z_i}(\theta) = \exp\left(-i\frac{\theta}{2}\hat{\sigma}_i^z\right) \\ \mathrm{R}_{X_iX_j}(\theta) = \exp\left(-i\frac{\theta}{2}\hat{\sigma}_i^x \otimes \hat{\sigma}_j^x\right) \\ \mathrm{R}_{Y_iY_j}(\theta) = \exp\left(-i\frac{\theta}{2}\hat{\sigma}_i^y \otimes \hat{\sigma}_j^y\right). \end{cases} \tag{7.B.53}$$

We recall that Trotterization is exact in the limit of large n_T or small t_m. In the case of a sparse Hamiltonian, i.e., $J_{ij} \neq 0$, Eq. 7.B.52 requires the execution of $\mathcal{O}(n_\mathrm{T}N^2)$ `CNOT` gates.

The application of the last dipole operator before the calculation of the trace is represented by the controlled gate associated with the operator

$$\hat{C}_\mathrm{S}^o(i) = \hat{\mathbb{1}} \otimes |0\rangle\langle 0|_\mathrm{a} + \hat{\sigma}_i^o \otimes |1\rangle\langle 1|_\mathrm{a}\,. \tag{7.B.54}$$

Finally, the result is obtained as for the single chromophore case, i.e., by measuring the expectation value of the ancilla operator $\hat{O} = 2\,|0\rangle\langle 1|$.

7.C. Scaling of the Algorithm

In the previous section, we have given details about the number of `CNOT` gates required during the algorithmic execution. In this appendix, we discuss the total number of circuits required for having an estimation of $\mathrm{Tr}\left\{\hat{\mu^-}\rho_\alpha^{(M)}(t)\right\}$.

The decomposition of the collective dipole moment operators into single chromophore operators (Eq. 7.B.42) generates N^{M+1} terms. Each of these terms is then divided into

# of circuits	# of CNOTs / circuit
$\mathcal{O}\left(N^{M+1}\right)$	$\mathcal{O}\left(n_{\mathrm{T}}N^2\right)$

Tab. 7.C.2: Algorithmic scaling. M is the order of the perturbation, N the number of chromophores in the aggregate and n_{T} the Trotter number.

2^{M+1} elements coming from the decomposition of ladder operators $\hat{\sigma}^+$ and $\hat{\sigma}^-$ into unitary operators $\hat{\sigma}^x$ and $\hat{\sigma}^y$ (see Eq. 7.B.44). Thus, the total number of TCFs to be evaluated is $(2N)^{M+1}$, i.e., polynomial with the number of chromophores and exponential in the order of the perturbation. However, as discussed in App. 7.A, the computation of the expectation value of the *ancilla* operator $\hat{O} = 2\,|0\rangle\langle 1|$ requires the independent measurement of the expectation values of $\hat{\sigma}^x$ and $\hat{\sigma}^y$ (see Fig. 7.C.6). Therefore, the total number of circuits is twice the number of TCFs mentioned above, i.e., $2^{M+2}N^{M+1}$.

We have noticed that, in some cases, the number of circuits can be slightly reduced. In fact, when the system energy is constant between two pulses (that is, in the absence of dissipations) and the initial state is the collective ground state, $\rho^{(0)}(\tau_0) = |0\rangle\langle 0|$, we can reduce the number of circuits to be evaluated. On the one hand, the first interaction acting on the *ket* and the first interaction acting on the *bra*, which has the effect of exciting from the ground state to the one-exciton manifold, can be performed with σ^x instead of decomposing σ^+ and σ^- since there is no possibility of promoting transitions to other manifolds. Moreover, the last operator, correspondent to the calculation of the polarization, can also be implemented with σ^x instead of decomposing σ^-, as the correct state is naturally selected by measuring the expectation value of $\hat{O}$. In this case, the number of circuits to run reduces to $2^M N^{M+1}$ when all the field interacts only with one side of the FD or to $2^{M-1}N^{M+1}$ when they interact with both sides. For example, for the GSB the total number of relevant circuits to be evaluated is thus $4N^4$ instead of $32N^4$.

Tab. 7.C.2 provides a concise summary of the scaling of the number of circuits and the number of CNOT gates per circuit.

7.D. Simulation Details

The single chromophore corresponds to a two-level system with Hamiltonian $H = -\frac{\epsilon}{2}\hat{\sigma}_z$ and excitation energy $\epsilon = 1.55$ eV.

For the dimer case, the system corresponds to two interacting two-level systems with

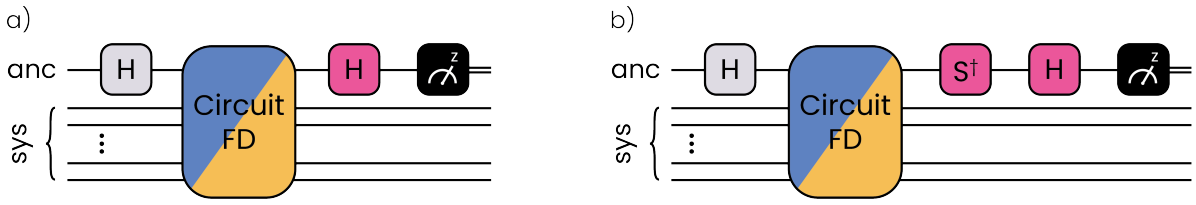

Fig. 7.C.6: Quantum circuits for measuring the expectation value of operators (a) $\hat{\sigma}^x$ and (b) $\hat{\sigma}^y$ of the *ancilla* quibit.

Hamiltonian 7.B.31 and excitation energies chosen to match the ones of the B800 ($\epsilon_1 = 1.55$ eV) and B850 ($\epsilon_2 = 1.46$ eV) rings of the LH2 complex [62]. The excitonic coupling is set to $J_{12} = -0.01$ eV. Since Trotterization is an overshooting technique for simulating the analyzed dimer system (besides being beyond the possibilities of the used quantum processor), the unitary Hamiltonian evolution between two pulses is converted in a short sequence of one- and two-qubit gates by the Qiskit transpiler.

To reduce the number of sampled points, we employed an undersampling of the delay times and then applied to the signal a rotating frame at frequency $\omega_{\mathrm{RF}} = 1.505$ eV [47, 48]. The computed temporal signal is multiplied by an exponential window function with decay time 140 fs and zero-padded. Measurement error mitigation is applied to the results of the quantum processor by means of a calibration matrix. In all the calculations we set the transition dipole moment $\mu_i = 1$ a.u. and the electric field amplitude $E_m^0 = 1$ eV.

7.E. Additional Figures

In Fig. 7.E.7, we show the typical emergence of an artifact at zero frequency (rotating frame not applied) in the absorption spectra of the excitonic dimer collected from ibmq_manila quantum processor without measurement-error mitigation. The artifact emerges because of the uneven probability of correctly measuring states 0 and 1. In Fig. 7.E.8, we show the temporal signals related to the excitonic dimer spectra reported in the main text. In Fig. 7.E.9, the variability of NISQ devices is evident by comparing the same 2D spectra for the ESA of the excitonic dimer collected during two different runs of the quantum algorithm. Data have been collected from the ibm_perth quantum processor without measurement-error mitigation. The intensity of the peaks and spurious noisy contributions are visibly different in the two cases.

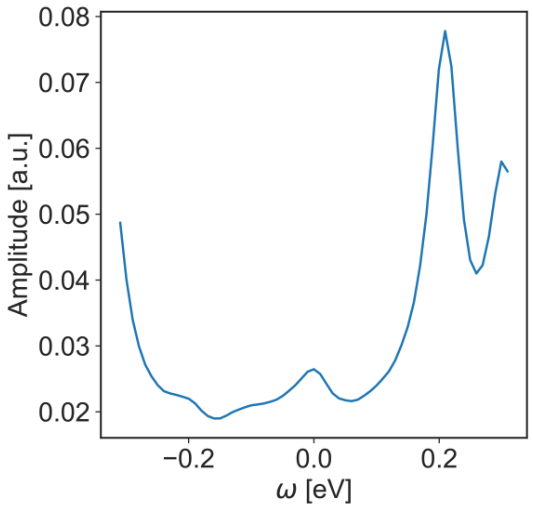

Fig. 7.E.7: Absorption spectra of the excitonic dimer collected from ibmq_manila quantum processor without measurement error mitigation. An artifact emerges at zero frequency due to the uneven probability of correctly measuring states 0 and 1.

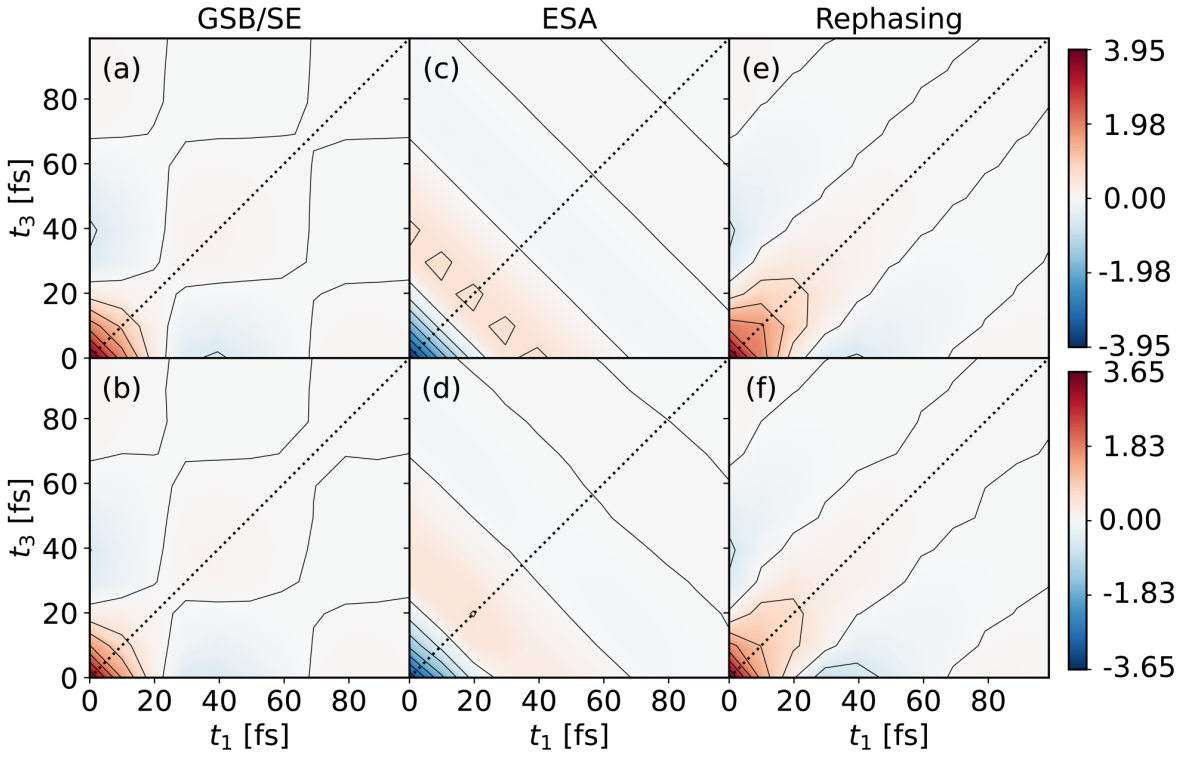

Fig. 7.E.8: Real parts of the third signal for the (a, b) GSB (equal to the SE), (c, d) ESA and (e, f) rephasing signal (obtained as the sum of the GSB, SE and ESA contributions). Panels (a, c, e) are obtained from Qiskit qasm_simulator, while (b, d, f) result from ibm_manila quantum processor.

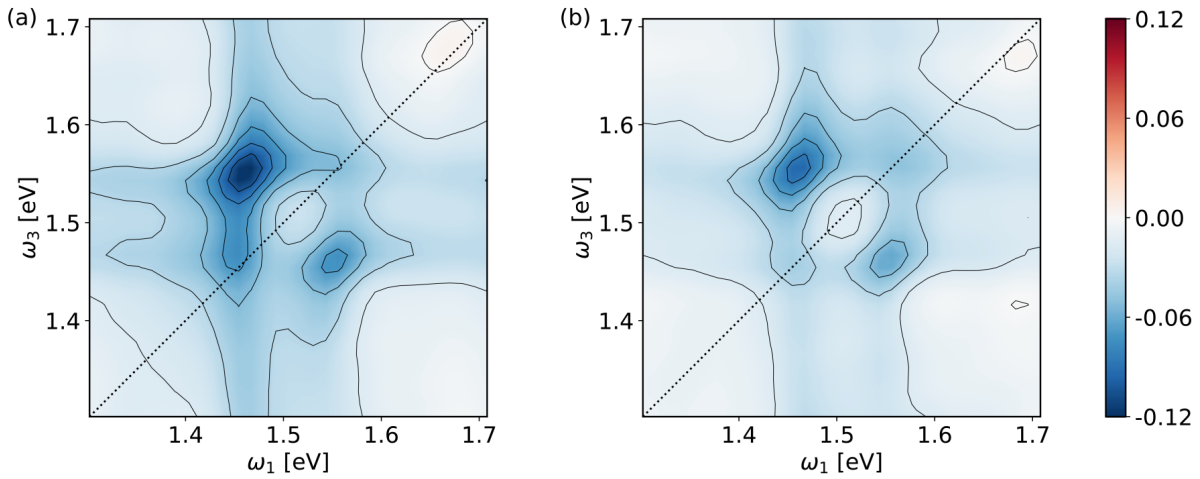

Fig. 7.E.9: Real part of the third order ESA spectra of the excitonic dimer collected during two independent runs of the quantum algorithm on the ibm_perth quantum processor

References

(1) Scholes, G. D.; Fleming, G. R.; Chen, L. X.; Aspuru-Guzik, A.; Buchleitner, A.; Coker, D. F.; Engel, G. S.; van Grondelle, R.; Ishizaki, A.; Jonas, D. M.; Lundeen, J. S.; McCusker, J. K.; Mukamel, S.; Ogilvie, J. P.; Olaya-Castro, A.; Ratner, M. A.; Spano, F. C.; Whaley, K. B.; Zhu, X. Using Coherence to Enhance Function in Chemical and Biophysical Systems. *Nature* **2017**, *543*, 647–656.

(2) Mančal, T. A Decade with Quantum Coherence: How our Past Became Classical and the Future Turned Quantum. *Chem. Phys.* **2020**, *532*, 110663.

(3) Kim, Y.; Eddins, A.; Anand, S.; Wei, K. X.; van den Berg, E.; Rosenblatt, S.; Nayfeh, H.; Wu, Y.; Zaletel, M.; Temme, K.; Kandala, A. Evidence for the Utility of Quantum Computing Before Fault Tolerance. *Nature* **2023**, *618*, 500–505.

(4) Engel, G. S.; Calhoun, T. R.; Read, E. L.; Ahn, T.-K.; Mančal, T.; Cheng, Y.-C.; Blankenship, R. E.; Fleming, G. R. Evidence for Wavelike Energy Transfer through Quantum Coherence in Photosynthetic Systems. *Nature* **2007**, *446*, 782–786.

(5) Collini, E.; Wong, C. Y.; Wilk, K. E.; Curmi, P. M. G.; Brumer, P.; Scholes, G. D. Coherently Wired Light-Harvesting in Photosynthetic Marine Algae at Ambient Temperature. *Nature* **2010**, *463*, 644–647.

(6) Fresch, E.; Meneghin, E.; Agostini, A.; Paulsen, H.; Carbonera, D.; Collini, E. How the Protein Environment Can Tune the Energy, the Coupling, and the Ultrafast Dynamics of Interacting Chlorophylls: The Example of the Water-Soluble Chlorophyll Protein. *J. Phys. Chem. Lett.* **2020**, *11*, 1059–1067.

(7) Policht, V. R.; Niedringhaus, A.; Willow, R.; Laible, P. D.; Bocian, D. F.; Kirmaier, C.; Holten, D.; Mančal, T.; Ogilvie, J. P. Hidden Vibronic and Excitonic Structure and Vibronic Coherence Transfer in the Bacterial Reaction Center. *Sci. Adv.* **2022**, *8*, eabk0953.

(8) Lim, J.; Paleček, D.; Caycedo-Soler, F.; Lincoln, C. N.; Prior, J.; von Berlepsch, H.; Huelga, S. F.; Plenio, M. B.; Zigmantas, D.; Hauer, J. Vibronic Origin of Long-Lived Coherence in an Artificial Molecular Light Harvester. *Nat. Commun.* **2015**, *6*, 7755.

(9) Righetto, M.; Bolzonello, L.; Volpato, A.; Amoruso, G.; Panniello, A.; Fanizza, E.; Striccoli, M.; Collini, E. Deciphering Hot- and Multi-Exciton dynamics in Core–Shell QDs by 2D Electronic Spectroscopies. *Phys. Chem. Chem. Phys.* **2018**, *20*, 18176–18183.

(10) Collini, E.; Gattuso, H.; Kolodny, Y.; Bolzonello, L.; Volpato, A.; Fridman, H. T.; Yochelis, S.; Mor, M.; Dehnel, J.; Lifshitz, E.; Paltiel, Y.; Levine, R. D.; Remacle,

F. Room-Temperature Inter-Dot Coherent Dynamics in Multilayer Quantum Dot Materials. *J. Phys. Chem. C* **2020**, *124*, 16222–16231.

(11) Finkelstein-Shapiro, D.; Mante, P.-A.; Sarisozen, S.; Wittenbecher, L.; Minda, I.; Balci, S.; Pullerits, T.; Zigmantas, D. Understanding Radiative Transitions and Relaxation Pathways in Plexcitons. *Chem* **2021**, *7*, 1092–1107.

(12) Mukamel, S., *Principles of Nonlinear Optical Spectroscopy*; Oxford Series on Optical and Imaging Sciences; Oxford University Press: 1995.

(13) Rose, P. A.; Krich, J. J. Numerical Method for Nonlinear Optical Spectroscopies: Ultrafast Ultrafast Spectroscopy. *J. Chem. Phys.* **2019**, *150*, 214105.

(14) Rose, P. A.; Krich, J. J. Efficient Numerical Method for Predicting Nonlinear Optical Spectroscopies of Open Systems. *J. Chem. Phys.* **2021**, *154*, 034108.

(15) Jansen, T. L. C. Computational Spectroscopy of Complex Systems. *J. Chem. Phys.* **2021**, *155*, 170901.

(16) Gelin, M. F.; Chen, L.; Domcke, W. Equation-of-Motion Methods for the Calculation of Femtosecond Time-Resolved 4-Wave-Mixing and N-Wave-Mixing Signals. *Chem. Rev.* **2022**, *122*, 17339–17396.

(17) Bruschi, M.; Gallina, F.; Fresch, B. Simulating Action-2D Electronic Spectroscopy of Quantum Dots: Insights on the Exciton and Biexciton Interplay from Detection-Mode and Time-Gating. *Phys. Chem. Chem. Phys.* **2022**, *24*, 27645–27659.

(18) Bruschi, M.; Bolzonello, L.; Gallina, F.; Fresch, B. Unifying Nonlinear Response and Incoherent Mixing in Action-2D Electronic Spectroscopy. *J. Phys. Chem. Lett.* **2023**, *14*, 6872–6879.

(19) Feynman, R. P. Simulating Physics with Computers. *Int. J. Theor. Phys.* **1982**, *21*, 467–488.

(20) Lloyd, S. Universal Quantum Simulators. *Science* **1996**, *273*, 1073–1078.

(21) Kassal, I.; Jordan, S. P.; Love, P. J.; Mohseni, M.; Aspuru-Guzik, A. Polynomial-Time Quantum Algorithm for the Simulation of Chemical Dynamics. *Proc. Natl. Acad. Sci. USA* **2008**, *105*, 18681–18686.

(22) Castaldo, D.; Rosa, M.; Corni, S. Quantum Optimal Control with Quantum Computers: A Hybrid Algorithm Featuring Machine Learning Optimization. *Phys. Rev. A* **2021**, *103*, 022613.

(23) Kovyrshin, A.; Skogh, M.; Tornberg, L.; Broo, A.; Mensa, S.; Sahin, E.; Symons, B. C. B.; Crain, J.; Tavernelli, I. Nonadiabatic Nuclear–Electron Dynamics: A Quantum Computing Approach. *J. Phys. Chem. Lett.* **2023**, *14*, 7065–7072.

(24) Chan, H. H. S.; Meister, R.; Jones, T.; Tew, D. P.; Benjamin, S. C. Grid-Based Methods for Chemistry Simulations on a Quantum Computer. *Sci. Adv.* **2023**, *9*, eabo7484.

(25) Young, S. M.; Häffner, H.; Sarovar, M. Quantum Simulation of Weak-Field Light-Matter Interactions. *Phys. Rev. Res.* **2023**, *5*, 013027.

(26) MacDonell, R. J.; Navickas, T.; Wohlers-Reichel, T. F.; Valahu, C. H.; Rao, A. D.; Millican, M. J.; Currington, M. A.; Biercuk, M. J.; Tan, T. R.; Hempel, C.; Kassal, I. Predicting Molecular Vibronic Spectra using Time-Domain Analog Quantum Simulation. *Chem. Sci.* **2023**, 16–22.

(27) Cai, X.; Fang, W.-H.; Fan, H.; Li, Z. Quantum Computation of Molecular Response Properties. *Phys. Rev. Res.* **2020**, *2*, 033324.

(28) Lee, C.-K.; Hsieh, C.-Y.; Zhang, S.; Shi, L. Simulation of Condensed-Phase Spectroscopy with Near-Term Digital Quantum Computers. *J. Chem. Theory Comput.* **2021**, *17*, 7178–7186.

(29) Chen, H.; Nusspickel, M.; Tilly, J.; Booth, G. H. Variational Quantum Eigensolver for Dynamic Correlation Functions. *Phys. Rev. A* **2021**, *104*, 032405.

(30) Huang, K.; Cai, X.; Li, H.; Ge, Z.-Y.; Hou, R.; Li, H.; Liu, T.; Shi, Y.; Chen, C.; Zheng, D.; Xu, K.; Liu, Z.-B.; Li, Z.; Fan, H.; Fang, W.-H. Variational Quantum Computation of Molecular Linear Response Properties on a Superconducting Quantum Processor. *J. Phys. Chem. Lett.* **2022**, *13*, 9114–9121.

(31) Cleve, R.; Ekert, A.; Macchiavello, C.; Mosca, M. Quantum Algorithms Revisited. *Proc. Math. Phys. Eng. Sci.* **1998**, *454*, 339–354.

(32) Somma, R.; Ortiz, G.; Gubernatis, J. E.; Knill, E.; Laflamme, R. Simulating Physical Phenomena by Quantum Networks. *Phys. Rev. A* **2002**, *65*, 042323.

(33) Pedernales, J. S.; Di Candia, R.; Egusquiza, I. L.; Casanova, J.; Solano, E. Efficient Quantum Algorithm for Computing *n*-time Correlation Functions. *Phys. Rev. Lett.* **2014**, *113*, 020505.

(34) Wecker, D.; Hastings, M. B.; Wiebe, N.; Clark, B. K.; Nayak, C.; Troyer, M. Solving Strongly Correlated Electron Models on a Quantum Computer. *Phys. Rev. A* **2015**, *92*, 062318.

(35) Xin, T.; Pedernales, J. S.; Lamata, L.; Solano, E.; Long, G.-L. Measurement of Linear Response Functions in Nuclear Magnetic Resonance. *Sci. Rep.* **2017**, *7*, 12797.

(36) Roggero, A.; Carlson, J. Dynamic Linear Response Quantum Algorithm. *Phys. Rev. C* **2019**, *100*, 034610.

(37) Del Re, L.; Rost, B.; Foss-Feig, M.; Kemper, A. F.; Freericks, J. K. Robust Measurements of N-point Correlation Functions of Driven-Dissipative Quantum Systems on a Digital Quantum Computer. **2022**, 1–10, arXiv: 2204.12400.

(38) Ollitrault, P. J.; Kandala, A.; Chen, C.-F.; Barkoutsos, P. K.; Mezzacapo, A.; Pistoia, M.; Sheldon, S.; Woerner, S.; Gambetta, J. M.; Tavernelli, I. Quantum Equation of Motion for Computing Molecular Excitation Energies on a Noisy Quantum Processor. *Phys. Rev. Res.* **2020**, *2*, 043140.

(39) McClean, J. R.; Kimchi-Schwartz, M. E.; Carter, J.; de Jong, W. A. Hybrid Quantum-Classical Hierarchy for Mitigation of Decoherence and Determination of Excited States. *Phys. Rev. A* **2017**, *95*, 042308.

(40) Higgott, O.; Wang, D.; Brierley, S. Variational Quantum Computation of Excited States. *Quantum* **2019**, *3*, 156.

(41) Lee, J.; Huggins, W. J.; Head-Gordon, M.; Whaley, K. B. Generalized Unitary Coupled Cluster Wave functions for Quantum Computation. *J. Chem. Theory Comput.* **2019**, *15*, 311–324.

(42) Gallina, F.; Bruschi, M. qudofedi, 2023.

(43) Gelin, M. F.; Borrelli, R.; Domcke, W. Efficient Orientational Averaging of Nonlinear Optical Signals in Multi-Chromophore Systems. *J. Chem. Phys.* **2017**, *147*, 044114.

(44) Rose, P. A.; Krich, J. J. Automatic Feynman Diagram Generation for Nonlinear Optical Spectroscopies and Application to Fifth-Order Spectroscopy with Pulse Overlaps. *J. Chem. Phys.* **2021**, *154*, 034109.

(45) Yuen-Zhou, J.; Krich, J. J.; Kassal, I.; Johnson, A. S.; Aspuru-Guzik, A., *Ultrafast Spectroscopy*; 2053-2563; IOP Publishing: 2014.

(46) IBM Quantum `https://quantum-computing.ibm.com/` (accessed 07/23/2023).

(47) Schlau-Cohen, G. S.; Ishizaki, A.; Fleming, G. R. Two-Dimensional Electronic Spectroscopy and Photosynthesis: Fundamentals and Applications to Photosynthetic Light-Harvesting. *Chem. Phys.* **2011**, *386*, 1–22.

(48) Bolzonello, L.; Volpato, A.; Meneghin, E.; Collini, E. Versatile Setup for High-Quality Rephasing, Non-Rephasing, and Double Quantum 2D Electronic Spectroscopy. *J. Opt. Soc. Am. B* **2017**, *34*, 1223–1233.

(49) Gallina, F.; Bruschi, M.; Fresch, B. Strategies to Simulate Dephasing-Assisted Quantum Transport on Digital Quantum Computers. *New J. Phys.* **2022**, *24*, 023039.

(50) Jansen, T. l. C.; Knoester, J. Nonadiabatic Effects in the Two-Dimensional Infrared Spectra of Peptides: Application to Alanine Dipeptide. *J. Phys. Chem. B* **2006**, *110*, 22910–22916.

(51) Chen, L.; Bennett, D. I. G.; Eisfeld, A. Calculating Nonlinear Response Functions for Multidimensional Electronic Spectroscopy using Dyadic Non-Markovian Quantum State Diffusion. *J. Chem. Phys.* **2022**, *157*, 114104.

(52) Hu, Z.; Head-Marsden, K.; Mazziotti, D. A.; Narang, P.; Kais, S. A General Quantum Algorithm for Open Quantum Dynamics Demonstrated with the Fenna-Matthews-Olson Complex. *Quantum* **2022**, *6*, 726.

(53) Gupta, P.; Chandrashekar, C. M. Digital Quantum Simulation Framework for Energy Transport in an Open Quantum System. *New J. Phys.* **2020**, *22*, 123027.

(54) Jaderberg, B.; Eisfeld, A.; Jaksch, D.; Mostame, S. Recompilation-Enhanced Simulation of Electron–Phonon Dynamics on IBM Quantum Computers. *New J. Phys.* **2022**, *24*, 093017.

(55) Ollitrault, P. J.; Mazzola, G.; Tavernelli, I. Nonadiabatic Molecular Quantum Dynamics with Quantum Computers. *Phys. Rev. Lett.* **2020**, *125*, 260511.

(56) Sanders, J. N.; Saikin, S. K.; Mostame, S.; Andrade, X.; Widom, J. R.; Marcus, A. H.; Aspuru-Guzik, A. Compressed Sensing for Multidimensional Spectroscopy Experiments. *J. Phys. Chem. Lett.* **2012**, *3*, 2697–2702.

(57) Roeding, S.; Klimovich, N.; Brixner, T. Optimizing Sparse Sampling for 2D Electronic Spectroscopy. *J. Chem. Phys.* **2017**, *146*, 084201.

(58) Wang, Z.; Lei, S.; Karki, K. J.; Jakobsson, A.; Pullerits, T. Compressed Sensing for Reconstructing Coherent Multidimensional Spectra. *J. Phys. Chem. A* **2020**, *124*, 1861–1866.

(59) Bolzonello, L.; van Hulst, N. F.; Jakobsson, A. Fisher Information in Time-Domain Spectroscopy, 2023, arXiv: 2303.07454 [physics.optics].

(60) Kowalewski, M.; Fingerhut, B. P.; Dorfman, K. E.; Bennett, K.; Mukamel, S. Simulating Coherent Multidimensional Spectroscopy of Nonadiabatic Molecular Processes: From the Infrared to the X-ray Regime. *Chem. Rev.* **2017**, *117*, 12165–12226.

(61) Baiz, C. R.; Błasiak, B.; Bredenbeck, J.; Cho, M.; Choi, J.-H.; Corcelli, S. A.; Dijkstra, A. G.; Feng, C.-J.; Garrett-Roe, S.; Ge, N.-H.; Hanson-Heine, M. W. D.; Hirst, J. D.; Jansen, T. L. C.; Kwac, K.; Kubarych, K. J.; Londergan, C. H.; Maekawa, H.; Reppert, M.; Saito, S.; Roy, S.; Skinner, J. L.; Stock, G.; Straub, J. E.; Thielges, M. C.; Tominaga, K.; Tokmakoff, A.; Torii, H.; Wang, L.; Webb, L. J.; Zanni, M. T. Vibrational Spectroscopic Map, Vibrational Spectroscopy, and Intermolecular Interaction. *Chem. Rev.* **2020**, *120*, 7152–7218.

(62) Damtie, F. A.; Wacker, A.; Pullerits, T.; Karki, K. J. Two-Dimensional Action Spectroscopy of Excitonic Systems: Explicit Simulation using a Phase-Modulation Technique. *Phys. Rev. A* **2017**, *96*, 053830.

8 | Perspectives

The investigation presented in this Thesis has clarified different aspects concerning the interpretation of the response in A-2DES. At the same time, however, it brought to light several questions and exposed a number of open problems to be tackled in future research.

A first aspect concerns the interplay between the non-linear response and incoherent mixing in the spectrum of complex excitonic systems. On the one hand, it is necessary to understand when incoherent mixing can actually provide information about the interaction network at play in the system. An example is provided by the investigation of long-range transport mechanisms in extended systems exploiting the exciton-exciton annihilation process, as demonstrated in the setting of two-pulse experiments [1, 2]. On the other hand, it is necessary to find effective strategies to reduce the amount of incoherent mixing to the spectrum in order to expose the clean non-linear response. Apart from the already mentioned use of time-gating of the signal during the detection-time, frequency-gating method has recently been proposed in order to isolate the stimulated emission contribution [3]. Furthermore, we believe that the use of cross-polarization pulse sequences [4] may aid in reducing the contribution of cross-peaks related to incoherent mixing.

In recent years, there has been a push towards exploring higher-order contributions of the non-linear response [5, 6]. This fact has gained relevance after the proposal of different techniques aimed at isolating multi-particle interactions and their dynamics [7–9]. In this context, the theoretical analysis of the associated spectral features is still under development due to the inherent complexity of these signal, however initial attempts have been proposed in this direction [10, 11]. In particular, the non-perturbative approach developed in this thesis is particularly promising for the investigation of higher-order response.

Another aspect that has received limited attention, from both theoretical and experimental perspectives, is the investigation of the dynamics of the spectral features of A-2DES during the waiting-time [12, 13]. Particular interest should be directed towards the study of coherences, whether inter-excitonic or inter-site in nature. Furthermore, the signatures of vibronic and vibrational features in the spectrum still remain to be explored.

References

(1) McNamee, M. G.; Ouyang, Z.; Yan, L.; Gan, Z.; Zhou, N.; Williams, O. F.; You, W.; Moran, A. M. Uncovering Transport Mechanisms in Perovskite Materials and Devices with Recombination-Induced Action Spectroscopies. *J. Phys. Chem. C* **2023**, *127*, 2782–2791.

(2) Rojas-Gatjens, E.; Yallum, K. M.; Shi, Y.; Zheng, Y.; Bills, T.; Perini, C. A. R.; Correa-Baena, J.-P.; Ginger, D. S.; Banerji, N.; Silva-Acuña, C. Resolving Nonlinear Recombination Dynamics in Semiconductors via Ultrafast Excitation Correlation Spectroscopy: Photoluminescence versus Photocurrent Detection. *J. Phys. Chem. C* **2023**, *127*, 15969–15977.

(3) Yang, J.; Gelin, M. F.; Chen, L.; Šanda, F.; Thyrhaug, E.; Hauer, J. Two-Dimensional Fluorescence Excitation Spectroscopy: A Novel Technique for Monitoring Excited-State Photophysics of Molecular Species with High Time and Frequency Resolution. *J. Chem. Phys.* **2023**, *159*, 074201.

(4) Read, E. L.; Engel, G. S.; Calhoun, T. R.; Mančal, T.; Ahn, T. K.; Blankenship, R. E.; Fleming, G. R. Cross-Peak-Specific Two-Dimensional Electronic Spectroscopy. *Proc. Natl. Acad. Sci. USA,* **2007**, *104*, 14203–14208.

(5) Mueller, S.; Brixner, T. Molecular Coherent Three-Quantum Two-Dimensional Fluorescence Spectroscopy. *J. Phys. Chem. Lett.* **2020**, *11*, 5139–5147.

(6) Malý, P.; Mueller, S.; Lüttig, J.; Lambert, C.; Brixner, T. Signatures of Exciton Dynamics and Interaction in Coherently and Fluorescence-Detected Four- and Six-Wave-Mixing Two-Dimensional Electronic Spectroscopy. *J. Chem. Phys.* **2020**, *153*, 144204.

(7) Malý, P.; Lüttig, J.; Rose, P. A.; Turkin, A.; Lambert, C.; Krich, J. J.; Brixner, T. Separating Single- from Multi-Particle Dynamics in Nonlinear Spectroscopy. *Nature* **2023**, *616*, 280–287.

(8) Lüttig, J.; Rose, P. A.; Malý, P.; Turkin, A.; Bühler, M.; Lambert, C.; Krich, J. J.; Brixner, T. High-Order Pump–Probe and High-Order Two-Dimensional Electronic Spectroscopy on the Example of Squaraine Oligomers. *J. Chem. Phys.* **2023**, *158*, 234201.

(9) Lüttig, J.; Mueller, S.; Malý, P.; Krich, J. J.; Brixner, T. Higher-Order Multidimensional and Pump–Probe Spectroscopies. *J. Phys. Chem. Lett.* **2023**, *14*, 7556–7573.

(10) Rose, P. A.; Krich, J. J. Automatic Feynman Diagram Generation for Nonlinear Optical Spectroscopies and Application to Fifth-Order Spectroscopy with Pulse Overlaps. *J. Chem. Phys.* **2021**, *154*, 034109.

(11) Rose, P. A.; Krich, J. J. Interpretations of High-Order Transient Absorption Spectroscopies, 2023, arXiv: 2309.02659 [physics.chem-ph].

(12) Tiwari, V.; Matutes, Y. A.; Konar, A.; Yu, Z.; Ptaszek, M.; Bocian, D. F.; Holten, D.; Kirmaier, C.; Ogilvie, J. P. Strongly Coupled Bacteriochlorin Dyad studied using Phase-Modulated Fluorescence-Detected Two-Dimensional Electronic Spectroscopy. *Opt. Express* **2018**, *26*, 22327–22341.

(13) Malý, P.; Lüttig, J.; Mueller, S.; Schreck, M. H.; Lambert, C.; Brixner, T. Coherently and Fluorescence-Detected Two-Dimensional Electronic Spectroscopy: Direct Comparison on Squaraine Dimers. *Phys. Chem. Chem. Phys.* **2020**, *22*, 21222–21237.